Volumetric Velocity Measurement of Aquatic Predator-Prey Interactions

A Thesis
SUBMITTED TO THE FACULTY OF
UNIVERSITY OF MINNESOTA
BY

Deepak Adhikari

IN PARTIAL FULFILLMENT OF THE REQUIREMENTS
FOR THE DEGREE OF
DOCTOR OF PHILOSOPHY

Adviser: Professor Ellen K. Longmire

December 2013

Acknowledgements

I had the privilege of working with exceptional individuals during the course of this work. I would like to thank all of them for making my experience a fruitful one.

Professor Ellen Longmire has been the central guide for my research, and it has been a pleasure working with her. Through her, I have gained insights into the art of scientific research and the ability to communicate my research work effectively to audience from various disciplines. I have gained much perspective to approach problems in fluid mechanics from a fundamental standpoint, and I am thankful for her patience and support through the years. Her office door never closes for discussion!

In addition, my appreciation goes to my committee members and reviewers - Professor Roger Arndt, Professor Krishnan Mahesh, and Professor Mihailo Jovanovic for agreeing to serve in the committee and providing useful feedback.

I would like to thank our collaborator Professor Edward Buskey (Marine Science Institute, University of Texas Austin) for providing many insights to the world of marine biology, providing lab space and accommodation during my visit to the institute.

I had a pleasure of working with talented post-doctoral associates. Dr. Brad Gemmell was instrumental in helping out with the experimental setup and providing insights on various organisms used for this thesis. Dr. Michael Hallberg contributed some ideas for particle tracking algorithms, and helped in transporting and assembling/disassembling the water channel facility to/from Texas.

I would like to thank Dr. Steve Anderson (LaVision Inc, USA), Dr. Dirk Michaelis (LaVision GmbH) and Dr. Bernd Wieneke (LaVision GmbH) for the various discussions on Tomographic PIV. I am also grateful to Dr. Wing Lai, Dr. Dan Troolin, Dr. Matt Stegmeir and Mr. Dan Bissell from TSI Inc, USA for the various information exchanges I had with them regarding imaging and volumetric PIV system.

I would like to thank Dave Hultman and his team during his time at the Research Shop at the University of Minnesota. His active involvement in discussing design ideas and machining various components has helped tremendously to develop the measurement system and water channel facility.

I had an excellent opportunity to work with various undergraduates in the project. I would like to thank Alex Schreiner (Summer 2011), Greg Hoepfner (Summer 2010), Michael Voller (Summer 2013) for taking immense interest, providing very unique perspective to problems, and helping the project.

Working in the fluid dynamics lab has been a very enriching experience. I would like to acknowledge all previous and current lab mates for the many social events, discussions, and help I have had over the years: Dr. Qi Gao, Dr. Zhengzhong Sun, Alonso Alvarado, Ankur Bordoloi, Anwar Chengala, David Green, Erik Haugen, Stephen Hu, Daniel Krizan, Jeshwanth Kundem, Mehdi Molaei, Mitch Ryan, Yan Ming Tan, Mostafa Toloui, Kyle Winters and Shaokai Zheng. It was great to have you all around, and the various "great success" moments will always be etched in my mind for years to come.

Finally, I am extremely grateful to my beautiful and loving wife, Seema Dahal, for her patience, support and care.

Funding from the National Science Foundation - IDBR Grant No #0852875, and the University of Minnesota Graduate Fellowship is gratefully acknowledged. Experiments were conducted under full compliance of the Institutional Animal Care and Use Committee at the University of Minnesota, and the University of Texas at Austin.

Dedication

To my parents and my brother for their tremendous inspiration and support.

Abstract

The aim of this study is to develop a novel multi-scale volumetric measurement system and flow facility, and apply it to improve understanding of aquatic predator-prey interactions. A combined infrared tomographic PIV + 3D PTV system was developed and demonstrated. Tomographic PIV was used to obtain the volumetric velocity field of the flow, while the 3D PTV was used to track the prey, and the eye of the predator, in the same volume. A visual hull technique was implemented to mask out the objects (such as fish) appearing within the reconstructed tomographic PIV volumes, ensuring that velocity vectors near the object/fish were not contaminated during PIV cross-correlation.

Copepods, which make up the majority of the oceanic zooplanktons, are known to sense flow disturbed by approaching predators and can execute sudden high-speed swim (or jump) to escape predation. Although their response to local flow disturbances has been studied, their sensing and swimming response to live predators (fish) is not well understood. Three series of experiments were implemented - (1): Copepod interactions with a wall-mounted cylinder in cross-flow; (2): Predator-prey interactions in still water; (3): Predator-prey interactions in unsteady/turbulent flow.

From the experiments, copepods appeared to respond (jump) to a large and sudden increase in local maximum principal strain rate (MPSR) of the fluid, instead of a fixed threshold quantity. For fish predation in still water, zebrafish were first observed to approach slowly, followed by sudden acceleration (ram feeding) to feed on copepods. Using a potential flow model, it was found that this strategy might not be sufficient to capture copepods successfully. Thus, zebrafish were found to execute suction feeding simultaneously to increase chances of predation success. In uniform cross flow, a coral reef fish (blenny) used a similar slow approach - ram feeding strategy to feed on copepods, but it rarely captured them. However, turbulent cross flow increased the chances of predation by allowing the fish to approach closer to a copepod, and preventing the copepod from detecting hydrodynamic signals from the approaching predator.

Table of Contents

Acknowledgement i
Dedication iii
Abstract iv
List of Tables x
List of Figures xi
Nomenclature xxvi

1. Introduction 1

1.1 Motivation 2

1.2 Previous work 7

1.2.1 Copepods 7

1.2.1.1 Sensing 7

1.2.1.2 Locomotion 9

1.2.2 Predator-prey interaction 12

1.2.2.1 Predation 12

1.2.2.2 Interaction with turbulence 13

1.2.3 Velocimetry and tracking 15

1.2.3.1 Volumetric velocimetry 17

1.2.3.2 Tomographic PIV 18

1.3 **Objectives 21**

2. Experimental Facilities and Methodologies 23

2.1 Water channel facility 23

2.1.1 Design 23

2.1.2 Development 27

2.1.3 Installation 28

2.1.4 Transportation 35

2.1.5 Flow qualification 37
2.1.5.1 Uniformity 37
2.1.5.2 Turbulence intensity 39
2.1.5.3 Calibration function of mean flow w.r.t the paddlewheel revolution 40
2.2 Measurement hardware 41
2.2.1 Laser 42
2.2.2 Cameras 43
2.2.3 Tracer particles 44
2.3 Experiment (1) setup: Copepod interactions with wall-mounted cylinder in cross-flow 47
2.3.1 Species 48
2.3.2 Experimental setup 48
2.3.2.1 Facility 48
2.3.2.2 Infrared tomographic PIV + 3D PTV: Measurement setup 51
2.3.2.3 Infrared tomographic PIV + 3D PTV: Methodology 54
2.3.2.4 Infrared tomographic PIV + 3D PTV: Uncertainty 57
2.3.2.5 Infrared tomographic PIV + 3D PTV: Velocity and velocity gradients 58
2.3.3 Experimental procedures 61
2.4 Experiment (2) setup: Predator-prey interactions in still water 61
2.4.1 Species 61
2.4.2 Experimental setup 62
2.4.2.1 Facility 62
2.4.2.2 Infrared tomographic PIV 65
2.4.2.3 Motion tracking of predator and prey 67
2.4.2.4 Uncertainty and signal-to-noise ratio 67
2.4.3 Experimental procedures 69
2.4.4 Organism behavior 70
2.5 Experiment (3) setup: Predator-prey interactions in unsteady/turbulent water 71

2.5.1 Species 71
2.5.2 Experimental setup 72
2.5.2.1 Facility 72
2.5.2.2 Infrared tomographic PIV + 3D PTV 74
2.5.2.3 Uncertainty 75
2.5.3 Experimental procedures 76

3. Visual Hull Method for Tomographic PIV of flow around Moving Objects 77
3.1 Introduction 78
3.2 Current techniques to isolate moving objects in PIV fields 80
3.2.1 Planar PIV fields 80
3.2.2 Volumetric PIV fields 81
3.3 Experimental apparatus 84
3.3.1 Experimental setup 84
3.3.2 Falling (Moving) objects 87
3.4 Visual hull and tomographic PIV methodology 88
3.4.1 Visual hull 88
3.4.1.1 Detection of Silhouette 88
4.3.1.2 Reconstruction of Object in 3D Space 90
3.4.2 Tomographic PIV 93
3.5 Results 97
3.5.1 Reconstructed object (Visual hull) 97
3.5.2 Vector field around the moving object 99
3.6 Discussion of visual hull implementation 103
3.7 Conclusions 115
3.8 Application: Fish 117

4. Results and Analysis 121
4.1 Experiment (1): Copepod interactions with wall-mounted cylinder in cross-flow 121

4.1.1 Upstream of cylinder 121
4.1.1.1 Detecting copepod jumps 121
4.1.1.2 Copepod jump locations 124
4.1.1.3 Copepod sensing 126
4.1.1.4 Copepod locomotion 141
4.1.2 Copepod distribution downstream of cylinder 149
4.1.2.1 Stokes number and hypothesis 150
4.1.2.2 Copepod spatial distribution and sensing 151
4.2 Experiment (2): Predator-prey interactions in still water 155
4.2.1 Free-swimming zebrafish 155
4.2.2 Zebrafish feeding on non-evasive prey 158
4.2.3 Zebrafish feeding on evasive prey 164
4.2.4 Capture and escape of evasive prey 173
4.3 Experiment (3): Predator-prey interactions in unsteady/turbulent flow 180
4.3.1 Predator-prey interaction in uniform cross-flow 180
4.3.2 Flow field surrounding feeding fish in cross-flow 183
4.3.3 Local flow quantities when copepod escapes 186
4.3.4 Velocity profile of fish and copepod 193
4.3.5 Flow field caused by fish feeding in cylinder wake 200

5. Discussions and Conclusions 208
5.1 Applications of measurement technique 208
5.1.1 Infrared tomographic PIV + 3D PTV 208
5.1.1 Visual hull method for tomographic PIV 209
5.2 Copepod sensing and locomotion 210
5.2.1 What local flow characteristics do copepods sense before they jump? 210
5.2.2 What is the direction and maximum speed of copepod jumps? 212
5.3 Fish motion and predation 213
5.3.1 What is the strategy for successful fish predation on copepods? 213
5.3.2 How do fish capture non-evasive and evasive prey? 218

6. Future Work 221

6.1 Towards advancing measurement system for multi-scale flows.....221

6.2 Towards modeling copepod sensing and locomotion.....223

6.2.1 Sensing.....233

6.2.1 Locomotion.....223

6.3 Universality of fish feeding on evasive prey 223

Bibliography.....225

Appendix A: Head loss calculation and motor power requirement for water channel.....234

Appendix B: Circular Hough transform.....236

Appendix C: Formulae derivations for obscured regions of a simple shape and standard four-camera configuration 238

Appendix D: Proof of $\{||d\underline{u}/dt|| \leq ||\underline{u}|| \times MPSR\}$ for steady-state, irrotational flow ...244

List of Tables

Table 2-1: Description of material and fabrication location for various parts of the water channel 28

Table 2-2: Velocity range and percentage variation in velocity measurement for cases of 1, 2, 5, 10 RPM. 39

Table 2-3: Table of tested seeding particles for Tomographic PIV and 3D PTV 45

Table 2-4: Experimental cases carried out for copepod interaction with cylinder (upstream and downstream) 50

Table 4-1: Experimental cases carried out for copepod interaction with cylinder (upstream) 124

Table 4-2: Summary of the number of copepod tracks, total number of jumps and number of jumps after cut-off for cases 1 – 4. 126

List of Figures

Figure 1-1: Typical food chain in an aquatic ecosystem 2

Figure 1-2: Image of a copepod (Acartia tonsa). Reproduced from http://www.sciencedaily.com..... 3

Figure 1-3: Schematic diagram showing the disturbance of fluid in front of the fish during fish-copepod interaction in still water..... 5

Figure 1-4: Schematic diagram showing the disturbance of fluid experienced by copepod during fish-copepod interaction in turbulent water..... 6

Figure 1-5: Schematic representation of a (a) regularly structured grid generated by planar PIV, and (b) unstructured grid generated by planar PTV. 16

Figure 1-6: Schematic diagram representing tomographic PIV (Reproduced from Elsinga et al 2006) 20

Figure 2-1: Schematic diagram of the water channel facility. (a) shows the bird's-eye view from the front, (b) shows the top view of the channel with channel dimensions and flow conditioners. The bold arrow represents the direction of flow. 26

Figure 2-2: Attachment of corner section with the straight section and the location of guide vanes..... 29

Figure 2-3: Arrangement of spacers, honeycombs, and screens (a) upstream and (b) downstream of the test section. 30

Figure 2-4: Paddlewheel connections, and clamps 32

Figure 2-5: Diagram depicting the signal passages in the motor-paddlewheel assembly 33

Figure 2-6: (a) image and (b) schematic front view of the cavity and PVC fixture. An acrylic plate is placed above the test section to prevent surface waves from interfering with the laser. 33

Figure 2-7: Completed water channel setup with the measurement system. 34

Figure 2-8: Map depicting the location where the channel was transported for seawater experiments. (a) and (b) show the same experimental facility at different locations. 36

Figure 2-9: Mean velocity flow field of 500 datasets for (a) 1 RPM, (b) 2 RPM, (c) 5RPM, and (d) 10 RPM. 38

Figure 2-10: Turbulence intensity of flow field from 500 datasets for (a) 1 RPM, (b) 2 RPM, (c) 5RPM, and (d) 10 RPM. 40

Figure 2-11: Calibration graph showing a linear relationship of mean flow velocity at the test section and rotational speed of the paddle wheel. 41

Figure 2-12: Images showing the scatter of near-infrared illumination (wavelength: 808 nm) by various particles. 46

Figure 2-13: Images showing the scatter of near-infrared illumination (wavelength: 808 nm) by previously tested particles. Epps and Techet (2007) used silver-coated hollow glass spheres, and Murphy *et al.* (2012) used titanium dioxide..... 47

Figure 2-14: Schematic diagram of the water channel setup for experiment (1). (a) shows the cylinder upstream of the test section to examine copepod interaction with the cylinder wake, and (b) shows the cylinder within the test section to study motion of copepods approaching the cylinder. 49

Figure 2-15: Schematic (a) front and (b) top view of the simultaneous tomographic PIV (cameras 1, 2, 3, 4) and 3D PTV measurement system (cameras 5, 6) to measure instantaneous flow field and location of the zooplankton and fish in a volume. Dashed box within the infrared illumination represents the measurement volume. 53

Figure 2-16: Typical image obtained for (a) tomographic PIV and (b) 3D PTV. Images were taken at the same time instance from different cameras. 54

Figure 2-17: Schematic steps for infrared tomographic PIV + 3D PTV technique used to obtain volumetric velocity field of fluid and 3D tracks of zooplankton. 56

Figure 2-18: Probability density function of the relative error distribution of the flow field behind the mounted cylinder. 58

Figure 2-19: Schematic diagram showing the location of a zooplankton with unknown local fluid velocity u_c, and the neighboring grid points with known velocities from tomographic PIV measurement. 59

Figure 2-20: Schematic diagram of the experimental setup. (a) x-y view, (b) x-z view .. 64

Figure 2-21: (a) intensity of reconstructed measurement volume integrated across y-direction, where the illuminated region is bounded by dashed lines. (b) average intensity profile across the z-axis to indicate the signal to noise ratio (signal: dashed line; noise: dotted line). 69

Figure 2-22: Selected time sequence showing zebrafish locating a passive flaked food, approaching it and feeding in the presence of ambient particles and near infrared laser. 71

Figure 2-23: (a) image and (b) schematic diagram of the setup for experiment (3). (i) shows the front view, (ii) shows the top view. 73

Figure 2-24: Sample images of the blenny-copepod interaction in unsteady flow. (a) Instance of tomographic PIV image used to obtain the volumetric velocity field, and (b) 3D motion tracking system (3D PTV) image used to obtain fish eye and copepod tracks. 75

Figure 3-1: Visual hull technique. (a) Projected silhouette of an object in individual image planes. (b) Back-projection for object reconstruction. Note that the cube (dotted

lines) in (b) is smaller than the intersection of back-projected volumes (dashed lines). 83

Figure 3-2: Image of the experimental setup. The light-red fan beam is a representation of the IR laser beam. 85

Figure 3-3: Schematic representation of the experimental setup. The plan view is shown in (a), while front view is shown in (b). The light-red fan beam is a representation of the laser illumination region. The dashed line window in (b) represents the illuminated field of view of the cameras. 86

Figure 3-4: Schematic drawing of the moving objects used in the experiment to demonstrate the application of the proposed technique. 88

Figure 3-5: Image processing sequence to obtain the silhouette of the object with surrounding particles. The raw image is first shown in (a). The image processing sequence are as follows: (a)-(b) median filtering, (b)-(c) standard deviation filtering, (c)-(d) Canny edge detection, (d)-(e) morphological closing, (e)-(f) filling the "holes", (f)-(g) minimum object size criterion. The silhouette (g) of the object is finally obtained, and the comparison of the original object with the silhouette outline shows good agreement (h). 89

Figure 3-6: Processing sequence from (a) image to (b) silhouette and eventually to (c) visual hull of the object. (c) shows the iso-surface of the reconstructed object, which is open at two ends beyond the illuminated volume. 92

Figure 7: Reconstructed volume including a sphere where the images were (a) not pre-processed, (b) pre-processed and (c) masked. The red dashed lines represent the location of the x-z plane (situated above x-y plane). The x-y plane is extracted from middle of x-z plane. In (a), the sphere creates a reconstruction artifact, while in (b) almost no reconstruction artifact is visible. Solid white line in both views of (c) represents the masked portion of the reconstructed particle volume. 95

Figure 3-8: Reconstructed visual hull, shown as translucent iso-surfaces, generated from raw images of a (a) sphere, (b) cube, (c) tetrahedron and (d) cylinder. The solid objects, shown in red, were constructed manually. The location and orientation of each object was estimated from calibrated raw 2D images. These objects are placed to illustrate the fit of the reconstruction. 98

Figure 3-9: Reconstructed visual hull for multiple object orientations. Reconstructed volume in (a) is larger than in (b). 99

Figure 3-10: Vector fields around moving objects for (a) a sphere and (b) a cube. Only two planes at z = 2 mm (blue) and z = 10 mm (red) are shown for clarity. 100

Figure 3-11: Vector field around the moving object for (a) a tetrahedron and (b) a cylinder. Only two planes at z = 2 mm (blue) and z = 10 mm (red) are shown for clarity. 101

Figure 3-12: Visual hull (gray) and "envelopes" of regions optically accessible by 3 cameras (blue), 2 cameras (green), and 1 camera (red). (a) shows the increasing thickness of the region optically accessible by 3 cameras as z decreases. (b) shows x-y view and the vector grid points. Note that four grid points represent an interrogation box length for the cross-correlation with 75% overlap. 103

Figure 3-13: Schematic diagram of the 4 camera projections on the object (cube) which shows the obscured regions when applying the visual hull. Black solid lines represent the edges of the visual hull. Dotted lines outline regions accessible by at most three cameras. Blue (outlined by dashed lines) is accessible by less than three cameras, and green is fully obscured. The visual hull also inherently masks a non-obscured region (yellow) in front of the object. The translucent white and red regions represent the back-projections from each camera and the illuminated volume, respectively. 105

Figure 3-14: Reconstructed particle volumes where a sphere is present in the measurement volume. (a) represents the intensity integrated over the range z = 65 to 140

voxels. The dashed circle in (a) represents the location of the sphere. (b) shows the reconstructed particle volume for (i) a plane with depth of 1 voxel intersecting the center of the sphere (reproduced from figure 3-7b), and (ii) a depth of 12 voxels (physical dimension: 1 mm) in y spanning the sphere centerplane. The insert images (i) and (ii) show close up views of the sphere boundary. 107

Figure 3-15: Schematic diagrams showing the variation in unresolved regions due to changes in object parameters. The (a) original object is compared with changes in its (b) size, (c) orientation, and (d) convexity. Black solid lines represent the edges of the visual hull. 109

Figure 3-16: Schematic diagrams depicting the variation in the unresolved regions due to changes in camera parameters, which include (a) camera viewing angle, (b) camera arrangement, and (c) number of cameras. Black solid lines represent the edges of the visual hull. 111

Figure 3-17: Schematic diagram of a specific "4-corners" camera arrangement. The inclination angles of cameras 1-4, with respect to the vertical direction, are α_1, α_2, α_3, and α_4 respectively. The dimensions of the cuboid are *a* (length) x *b* (width) x *c* (depth), where *a* and *b* are parallel to the laser sheet, and the side faces of the object are aligned with the camera angles. The distance from the rear of the object (relative to the cameras) to the rear edge of the laser sheet is given by *t*. 114

Figure 3-18 Processing sequence from (a) image to (b) silhouette to (c) visual hull of the fish (translucent iso-surface). 119

Figure 3-19: Schematic representation of the various approaches of fish into the measurement volume. (a) Fish enters from the side of the measurement volume (parallel to x-y plane); (b) fish enters the back of the volume (parallel to y-z plane)..... 120

.....

Figure 4-1: Copepod tracks upstream and downstream of the cylinder where U_0 = 0.77 m/s. (a) shows the original tracks where the copepods are observed to execute high-speed jumps upstream of the cylinder (insert), (b) shows the contours on the tracks depicting the ID number of the copepod, and (c) shows only those upstream tracks that include jumps. The circles in (c) represent the locations where the jumps were initiated. 123

Figure 4-2: Locations where high-speed jumps were initiated. (a)-(d) represent Cases 1 – 4 (see table 4-1). The dashed line represents the cut-off location upstream of which behavior was not included for further analysis. 125

Figure 4-3:Probability distribution of the maximum principal strain rate (MPSR) of fluid at the location where a copepod jump was initiated. (a)-(d) represent cases 1 – 4 (see table 4-1) 129

Figure 4-4: Probability distribution of MPSR of fluid upstream of the cylinder. (a)-(d) represents cases 1 – 4 (see table 4-1). 130

Figure 4-5: Probability distribution of vorticity of fluid at the location where copepod jump was initiated. (a)-(d) represents cases 1 – 4 (see table 4-1) 133

Figure 4-6: Probability distribution of vorticity of fluid upstream of the cylinder. (a)-(d) represents cases 1 – 4 (see table 4-1). 134

Figure 4-7: Probability distribution of the Lagrangian acceleration of fluid (following the copepod) at the location where copepod jump was initiated. (a)-(d) represents cases 1 – 4 (see table 4-1)..... 135

Figure 4-8: Probability distribution of Lagrangian acceleration of fluid upstream of the cylinder. (a)-(d) represents cases 1 – 4 (see table 4-1). 136

Figure 4-9: Graphs of reaction distance against (a) free stream velocity (cylinder radius maintained at 6.35 mm), and (b) cylinder radius (free stream velocity maintained at

0.0384 m/s). Dashed line curves represent 2D potential flow model, and scatter points represent the experimental values. 139

Figure 4-10: Graph of acceleration ($\|d\boldsymbol{u}/dt\|$) against ($\|\boldsymbol{u}\| \times MPSR$). The dashed line is linear relationship derived from 2D potential flow model $\|d\boldsymbol{u}/dt\| = \|\boldsymbol{v}\| \times MPSR_{potential}$. The scattered points represent experimental data: cases 1(●), 2(▲), 3(■), and 4(*). The color contour represents the distance of the copepod from the center of the cylinder in mm. 141

Figure 4-11: Speed relative to the local flow velocity. (a) Experimental and (b) schematic speed-time graph of copepod jump. Dashed curve in (a) represents the outline of the dominant experimental speed-time profile. 143

Figure 4-12: Probability distribution of maximum copepod speed during jumps. Speeds are relative to local flow velocity. (a)-(d) represents cases 1 – 4 (see table 4-1)..... 145

Figure 4-13: Angle histogram (x-y plane) of jump direction of copepod upstream of the cylinder. The cylinder in the middle represents the orientation of the cylinder in this plane. Thick arrows in the plot represent the direction flow. (a)-(d) represent cases 1 – 4 (see table 4-1), (e) represents the total number of copepods from (a)-(d). 147

Figure 4-14: Angle histogram (x-z plane) of jump direction of copepod upstream of the cylinder. The cylinder in the middle represents the orientation of the cylinder in this plane. Thick arrows in the plot represent the direction flow.(a)-(d) represents cases 1 – 4 (see table 4-1), (e) represents the total number of copepods from (a)-(d). 148

Figure 4-15: Volumetric flow field and copepod distribution behind a vertically mounted cylinder located at x = -80 mm, z = 9.5mm. Height of the cylinder has been truncated for clarity. The vorticity iso-surface is $\|\omega\| = 25\ s^{-1}$. 150

Figure 4-16: Zooplankton count against z-direction for (a) brine shrimp and (b) copepods. The count has been normalized with the average value of the respective zooplankton for

clarity in comparison. Counts at each z location include all x and y locations within the field of view (i.e. -40 mm < x < 40 mm; -32 mm < y < 8 mm). 151

Figure 4-17: Probability distribution of the maximum principal strain rate (MPSR) of fluid at the location of brinshrimp (red) and copepods (blue) downstream of cylinder. The x-y plane for all cases was -40 mm < x < 40 mm, -32 mm < y < 8 mm. The z-locations of the measurement volume were (a) directly behind the cylinder (0 < z < 19 mm), (b) offset from cylinder axis 1.5 cm in positive z-direction, (c) offset from cylinder axis by 3.0 cm in positive z-direction. 153

Figure 4-18: (a) Brine shrimp and (b) copepods showing their time series tracks (12 seconds) upstream and downstream of the cylinder with end-on views. Dotted ellipses show some instances of escape response by copepods when nearing the cylinder. 154

Figure 4-19: (a) Selected image sequences of a fish executing free swimming. Grey dot depicts the center of the eye used to track the fish motion. (b) Volumetric velocity field of fluid in absolute frame at a selected time (t = 20ms). Eye center is marked as a grey sphere within the visual hull. White '+' is the estimated location of the fish mouth..... 157

Figure 4-20: (a) Selected image sequences of a fish feeding on non-evasive prey (water flea). White dot depicts the location of the prey. Grey dot is location of eye center. (b) Corresponding fluid velocity fields in absolute frame. Only vectors in the sagittal plane of the fish are shown. 160

Figure 4-21: Absolute velocity of fluid as fish captures non-evasive prey, t = 20 ms. The black dot gives the location of the prey at t = 0 ms, white dot depicts the location of the prey, and grey dot is location of eye center. 161

Figure 4-22: Z-component vorticity contours as the fish captures non-evasive prey at t = 20 ms. Only the contours in the sagittal plane of the fish are shown. A large vortex is sustained near the head of the fish during suction feeding from t = 14 - 30 ms. The black

dot gives the location of the prey at t = 0 ms, white dot depicts the location of the prey, and grey dot is location of eye center. 162

Figure 4-23: Velocity field relative to the fish. t = 20 ms. Projections of vectors in the sagittal plane of the fish are shown. Color/contour gives magnitude of 3-component vectors. The black dot gives the location of the prey at t = 0 ms, white dot depicts the location of the prey, and grey dot is location of eye center. 163

Figure 4-24: The velocity magnitude of predator (solid line; ●), prey (dashed line; ■), and local fluid velocity at the location of prey (dotted line; ▲). 164

Figure 4-25: (a) Selected image sequence of a fish feeding on evasive prey (copepod). White dot depicts the location of the prey. Grey dot depicts fish eye center. (b) Corresponding fluid velocity fields in absolute frame. Only vectors in the sagittal plane of the fish are shown. 166

Figure 4-26: Absolute velocity of fluid surrounding fish capturing evasive prey at t = 12 ms. The black dot gives the location of the prey at t = 0 ms, white dot depicts the location of the prey, and grey dot is location of eye center. 167

Figure 4-27: Z-component vorticity contours as fish captures evasive prey at t = 12 ms. Only the contours in the sagittal plane of the fish are shown. The black dot gives the location of the prey at t = 0 ms, white dot depicts the location of the prey, and grey dot is location of eye center. 168

Figure 4-28: Velocity field relative to the fish. t = 12 ms. Projections of vectors in the sagittal plane of the fish are shown. Color/contour gives magnitude of 3-component vectors. The black dot gives the location of the prey at t = 0 ms, white dot depicts the location of the prey, and grey dot is location of eye center. 170

Figure 4-29: Predator eye and prey tracks for time sequence from t = 0 ms to 12 ms. Final (t = 12 ms) location of the predator and prey is shown by the white sphere. The initial (t = 0 ms) location of both predator eye and prey is given by the black sphere... 171

Figure 4-30: The velocity magnitude of predator (solid line; ●), prey (dashed line; ■), and local fluid velocity at the location of prey (dotted line; ▲). 172

Figure 4-31: Volumetric velocity field of the fish capturing evasive prey (copepod) at t = 12 ms. (a) Image and (b) volumetric vector field. White dot depicts the location of the prey, and grey dot depicts the center of the fish eye used track its motion. Black dot depicts the initial (t = 0 ms) location of the prey. 174

Figure 4-32: An instance of volumetric velocity field of the fish failing to capture evasive prey (copepod) at t = 12 ms. (a) Image and (b) volumetric vector field. White dot depicts the location of the prey, and grey dot depicts the center of the fish eye used track its motion. Black dot depicts the initial location of the prey. 176

Figure 4-33: The velocity magnitude of predator (solid line; ●), prey (dashed line; ■), and local flow velocity at the location of prey (dotted line; ▲). (a) Predation success, (b) Predation failure. 177

Figure 4-34: Predator and prey tracks with Δt = 2 ms time intervals for successful prey capture by ram feeding. The white sphere shows final location of the prey and predator, while the black sphere gives the initial locations. 178

Figure 4-35: Predator and prey tracks with Δt = 2 ms time intervals for failed prey capture by ram feeding. The white sphere shows final location of the prey and predator, while the black sphere gives the initial locations. 179

Figure 4-36: (a) Selected images from sequence of a fish feeding on copepod in a uniform cross-flow. Red dot depicts the location of the prey. Blue dot is location of eye center. (b) Corresponding fluid velocity fields in absolute frame. Only vectors in the x-y plane intersecting the location of the copepod are shown. 182

Figure 4-37: Absolute velocity of fluid as blenny attempts to capture copepod at (a) t = 169 and (b) t = 183 ms. The red dot depicts the location of the prey, and blue dot is

location of eye center. The green dot in (b) gives the location of the prey at t = 169 ms. 185

Figure 4-38: Velocity field relative to the fish, at t = 183 ms. Projections of vectors in the x-y plane where copepod is located are shown. Color/contour gives magnitude of 3-component vectors. The green dot gives the location of the prey at t = 169 ms, red dot depicts the location of the prey, and blue dot is location of eye center. 186

Figure 4-39: (a) Trajectory of copepod from x-y perspective. (b) Velocity gradient values (MPSR, vorticity magnitude, total acceleration) against time graph of the fluid at the location of the copepod as it moves in the trajectory shown in (a). Event corresponds with figure 4-38. U_0 = 0.0384 189

Figure 4-40: (a) Trajectory of copepod from x-z perspective. (b) Velocity gradient values (MPSR, vorticity magnitude, total acceleration) against time graph of the fluid at the location of the copepod as it moves in the trajectory shown in (a). U_0 = 0.0384 190

Figure 4-41: (a) Trajectory of copepod from x-z perspective. (b) Velocity gradient values (MPSR, vorticity magnitude, total acceleration) against time graph of the fluid at the location of the copepod as it moves in the trajectory shown in (a). U_0 = 0.077 191

Figure 4-42: (a) Trajectory of copepod from x-y perspective. (b) Velocity gradient values (MPSR, vorticity magnitude, total acceleration) against time graph of the fluid at the location of the copepod as it moves in the trajectory shown in (a). U_0 = 0.077 192

Figure 4-43(a) and (b): The speed-time graph of two different predator-prey interaction events with uniform cross flow velocity, U_0 = 0.0384 m/s. Predator (solid line; ●) and prey (dashed line; ■). 195

Figure 4-44(a) and (b): The speed-time graph of two different predator-prey interaction events with uniform cross flow velocity, U_0 = 0.077 m/s. Predator (solid line; ●) and prey (dashed line; ■). 196

Figure 4-45: Predator and prey tracks with Δt = 7 ms time intervals for success prey capture event of figure 4-41(b). The white sphere shows final location of the prey and predator, while the black sphere gives the initial locations. 198

Figure 4-46: Predator and prey tracks with Δt = 7 ms time intervals for failed prey capture event of figure 4-42(a). The white sphere shows location at of the prey and predator immediately after the prey successfully escapes predation, while the black sphere gives the initial locations. 199

Figure 4-47: (a) Selected image sequences of a fish feeding on copepod behind a cylinder (cylinder location: x = -80 mm, z = -5.5 mm). Red dot depicts the location of the prey. Blue dot is location of eye center. (b) Corresponding fluid velocity fields in absolute frame. Vectors in x-y plane intersect the location of the copepod at t = 140 ms. Free stream velocity, U_0 = 0.077 m/s, and cylinder diameter, d_c = 12.7 mm. 201

Figure 4-48: Absolute velocity of fluid (a) just before (t = 133 ms), and (b) when (t = 140 ms) the blenny attempts to capture copepod. The green dot gives the location of the prey at t = 0 ms, red dot depicts the location of the prey, and blue dot is location of eye center. 204

Figure 4-49: (a) Trajectory of copepod from x-y perspective. (b) Velocity gradient values (MPSR, vorticity magnitude, total acceleration) against time graph of the fluid at the location of the copepod as it moves in the trajectory shown in (a). Event corresponds with figure 4-45, U_0 = 0.077 205

Figure 4-50: (a) Trajectory of copepod from x-y perspective. (b) Velocity gradient values (MPSR, vorticity magnitude, total acceleration) against time graph of the fluid at the location of the copepod as it moves in the trajectory shown in (a). Event carried out with fish housing placed in the cylinder wake (cylinder location: x = -80 mm, y = 9.5 mm), U_0 = 0.077. 206

Figure 4-51: The speed-time graph of predator (solid line; ●) and prey (dashed line; ■) with unsteady cross flow velocity within the cylinder (cylinder location x = -80, y = 9.5 mm), U_0 = 0.077 m/s. 207

Figure 5-1: (a) Schematic representation of axisymmetric Rankine body model. (b) Schematic representation of the diverging flow generated by the fish during its motion, and the (c) moving source based on the Rankine body model. 214

Figure 5-2: Schematic representation of the fish model (i.e. moving source) moving towards a copepod. The distance from the source to the nose is R = 2 mm. 217

Figure 5-3: Graph of MPSR at the location of the copepod against the distance of zebrafish model from the copepod. The graphs are plotted for U_{fish} = 0.03 m/s (solid line; —), 0.25 m/s (dashed line; - -), 0.5 m/s (dotted line; · ·). 217

Figure 5-4: Schematic representation of suction feeding on non-evasive prey. The generation of a vortex near the fish head is shown as a result of head motion and suction. 218

Figure 5-5: Schematic representation of feeding on evasive prey. This feeding technique occurs in a two-step process. (1) Initial slow approach towards the prey, followed by (2) a sudden acceleration (ram feeding mode) to capture the prey. 219

Figure 5-6: Schematic representation of the flow field in front of the fish in a uniform cross-flow. A disturbance region is generated in front of the fish head. The boundary of this region is depicted by a large change in velocity direction within a small length. The forward extent of the disturbance region increases with the fish motion. 220

Figure 6-1: Schematic representation of a proposed multi-grid measurement system. Two separate volumetric measurement system is used to measure at large and small spatial resolution. 222

Figure A-1: Graph of horsepower needed to drive the paddlewheel against the velocity of the fluid. 235

Figure B2-2: (a) Image space showing 4 points representing a circle. (b) Accumulator space with four circles corresponding to the 4 points in the image. The peak location *(a_1, b_1)* in the accumulator represents the center of the circle in the image. 237

Figure C-1: Schematic diagram of a specific "4-corners" camera arrangement. The inclination angles of cameras 1-4, with respect to the vertical direction, are α_1, α_2, α_3, and α_4 respectively. The dimensions of the cuboid are *a* (length) x *b* (width) x *c* (depth), where *a* and *b* are parallel to the laser sheet, and the side faces of the object are aligned with the camera viewing angles. The distance from the rear of the object (relative to the cameras) to the rear edge of the laser sheet is given by *t*. 241

Figure C-2: Schematic representation of the (a) trapezoidal fully obscured region, and (b) an exploded view of the various subvolumes. 242

Figure C-3: Schematic drawing and dimensions of a cuboid (blue), half cuboid (red) and pyramid (green) that make up the trapezoid. 242

Figure C-4: Schematic diagram of a specific "4-corner" camera arrangement where *t* is large such that $\tan(\alpha) > a/2t$. The white region is optically accessible by all cameras. 243

Nomenclature

Abbreviations

MPSR	Maximum principal strain rate
PIV	Particle image velocimetry
PTV	Particle tracking velocimetry

Greek Symbols

α	camera angle
$\boldsymbol{\Omega}$	anti-symmetric rotation tensor
ω	local vorticity
θ	angular coordinate
γ_{max}	threshold value of MPSR
$\tau_{f/p}$	time constant of fluid/particle
$\rho_{f/p}$	density of fluid/particle
$\upsilon_{f/p}$	kinematic viscosity of fluid/particle

Roman Symbols

a, d_c	cylinder diameter
d_p	diameter of particle

$\boldsymbol{D}$	symmetric deformation tensor
u	local streamwise velocity
v	local wall-normal velocity
w	local spanwise velocity
x	streamwise direction
X	horizontal image direction
y	wall-normal direction
Y	vertical image direction
z	spanwise direction
U_0	freestream velocity
U_{fish}	velocity of fish model during slow approach
U_{ram}	velocity of fish model during ram feeding
r	radial coordinate
r_d	reaction distance
Re	Reynolds number
R	distance between the stagnation point and source in fish model
Sk	Stokes number
t	time
$t_{latency}$	time required for copepod to respond after fluid disturbance

s_{close}	closest distance from the fish mouth to copepod before ram feeding
t_{ram}	time taken during ram feeding

Chapter 1

Introduction

The interest in relating fluid dynamics to biological systems has grown significantly in the last few decades. Studies of flow interacting with small organisms (~ μm to mm in size) in aquatic environments have gained much attention since these organisms support the food web, and significantly affect the ocean physics and biogeochemistry (Guasto *et al.* 2012; Prairie *et al.* 2012). Locomotion of larger organisms (> 1 cm in size), such as fish and jellyfish, have brought about bio-inspired engineering applications such as propulsion, maneuvering and control in unsteady flow (Triantafyllou *et al.* 2000; Fish and Lauder 2006; Dabiri 2009).

These aquatic organisms thrive in their respective ecosystems, living harmoniously within a network of food chains. However, their survival can be strongly affected by aquatic turbulence. In particular, organisms residing in coral reefs continually face turbulent water motion due to oceanic currents, waves, coastal upwelling and tides. Changes in local environment, such as temperature and weather, can also cause unexpected turbulence and flow disturbances. With changing climates, these organisms (e.g. coral reef fish) may face unusual changes in local flow properties (e.g. cross flow velocity, turbulence intensity) that affect their ability to capture food (e.g. zooplankton). Significant changes in flow turbulence can thus upset the ecological balance, potentially leading to the demise of the ecosystem. Since changes in global climate are associated with redistribution of global oceanic turbulence, the relationship between turbulence and predator-prey interaction is important to predict potential effects on ocean ecology (Jumars *et al.* 2009).

1.1 Motivation

A typical food chain in an aquatic ecosystem is shown in figure 1-1. The food chain begins with phytoplankton, such as algae, which are micro-organisms with size of *O*(~μm). Phytoplankton is derived from Greek - *phyton* and *planktos*, which refer to "plant" and "drifter", respectively. Phytoplankton photosynthesize and drift with the flow; thus they are the primary producers of organic compounds that sustain the food chain. Zooplankton (derived from *zoon* – a Greek word for animals, and *planktos*, which refers to "drifter") feed primarily on phytoplankton, and they consist of a myriad of organisms ranging in size over *O*(μm - cm). Zooplankton generally drift with the flow, and serve as inter-trophic level organisms within the food chain that connect primary producers (phytoplankton) with the variety of fish and larger organisms present in the aquatic environment.

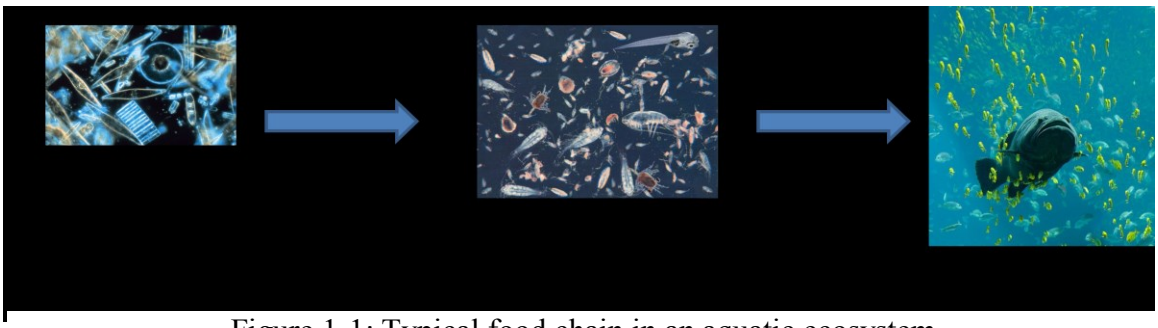

Figure 1-1: Typical food chain in an aquatic ecosystem

Copepods are an example of zooplankton present in both freshwater and seawater environments, and are important sources of food for a diverse group of organisms. A particular group of copepods known as calanoid copepods make up about 75% of all planktons (Mauchline 1998), thus making copepods the most abundant zooplankton in the aquatic environment. Figure 1-2 shows a typical calanoid copepod with a pellet-shaped body, and two long antennae spanned out laterally from their head. These antennae have smaller setae that are known to detect very small flow disturbances (Strickler and Bal 1973; Yen and Fields 1992). Copepods also have a smaller set of antennae that they use for feeding, and a set of swimming legs ("oars") on their body

which deflect progressively when executing a sudden high-speed swim. Studies have shown that copepods are able to sense flow disturbances of an approaching predator using their setae, and escape rapidly by moving their oars (Yen *et al.* 1992; Lenz and Yen 1993; Kiørboe and Visser 1999; Lenz *et al.* 2000). These characteristics make copepods a model organism for study in predator-prey interactions and an important subclass of organisms, which can influence global ecological dynamics.

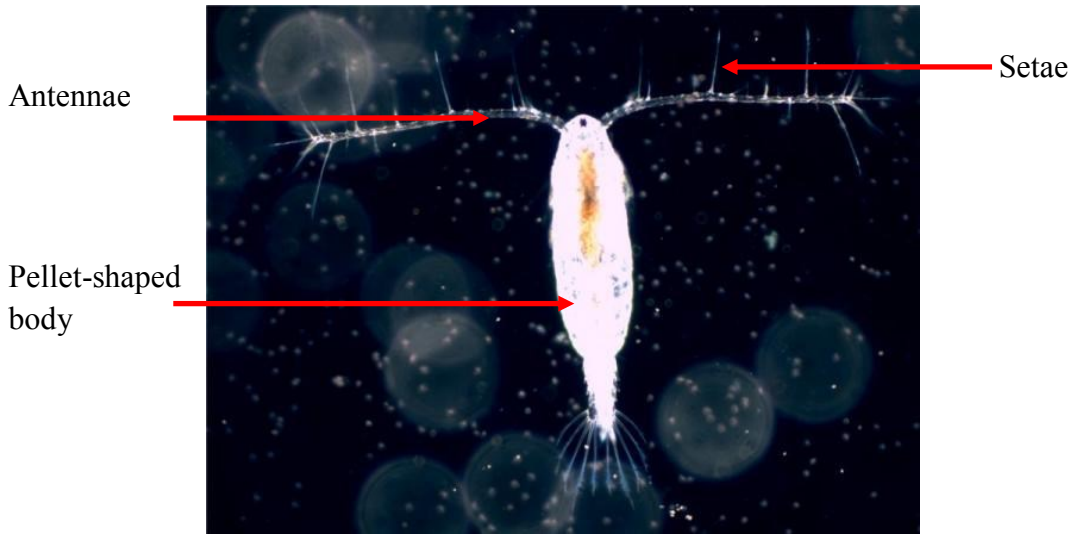

Figure 1-2: Image of a copepod (Acartia tonsa). Reproduced from http://www.sciencedaily.com

Fish represent a large group of organisms that thrive in the aquatic environment, where many feed on zooplanktons (as depicted in figure 1-1). Generally, fish exhibit three different kinds of feeding techniques: suction feeding, ram feeding, and manipulation feeding. During suction feeding, a fish ingests the prey by sucking the surrounding water. Ram feeding occurs when a fish propels itself forward with its mouth open, thus engulfing the prey. Manipulation feeding, however, encapsulates different techniques that are specific to individual species. For instance, an archerfish spits water jets at a terrestrial insect to make it fall before using ram or suction feeding to feed on the submerged insect. Others bite bigger zooplanktons before ingesting. In general, fish apply a combination of these three techniques for successful predation.

Aquatic fish and copepods differ significantly in their length and time scales. For instance, a typical fish (~100 mm) feeds on copepods (~1 mm), a difference of $O(10^2)$ in length scale. A larger difference can be illustrated by considering a whale shark (~10 m) feeding on copepods – a difference in length scale of $O(10^4)$. During cruising, a small fish may move at a velocity of O(~100 mm/s) , while a copepod may move at O(~1 mm/s). Thus, both species, exhibit equivalent time scales of O(~1 s). During predator-prey interaction, however, copepods may swim at velocities that are higher than the fish to escape successfully. This creates a large difference in copepod escape and cruise time scale. For instance, a calanoid copepod nominally traveling at a cruising speed of ~1mm/s (time scale ~ 1 s) is capable of swimming intermittently at speeds up to 0.5 m/s (time scale ~ 2 ms) when attempting to escape a potential predator.

The different length and time scales of fish and copepods influence the surrounding fluid differently. In fluid mechanics, Reynolds number is a dimensionless parameter that provides a ratio of the inertial to viscous forces. The Reynolds number, Re, is given by $Re = UL/\upsilon$, where U is the velocity of fluid relative to the organism, L is a characteristic length (e.g. length of organism), and υ is the kinematic viscosity of the fluid. The Reynolds number for a small fish can range over O ($10^3 - 10^4$), which implies that the fluid dynamics around the fish is dominated by inertia. However, copepod velocities ranging from 1 mm/s – 500 m/s, translate to Re ~ 1 – 500. This shows that fluid motion around copepods can be modeled as viscous (Re ~1) or inertial (Re > 100) depending on the copepod motion (Yen 2000).

Figure 1-3 shows a schematic representation of a small fish-copepod (predator-prey) interaction. The fish approaches the copepod in an attempt to feed on it. This results in disturbances of fluid in front of the fish and around the copepod. Upon sensing this disturbance, the copepod may swim away from the fish to escape predation. This apparently simple interaction is dependent on the fish motion, copepod motion, and the multi-scale dynamics of fluid motion surrounding the organisms.

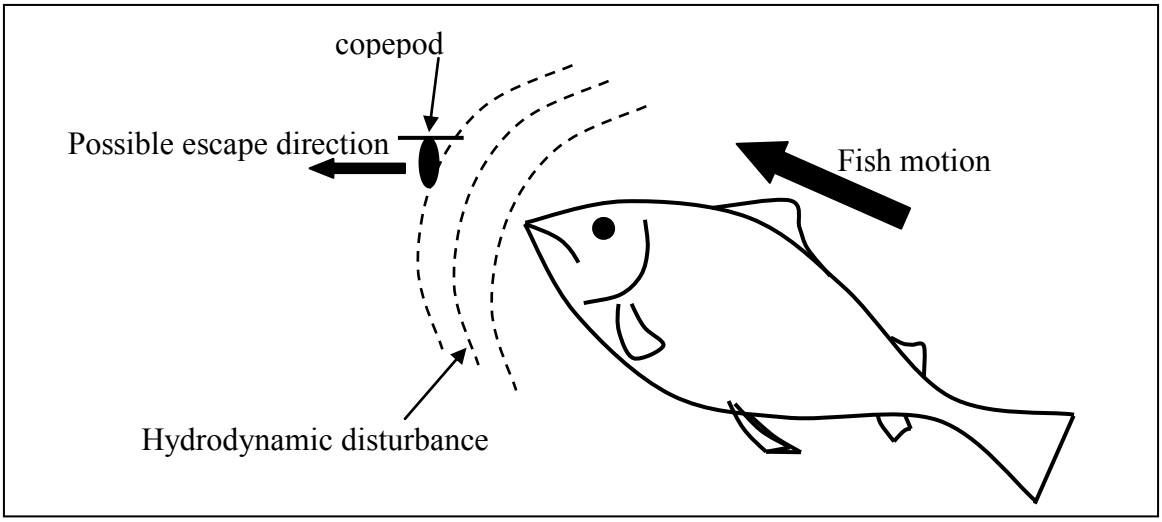

Figure 1-3: Schematic diagram showing the disturbance of fluid in front of the fish during fish-copepod interaction in still water.

In the ocean, coral reefs experience turbulent fluid motion continually due to oceanic currents, tides, waves, upwelling and local environmental changes. Turbulence is a highly disordered three-dimensional flow, which contains a cascade of eddies with a range of length and time scales. According to Pope (2000), an eddy is *"...conceived to be a turbulent motion, localized within a region of size l, that is at least moderately coherent over this region"*. The turbulence eddy size in the ocean extends from millimeters to kilometers, therefore over a six orders of magnitude.

For studying fish (30 mm) and copepods (1 mm), larger eddies are neglected as they affect both species in the same way. However, eddies ranging in size over 1 – 30 mm can affect the organisms differently. For the purpose of this study, we can consider eddies ranging from 1 – 30 mm, where 30 mm may be generated by a flow past a small coral branch, to the smallest eddy, which can be represented by a Kolmogorov length scale (O (1 mm); Granata and Dickey 1991). These length scales are similar to the sizes of fish and copepods. Oceanic water motions also generate a wide range of bulk velocities. At high velocities, fish and copepods drift with the flow. However, they behave differently at velocities 0 – 10 cm/s, where copepods drift with the flow unless executing a high-speed jump, and fish adjust themselves to maneuver in the flow. We consider a velocity range within 0 – 10 cm/s for this study.

Various predator-prey interactions occurring within a coral reef can be affected by oceanic turbulence. For instance, figure 1-4 shows a schematic diagram of ambient turbulent fluid motion during predator-prey interaction within a coral reef. The fish approaches the prey, creating a hydrodynamic disturbance. Unlike figure 1-3, the disturbance created by the fish is now modified by the turbulent flow. Thus, the copepod may not sense the fish approach. Furthermore, the turbulent fluid motion can also influence the locomotion of the fish and copepod. This highly complex interaction depends on the specific velocity field, the organism trajectory and prey sensing characteristics.

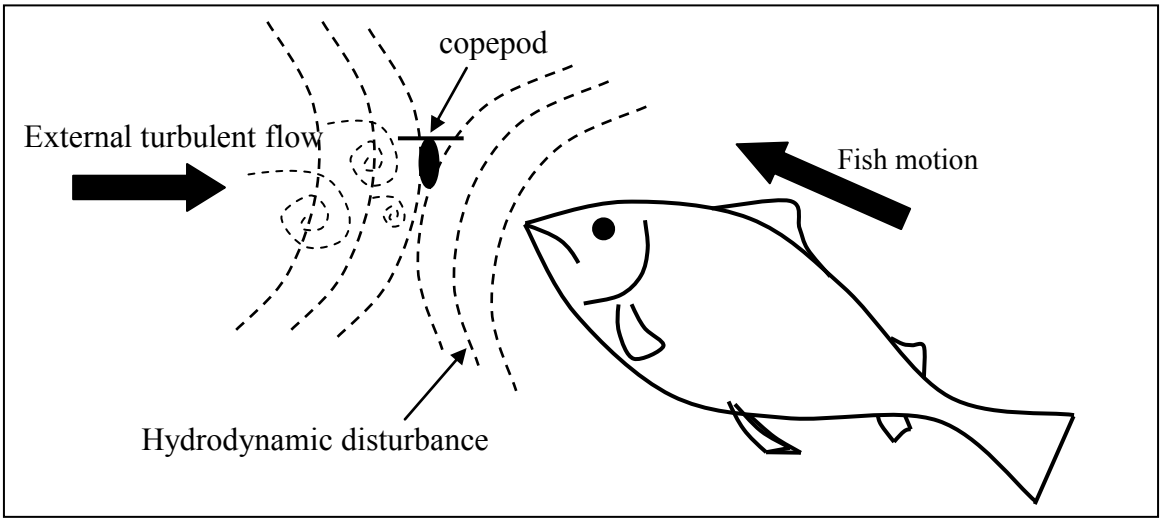

Figure 1-4: Schematic diagram showing the disturbance of fluid experienced by copepod during fish-copepod interaction in turbulent water.

Thus, this study is motivated by the need to understand the influence of turbulence on aquatic predator-prey interaction. An experimental investigation is carried out using a combination of high-speed three-dimensional particle tracking velocimetry (PTV), and high-speed tomographic particle image velocimetry (PIV). Both techniques are time resolved and capture all three-velocity components with a volumetric domain. PTV is capable of tracking aquatic organisms within a volume, while PIV is capable of obtaining volumetric velocity, temporal velocity gradient and complete spatial velocity gradient tensors. These measurements will allow better insight into organism behavior during the predator-prey interaction.

1.2 Previous work

In this section, previous work relevant to the study of copepods, fish, predator-prey interactions, and velocimetry techniques is reviewed. Section 1.2.1 reviews studies of copepod sensing and locomotion, and Section 1.2.2 reviews studies of predator-prey interaction, where both predation strategies and interactions with turbulence are reviewed. Finally, various volumetric velocimetry techniques applied to measure flow around aquatic organisms are discussed in Section 1.2.3.

1.2.1 Copepods

1.2.1.1 Sensing

Copepods are known to respond primarily to hydrodynamic signals. These hydrodynamic signals have been associated with fluid velocity and velocity gradient magnitude based on the differential bending of the setae on their antennae. They respond to this stimulus by executing a high velocity swim (sometimes also referred to as a "jump"; Strickler and Bal 1973; Fields and Yen 1997; Kiørboe and Visser 1999; Buskey *et al.* 2002). Kiørboe and Visser (1999) argued that copepods respond to nearby predators by sensing local velocity gradients. From a fluid mechanics standpoint, a velocity gradient can be associated with either temporal gradient (Lagrangian acceleration; $D\boldsymbol{u}/Dt$) assuming the organism is following the fluid, or a spatial gradient (velocity gradient tensor, $\nabla\boldsymbol{u}$). The velocity gradient tensor can be decomposed into symmetric and anti-symmetric parts, which separately provide deformation rate, and vorticity terms. The deformation rate (symmetric part) includes components of normal and shear strain rate.

The components of deformation rate change with the coordinate system. It has been noted that a given coordinate system does not necessarily align with the copepod orientation (Catton *et al.* 2012). Thus, the maximum principal strain rate, hereforth known as MPSR, has been used to determine the spatial extent of the hydrodynamic

disturbance independent of the orientation of the copepod (i.e. invariant to the coordinate system). The MPSR was calculated by finding the eigenvalues of the symmetric component of the complete velocity gradient tensor (i.e. deformation rate):

$$D_{ij} = \begin{bmatrix} \frac{\partial u}{\partial x} & \frac{1}{2}\left(\frac{\partial u}{\partial y} + \frac{\partial v}{\partial x}\right) & \frac{1}{2}\left(\frac{\partial u}{\partial z} + \frac{\partial w}{\partial x}\right) \\ \frac{1}{2}\left(\frac{\partial u}{\partial y} + \frac{\partial v}{\partial x}\right) & \frac{\partial v}{\partial y} & \frac{1}{2}\left(\frac{\partial v}{\partial z} + \frac{\partial w}{\partial y}\right) \\ \frac{1}{2}\left(\frac{\partial u}{\partial z} + \frac{\partial w}{\partial x}\right) & \frac{1}{2}\left(\frac{\partial v}{\partial z} + \frac{\partial w}{\partial y}\right) & \frac{\partial w}{\partial z} \end{bmatrix}$$

where u, v, w are the velocity components in the orthonormal x, y, z directions, and

$$det\left(D_{ij} - \lambda_k \delta_{ij}\right) = 0.$$

In the above equation, *det* refers to the determinant of the tensor, δ_{ij} is the Kronecker delta tensor, and λ_k (k = 1, 2, 3) represent the eigenvalues, or principal strain rates. The maximum principal strain rate is then obtained as $\lambda max = \max(|\lambda_1|, |\lambda_2|, |\lambda_3|)$.

Kiørboe *et al.* (1999) constructed four different facilities capable of isolating various velocity gradient components to investigate their relationship with copepod sensing. They estimated the velocity gradient quantities using model flow equations based on each facility. In their work, they found that copepods respond to both normal and shear strain rates with similar thresholds. They obtained these strain rate thresholds for copepod escape ranging from 0.5 – 5 s^{-1}.

Kiørboe *et al.* (1999) also noted that copepods can perceive fluid acceleration and respond with a high-speed jump, but the acceleration does not elicit escape responses from the copepods. The authors considered a jump as an escape response, only when the copepod travelled more than two body lengths in a single jump. In their experiment, copepods were placed in an oscillating chamber, where they were subjected to maximum accelerations of 0.39, 1.58, 3.55, 5.88, and 9.87 m/s^2. The authors found that the jumping frequency of the copepods decreased as acceleration increased, but the jumps were not attributed to escape responses. Finally, it was also found that vorticity did not elicit

escape response from copepods, even though the magnitudes exceeded those obtained for strain rate (i.e. 0.5 – 5 s^{-1}).

Murphy (2012) provides a tabulated result summarizing previous studies that have measured or estimated thresholds for copepod escape. It shows a wide range of strain rate thresholds documented in the literature. For instance, Fields and Yen (1996, 1997), who used a siphon flow to mimic a predator, found that shear strain rate was the least variable parameter that initiated escape response for various species of copepods. This parameter ranged from 1.5 - 51.5 s^{-1}. In another case, Buskey *et al.* (2002) reported that copepods respond to a vibrating cylinder and provided a strain rate threshold of 0.4 - 12 s^{-1}.

Although a consensus exists amongst researchers that copepods respond to velocity gradients, the influence of various components of the gradients is still not clear. Furthermore, experimental measurements of the complete velocity gradient tensor and the effects of MPSR on the copepod response are extremely limited.

1.2.1.2 Locomotion

Copepods respond to velocity gradients by executing a sudden high-speed swim (i.e. jump). A copepod jumps by closing its antenna and oaring its set of swimming legs (Yen 2000). When detecting an approaching predator in this way, the jump serves as an attempt to evade the predator (Jiang and Kiørboe 2011). The copepod may execute multiple oar strokes to move away by a significant distance (Yen 2000).

A copepod jump can last over a period of 10 – 30 ms. This implies that the motion of the copepod can be resolved only by high-speed imaging (repetition rate ~ 1000 frames a second). Using such a technique, the escape speed of copepods (*Acartia tonsa* species) has been observed to reach 0.4 m/s (Buskey et al 2002). Considering a body length of 1 mm, this speed translates to a Reynolds number, $Re \sim 400$. Kiørboe *et al.* (2010) reported Reynolds numbers of copepod jumps ranging from 20 – 100, while Yen (2000) pointed out that Reynolds numbers may reach up to 1000. Although these values were obtained

for different species of copepods, it is clear that the range of speed during a jump enables the copepod to move from a viscous-dominated regime (Re ~ 1) to an inertia-dominated regime (Re > 100).

While executing a jump, the copepod creates flow structures in the surrounding fluid due to momentum transfer. Murphy *et al.* (2012) applied high-speed tomographic particle image velocimetry (PIV) on flow around a jumping copepod, and observed the flow structures generated. These flow structures included a wake vortex ring and a similar-sized body vortex ring. The wake vortex is shed at the initial position of the copepod, while the body vortex moves with the copepod. These flow structures have also been observed computationally (Jiang and Kiørboe 2011), and their length scale was *O* (~1mm; i.e. of similar order to the copepod itself).

During inertia-dominated high-speed jumps, copepods have been found to move at various velocities (and Reynolds numbers). However, probability distributions of copepod jump speed and direction, and the relationship between the copepod locomotion and the sensing is not clear. Understanding such distributions and relationships can aid in modeling motion of copepods.

When a copepod is not executing its high-speed swim, it can be modeled as a particle. Maxey-Riley equation (Maxey and Riley 1983) governs the acceleration of a spherical particle of density ρ_p, within a flow field in the limit of zero Reynolds number (Re_p) of particle motion. The equation is given as:

$$\frac{4}{3}\pi a^3 \rho_p \frac{d\boldsymbol{v}}{dt} = 6\pi a\mu\left(\boldsymbol{v}-\boldsymbol{u}+\frac{1}{6}a^2\nabla^2\boldsymbol{u}\right)+\frac{4}{3}\pi a^3(\rho_p-\rho_f)\boldsymbol{g}+\frac{4}{3}\pi a^3\rho_f\frac{D\boldsymbol{u}}{Dt}+\frac{4}{3}\pi a^3\frac{\rho_f}{2}\frac{d}{dt}\left(\boldsymbol{u}-\boldsymbol{v}+\frac{1}{10}a^2\nabla^2\boldsymbol{u}\right)+6\pi a^2\mu\int_0^t\frac{d}{d\tau}\times\left(\boldsymbol{u}-\boldsymbol{v}+\frac{1}{6}a^2\nabla^2\boldsymbol{u}\right)\frac{d\tau}{\sqrt{\pi\nu(t-\tau)}} \quad (1\text{-}1)$$

where **v** is the velocity of the particle; $\boldsymbol{u}$ is the local velocity of the fluid; ρ_p and a are the density and radius of the particle (i.e. copepod), respectively; ρ_f and μ are the density and kinematic viscosity of the fluid, respectively; $\nu = \mu/\rho_f$; and g is gravitational acceleration. *D/Dt* is the material derivative following the fluid particle, while *d/dt* is the total

derivative following the solid particle. The term on the left hand side is the force per unit volume) on the particle. On the side hand side of the equation, the first term is viscous drag force, second term is buoyancy force, third term is force due to added mass, and fourth term is the Basset-Boussinesq force term (also known as the history term).

After neglecting the $a^2 \nabla^2 u$ terms, which are normally small in comparison to any of the remaining terms (Mei 1996), neglecting the history term, and considering the added-mass term as $2/3\pi a^3 \rho f(D\boldsymbol{u}/Dt - d\boldsymbol{v}/dt)$ (Mei 1996; Michaelides 1997), the equation is reduced to:

$$\left(2\rho_p + \rho_f\right)\frac{d\boldsymbol{v}}{dt} = \frac{9\mu}{a^2}(\boldsymbol{v} - \boldsymbol{u}) + 3\rho_f \frac{D\boldsymbol{u}}{Dt} + \left(\rho_p - \rho_f\right)\boldsymbol{g} \qquad (1\text{-}2)$$

where the first term on left hand side is drag force, second term is local acceleration with added mass, and third term is the buoyancy force. Equation (1-2) can be used to model copepod acceleration in a fluid velocity field when the copepod is not executing a jump (Peng and Dabiri 2009; Kiørboe *et al* 1999).

When a copepod executes a high-speed jump, the Reynolds number of the copepod increases. For finite Reynolds number, the drag force term in equation (1-1) can be represented as $6\pi a\mu\phi(\mathrm{Re_p})(v\text{-}u+1/6\, a^2 \nabla^2 u)$, where $\phi(Re_p)$ accounts for the deviations from the Stokes drag (Mei 1996). With similar assumptions used for equation (1-2), and an additional force term, $\boldsymbol{F_c}$, included to model copepod propulsive force during the jump, the equation is modified to:

$$\left(2\rho_p + \rho_f\right)\frac{d\boldsymbol{v}}{dt} = \frac{9\mu\phi(Re_p)}{a^2}(\boldsymbol{v} - \boldsymbol{u}) + 3\rho_f \frac{D\boldsymbol{u}}{Dt} + \left(\rho_p - \rho_f\right)\boldsymbol{g} + \boldsymbol{F_c} \qquad (1\text{-}3)$$

where $\phi(Re_p) = 1 + 0.1935\mathrm{Re}^{0.6305}$ for $20 < \mathrm{Re_p} \leq 260$ (Clift *et al*. 1978).

Although the above equation is relevant to model the copepod moving within a flow field, limited previous work is available on values of $\boldsymbol{F_c} = \rho_p \boldsymbol{a_c}$, where $\boldsymbol{a_c}$ is the propulsive acceleration. Understanding sensing and locomotion characteristics of copepods can provide expressions for $\boldsymbol{F_c}$ in models as well as aid understanding of acceleration in general.

1.2.2 Predator-prey interaction

1.2.2.1 Predation

A fish must approach a prey before successfully capturing it. During this approach, the fish perturbs the flow in front of its head. Intuitively, a diverging velocity field is expected in front of a fish head as it moves. Jiang and Osborn (2003) illustrated a diverging flow in front of the fish head in their schematic diagram. But, Heuch *et al.* (2007) confirmed the existence of this divergent flow quantitatively in their work. The authors constructed a mould out of a frozen salmon, and casted the head shape in silicone rubber. Then, the cast was propelled through still water to mimic a fish motion. The authors applied planar PIV to measure two-component velocity vectors in a plane of fluid to analyze the flow field in front of the fish head. Their results show that the flow velocity near the head was lower than the fish speed, and progressively decreased in magnitude further from the head. If the fish applied suction during this motion, it could alter the velocity field upstream of the fish mouth.

When a fish nears the prey, it executes either suction feeding or ram feeding. Day *et al.* (2005) used planar PIV to study the surrounding fluid motion when a bluegill sunfish executes a suction feeding, and they estimated the volume of fluid ingested by assuming axisymmetric flow during suction. The authors found that during suction feeding, the total volume ingested by the fish can exceed the volume of their buccal cavity by up to 260%. This large volume suction is possible due to the release of the ingested fluid from the posterior opercular slits (gills) of the fish. The authors concluded that a good control of gape, suction and outflow through the gills could promote high volume ingestion during suction feeding in a short time.

In another study, two different fishes – bluegill sunfish and largemouth bass were compared while feeding on a non-moving prey (Higham et al 2006). The authors found that the sunfish was more accurate than bass in capturing prey, even though bass ingested a larger volume of water, sucked with higher flow rate. The lack of accuracy for bass was attributed to its faster ram speed towards the prey. The method of swimming

forward (ram) while executing suction was shown to "elongate and narrow" the ingested fluid parcel in front of the fish mouth (Higham *et al*. 2005). The authors concluded that combining ram and suction feeding improves the closing speed of the predator to the prey, but might lower the accuracy of successful capture. It was then suggested that braking could increase the accuracy of suction feeding on a non-evasive prey, and might be more important for fish that ingest relatively small volumes of water (Lauder and Drucker 2004; Higham et al 2005).

Although braking followed by suction feeding may be a good strategy for non-evasive prey, it may not be optimal for capturing evasive prey that are capable of sensing a hydrodynamic disturbance. Holzman and Wainwright (2009) carried out planar PIV measurements on bluegill sunfish when it approached the prey and sucked the fluid to draw the prey into its mouth. Maximum principal strain rate (in two-dimensions) was then obtained from the data. The authors found that normally higher strain was present in front of the mouth during suction, then within the bow wave generated during fish approach. This implied that evasive prey might detect suction more easily than a bow wave. The authors concluded that quick strikes of planktivore fishes are adaptations that can aid in successful predation of evasive prey.

While ram and suction feeding each create disturbances in the flow field, a strategic combination of the two may help capture copepods. However, the flow disturbance measurements in front of the fish, in combination with trajectory of the fish have not been quantified during successful predation of a copepod.

1.2.2.2 Interaction with turbulence

Clarke *et al* (2005) investigated some effects of turbulent water motion on predator-prey interaction. Two types of coral reef fish (blennies – *Acanthemblemaria aspera*, *Acanthemblemaria spinosa*) feeding on copepods and brine shrimp in a chamber were studied. Brine shrimp are zooplankton of similar size to copepods that are incapable of actively escaping the predator. Turbulence was generated in the chamber by directing water from a submersible pump through two plastic tubing along the sides of the

chamber. The water would flow towards the opposite end of the chamber where they were deflected back towards the center, interacting to create turbulent water motion. In their statistical analysis, the authors found that both fish had a higher success rate preying on brine shrimp in still water than in turbulent water. This was attributed to the erratic flow motion that hinders the capture success. With copepods, however, both fish were more successful in turbulent water than in still water. The authors hypothesize that, although turbulence reduces capture success by adding unpredictable movement to brine shrimp due to eddy motions, it increases predation success of copepods by interfering with their ability to sense the predator.

In a separate field study, Finelli *et al.* (2009) discuss how the feeding behavior of the same two blennies in the ocean (*A. aspera* and *A. spinosa*) is adapted to their location within the coral reef. *A. spinosa*, the stronger swimmer, locates at topographically higher locations where it can feed on fast-moving evasive prey. *A. aspera* occupies lower shelters in the coral reef where it can feed on non-evasive prey. Their findings on feeding behaviors of the blennies were further substantiated in a laboratory experiment (Clarke *et al.* 2009). The experiment was conducted in a water channel, where the fish was located in a specific housing with water moving past it. Copepods were distributed throughout the channel, such that the fish would attempt to feed on the prey in the cross flow. Number of attempts, distance travelled, and the speeds of fish during foraging were analyzed. The *A.spinosa* species was found to exhibit greater foraging efforts, move greater distance, and execute greater mean speed than *A. aspera*. These characteristics indicate that higher location in the coral reef, away from the ocean boundary layer, requires the swifter capability of *A. spinosa* for high predation success. In the same experiment, Clarke *et al.* (2009) also noted that for both fish, success of predation on evasive prey remained the same for varying flow speed (over the range of 3.2 – 9.2 cm/s), but dropped when the speed went past 9.2 cm/s. Furthermore, when a branched coral was placed upstream of the blennies, turbulence generated downstream increased predation success rate of copepods by both *A. aspera* and *A. spinosa*.

Turbulence appears to aid predation of evasive prey. A turbulent flow field consists of myriad of velocity fluctuations and gradients. Since evasive prey (such as copepods) respond to local velocity gradients, turbulent flow fields can influence the response of the prey. However, the role of specific turbulent structures on enabling higher predation success is unclear.

1.2.3 Velocimetry and tracking

Historically, quantitative measurements of fluid velocity fields around aquatic organisms have been obtained by observing and tracking particles around the organism. For instance, Lauder and Clark (1984) studied the water flow into the mouth cavity of a fish during prey capture, by using neutrally buoyant brine shrimp eggs as flow tracers. They extended the exposure time of the camera to obtain streak patterns generated by the movement of the eggs. The streak patterns were used to estimate the local velocity of the fluid.

Over the last two decades, PIV has been used almost exclusively to study flow fields around organisms. In PIV, a fluid volume is seeded with a uniform distribution of tracer particles throughout. A thin sheet of light from a pulsed laser illuminates a plane of the seeded fluid. A camera then obtains a sequence of two images (or image pair) synchronized with a pair of laser pulses. An image pair is separated by a known time interval, Δt. For high-speed PIV, images are acquired at high frame rate where the time between any consecutive images can be taken as Δt, thus, providing time-series data. After images are acquired and recorded, the two consecutive images (or image pair) are divided into a grid of square or rectangular sub-areas (interrogation areas). The size of the interrogation area is chosen such that a certain minimum number of particles (usually 5 – 10) appear within it. The interrogation area from the first image and the corresponding interrogation area from the second image of the image pair are cross-correlated. The peak value of the cross-correlation is obtained. This value corresponds to the displacement vector, $\Delta \boldsymbol{s}$, of the group of particles within the interrogation area.

These displacement vectors, $\Delta \boldsymbol{s}$, are then converted to velocity vectors, $\boldsymbol{v}$, by applying: $\boldsymbol{v} = \Delta \boldsymbol{s}/\Delta t$. After obtaining the velocity for all interrogation areas, a two-dimensional regularly structured grid of two-component velocity vectors is obtained (see figure 1-5a). Various spatial derivatives of the velocity can then be obtained from this measurement and analyzed. Readers are referred to Raffel *et al.* (1993), and Adrian and Westerweel (2011) for detailed explanations of PIV.

In particle tracking velocimetry (PTV) the algorithm for measuring the fluid velocity is different. After consecutive images are acquired, displacement of every particle in the image is obtained by locating the corresponding particle in the second image. Every particle is tracked independently. Therefore, PTV does not require minimum particle number density constraints, which are important in determining the minimum PIV interrogation area. PTV provides velocity vectors in an unstructured manner (depicted in figure 1-5b). Such a measurement technique is useful for tracking individual organisms (e.g. Sutherland *et al.* 2011).

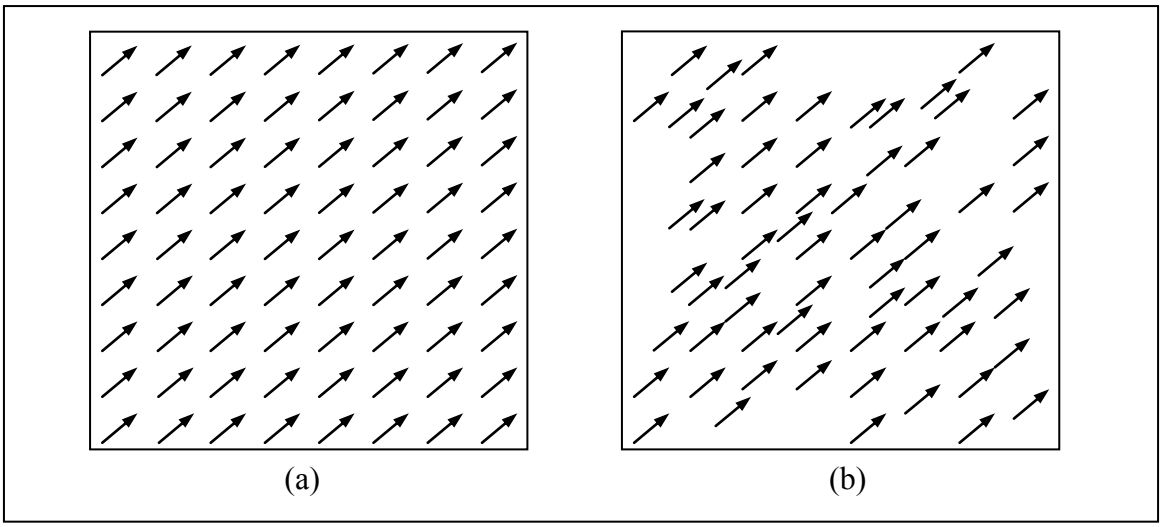

Figure 1-5: Schematic representation of a (a) regularly structured grid generated by planar PIV, and (b) unstructured grid generated by planar PTV.

1.2.3.1 Volumetric velocimetry

One of the many applications of PIV includes its use in studying locomotion and predation of aquatic organisms. Planar PIV, which measures two-component velocity vectors in two dimensional space, has been used to study fish (e.g. Higham *et al.* 2005; Epps and Techet 2007), eels (e.g. Tytell and Lauder 2004), copepods (e.g. Catton et al 2007), jellyfish (e.g. Dabiri et al 2010), ctenophores (e.g. Colin et al 2010), salps (e.g. Sutherland and Madin 2010), and even sharks (Wilga and Lauder 2004). Stereo-PIV, which measures three-component velocity vectors in two-dimensional space, has also been used to study fish maneuvers (Sakakibara *et al.* 2004).

Recent advances in imaging and reconstruction capabilities have made it possible to resolve all three components of velocity in three-dimensional (3-D) space. In volumetric velocimetry, either additional cameras placed at different angles (e.g. synthetic aperture PIV, tomographic PIV, 3D PTV), or "coded information" within a single camera image (e.g. holography), is used to resolve the third spatial and velocity component. Only a handful of studies on flow around aquatic organisms have been carried out with volumetric velocimetry.

Flammang *et al.* (2011) used 3-D PTV to understand the wake structure generated by a shark's tail. The authors noted specifically that their 3-D measurements yielded a different interpretation of the wake structure than their previous hypothesis based on planar PIV (Wilga and Lauder 2004). Thus, they concluded that extrapolating three-dimensional vortical wake structures from planar measurements could lead to misinterpretation and erroneous representations. This study in particular obviates the need for volumetric measurements when the flow of interest is complex and three-dimensional as would occur in cases of predator-prey interaction.

Malkiel *et al.* (2003) applied digital holography to obtain 3-D velocity fields around a feeding copepod. The flow was seeded with particles, and an in-line hologram was recorded where the resulting diffraction patterns could be decoded to determine the plane locations of the particles. The hologram was reconstructed using digital filters and the

Fresnel diffraction equation into a volume of particles. The authors then applied PTV, where they tracked individual particles in consecutive volumes and presented unstructured velocity fields around the feeding copepod. Although holography is a good measurement tool for relatively small field of view, a potential drawback of holography is that only a limited number of particles can be resolved in the single camera frame.

Murphy *et al.* (2012) applied tomographic PIV to obtain velocity fields generated by a copepod during its high-speed jump. The vector spacing in their regular grid was 0.2 mm (spatial resolution: 0.8 mm), which provided sufficient resolution to observe small-scale flow structures around the copepod during its motion. The authors utilized high-speed imaging (200 frames per second) to resolve the small-scale flow structures. Since copepods respond to visible light (Catton et al. 2007), a near infrared laser was used for illumination (see also Epps and Techet 2007; Mendelson and Techet 2013). For tracking the copepod motion, the authors manually tracked three locations on the copepod, and applied direct linear transform (DLT) to find the location in the three-dimensional space.

For predator-prey interaction, a volumetric velocimetry technique capable of resolving relatively small length scales (related to copepods) within a larger field of view (related to fish) is desired. Since holography and 3D PTV has limitations on particle density, tomographic PIV was chosen for the current work to measure the fluid velocity field. Next, details of tomographic PIV are discussed.

1.2.3.2 Tomographic PIV

Figure 1-6 shows a schematic diagram of a tomographic PIV setup (Elsinga *et al.* 2006). It uses multiple cameras, a laser (configured to spread into a thick sheet), and tracer particles in the fluid. Similar to planar PIV, the cameras acquire sets of consecutive images (or image pairs) separated by a time interval, Δt. All the cameras acquire images of the same volume of interest from different angles (as shown in figure 1-6). The acquired images are mapped, via a known calibration, to the unknown volume of particles. For this reconstruction, an iterative algorithm such as Multiplicative Algebraic Reconstruction Technique (MART) is applied. Consecutive reconstructed volumes are

then cross-correlated to generate volumetric three-component velocity field in a regularly structured grid.

When MART is applied, the generated volume may contain noise and thus, reduce its quality. Elsinga *et al.* (2006) studied the changes to volume reconstruction quality by varying number of cameras, camera angle, seeding density of particles, calibration error, and number of MART iterations. They found that the reconstruction quality increases with the number of cameras, but the quality increment rate is reduced substantially after four cameras. Thus, four cameras are used typically for tomographic PIV, considering the high cost of adding additional cameras. Furthermore, the volume reconstruction quality increases with the number of iteration but quality increment is reduced after about five iterations. Optimal camera angle with respect to out-of-plane direction was found to be 30º. The recommended seeding particle density is 0.05 particles per pixel (*ppp*) for optimal performance.

The reconstruction and cross-correlation steps in tomographic PIV demand high computational cost. There are ongoing efforts in software development to reduce the computational cost of tomographic PIV (Atkinson et al. 2008; Atkinson and Soria 2009; Worth and Nickels 2008; Discetti and Astarita 2011). For instance, algorithms such as multiplicative line-of-sight simultaneous MART (MLOS-SMART; Atkinson and Soria 2009) have been introduced to accelerate the reconstruction process.

Furthermore, tomographic PIV has been applied to myriad of flow problems, since its introduction. These include large-scale (~ 1 m) flows (Kuhn et al. 2010) and flow within a small droplet (~1 mm) using a microscopic objective (Kim et al. 2011).

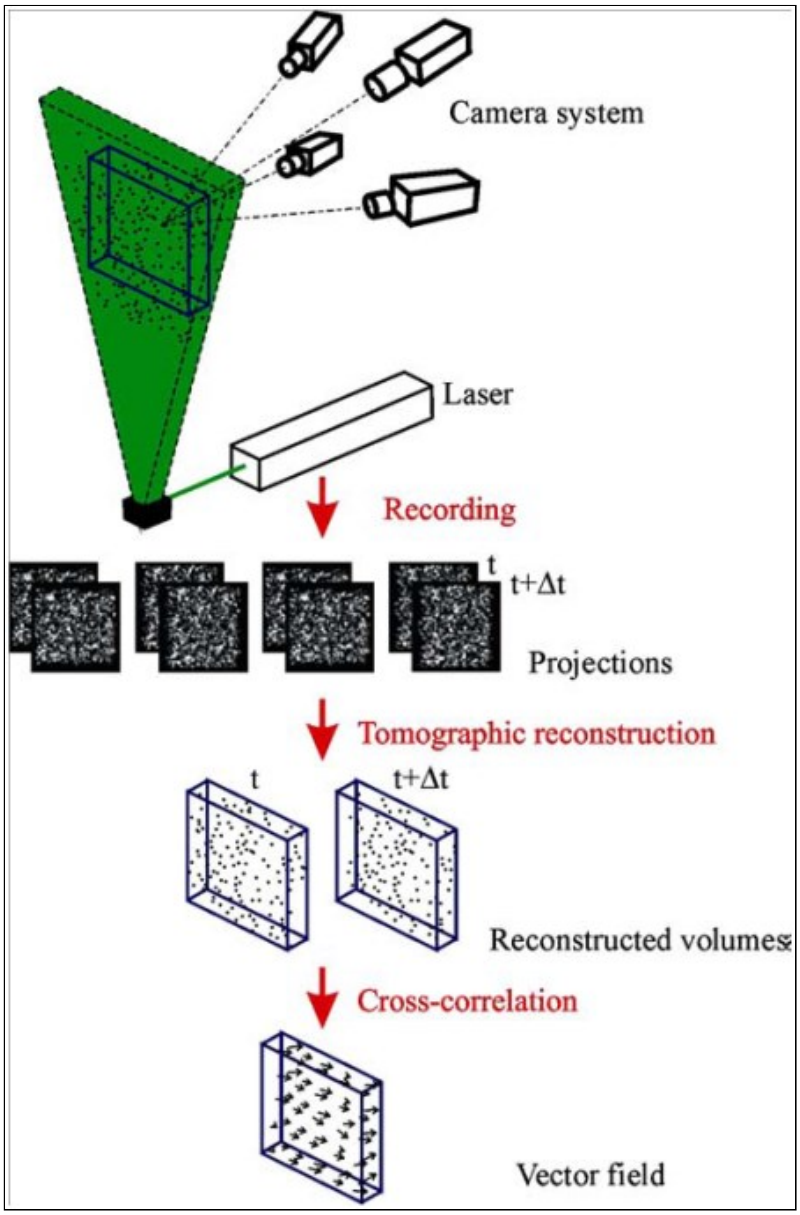

Figure 1-6: Schematic diagram representing tomographic PIV (Reproduced from Elsinga et al 2006)

1.3 Objectives

The objectives of the thesis are two-fold:

(1) Develop and demonstrate a flow facility and measurement system

i. Flow facility requirements
   a. A recirculating channel facility to simulate uniform and unsteady cross flow to study behavior of copepods and predator-prey interactions in moving water.

ii. Measurement system requirements
   a. A volumetric velocimetry system (tomographic PIV) that enables all velocity and velocity gradient components to be resolved. This enables understanding inherently three-dimensional flow field around organisms.
   b. A motion tracking velocimetry system (3D PTV) that is capable of tracking both predator and prey during their interaction in a volumetric domain. This enables the study of copepod behavior and the organism motion during predator-prey interactions.
   c. Fully time-resolved measurements (i.e. high-speed imaging) that will aid in understanding the quick motion of organisms during predator-prey interactions.
   d. Illumination that allows measurement while not disturbing the organism behavior during predator-prey interaction.

(2) Apply the system and facility to investigate aquatic predator-prey interactions.

The measurement system and flow facility are used to address some previously unanswered questions, which are as follows:

- *How do copepods detect approaching fish?*
- *How do copepods escape fish predation?*
- *What flow field is generated by approaching fish?*
- *How do fish capture non-evasive and evasive prey in still water?*

- *How do fish capture evasive prey in moving/unsteady flow?*
- *What is the strategy for successful fish predation on copepods?*

Three separate experiments are designed to facilitate answers to the above questions. The experiments to be investigated are as follows:

Experiment (1): Copepod interactions with wall-mounted cylinder in cross-flow

Experiment (2): Predator-prey interactions in still water

Experiment (3): Predator-prey interactions in turbulent/unsteady flow

The rest of this thesis is organized as follows: Chapter 2 describes experimental facilities, measurement hardware, and the specific setup for various experiments that were carried out. Chapter 3 describes a novel technique developed for masking objects in volumetric particle image velocimetry. This technique was applied consistently to all results including fish study. Chapter 4 presents the results of Experiments (1) – (3). Chapter 5 discusses and summarizes the most important results, and Chapter 6 provides direction for future work.

Chapter 2

Experimental Facilities and Methodologies

This chapter first describes the design, development, and installation of the water channel facility (Section 2.1). In Section 2.2, the measurement hardware (i.e. laser, cameras, and tracer particles) requirements for PIV and PTV on aquatic organisms are discussed. Sections 2.3, 2.4, and 2.5 discuss the specific experimental setup for Experiment (1): Copepods interaction with wall-mounted cylinder in cross-flow, Experiment (2): predator-prey interaction in still water, and Experiment (3): Predator-prey interaction in unsteady/turbulent flow, respectively.

2.1 Water channel facility

A water channel facility was used for experiments (1) and (3). In this section, the design, development, and installation processes of the water channel are discussed in detail. Experiment (2) utilizes a simple tank, which may be bought off-the-shelf, to study predator-prey interactions.

2.1.1 Design

A water channel facility driven by a paddle wheel is implemented. Unlike an impeller driven channel, flow driven by a paddle wheel prevents damaging or killing of zooplankton as they circulate around the channel (Robinson *et al.* 2007; Clarke *et al.* 2009). In the current work, further considerations were made for the water channel so that it could be integrated with the tomographic PIV and 3D PTV measurement system. These considerations included:

1. Optical access: Test section should be at least 15 cm in height for optical access by the cameras.

2. User access: Access to both sides of the test section is required for mounting lights, lasers and cameras, where needed.
3. Flow conditioners: Screens and honeycombs are needed to generate a uniform base flow with low turbulence intensity.
4. Test section: Test section should be at sufficient distance downstream of the flow conditioners to allow zooplankton to re-orientate after passing through the honeycomb and screens.
5. Flow velocity: Velocity of the flow ranges from 0cm/s to 30cm/s (since blennies do not respond above 30cm/s; Clarke *et al.* 2009).
6. Portability: Channel should consist of smaller components, which are easy to assemble/disassemble. This was required to enable transportation of the completed water channel to University of Texas Marine Science Institute for experiments.
7. Materials: Materials inert to seawater and freshwater should be chosen for various channel components. Seawater, in particular, can easily promote corrosion of iron.

The above considerations led to the design shown in figure 2-1. The channel consists of an assembly of four main components: (1) straight sections, (2) corner sections, (3) paddle wheel, and (4) supports. The channel has a uniform cross section of 15 cm (span) × 26 cm (height) throughout the closed-loop. The channel can be filled with water to a height of 15 cm, and the additional height prevents spillage if a large head difference occurs when the flow is driven.

The channel and supports are designed such that the user can easily access all areas of the channel, including the interior of the closed loop. The test section is located in the straight acrylic section, 1.5 m downstream from the screens (see figure 2-1b). The test section is required to be transparent for optical access. A cavity, 17 cm (stream) × 15cm (span) × 10cm (height), is included in the channel floor at the test section (see figure 2-1a). This cavity allows for placement of cylindrical obstacles and fish housing (see details in section 2-3 and 2-5), where needed.

Screens and honeycombs (i.e. flow conditioners; see figure 2-1b) are located 1.5 m and 1.25 m upstream of the test section, respectively. This allows sufficient development length for zooplanktons (e.g. copepods) to re-orient themselves after passing through the flow conditioners before reaching the test section. Two mesh screens with open sections 10 mm^2 and 4 mm^2, and wire diameters of 1 mm and 0.3 mm, respectively, are placed 5 cm apart. Their mesh dimensions translate to open areas of 60% and 75%, respectively. The screens reduce pressure differences across the flow span and deflect the flow perpendicular to the screen (Mehta and Bradshaw 1979). Downstream of the second screen, two honeycomb sections with hole diameters 7.1 mm, and 3.8 mm are placed. The thickness of both sections is 25 mm, and they are placed 5 cm apart. Honeycombs reduce streamwise swirling and lateral mean velocity variations that may exist within the flow (Mehta and Bradshaw 1979). The hole sizes for both screens and honeycombs were designed deliberately to be > 2mm to allow zooplanktons (~ 1 mm) to flow through them easily. Guide vanes are placed at the corner sections (see figure 2-1a) to prevent persistent flow separation and secondary flows (Ramamurthy et al 2013).

The paddle wheel, consisting of a disk and attached paddles, is 0.73 m in diameter. Each paddle has a cross-section 14.5 cm (width) × 26 cm (height). A motor, connected to the paddlewheel via a timing belt and gear arrangement, is used to drive the flow. Specifications of the motor were decided based on a simple head-loss calculation (details in Appendix A) for the designed flow velocity range of 3 cm/s to 30 cm/s. Based on the calculation, a Leeson® 1/4 horsepower permanent magnet was chosen (Model No: CM34D25NZ52C). Furthermore, high torque and low revolution speed is needed to drive the flow, thus, a motor fitted with a gear assembly (gear ratio: 124:1) was selected. With this assembly, the motor is designed to operate at a torque of 371 lb/inch, and a maximum revolution speed of 21 revolutions per minute (RPM). A Dart® motor controller (Model: MD10P), with a Hall-effect pickup (Model No: PU-40E) feedback sensor, was purchased for precise control of the motor speed.

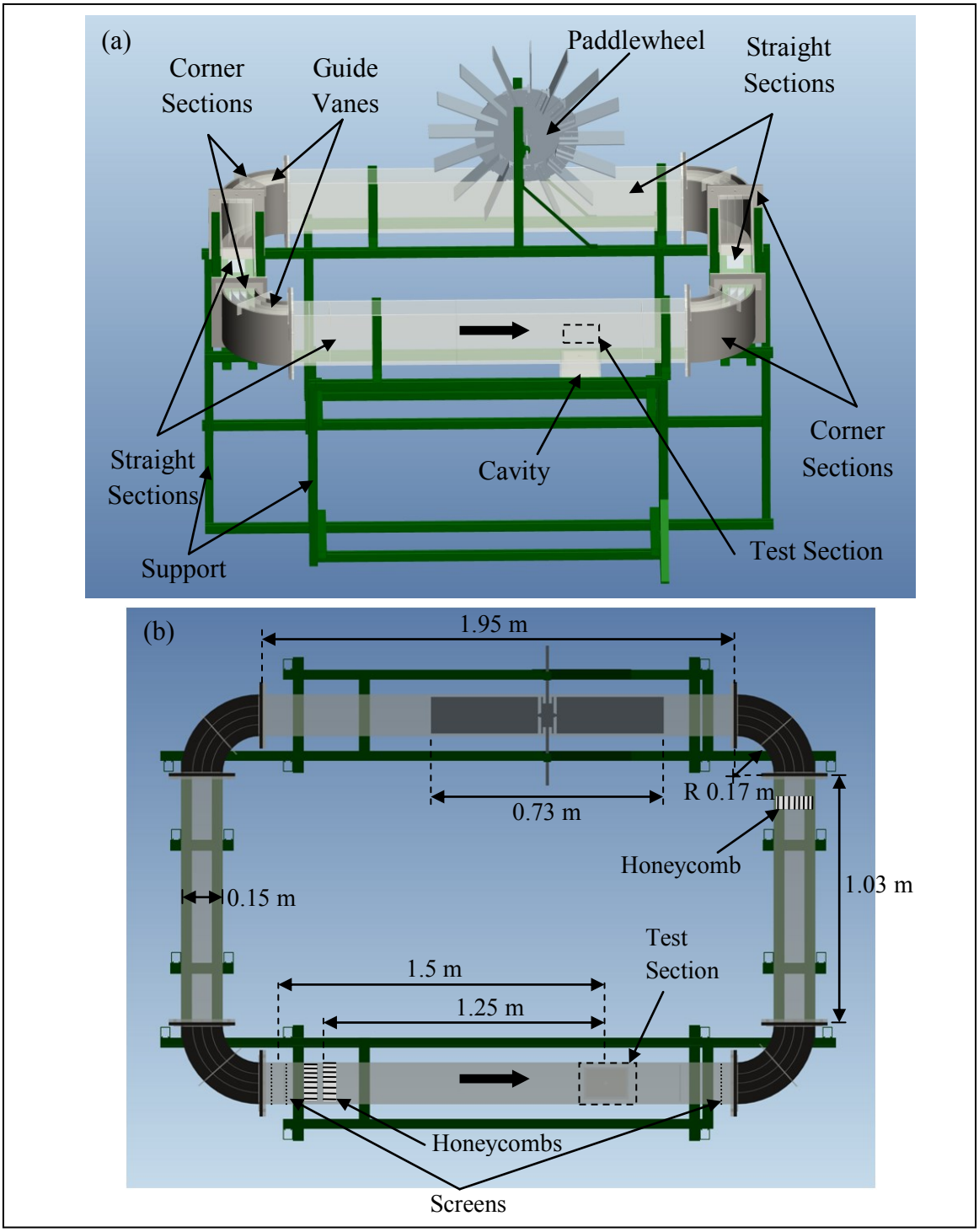

Figure 2-1: Schematic diagram of the water channel facility. (a) shows the bird's-eye view from the front, (b) shows the top view of the channel with channel dimensions and flow conditioners. The bold arrow represents the direction of flow.

2.1.2 Development

Material for each section (labeled in figure 2-1a) was chosen and fabricated based on the design requirements (see table 2-1). The straight sections were fabricated with acrylic for optical access inside the channel. The wall thickness of the acrylic was 0.5 inch. Corner sections, however, were not required to be transparent, thus stainless steel was chosen due to greater ease in fabricating (or rolling) the bends. Stainless steel was chosen, instead of other metals, since it is more resistant to corrosion when in contact with seawater. The wall thickness of the corner section is 0.19 inch. Both straight and corner sections were fitted with flanges. Ten evenly spaced holes (diameter: 0.5 inch) were designed so that 3/8 inch bolt-washer-nut assemblies could be used to secure the sections together. Fabrication of straight and corner sections was outsourced to local companies – Kreative Acrylics, and Twin Cities MetalFab Inc., respectively. Acrylic guide vanes (see figure 2-2) were outsourced to Crown Plastics Inc. for fabrication.

Polyvinyl chloride (PVC) was used for the paddle wheel. PVC is inert to seawater, relatively lightweight, and less brittle than acrylic, making it a suitable material. The paddle wheel consists of a disk and a set of paddles. The paddles were attached to the disk using a PVC L-plate, and secured using 1/4 inch bolt-nut assemblies. Fabrication of the paddle wheel was carried out in the research shop at the University of Minnesota.

Finally, strut beams (Unistrut®), made of steel, were used for support. Since the supports are not in direct contact with seawater, steel was considered appropriate for design. Unistrut® beams were cut to a desired length at the student shop (University of Minnesota), using a hydraulic-feed band saw.

Table 2-1: Description of material and fabrication location for various parts of the water channel

Part	Material	Fabricated and assembled at:
Straight Sections	Acylic	Kreative Acrylics 6174 Olson Memorial Highway, Golden Valley, MN 55422
Corner Sections	Stainless Steel	Twin Cities MetalFab Inc 1319 Pierce Butler Rte, St Paul MN 55104
Paddlewheel	PVC	Research Shop University of Minnesota 2-134 Mechanical Engineering
Support	Steel (Unistrut)	Student Shop University of Minnesota 180Mechanical Engineering
Guide Vanes	Acrylic	Crown Plastics Inc. 12615 16th Ave N, Plymouth, MN 55441

2.1.3 Installation

Once the components of the water channel were fabricated and gathered, they were installed as follows:

(i) Unistruts® were assembled to support the water channel.

(ii) The acrylic straight sections and the stainless steel corner sections of the channel were placed to form a "rectangular (rounded edge) path" for the water channel. Rubber pads were placed underneath the straight sections to prevent scratches from the Unistrut® on the acrylic surface.

(iii) Foam gaskets were placed between the straight and corner sections to seal the acrylic and steel flanges (see figure 2-2). The corner section, gasket and straight section were secured using 3/8 inch bolt-washer-nut assemblies. After securing, the connection was further improved by applying a very thin layer of marine-grade silicone sealant inside the channel. This prevented any water leakage when the channel was filled.

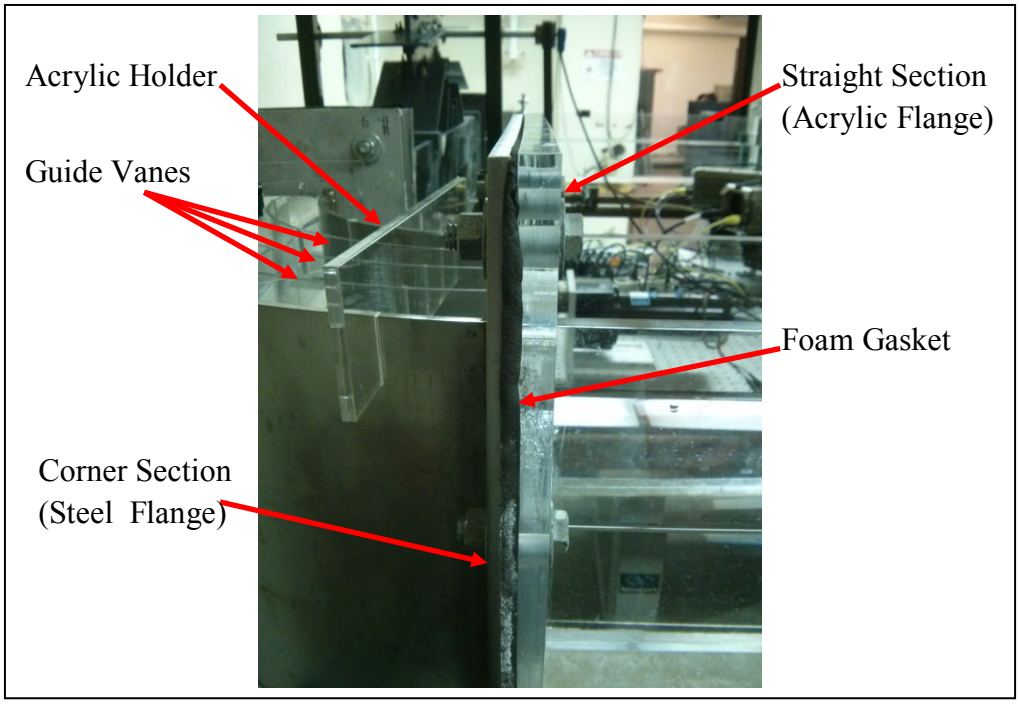

Figure 2-2: Attachment of corner section with the straight section and the location of guide vanes

(iv) Acrylic guide vanes were placed in the corner sections (see figure 2-2). Custom-made acrylic holders held the vanes in place to guide the flow around the corner.

(v) Additional spacers in the water channel were included to facilitate addition of screens through screen slots (see figure 2-3). Spacers were also used to "fill-in" the gap when closing the channel loop. This gap was caused by imperfection in fabricating the corners to the correct angle.

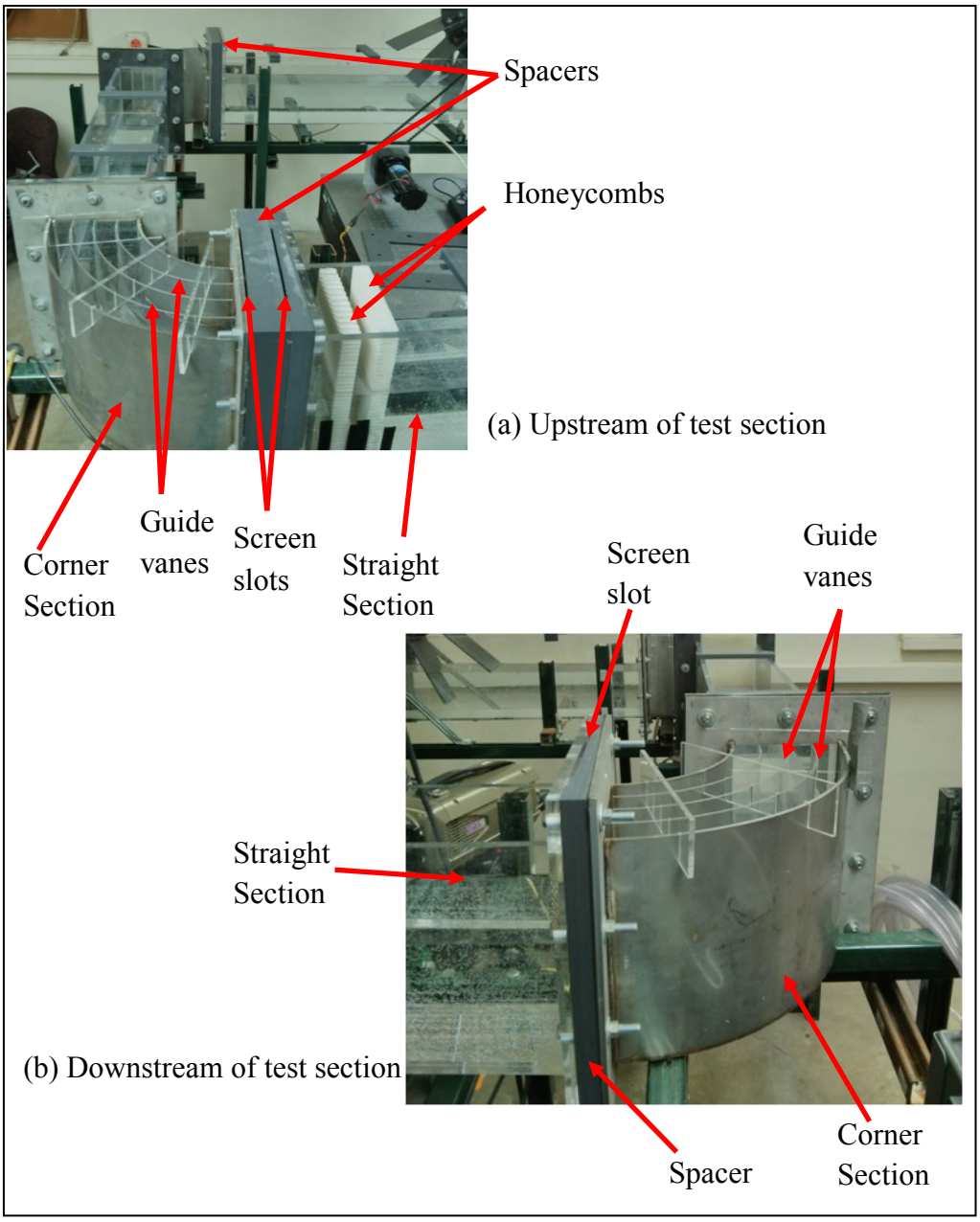

Figure 2-3: Arrangement of spacers, honeycombs, and screens (a) upstream and (b) downstream of the test section.

(vi) Screens and honeycombs were installed upstream of the test section as described in section 2.1.1. In addition, a screen and a honeycomb were also placed downstream of the test section. The screen was used to prevent fish from being swept further downstream. The honeycomb was added to minimize any perturbation of the flow propagating upstream from the paddlewheel.

(vii) The paddle wheel was connected concentrically to a 3/4 inch stainless steel shaft, using a flanged shaft collar. The shaft was mounted on two vertical Unistrut® beams using a mount bearing, and carefully aligned such that the wheel could rotate freely without interference (see figure 2-4). The clearance gap between a vertical paddle and channel floor was about 3 - 5 mm. The Leeson® motor was connected to the paddlewheel using a timing belt. The motor was secured on a separate table to prevent the motor vibration from propagating to the water channel. The gear ratio between the timing belt pulley attached to the motor and the paddle wheel was 1. A Hall effect feedback sensor was attached to the paddle wheel. The Dart® motor controller, which was connected to the motor and the feedback sensor, ensured that the paddlewheel rotated consistently at the desired revolution speed by measuring the paddlewheel rotation directly and adjusting the armature current fed to the motor (see figure 2-4). The gain of this closed-loop feedback was set relatively low to prevent any undesirable oscillations by the paddlewheel.

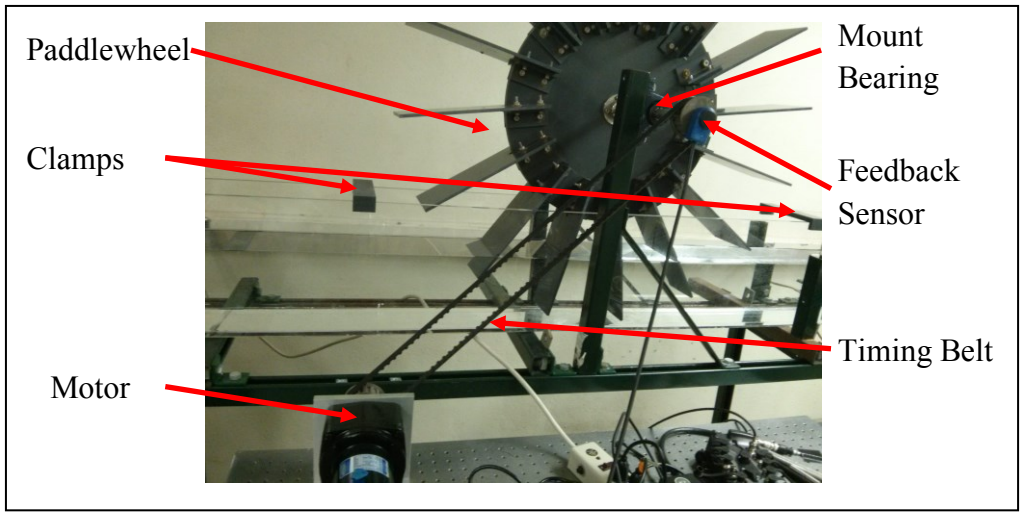

Figure 2-4: Paddlewheel connections, and clamps

(viii) PVC clamps were designed, fabricated and placed over the top of the straight sections throughout the channel (see figure 2-4) to prevent the acrylic from warping when the channel was filled with water.

(ix) At the test section, the top of the cavity was made level with the channel floor by inserting a PVC fixture (see figure 2-6). Since the fixture was removable, modifications to the fixture could be carried out for specific experiments, as needed (e.g. drilling a hole for fish housing).

(x) Finally, an acrylic plate was secured at the surface of the water (see figure 2-6b) to prevent any surface waves from refracting laser or light source as it entered the water to illuminate the test section.

The complete water channel setup with the measurement system is shown in figure 2-7.

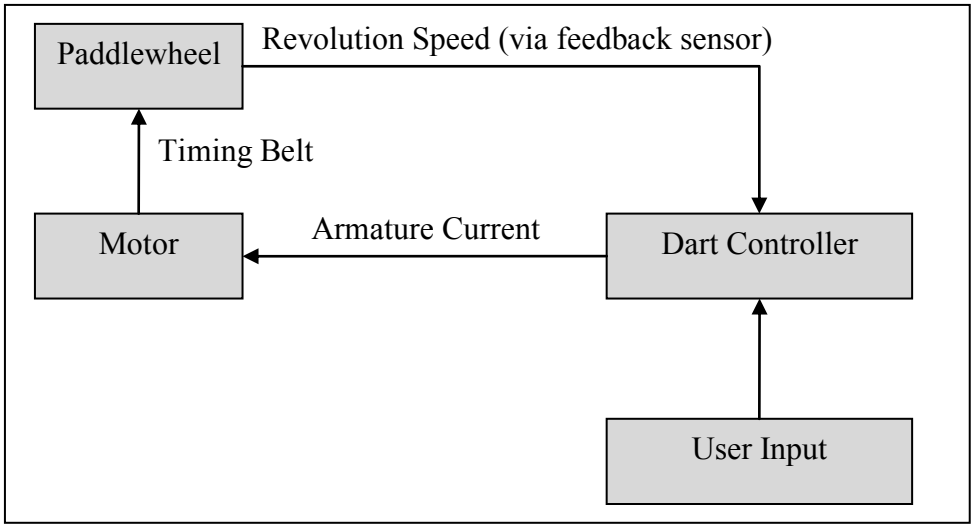

Figure 2-5: Diagram depicting the signal passages in the motor-paddlewheel assembly

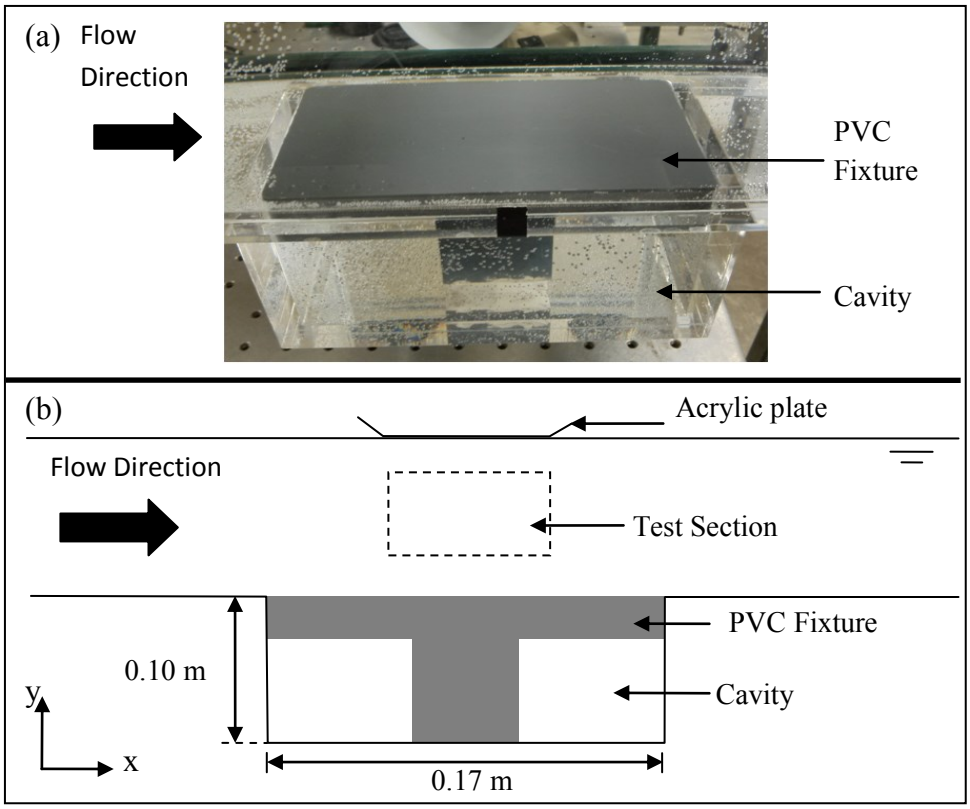

Figure 2-6: (a) image and (b) schematic front view of the cavity and PVC fixture. An acrylic plate is placed above the test section to prevent surface waves from interfering with the laser.

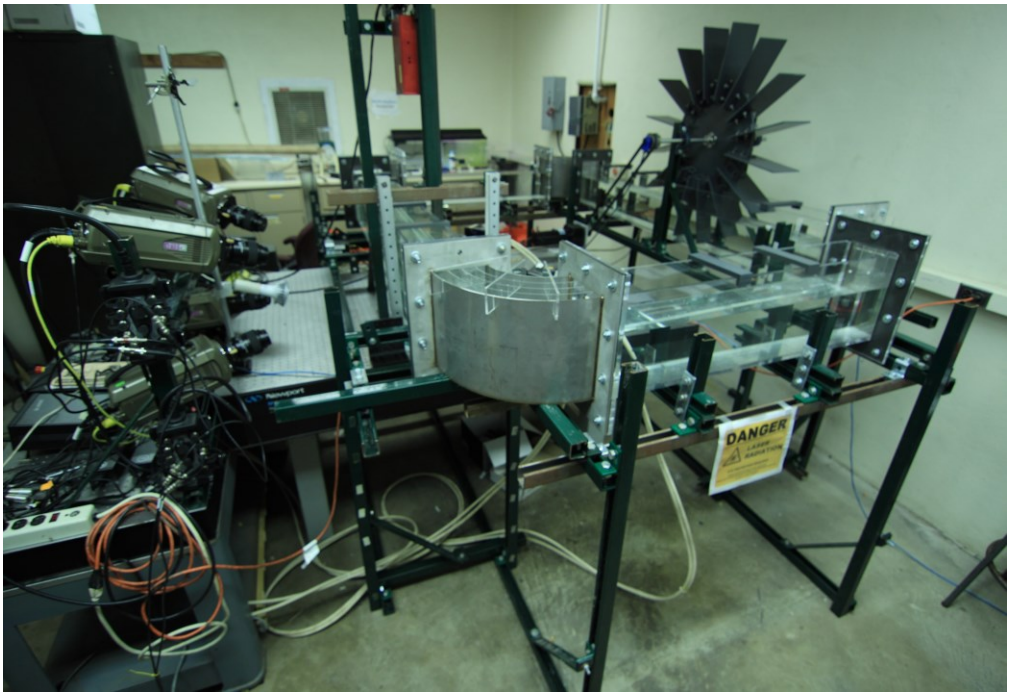

Figure 2-7: Completed water channel setup with the measurement system.

2.1.4 Transportation

The channel was designed and built to be portable when disassembled. A 5-step disassembly sequence is as follows:

(1) Drain the existing water from the channel;
(2) Remove the motor, timing belt, feedback sensor and paddle wheel;
(3) Remove the silicone sealant, and unscrew the bolt/nut assembly connecting the corner and the straight sections;
(4) Remove the corner and straight sections, and the rubber pads used to support the straight sections.
(5) Remove the Unistrut® beams below the shorter straight sections. Once removed, the entire support section is separated into two parts, which can be carried by 2-3 individuals.

The channel was built and assembled at the Fluid Dynamics Lab in University of Minnesota. It was transported to the University of Texas Marine Science Institute at Port Aransas, TX to perform the seawater experiments (see figure 2-8). A total of about 21 hours of drive time is required to transport the facility to Port Aransas, TX from Minneapolis, MN. After the experiments, the channel was transported back to the Fluid Dynamics lab at the University of Minnesota.

The water channel, together with the measurement system, took 2 days to dissemble and load into a 14-feet truck (U-Haul International) by four people (at Minneapolis, MN), and took slightly less than 2 days by two people to unload and re-assemble (at Port Aransas, TX).

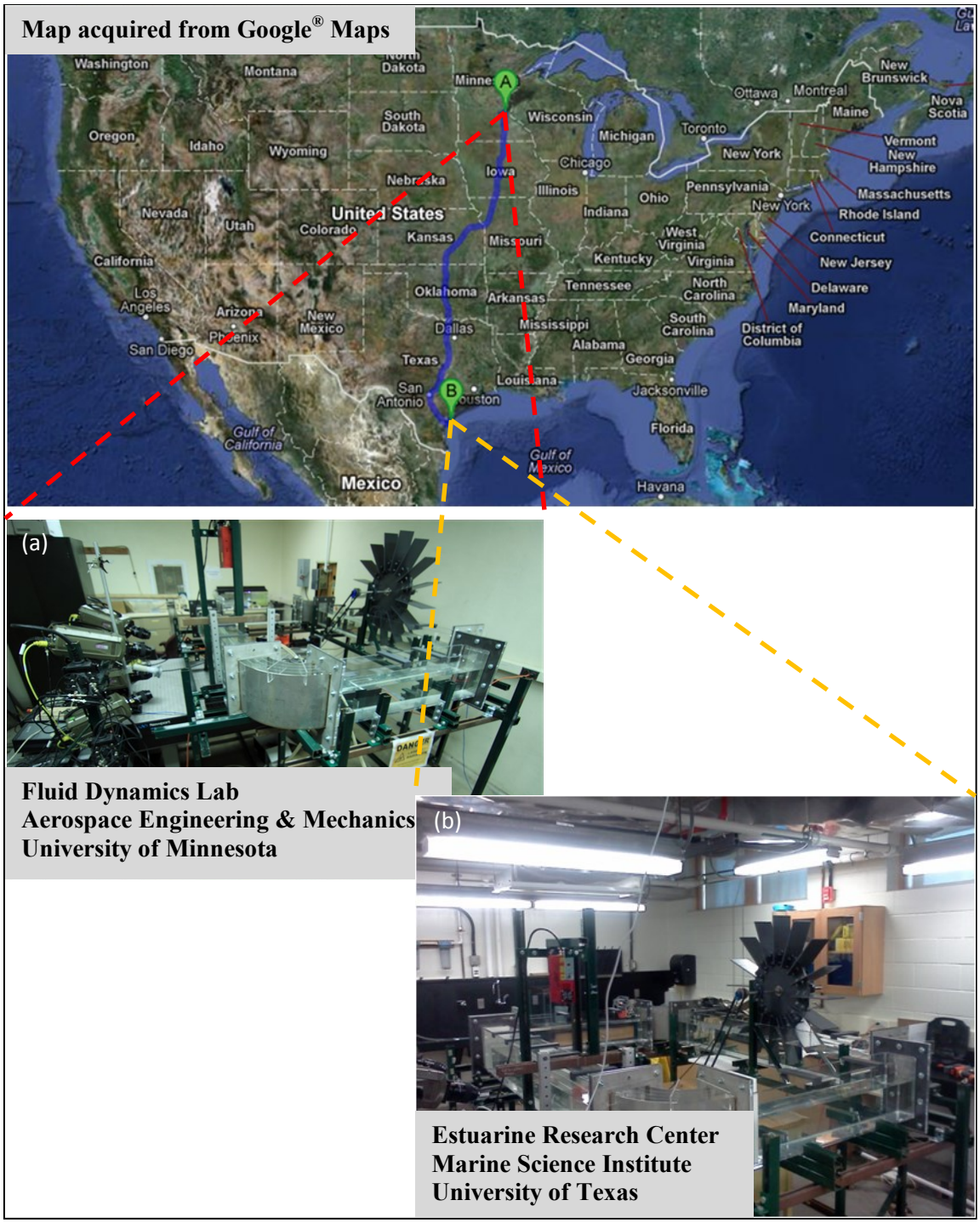

Figure 2-8: Map depicting the location where the channel was transported for seawater experiments. (a) and (b) show the same experimental facility at different locations.

2.1.5 Flow qualification

After the water channel was installed and filled, the flow was qualified to meet its desired uniformity, and low turbulence intensity. Free stream flow velocity was also calibrated by measuring streamwise velocities at known revolution speeds of the paddle wheel. These revolution speeds were 1, 2, 5, and 10 revolutions per minute (RPM).

Stereo-PIV was used to measure the three-component velocity field in a stream wise-wall normal plane within the test section. The measurement plane was situated at the center of the channel (center of spanwise direction), and about 6.5 cm above the channel floor (6.5 cm in wall normal direction). Sets of 500 independent vector fields for each paddle wheel revolution were obtained.

The time interval, Δt, between consecutive images was 15 ms, 7.5 ms, 3 ms, 1.5 ms, for revolution speeds 1, 2, 5, 10 RPM, respectively. The time interval was chosen such that a particle moving at the free stream velocity, U_0, traveled about 8 pixels/Δt between images. In this arrangement, the uncertainty in instantaneous velocity for PIV can be estimated as 0.1 pixel/Δt, and this translates to a velocity uncertainty of (0.1/8 * U_0) = 0.0125U_0 (or 1.25% of free stream velocity) for the current measurement.

The uniformity and turbulence level were analyzed. A calibration function of the mean flow with respect to the paddle wheel revolution speed was also derived. The uniformity, turbulence and calibration analyses are provided below.

2.1.5.1 Uniformity

Figure 2-9 shows the mean flow velocity field in the channel at various revolution speeds of the paddle wheel (1, 2, 5, and 10 RPM). Table 2-2 shows the range of velocities and the percentage velocity variation within each field. From table 2-2, cases 1 - 4 RPM show that velocity varies within the field of view by 2.6%, 1.6%, 1.0% and 0.8, respectively. For all cases, systematic (instead of random) variation of mean velocity is observed. This variation is a result of calibration error and uneven focus of image when stereo-PIV was carried out. However, these errors are relatively small, considering the

arrangements made to accommodate living organism in the design of the water channel (e.g. limiting the size of honeycomb to > 2 mm).

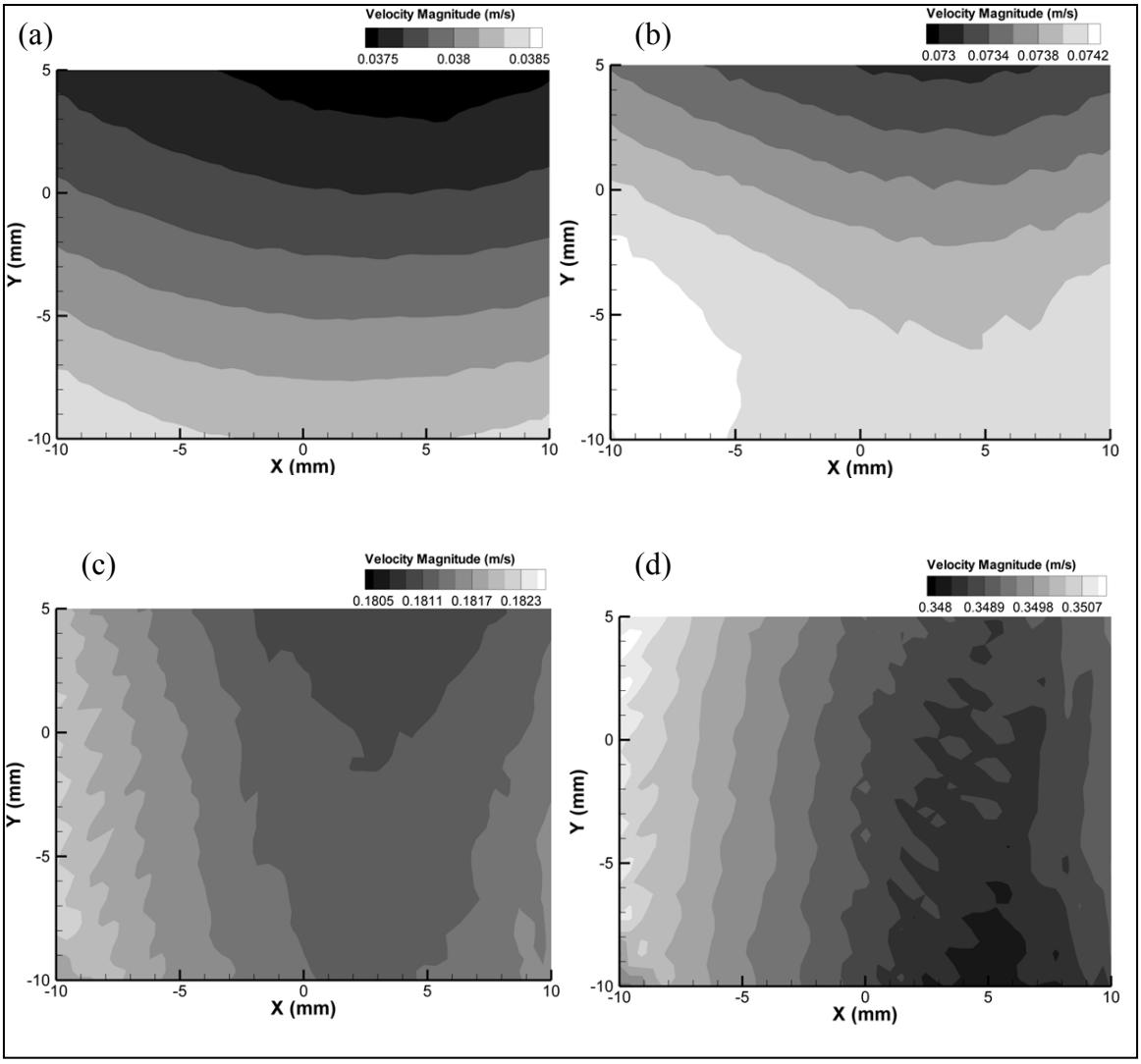

Figure 2-9: Mean velocity flow field of 500 datasets for (a) 1 RPM, (b) 2 RPM, (c) 5RPM, and (d) 10 RPM.

Table 2-2: Velocity range and percentage variation in velocity in velocity measurement for cases of 1, 2, 5, 10 RPM.

RPM	Velocity min-max (m/s)	Velocity range (m/s)	% variation in velocity
1	0.0375 - 0.0385	0.001	2.6
2	0.073-0.0742	0.0012	1.6
5	0.1805-0.1823	0.0018	1.0
10	0.348-0.3507	0.0027	0.8

2.1.5.2 Turbulence intensity

Turbulence intensity, *T.I.*, of the water channel is defined as follows:

$$T.I. = \frac{u'}{U} = \frac{\sqrt{\frac{1}{3}\left(\overline{u_x'^2} + \overline{u_y'^2} + \overline{u_z'^2}\right)}}{\sqrt{U_x^2 + U_y^2 + U_z^2}} \tag{2-1}$$

where U_i for i = *x, y, z* represents the mean velocity component in each direction, while u_i' represents the root-mean-square velocity fluctuation in each direction. The bar above the rms terms represents the mean of $u_i'^2$.

Figure 2-10 shows the turbulence intensity field for 1, 2, 5, 10 RPM cases. Coherent patterns of turbulence intensity values are observed in figure 2-10, instead of random and incoherent patterns. This is likely a result of calibration error and uneven focus of particles during image acquisition. However, a general trend in the range of turbulence intensity scales show that as the mean flow velocity increases, the turbulence intensity decreases. The turbulence intensity range in figure 2-10 is consistent with the percentage variation in the mean flow shown in table 2-2, which suggests that magnitude of $\boldsymbol{u'}$ is dominated by small calibration and camera defocus error ranging between 0.5% to 2.5%. Thus, the turbulence intensity of the channel is under this range.

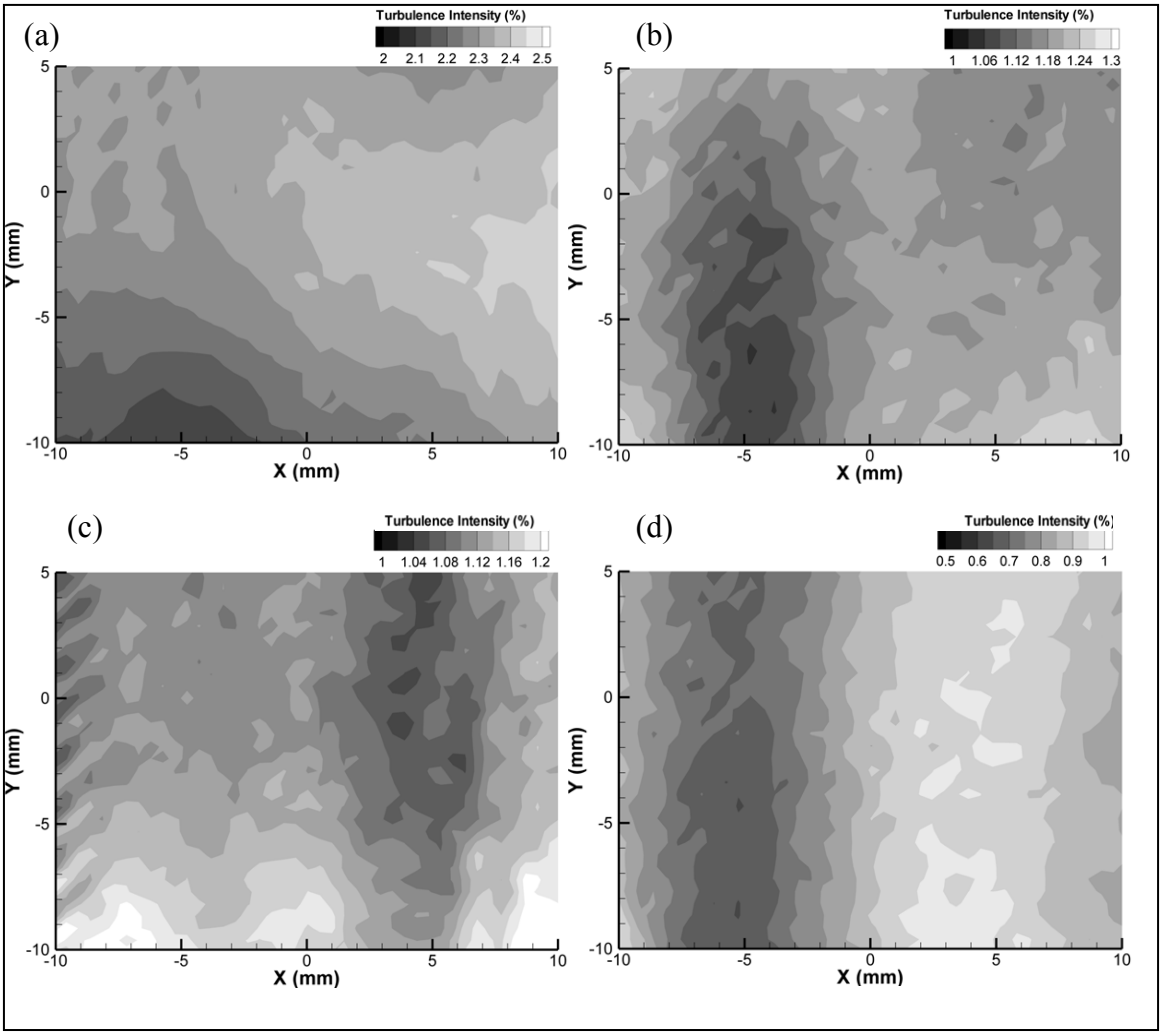

Figure 2-10: Turbulence intensity of flow field from 500 datasets for (a) 1 RPM, (b) 2 RPM, (c) 5RPM, and (d) 10 RPM.

2.1.5.3 Calibration function of mean flow w.r.t the paddlewheel revolution

The mean velocity in the water channel was calibrated with the rotational speed of the paddlewheel. The mean velocity was obtained from spatially averaging the stereo-PIV results in figure 2-9. Figure 2-11 shows the linear relation, given by

$$U_0 = 0.0384\omega \tag{2-2}$$

where U_0 is the mean velocity of the flow (in m/s), and ω is the rotational speed (in RPM).

This linear relation is expected since the velocity of the paddle, which is similar to the velocity of water it displaces, is linearly proportional to the revolution of the paddlewheel.

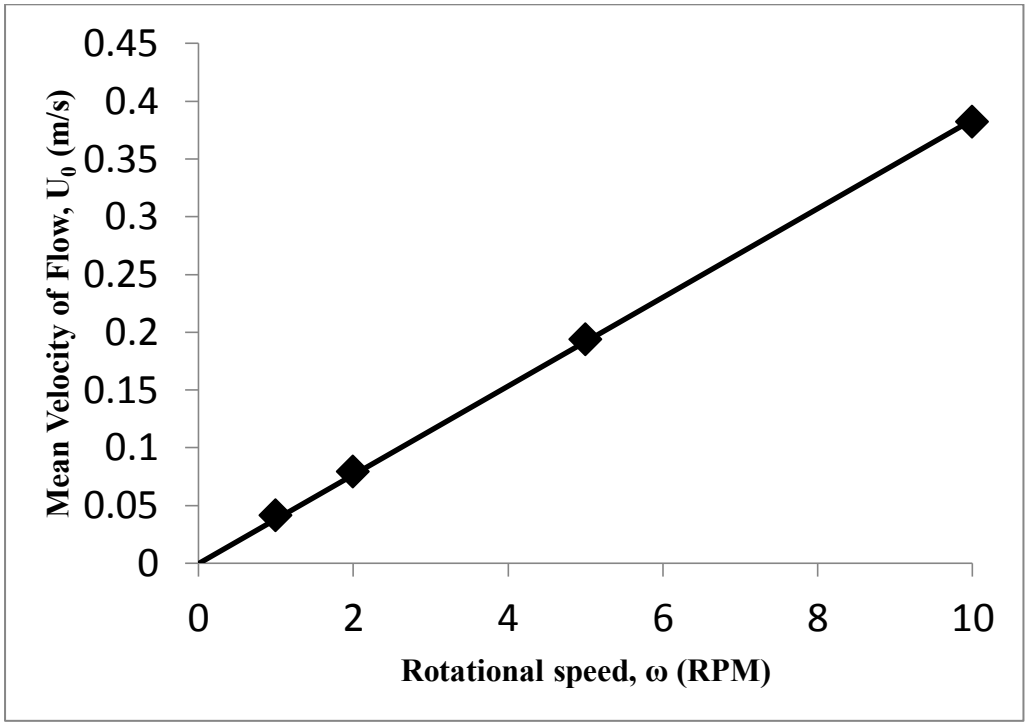

Figure 2-11: Calibration graph showing a linear relationship of mean flow velocity at the test section and rotational speed of the paddle wheel.

2.2 Measurement hardware

For quantitative measurement of volumetric flow fields and trajectories of organisms, tomographic particle image velocimetry (PIV; Elsinga et al 2006) and 3-D particle tracking velocimetry (PTV; Maas et al 1993) were used, respectively. Tomographic PIV and 3-D PTV systems typically need a laser, cameras, and tracer particles. Since natural behavior of predator-prey interaction of living organisms was desired without compromising the data quality, specific hardware considerations included:

(1) Laser

a. Wavelength invisible to fish and copepods to prevent interference with natural responses;
b. High pulse frequency required to resolve high-speed motion of fish and copepods;
c. High-powered laser for high intensity of scattering by the tracer particles over the volumetric field.

(2) Cameras

a. High frame-rate required to image high-speed motion of fish and copepods (camera images are synchronized with laser pulses);
b. High bit-depth of sensor for capture of broad range of intensity values, is useful in detecting tracer particles and plankton.
c. High sensitivity at the illumination wavelength required for high signal to noise ratio.

(3) Tracer Particles

a. Ideally, a naturally occurring phytoplankton is best to mimic a natural environment for organisms;
b. If synthetic particles are used, they should not be harmful to organisms (fish or zooplanktons);
c. Size ranging from 15 - 65 μm to provide ideal scatter size for tomographic PIV;
d. Neutrally buoyant;
e. Capable of effectively scattering laser wavelength.

2.2.1 Laser

A near-infrared laser (Oxford Lasers Firefly 300W) with wavelength of 808 nm was chosen because it is invisible to the fish (Lythgoe and Partride 1989) and copepods (Catton *et al.* 2007; Murphy *et al.* 2012), preventing any unnatural behavior, yet within the sensitivity range of CMOS cameras. The laser is capable of emitting a pulse frequency of up to 10 kHz with 1% duty cycle.

A major drawback of near infrared, as opposed to visible wavelength illumination, is the increased absorption of the illumination by water. The attenuation equation of an electromagnetic wave is given from the Beer-Lambert law as

$$I = I_0 e^{-\alpha x}, \tag{2-3}$$

where I is the local intensity, I_0 is the initial intensity before entering the medium, α is the absorption coefficient that may be derived from the imaginary part of complex refractive index, and x is the distance traveled by the illumination through the medium. From Hale and Querry (1973), it is found that in water, the absorption coefficient of a near-infrared wavelength (λ = 808 nm) is α = 0.022 cm^{-1}, while for typical green Nd:YAG laser wavelength (λ = 532 nm), it is α = 0.0035 cm^{-1}. By applying these absorption coefficients to equation (2-3), the reduction of intensity for the corresponding wavelength can be determined. For instance, the near-infrared illumination passing through 120 mm of water is attenuated by 41%, compared to a green wavelength that attenuates by only 9%.

2.2.2 Cameras

Six high-speed cameras (four Phantom v210; two Phantom M110) from Vision Research Inc., each with a 12-bit monochrome CMOS sensor and 1280 × 800 pixel resolution were used for image acquisition. The cameras are capable of acquiring up to 2200 frames per second (fps) at full resolution. The bit depth of the sensor can be configured up to 12-bit.

The cameras needed to be sufficiently sensitive in the near-infrared wavelength, with sensitivity usually measured by the quantum efficiency of the CMOS sensor. The quantum efficiency (QE) is defined as the ratio of the number of electrons released from the sensor per number of incident photons. Based on the manufacturer's specification, the QE of the Phantom camera sensors was about 23% for λ = 808 nm, compared with about 30% for a green wavelength (λ = 532 nm).

2.2.3 Tracer particles

In PIV, various particles have been recommended and used effectively with Nd:YAG (wavelength: 532 nm), Nd:YLF (wavelength: 527 nm), Ruby (wavelength: 694 nm) and Argon Ion (various visible wavelengths) lasers for planar PIV (Melling 1997; Adrian and Westerweel 2011). However, only a few have been tested with near-infrared lasers. Silver coated hollow glass spheres have been used (Epps and Techet 2007) with near-infrared illumination to study fish swimming. In another study, Murphy *et al.* (2009) used titanium dioxide to study the flow around copepods in near-infrared illumination. For the current work, various particles were tested and evaluated, and they are summarized in Table 2-3.

From Table 2-3, Polyamide (with 11% titanium dioxide) particles were eventually chosen for the current work. Green algae and diatoms satisfy most of the conditions, but they did not provide good scattering of near-infrared wavelength. Other particles that did not provide good scatter images include silicone dioxide, nylon, borosilicate glass, silicon carbide and polystyrene. Figure 2-12 shows sample images with some of these particles. It can be observed that polyamide particles (with 11% titanium dioxide) appear to give the best contrast (i.e. highest signal to noise ratio) compared to the others.

Hook and Fisher (2001) reported that silver is toxic to zooplankton. For the current work, a test was carried out to examine the effects of silver-coated glass spheres on copepods. Two containers with copepods were prepared (a test container, and a control container). Silver-coated glass spheres were added to the test container, and both containers were left undisturbed for 24 hours. After 24 hours, the copepods in the test container were inactive, while the other container showed active copepods. Thus, it was concluded that silver-coated glass spheres were not appropriate for the current work.

Murphy *et al.* (2012) used titanium dioxide to study flow fields around copepods. In their work, however, the field of view was small (19 mm × 13 mm), and the particle diameter was less than 10 μm. For the current study, the required field of view is much larger (~ 80 mm × 40 mm), and the available titanium dioxide particles are smaller (3

μm; see Table 2-2). Figure 2-13 shows that these particles were too small to obtain a high contrast scatter. Thus, the polyamide with titanium dioxide combination was used, as it is larger and provided better contrast at near-infrared wavelength.

Table 2-3: Table of tested seeding particles for Tomographic PIV and 3D PTV

Particles	**Phytoplankton?**	**Harmless to fish and zooplankton ?**	**Particle Diameter (μm)**	**Neutrally buoyant with water/ seawater?**	**Good scatter of IR wave-length?**
Green Algae (*D. primolecta; D. salina*)	✓	✓	10	✓	×
Diatoms (*C. quillensis; C. meneghiniana*)	✓	✓	10-20	✓	×
Silicon Dioxide	×	unknown	65	✓	×
Silicon Carbide	×	unknown	1.5	×	×
Nylon	×	unknown	4	✓	×
Borosilicate Glass	×	✓	35	✓	×
Silver Coated Hollow Glass	×	×	10	✓	✓
Titanium Dioxide	×	✓	3	×	✓
Polystyrene	×	✓	20	✓	×
Polyamide	×	✓	20	×	×
Polyamide (with 11% Titanium Dioxide)	×	✓	55	✓	✓

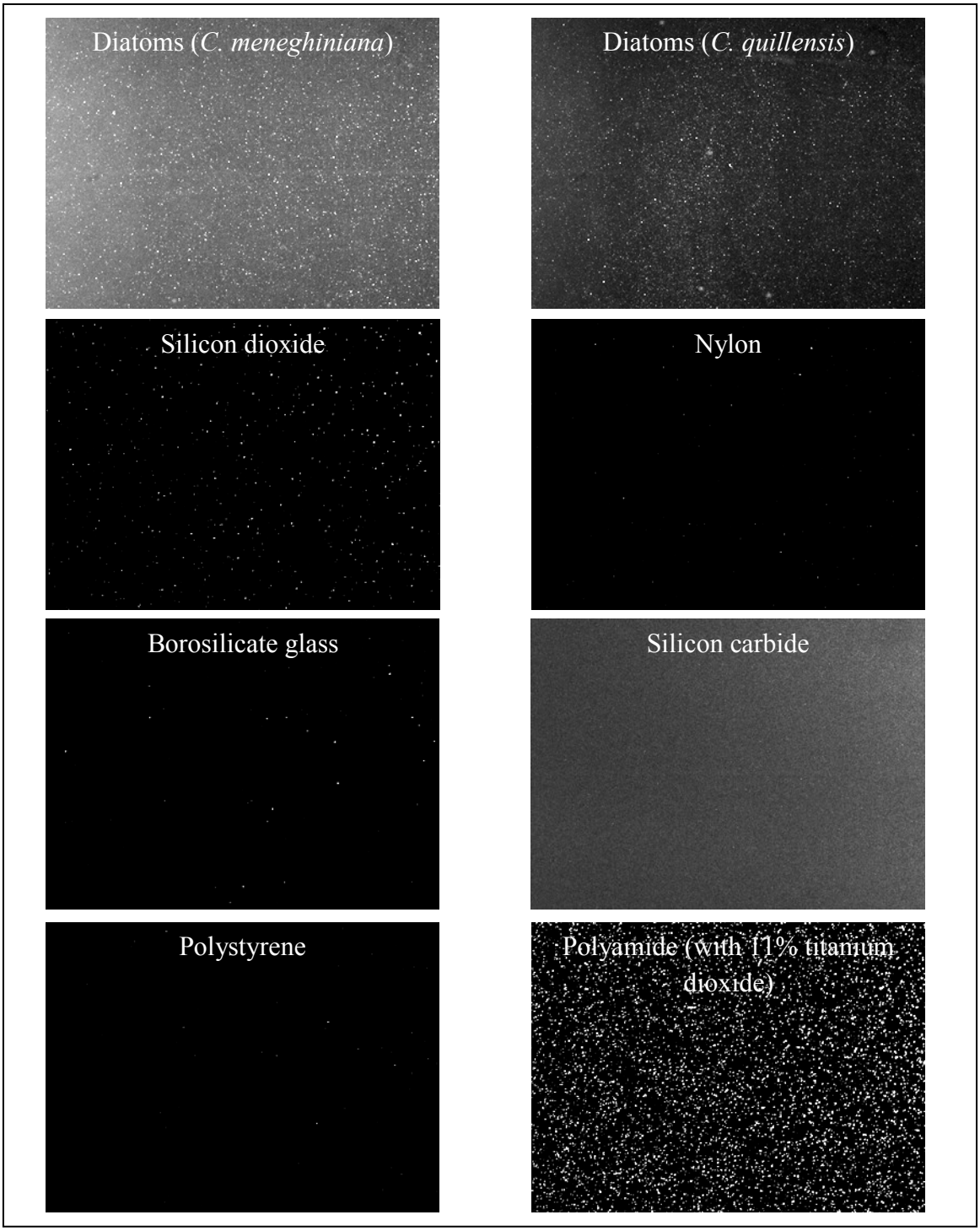

Figure 2-12: Images showing the scatter of near-infrared illumination (wavelength: 808 nm) by various particles.

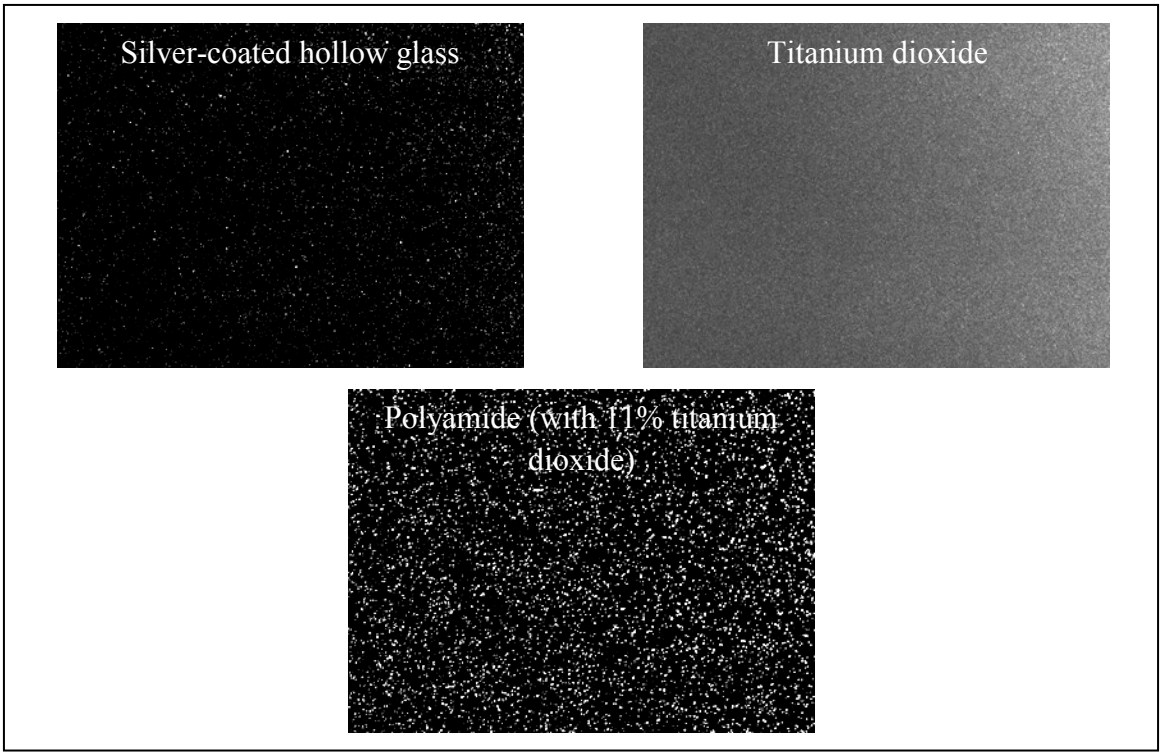

Figure 2-13: Images showing the scatter of near-infrared illumination (wavelength: 808 nm) by previously tested particles. Epps and Techet (2007) used silver-coated hollow glass spheres, and Murphy *et al.* (2012) used titanium dioxide.

2.3 Experiment (1) setup: Copepod interactions with wall-mounted cylinder in cross-flow

The goal of this study is to understand the behavior of the copepods quantitatively as they approach and move past a wall-mounted cylinder in the flowing water channel. Brine shrimp (non-evasive prey) are also used in this experiment for comparison. The flow field and trajectory of both zooplanktons are measured using a four-camera tomographic PIV and two-camera 3D motion tracking system, respectively. This section describes the species, detailed measurement setup, and experimental procedures.

2.3.1 Species

The zooplankton species examined were copepods (size ~ 1 mm) and brine shrimp (size ~ 1 mm). Brine shrimp were used for comparison, as they have similar size and inertia, but non-evasive and incapable of executing an escape response. The copepods (*Acartia tonsa*) were collected from Mustang Island, Texas (27°48′N, 97°05′W). In order to ensure that only one species of copepod was used for the experiment, the collected water sample was first passed through a 4000 μm mesh to filter off bigger plants and organisms. Next, the filtered sample was passed through a 150 μm mesh to remove smaller planktons. Then, a point source light was used to attract the copepods to one end of a container before they were captured and transferred to the water channel. Finally, a microscope was used to ensure that only one species of copepods was obtained. The brine shrimp (*Artemia salina*) were cultured in the laboratory. Brine shrimp eggs were placed in a hatchery. After 2 days, a point light source was used to attract hatched brine shrimp and contain them before they were transferred to the water channel.

2.3.2 Experimental Setup

The coordinates in the experimental setup is defined such that x-axis is streamwise, y-axis is wall normal, and z-axis is spanwise direction.

2.3.2.1 Facility

Experiments were performed in the water channel facility described in Section 2.1. A cylinder was mounted in the test section at two locations such that copepods upstream and downstream of the cylinder could be observed. Figure 2-14 shows the front and top view of the test section with two separate cylinder placements.

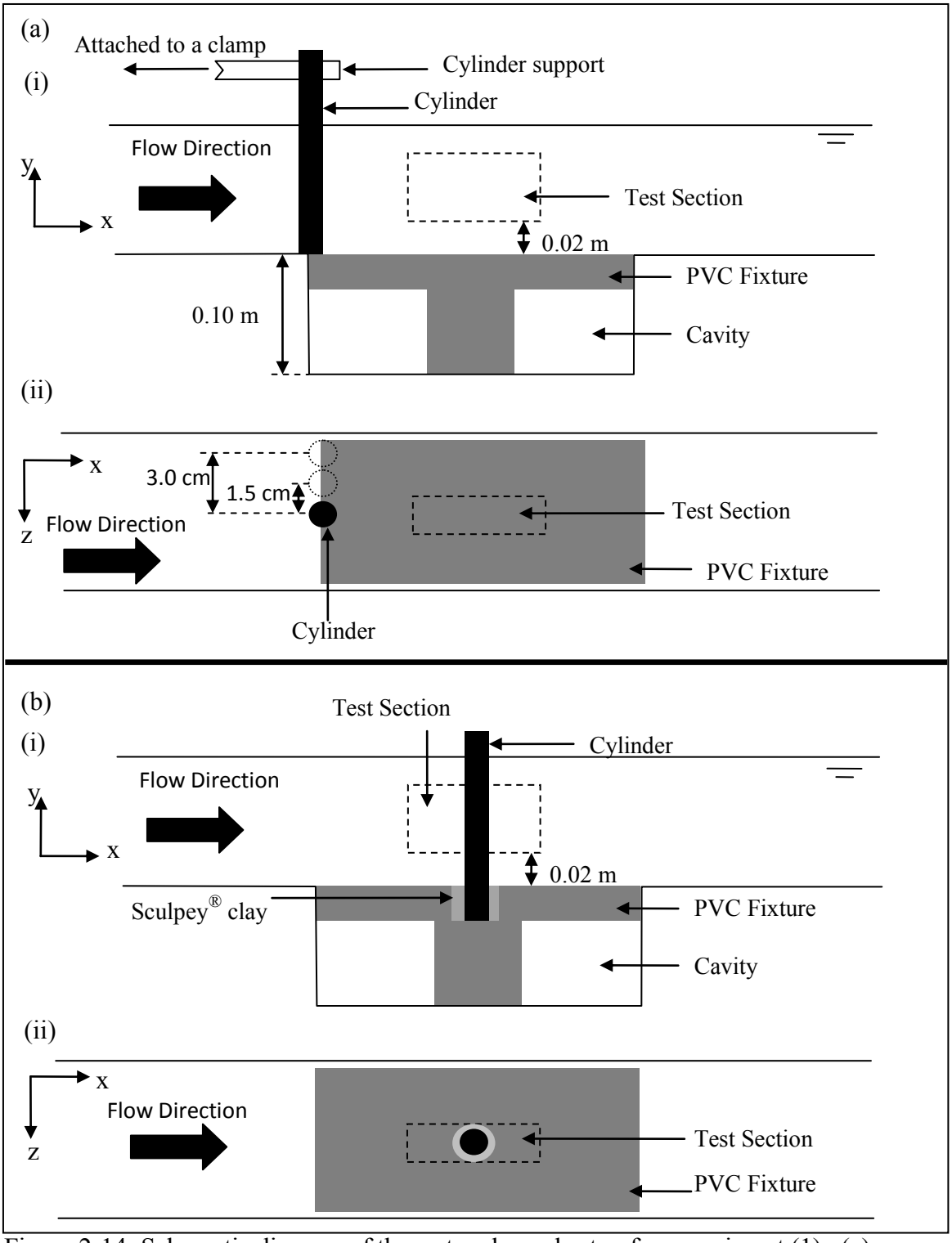

Figure 2-14: Schematic diagram of the water channel setup for experiment (1). (a) shows the cylinder upstream of the test section to examine copepod interaction with the cylinder wake, and (b) shows the cylinder within the test section to study motion of copepods approaching the cylinder.

Figure 2-14(a) cylinder configuration was used to study the response of copepods to specific eddy scales generated in the cylinder wake, while figure 2-14(b) configuration (cylinder within the test section) was used to study the response of copepods to disturbances (such as deceleration and strain rate) as it approached the cylinder.

The cylinder was mounted with a support that is attached to the channel clamp 8 cm upstream from the center of the test section, at the spanwise center (see figure 2-13a). Two other locations of 1.5 cm and 3.0 cm spanwise offset from the center (depicted as dotted circles in the figure 2-14a(ii)) was also studied. These offset arrangements were used to study the difference in copepod behavior outside of the cylinder wake.

The cylinder was placed inside a 2-inch hole, which was drilled into the PVC fixture (see figure 2-14b). The gap between the smaller diameter cylinder and larger diameter hole was filled with Sculpey® clay. Results upstream of the cylinder are of interest for this case.

For both cases, two cylinders, with diameters d_c = 6.35 mm and 12.7 mm, and three free stream velocities, U_0 = 0.038 m/s, 0.077 m/s, and 0.115 m/s, were considered. The combination of cases studied and their respective cylinder diameter, free stream velocity, cylinder Reynolds number, estimated eddy frequency, and estimated dominant eddy size are shown in table 2-4. The eddy frequency is estimated by assuming Strouhal number, $St \sim 0.2$ for the cylinder wake, and the eddy size is estimated to be the diameter of the cylinder.

Table 2-4: Experimental cases carried out for copepod interaction with cylinder (upstream and downstream)

Case	Cylinder diameter, d_c (mm)	Free stream velocity, U_0 (m/s)	Eddy frequency, $f = 0.2U_0/d_c$ (s^{-1})	Eddy size, (m)	Reynolds number, $Re = U_0 d_c/\upsilon$
1	6.35	0.038	1.2	0.006	230
2	12.7	0.038	0.6	0.013	460
3	12.7	0.077	1.2	0.013	930
4	12.7	0.115	1.8	0.013	1460

2.3.2.2 Infrared Tomographic PIV + 3D PTV: Measurement Setup

Figure 2-15 shows the setup for the simultaneous infrared tomographic PIV and 3D PTV applied to measure fluid motion and zooplankton distribution. The tomographic PIV measured volumetric velocity variation within the fluid, while the 3D PTV tracked the zooplankton independently. For tomographic PIV, the channel was seeded with 55μm polyamide (with 11% titanium dioxide) particles. The measurement volume was illuminated with an Oxford Firefly infrared laser (wavelength: 808 nm) with 3 mJ/pulse and pulse duration of 10 μs. The beam was expanded into a sheet with spanwise thickness ~20 mm. Four high-speed cameras (cameras 1, 2, 3, and 4; 1280 × 800 pixels), each fitted with a 105 mm Nikon Micro-Nikkor lens and infrared-pass optical filter, were mounted and aimed at the measurement volume. The lens f-stop was set to *f*/11. The infrared-pass filters were needed to allow only the infrared illumination scattered from the tracer particles to pass through the lens. The cameras were placed in a "square" configuration, and tilted approximately 30º to the z-axis. In the measurement setup, the x-axis (horizontal) and y-axis (vertical) are defined parallel to the laser sheet, and the z-axis is defined positive towards the cameras with z = 0 furthest from the cameras.

Simultaneously, for 3D PTV, the measurement volume was illuminated with two white LED lamps (Philips LED lamps 120 W) placed in a dark-field illumination configuration. In this configuration, the LED lamps were angled at about 60º to the negative z-axis (see figure 2-15). The lamps were also tilted towards the negative y-axis to mimic the presence of the sun in the natural environment. Two additional high-speed cameras (cameras 5 and 6; 1280 × 800 pixels), fitted with 105 mm Micro-Nikkor lenses and infrared-blocking optical filters, were aimed at the measurement volume to image the zooplankton. The lens f-stop was set to f/11. The cameras were placed in a "top-bottom" configuration (see figure 2-15a), and tilted slightly less than 30º to the z-axis. The LED lamps and infrared-blocking filters were effective at illuminating the zooplankton but not the tracer particles. Typical images acquired for tomographic PIV and 3D PTV are presented in figure 2-16(a) and (b), respectively. Note that the dark circular edge (i.e. mechanical vignette) in figure 2-16(b) is a partial block caused by the lens mount of the

Phantom M110 cameras. Nevertheless, the optical block is limited to the outer edges of the image only. Figure 2-16(a) shows the tracer particles, while figure 2-16(b) shows zooplankton (brine shrimp) within the flow. These images demonstrate successful segmentation of the zooplankton from the tracer particles by this combination of cameras and optical filters.

Image acquisition from the cameras was synchronized by supplying the frame synchronization signal from one master camera to the other five cameras and the laser.

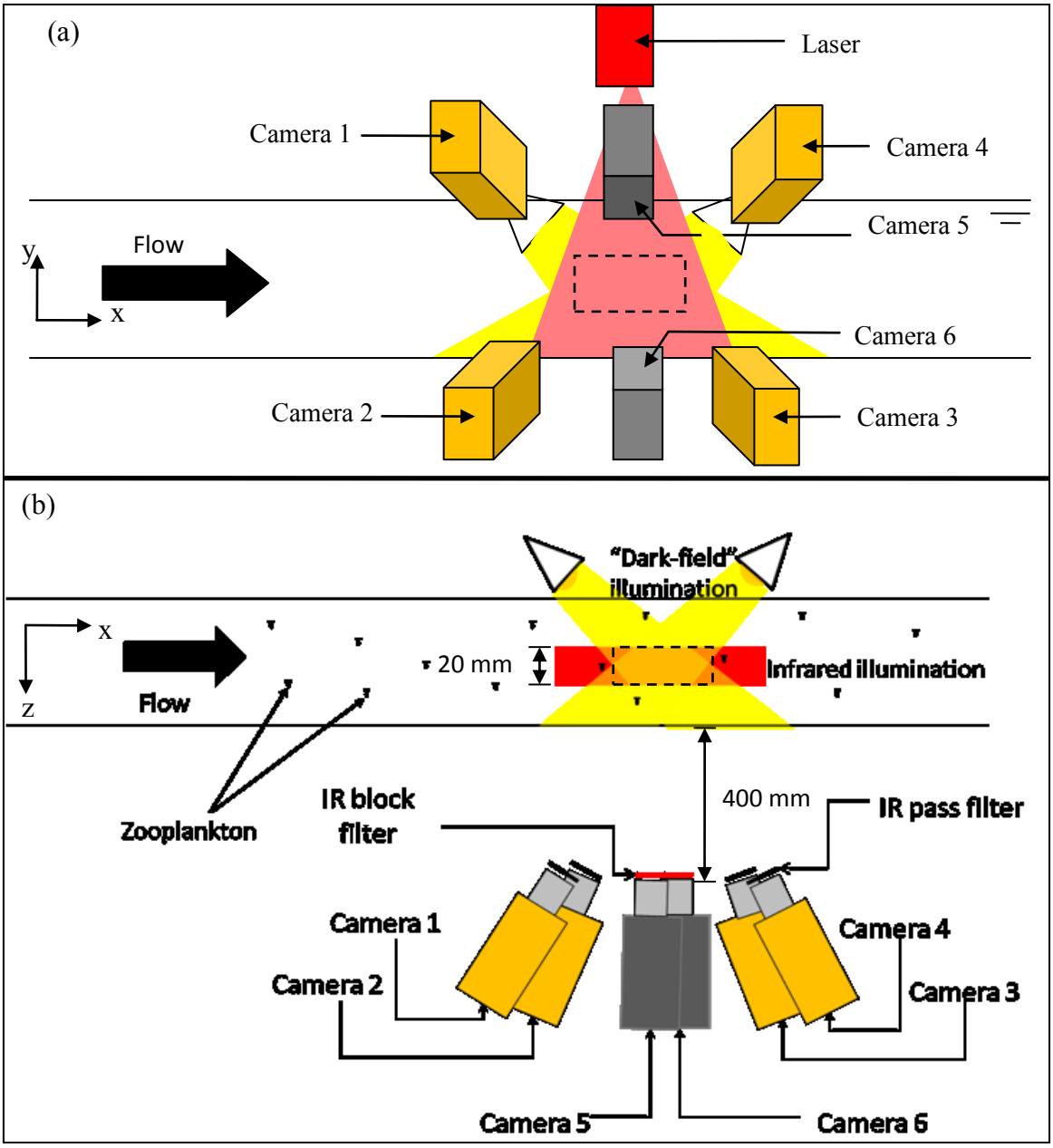

Figure 2-15: Schematic (a) front and (b) top view of the simultaneous tomographic PIV (cameras 1, 2, 3, 4) and 3D PTV measurement system (cameras 5, 6) to measure instantaneous flow field and location of the zooplankton and fish in a volume. Dashed box within the infrared illumination represents the measurement volume.

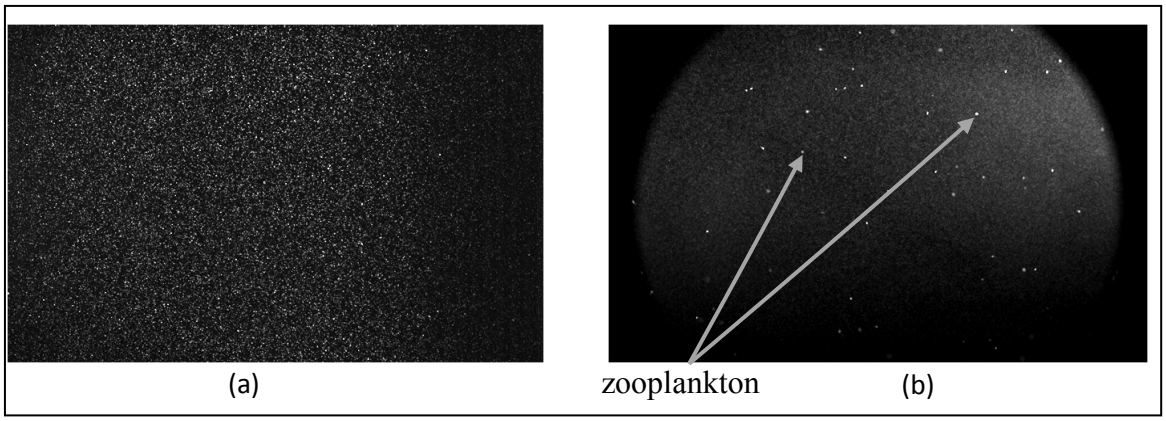

Figure 2-16: Typical image obtained for (a) tomographic PIV and (b) 3D PTV. Images were taken at the same time instance from different cameras.

2.3.2.3 Infrared Tomographic PIV + 3D PTV: Methodology

A calibration plate was traversed to nine positions spanning the depth of the measurement volume, and a preliminary mapping function for all cameras was determined from the resulting camera images. A self-calibration procedure reduced disparity errors and hence corrected the calibration mapping function for all cameras leading to a reduced calibration error (Wieneke 2008). The recordings in all cameras were synchronized with the laser pulse frequency at 66 fps, 130 fps, and 165 fps, corresponding to free stream velocities 0.038 m/s, 0.077 m/s and 0.115 m/s for the study of copepods downstream of the cylinder. About 495 independent instances of copepod locations and velocity fields downstream of the cylinder were analyzed. An instance was considered independent when more than half of the zooplanktons in the preceding images move out of the field of view. The cameras and laser was synchronized at 330 fps for the study of copepods approaching the cylinder from upstream. This allowed tracking the copepods and observing their escape response as they approached the cylinder.

Figure 2-17 shows the methodological steps applied for infrared tomographic PIV and 3D PTV technique to obtain the fluid velocity field and zooplankton tracks, simultaneously. For tomographic PIV, pre-processing step was first performed in LaVision's DaVis 8.0 to eliminate background noise, and compensate for intensity differences between images.

In this step, a sliding minimum convolution filter was applied with a 5×5 pixel window (the average particle size in the images was 5×5 pixels). This eliminated the background noise and reduced the intensity of the fish image by subtracting minimum intensity values within the window. Then, the images were normalized with a reference image to compensate for differences in background intensity. This pre-processing was necessary to ensure good reconstruction quality of the particles. Particle intensity volumes were then reconstructed using the MLOS-SMART algorithm implemented in DaVis 8.0. The size of the measurement volume was -40 mm < x < 40mm, -3mm < y < 7.5 mm and 0 mm < z < 19 mm. It is noted that zooplankton may be visible, albeit indistinguishable, in figure 2-16(a). Thus, a mask was applied on the reconstructed volume to remove any zooplankton that may contaminate the local flow velocity vectors during cross-correlation. Each interrogated fluid volume was masked at locations where zooplankton were present (identified in the PTV images) with a cubic mask of 7 × 7 × 7 voxels. Masking was carried out to avoid contamination of fluid vectors near the zooplankton. Cross-correlating masked volume pairs separated by Δt yielded velocity fields. The smallest interrogation volume yielding high quality results was 48 × 48 × 48 voxels, providing a spatial resolution in all three directions of 3.65mm. Using a 75% overlap resulted in fields of 88 × 43 × 21 vectors. For 3D PTV, the zooplankton images were pre-processed in DaVis 8.0, and 3D PTV operation was then applied to locate the position of each zooplankton in the three-dimensional volume and to measure its velocity. The resulting vector fields from the tomographic PIV operation and the tracks from the 3D PTV were combined in Tecplot® for visualization and analysis.

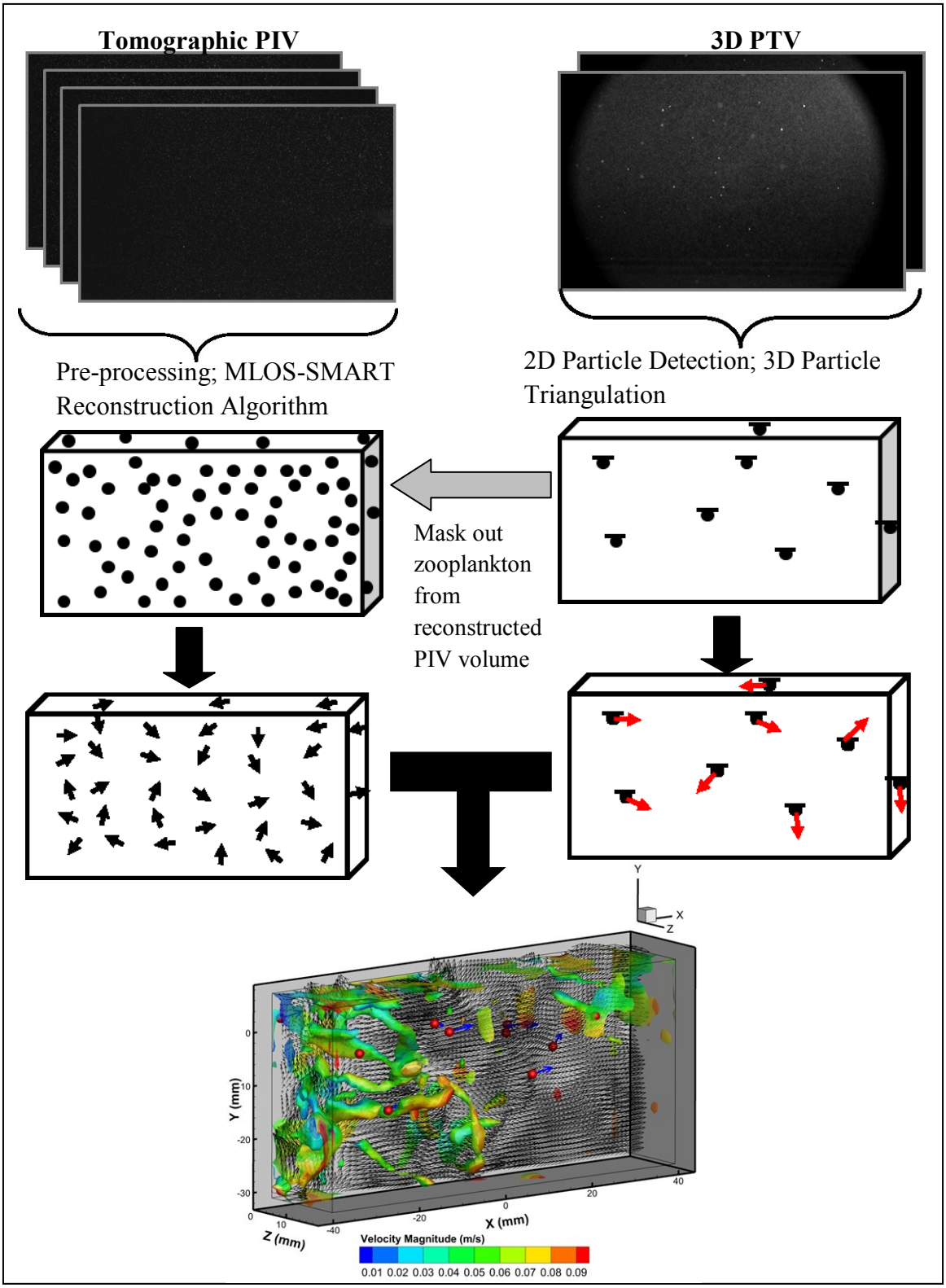

Figure 2-17: Schematic steps for infrared tomographic PIV + 3D PTV technique used to obtain volumetric velocity field of fluid and 3D tracks of zooplankton.

2.3.2.4 Infrared tomographic PIV + 3D PTV: Uncertainty

For tomographic PIV, the measured uncertainty in the spatial derivatives can be ascertained using the mass conservation principle for incompressible flow (Scarano and Poelma 2009). Figure 2-18 shows the divergence of the velocity computed at all grid points within each measurement domain for all of the 500 independent data sets of flow behind the mounted cylinder. The statistical distribution of the divergence estimated by a central difference technique results in a fitted Gaussian curve centered at zero with a width of 0.04. Adrian and Westerweel (2011) estimated a relative error distribution for all voxels that can be expressed as

$$\overline{\left(\frac{\partial u}{\partial x}+\frac{\partial v}{\partial y}+\frac{\partial w}{\partial z}\right)^2} \cong \left(\frac{\sigma_{\Delta x}}{D_I \Delta t}\right)^2 \quad (3)$$

where $\sigma_{\Delta x}$ is the overall error amplitude of the displacement, D_I is the dimension of non-overlapping interrogation domain in the cross-correlation procedure, and Δt is the time delay between two consecutive frames. Using equation (3), the uncertainty of displacement, $\sigma_{\Delta x}$, is given as 0.3 voxels, which implies uncertainty of an individual velocity field vector as 0.003m/s ($\sim 0.04U_0$) for U_0 = 0.077 m/s.

For 3D PTV, the detected zooplankton occupied areas of 7 × 7 pixels. With a Gaussian fit operation, the uncertainty of the zooplankton location is estimated to be within 0.5 pixels (or 0.04 mm). Thus, the velocity error was estimated to be 0.006 m/s ($\sim 0.07U_0$) if consecutive images are used.

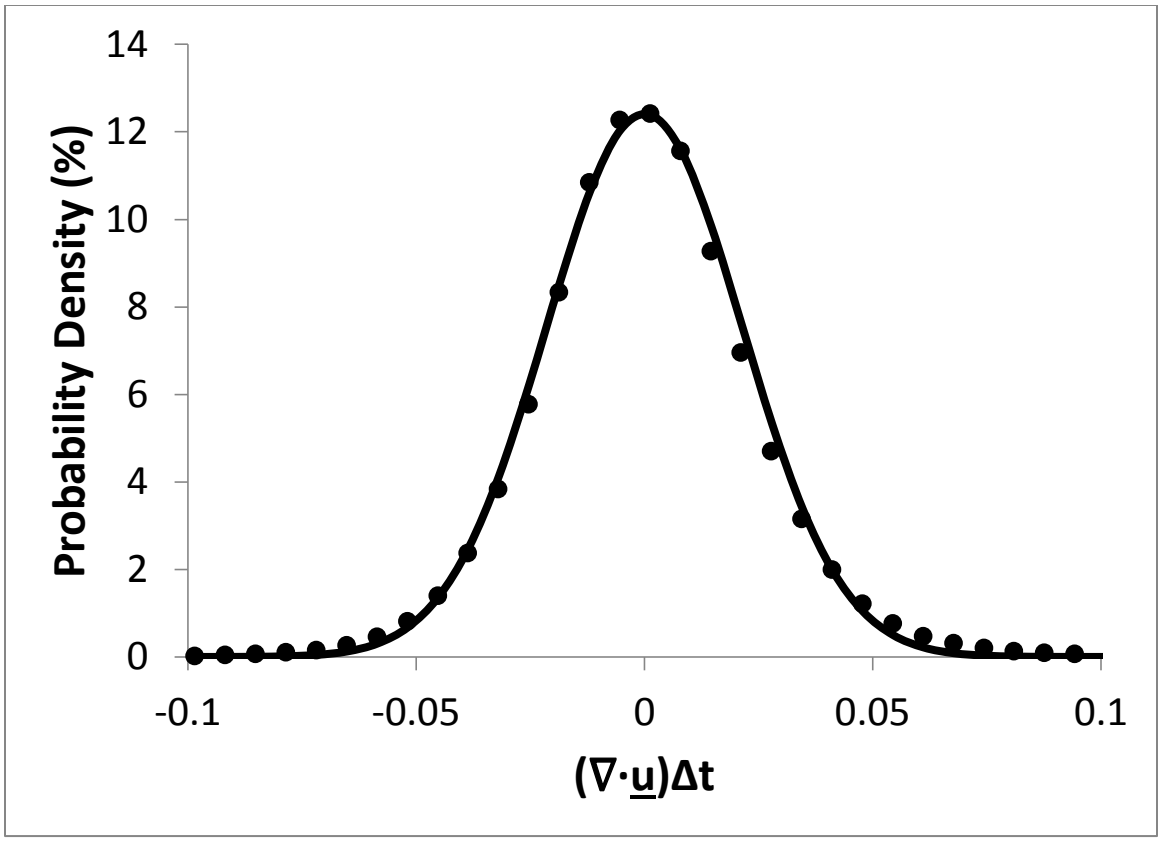

Figure 2-18: Probability density function of the relative error distribution of the flow field behind the mounted cylinder.

2.3.2.5 Infrared tomographic PIV + 3D PTV: Velocity and velocity gradients

Measuring fluid velocity and its derivatives at the location of the zooplankton requires an interpolation scheme. Figure 2-19 shows a schematic representation of the known location of the zooplankton with an unknown local *fluid* velocity, $\boldsymbol{u}_c$, and the neighboring grid points with known velocities from tomographic PIV measurement.

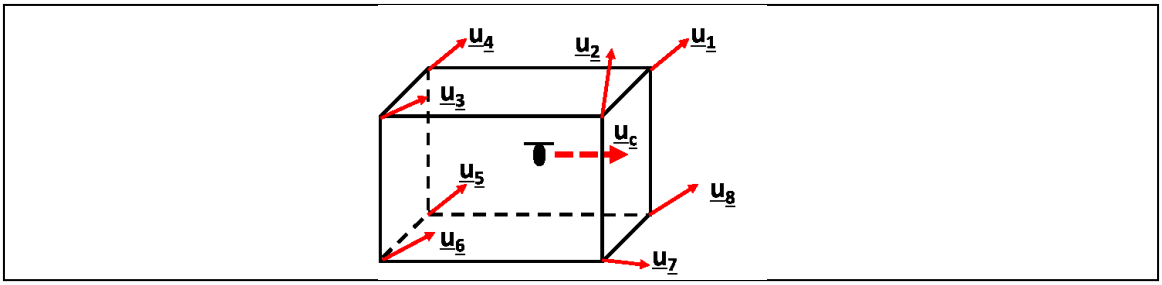

Figure 2-19: Schematic diagram showing the location of a zooplankton with unknown local fluid velocity u_c, and the neighboring grid points with known velocities from tomographic PIV measurement

The interpolation scheme proposed to obtain $\boldsymbol{u_c}$ and its spatial derivatives is the Taylor-series least-square technique (e.g. Talapatra and Katz 2013). This technique utilizes the Taylor-series expansion of the neighboring grid points about the location of the zooplankton. For *N* neighboring grid points, the set of equations is:

$$u_1 = u_c + \left.\frac{\partial u}{\partial x}\right|_c (x_1 - x_c) + \left.\frac{\partial u}{\partial y}\right|_c (y_1 - y_c) + \cdots + \left.\frac{\partial^2 u}{\partial x^2}\right|_c \frac{(x_1 - x_c)^2}{2} + \cdots$$

$$v_1 = v_c + \left.\frac{\partial v}{\partial x}\right|_c (x_1 - x_c) + \left.\frac{\partial v}{\partial y}\right|_c (y_1 - y_c) + \cdots + \left.\frac{\partial^2 v}{\partial x^2}\right|_c \frac{(x_1 - x_c)^2}{2} + \cdots$$

$$\vdots$$

$$v_N = v_c + \left.\frac{\partial v}{\partial x}\right|_c (x_N - x_c) + \left.\frac{\partial v}{\partial y}\right|_c (y_N - y_c) + \cdots + \left.\frac{\partial^2 v}{\partial x^2}\right|_c \frac{(x_N - x_c)^2}{2} + \cdots$$

$$w_N = w_c + \left.\frac{\partial w}{\partial x}\right|_c (x_N - x_c) + \left.\frac{\partial w}{\partial y}\right|_c (y_N - y_c) + \cdots + \left.\frac{\partial^2 w}{\partial x^2}\right|_c \frac{(x_N - x_c)^2}{2} + \cdots$$

where *u, v,* and *w* are the three velocity components, and *N* is the total number of neighboring points.

Considering 64 neighboring grid points, and Taylor-series expansion of up to second-order derivatives, the above equation system can be written in a matrix form given by:

$$\boldsymbol{u_n} = \boldsymbol{B u'_c}$$

where $\boldsymbol{u_n}$ is a (192 × 1) matrix; $\boldsymbol{B}$ is a (192 × 30) matrix; and $\boldsymbol{u'_c}$ is a (30 × 1) matrix.

$$\boldsymbol{u_n} = \begin{pmatrix} u_1 \\ v_1 \\ w_1 \\ \vdots \\ u_N \\ v_N \\ w_N \end{pmatrix}; \boldsymbol{u'_c} = \begin{pmatrix} u_c \\ v_c \\ w_c \\ \frac{\partial u}{\partial x} \\ \frac{\partial v}{\partial x} \\ \vdots \\ \frac{\partial^2 u}{\partial z^2} \\ \frac{\partial^2 v}{\partial z^2} \\ \frac{\partial^2 w}{\partial z^2} \end{pmatrix}$$

$$\boldsymbol{B} = \begin{pmatrix} & & & & & & & \frac{(x_1 - x_c)^2}{2} & 0 & 0 & \\ 1 & 0 & 0 & (x_1 - x_c) & 0 & 0 & & & & & \\ 0 & 1 & 0 & 0 & (x_1 - x_c) & 0 & \cdots & 0 & \frac{(x_1 - x_c)^2}{2} & 0 & \cdots \\ 0 & 0 & 1 & 0 & 0 & (x_1 - x_c) & & & & & \\ & & & & & & & 0 & 0 & \frac{(x_1 - x_c)^2}{2} & \\ & \vdots & & & \vdots & & & & \vdots & & \\ & & & & & & & \frac{(x_N - x_c)^2}{2} & 0 & 0 & \\ 1 & 0 & 0 & (x_N - x_c) & 0 & 0 & & & & & \\ 0 & 1 & 0 & 0 & (x_N - x_c) & 0 & \cdots & 0 & \frac{(x_N - x_c)^2}{2} & 0 & \cdots \\ 0 & 0 & 1 & 0 & 0 & (x_N - x_c) & & & & & \\ & & & & & & & 0 & 0 & \frac{(x_N - x_c)^2}{2} & \end{pmatrix}$$

The system of equations is over-defined since $\boldsymbol{B}$ is not a square matrix. Thus, a least-square method is implemented to solve $\boldsymbol{u'_c}$, which is given by:

$$\boldsymbol{u'_c = (B^T B)^{-1} B^T u_n}$$

The advantage of this approach to a linear interpolation technique is that (1) velocity and velocity gradients can be obtained simultaneously when solving for $\boldsymbol{u'_c}$, and (2) the velocity gradients are less noisy since the "best-fit" solution is obtained using the least-square technique.

2.3.3 Experimental procedures

In this experiment, the water channel was filled from a pipeline connected to the Gulf of Mexico. The water was passed through a 2-μm filter before filling the channel to remove any plankton that might be present in the water. The channel was seeded with 55μm titanium dioxide-filled polyamide tracer particles, and zooplankton (either brine shrimp or copepod, but not a mixture of both) were distributed throughout the fluid. The cylinder was placed at its desired location (see figure 2-14). The motor controller was then used to progressively increase the speed of the paddle wheel to the desired speed (see table 2-4). Data acquisition was then initiated. Experiments were conducted on the same day of copepod collection, and none of the zooplankton was in the facility for more than 24 hours.

2.4 Experiment (2) setup: Predator-prey interactions in still water

This Section is taken from:

Adhikari, D. & Longmire, E. K. (2013) "Infrared tomographic PIV and 3-D motion tracking system applied to aquatic predator-prey interaction" Meas. Sci. Tech.(Special issue: Advances in 3D Velocimetry) Vol. 24 (2), 024011

This study is aimed to understand predator-prey interaction in a still water tank. Freshwater fish was allowed to feed on various species of zooplanktons. The flow field and trajectory of organisms were measured quantitatively using tomographic PIV and 3D motion tracking system, respectively.

2.4.1 Species

Twelve zebrafish (*Danio rerio*; length ~30 mm, width: ~4 mm), purchased from a local pet store, were housed in a 38-liter aquarium at 25ºC. The fish were provided with 12 hours of light per day and fed daily with a mixed diet of flaked food and brine shrimp.

Copepods (*Diaptomus* species; size: ~1 mm) and water fleas (*Daphnia* species; size: ~1 mm) were collected from Lake of the Isles, Minneapolis, MN (44°57'6.42"N 93°18'27.28"W) using a 0.25 m diameter plankton net (mesh size: 150 μm). They were kept in 20-liter aerated containers and used within 24 hours of collection. Brine shrimp (*Artemia* species; size: ~1 mm) were cultured in the lab. Brine shrimp were used within 2 days after they were hatched from the eggs.

Brine shrimp or water fleas were used as non-evasive prey, while copepods were used as an evasive prey in the experiments. In the current study, evasive prey (e.g. copepod) are defined as organisms that are able to sense and respond to the hydrodynamic disturbance generated by the presence of a nearby fish (see Yen et al 1992; Buskey et al 2002), and thus potentially escape the fish. Non-evasive prey (e.g. water flea and brine shrimp) exhibit locomotion, but do not have similar sensing characteristics or high-speed propulsion capability for active escape.

2.4.2 Experimental setup

2.4.2.1 Facility

Experiments were performed in a transparent tank measuring 300 mm (L) × 150 mm (W) × 205 mm (H), filled with water to depth of 120 mm (see figure 2-20).

The water was seeded with 55 μm polyamide (filled with 11% titanium dioxide) tracer particles of density 1.23 g/. An Oxford Firefly laser with average power of 300W and duty cycle of 1% was used for illumination. The laser was pulsed at 500 Hz, with a pulse duration and energy of 20μs and 6mJ, respectively. The perpendicular fan angle in the vertical direction was 10º (figure 2-20a). The laser expanded laterally at an angle of 1º into a sheet with thickness 13 mm at the test section (figure 2-20b). Based on the Beer-Lambert law (equation 2-3), the near-infrared illumination passing through 120 mm of water is attenuated by 41%. Furthermore, the illumination scattered by the tracer particles, which travels through the water, is also attenuated. The attenuation of the

scattered light was minimized in the current setup by placing the illuminated measurement volume 40 mm behind the front of the tank (see figure 2-20b). Front surface mirrors were installed at the bottom of the tank in an inclined manner in order to reflect the laser sheet back towards the measurement domain. This increased the particle intensity within the volume and illuminated particles otherwise obstructed by the shadow of the fish.

Four high-speed cameras (Phantom v210) were used for image acquisition. The camera frame rate was set to 500 Hz, and synchronized with the laser modulation frequency. Each camera was fitted with a Scheimpflug adapter, and angled such that the image focus remained the same throughout. Four camera lenses (Nikon Micro-Nikkor) of focal length 200 mm were used with aperture of *f*/11. All four cameras were mounted on the same side of the laser sheet in a "square" configuration. The distance between the cameras and the measurement volume was approximately 600 mm (see figure 2-20b). In results and discussion, the x-axis (horizontal) and y-axis (vertical) are defined parallel to the laser sheet, and the z-axis is defined positive towards the cameras with z = 0 furthest from the cameras. Image acquisition from the cameras was synchronized by supplying the frame synchronization signal from one master camera to the other three cameras and the laser.

Tomographic PIV and 3D motion tracking techniques were applied to measure the velocity field of the fluid during interaction, and the tracks of the fish and zooplankton in the experiment.

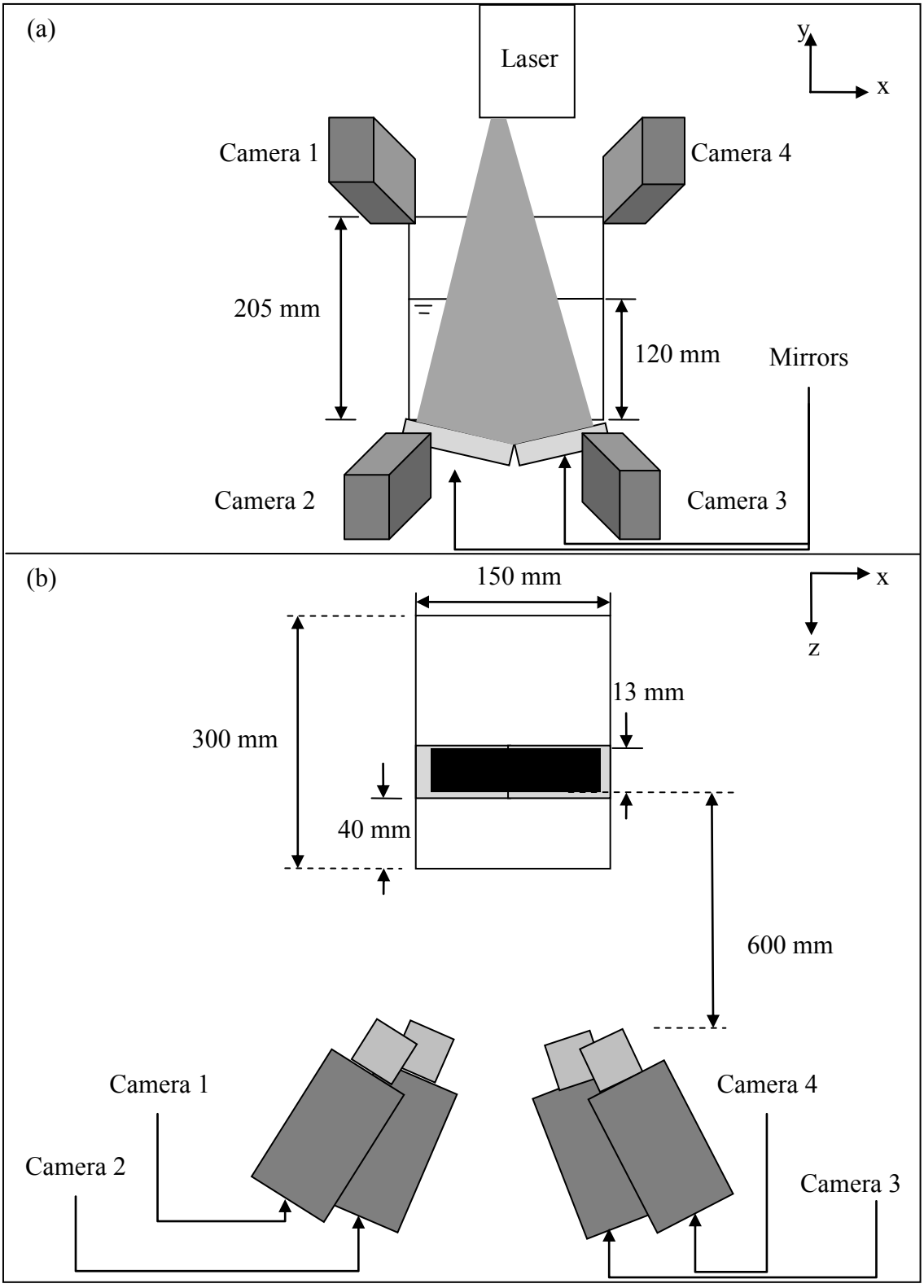

Figure 2-20: Schematic diagram of the experimental setup. (a) x-y view, (b) x-z view

2.4.2.2 Infrared tomographic PIV

The tomographic PIV process was executed using LaVision's DaVis 8.0 software. First, a calibration was carried out to generate a mapping function between image coordinates (*x, y*) and the physical volume coordinates (*X, Y, Z*). The volume was calibrated using a standard black target plate of area 64 mm × 38 mm. The calibration plate had white dots located every 1 mm along its surface (in x and y directions). The plate was traversed in the z-direction to seven positions, spanning the volume depth of 18 mm and recorded by each camera. The resulting images were mapped into the physical space volume based on a third order polynomial function. In addition, the self-calibration procedure of Wieneke (2008) was applied to correct and improve the fit of the mapping function. For the self-calibration procedure, we acquired 300 sets of simultaneous particle images (without fish and copepods), which were used to minimize disparity errors associated with particle triangulation. This step was also used to determine the effective volume thickness (z-dimension) where particle seeding intensities were sufficient for correcting disparity errors. The x and y dimensions were determined from the overlapped camera views.

After self-calibration, the raw experimental images (with fish and copepods) were pre-processed (see Section 2.3.2.3). After pre-processing, particle intensity volumes were reconstructed from sets of four images using five iterations of the MART algorithm implemented within DaVis 8.0 software. The voxel to pixel size ratio was set to 1, and the reconstructed volume was selected to cover -12.5 mm < x < 10 mm, -4 mm < y < 6.5 mm and 0 mm < z < 12 mm, which lay within the self-calibrated volume.

Any given reconstruction volume could include artifacts caused by the presence of the fish within the measurement volume. A 3-D mask is required to remove these artifacts before cross correlating in order to obtain accurate velocity vector fields. The visual hull technique (see chapter 3) was applied to mask these volumetric regions. Specific application of the technique is described in Chapter 3.

Consecutive masked volumes were cross-correlated to obtain a given volumetric velocity field. A multi-pass cross-correlation was employed whereby the interrogation volume was decreased from an initial size of 128 voxel^3 to a final size of 96 voxel^3. The magnification factor was 20 μm/voxel. Thus, the dimension of the resulting interrogation volume was 2 mm in all three directions. The particle number density was about 14 per interrogation volume. The particle number density was estimated after determining the ghost particle intensity in a volume immediately outside of the illuminated region and using this value to set a minimum intensity threshold within the illuminated region. The seeding particles were added in steps of small quantities (~0.05 ml), and the feeding pattern and movement of the fish were observed. When the visibility through the water decreased to about 10 cm, no more particles were added. Using 75% overlap resulted in approximately 27,648 (48 × 24 × 24) grid points for each time step. The crosswise dimension of the fish spans approximately two interrogation volumes (or 8 grid points), while the length of the prey is one half the length of the interrogation volume (or 2 grid points). Vectors were computed only on points located outside of the reconstructed visual hull of the fish, and any vectors centered within the object were again masked during post-processing. These steps together with the self-calibration step ensured that less than 1% of all vectors were spurious and these occurred at random locations throughout the measurement volume. In addition, the visual hull technique allowed for accurate determination of fluid velocity vectors up to the boundary of the hull, which was typically very close to the fish boundary (i.e. less than 1 mm; see Chapter 3).

The calibration, self-calibration and pre-processing steps of tomographic PIV were carried out on a 64-bit Windows PC with 4 processors and 8 GB of memory. Particle reconstruction and volume correlation, which were more computationally intensive, were processed in parallel on 5 similar computers.

2.4.2.3 Motion tracking of predator and prey (3D PTV)

The motion tracking procedures for both predator and prey consisted of two steps: (1) locating a point on the organism in the images, and (2) triangulating the point into a 3-D location based on two or more camera images.

In order to track the fish motion, the center of the fish eye was selected from each camera image. A Circular Hough Transform (CHT) scheme was applied to automatically identify and locate the center of the eye in all of the images. The CHT is a feature extraction technique that identifies circular object in an image by mapping the spatial space to parameter space (i.e. radius and center of circle parameters). Appendix B provides the details of this transform. Reader may also refer to Schreiner (2011) for a complete in-house documentation and implementation of CHT. Since the prey was small (20 - 40 pixels), the head of the prey was identified manually in all image sequences, and its coordinates were recorded.

After identifying the location of the fish eye and prey within the planar images, a separate image file consisting of only the identified point location ('particle') was generated. Thereafter, a 3-D particle tracking velocimetry (3-D PTV) operation within LaVision DaVis 8.0 was applied to reconstruct the volumetric location of each 'particle'. Since time-resolved images were acquired using high-speed cameras, the 3-D PTV operation was applied on sequential image sets to obtain the translation velocity for both predator and prey.

2.4.2.4 Uncertainty and signal-to-noise ratio

The uncertainty in measuring velocity vectors by tomographic PIV was dominated by the sub-pixel location accuracy, which was about 5% of the maximum velocity in the field (maximum velocity: 0.02 m/s). The uncertainty of the fish location using the CHT eye detection technique, and the zooplankton location using manual detection can be estimated to be 1 pixel. This translates to a location uncertainty of 0.02 mm, and a

velocity uncertainty of 0.028 m/s in each of the x, y, and z components for both predator and prey.

As described in Chapter 2.1, the infrared illumination wavelength attenuates in water, and the cameras had a quantum efficiency that was lower at this wavelength as compared to visible wavelengths. Furthermore, white fluorescent light in the laboratory was switched on providing a visual means for the fish to locate prey. The use of the infrared laser, cameras, and the background light could contribute to image noise. Therefore, the signal-to-noise ratio (SNR) of reconstructed volumes was evaluated *a posteriori*. The SNR associated with tomographic reconstruction was analyzed by Elsinga *et al.* (2006), who reported its dependence on the calibration error, number of MART iterations, number of camera views, camera angles, the seeding density, and image noise.

The SNR may be assessed based on a comparison between the reconstructed pixel intensity levels measured within the volume illuminated by the laser and the levels measured outside of it (Scarano and Poelma 2009). This gives a measure of the ratio between actual and ghost particle intensities. Ghost particles occur in tomographic reconstruction because several independent voxel intensity distributions can satisfy similar intensity projections on the camera sensor planes (Elsinga *et al.* 2006). Figure 2-21a shows the particle intensity integrated across the y-direction from a reconstructed volume without the organisms. In the figure, the region illuminated by the laser is clearly observable compared to the region outside of the thick sheet. Figure 2-21b shows that the reconstructed intensity averaged over the z-direction is ~150 (dashed line) within the illuminated volume, while the reconstructed intensity outside of the illuminated volume due to ghost particles (noise) is ~25 (dotted line). This gives the reconstruction SNR of 150/25 = 6, which is significantly greater than the minimum value of 2 recommended by Elsinga et al (2006). Based on this assessment, the combination of the current infrared illumination, seeding particle choice, and camera choice is sufficient for accurate reconstruction of particle volumes from a set of four projected images.

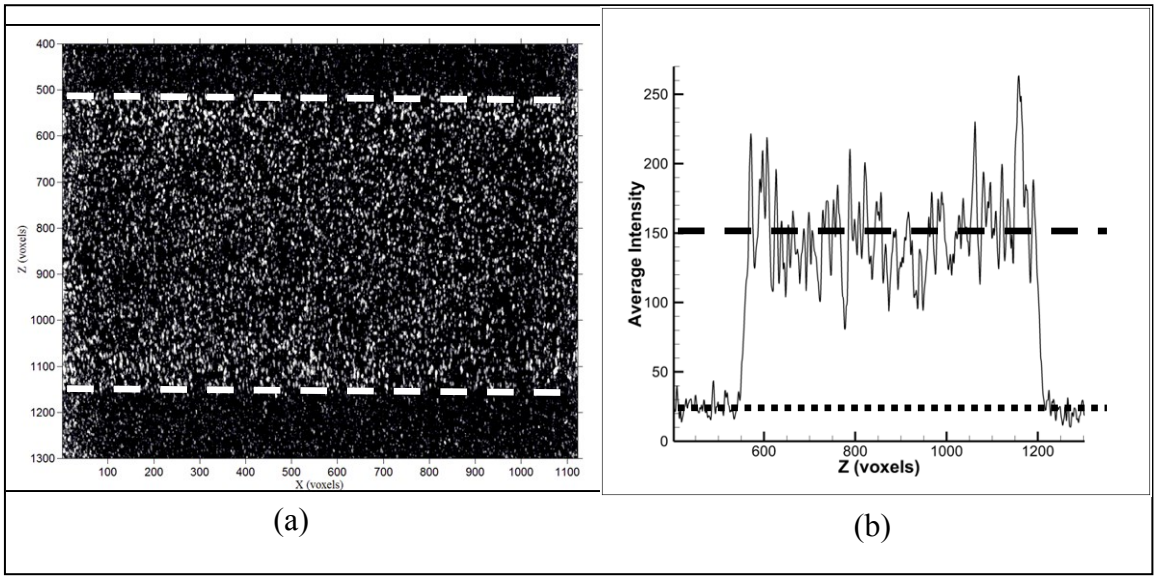

Figure 2-21: (a) intensity of reconstructed measurement volume integrated across y-direction, where the illuminated region is bounded by dashed lines. (b) average intensity profile across the z-axis to indicate the signal to noise ratio (signal: dashed line; noise: dotted line).

2.4.3 Experimental Procedures

A zebrafish was transferred from the aquarium to the measurement tank and allowed to acclimate for 15 minutes before laser illumination and data acquisition. The illumination and acquisition were then initiated, whereby the cameras acquired images continuously in a 12-second buffered loop. Evasive copepods or non-evasive foods were then placed judiciously near the illuminated volume in order to ensure a good chance of predator-prey interaction within this volume. A post-trigger was applied when the fish was observed executing its predation within the real-time video. Video sequences were examined, and only those showing predator-prey interaction were saved in the computer for later tomographic PIV processing and organism motion tracking. These sequences included fish approaching the prey in the x, y, or positive z directions. Sequences with fish approaching the volumetric field in the negative z-direction were not saved since the fish obscured the camera views of its interaction with the prey.

For a given fish, fewer than 10 recordings were obtained in order to prevent satiation. After being subject to an experimental series, the fish were placed into a second, identical 38-liter aquarium to avoid being used twice. Several image sequences of a given fish feeding on both an evasive copepod and a non-evasive food were acquired. For comparison, the motion of a freely swimming fish in the absence of prey was also acquired.

2.4.4 Organism Behavior

The motion and feeding behavior of multiple zebra fish was observed carefully for conditions under which the water was seeded with the titanium dioxide-filled polyamide tracer particles, and illuminated by the near-infrared laser sheet. Figure 2-22 shows a selected time sequence of a fish locating a flaked food amidst the tracer particles, and responding towards the food for feeding. In general, the fish did not exhibit any behaviors which might have suggested stress (e.g. erratic motion, reclusion), nor did they exhibit abrupt changes in motion or feeding patterns when the laser was switched on or off. After the experiments, fish exposed to the laser and particles were observed in their housing aquarium for short-term (next day) and long-term (two months) effects. No abnormal behavioral patterns were found. Therefore, we concluded that the selected laser sheet and particles were suitable for use with the fish in order to perform PIV and tracking analysis.

Behavior of zooplanktons (i.e. copepod, brine shrimp, and water flea) was also evaluated. Zooplanktons were exposed to titanium dioxide-filled polyamide tracer particles for 24 hours, and observed visually. The zooplanktons were observed to be moving, which showed that they were alive and active when exposed to the tracer particles. Furthermore, no sudden or erratic motion was observed when near-infrared laser was exposed. This indicates that zooplanktons are non-reactive to near-infrared laser.

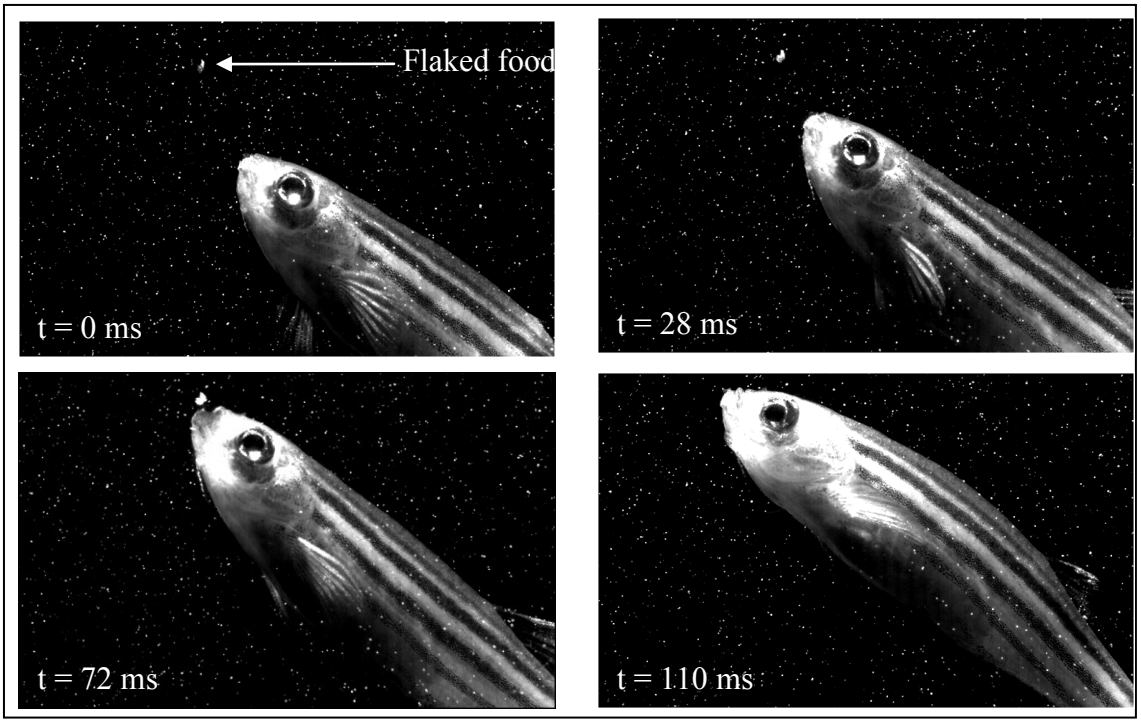

Figure 2-22: Selected time sequence showing zebrafish locating a passive flaked food, approaching it and feeding in the presence of ambient particles and near infrared laser.

2.5 Experiment (3) setup: Predator-prey interaction in unsteady/turbulent flow

This study aims to understand the effects of unsteady/turbulent water motion on predator-prey (fish-copepod) interaction. Turbulent flow is generated by placing a wall-mounted cylinder upstream of fish in the water channel. The trajectory of fish and copepods were measured using two-camera 3D motion tracking system, and the fluid velocity surrounding the interaction was measured using four-camera tomographic PIV.

2.5.1 Species

Six coral reef fish, known as blennies (*Acanthemblemaria aspera;* length ~20 mm, width: ~3 mm), were purchased from KP Aquatics LLC (Tavernier, FL). The blennies were housed in a 38-liter aquarium at 25ºC, in small clay blocks (Sculpey® clay) with a cavity

(5 mm in diameter) where the fish would reside. The fish were provided with 12 hours of light per day and fed daily with a mixed diet of copepod and brine shrimp.

The zooplankton species examined were copepods (species: *Acartia tonsa*; size ~ 1 mm) and brine shrimp (species: *Artemia salina*; size ~ 1 mm). Description of their collection procedure has been discussed in Section 2.3.1.

2.5.2 Experimental setup

2.5.2.1 Facility

Experiments were performed in the water channel facility. The blenny housing clay block was placed inside the 2-inch hole in the PVC fixture (see figure 2-23). The clay housing of the blenny was raised from the channel floor by ~ 20 mm, since blennies were observed to feed on zooplanktons on the channel floor when the housing was not raised. Vertical cylinders were placed upstream of the blenny to observe their effects on the blenny-copepod (predator-prey) interaction. Figure 2-13 shows the front and top view of the test section for this experiment.

This experiment was carried out with a free stream velocity maintained at U_0 = 0.077 m/s. A cylinder with diameter d_c = 12.7 mm was used. Cylinder was placed 8 cm upstream from the center of the test section, at the span wise center. Two other locations of 1.5 cm and 3.0 cm span wise offset from the center (depicted as dotted circles in the figure 2-23) is also studied. These arrangements were used to study the difference in predator-prey behavior inside and outside of the cylinder wake.

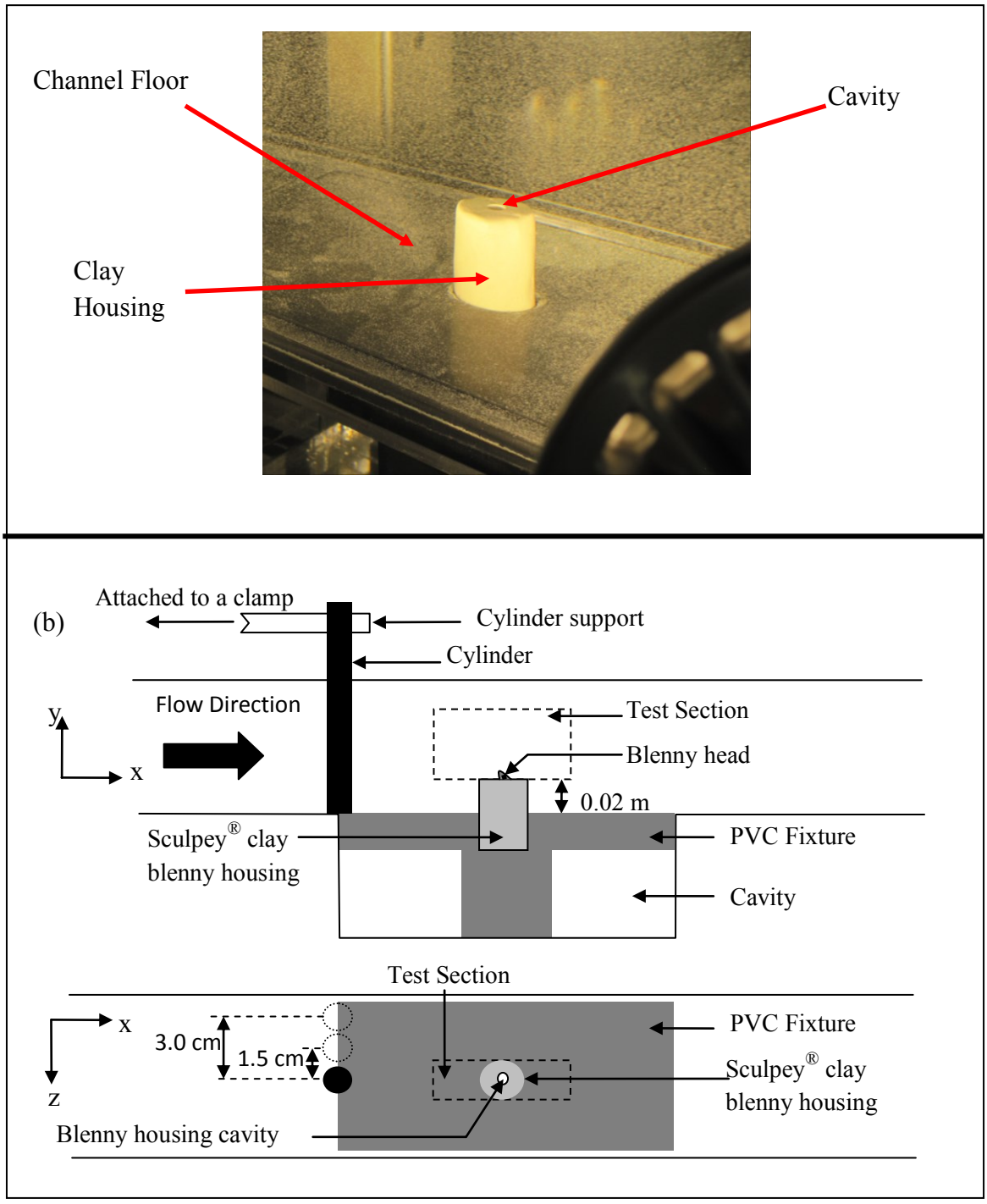

Figure 2-23: (a) image and (b) schematic diagram of the setup for experiment (3). (i) shows the front view, (ii) shows the top view.

2.5.2.2 Infrared Tomographic PIV + 3D PTV

The measurement setup, methodology, and velocity interpolation scheme for this experiment is the same as that described in for Experiment (1) (see section 2.3.2). Since the same experimental facility was used without any modification to the measurement setup, the specifications of tomographic PIV and 3D PTV can be found in Section 2.3. Sample images for (a) tomographic PIV and (b) 3D PTV was shown in figure 2-24. Figure 2-24(a) shows the tracer particles around the fish used to measure the volumetric flow velocity field, while figure 2-24(b) shows the copepods within the field of view. The latter figure was used to track the location and velocity of the fish eye and the copepod it attempts to feed on.

Unlike Experiment (1), fish were used in this experiment, thus, the Circular Hough Transform (CHT) was applied to track the eye of the fish (as described in 2.3.2.2). The visual hull technique was also applied to mask the presence of the fish within the PIV field of view (Described in detail in chapter 3).

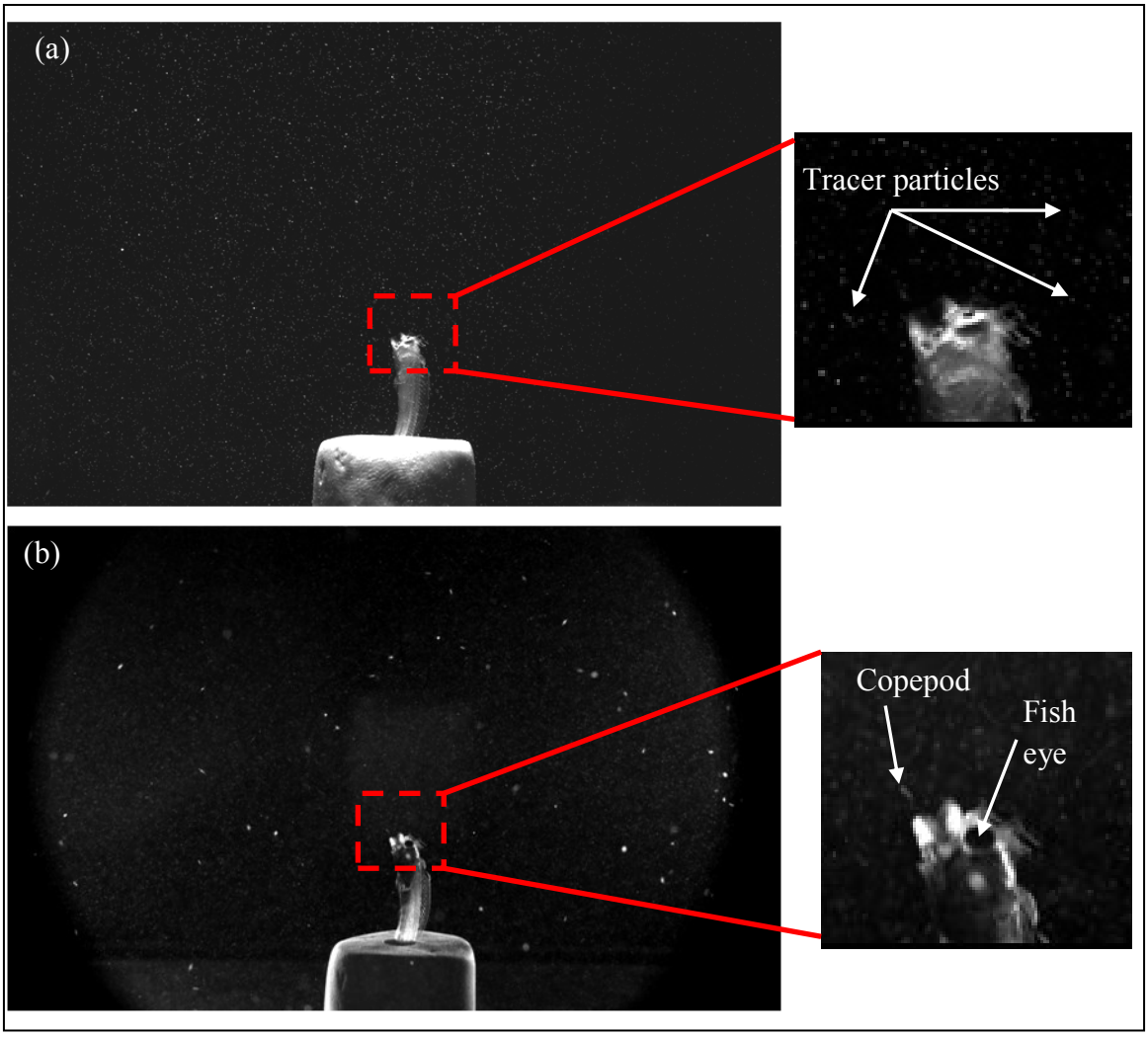

Figure 2-24: Sample images of the blenny-copepod interaction in unsteady flow. (a) Instance of tomographic PIV image used to obtain the volumetric velocity field, and (b) 3D motion tracking system (3D PTV) image used to obtain fish eye and copepod tracks.

2.5.2.3 Uncertainty

The uncertainty of the fish location using the CHT eye detection technique and the zooplankton location using manual detection is estimated to be 1 pixel. This translates to a location uncertainty of 0.076 mm, and a velocity uncertainty of 0.01 m/s (or ~0.1U_0) in each of the x, y, and z components for both predator and prey.

2.5.3 Experimental procedures

In this experiment, the procedure to fill the channel was similar to Experiment (1). After filling the channel, a blenny was transferred from the aquarium to the measurement tank by carrying the clay housing and placing it into the PVC fixture. The blenny was allowed to acclimate in the channel for 15 minutes before laser illumination and data acquisition. During acclimatization, the room was kept dark to prevent the fish from feeding on the zooplankton present in the channel. After 15 minutes, room lights were switched on, and data acquisition was initiated, whereby the cameras acquired images continuously in a 12-second buffered loop. A post-trigger was applied when the fish was observed executing its predation within the real-time video. Video sequences were examined, and only those showing predator-prey interaction were saved in the computer for later tomographic PIV processing and 3D organism motion tracking (3D PTV). These sequences included fish approaching the prey in the x-y plane. Sequences with fish approaching the volumetric field in the z-direction were not saved since the fish obscured the camera views of its interaction with the prey.

For a given fish, fewer than 20 recordings were obtained in order to prevent satiation. After being subject to an experimental series, the fish were placed into a second, identical 38-liter aquarium to avoid being used twice. In addition, experiments were conducted on the same day of copepod collection, and none of the zooplankton was in the facility for more than 24 hours.

Chapter 3

Visual Hull Method for Tomographic PIV of Flow around moving Objects

Most of this chapter is taken directly from*:*

Adhikari D and Longmire EK "Visual hull method for tomographic PIV measurement of flow around moving objects" Exp. Fluids. 53:943-964 (2012)

Section 3.8 is taken from*:*

Adhikari D, Longmire E, Gemmell B "Infrared tomographic PIV measurement of aquatic predator-prey interaction" 16th Int Symp on Applications of Laser Techniques to Fluid Mechanics, Lisbon, Portugal (2012)

Abstract

Tomographic particle image velocimetry (PIV) is a recently developed method to measure three components of velocity within a volumetric space. We present a visual hull technique that automates identification and masking of discrete objects within the measurement volume, and we apply existing tomographic PIV reconstruction software to measure the velocity surrounding the objects. The technique is demonstrated by considering flow around falling bodies of different shape with Reynolds number ~1000. Acquired image sets are processed using separate routines to reconstruct both the volumetric mask around the object and the surrounding tracer particles. After particle reconstruction, the reconstructed object mask is used to remove any ghost particles that otherwise appear within the object volume. Velocity vectors corresponding with fluid motion can then be determined up to the boundary of the visual hull without being contaminated or affected by the neighboring object velocity. Although the visual hull method is not meant for precise tracking of objects, the reconstructed object volumes nevertheless can be used to estimate the object location and orientation at each time step.

3.1 Introduction

Flow around moving objects encompasses a myriad of interests in fluid mechanics. For example, in biological fluid mechanics, flow surrounding marine animals has revealed characteristics which have been used to develop underwater vehicles (Bandyopadhyay 2005; Yu *et al.* 2009; Ruiz *et al.* 2011) or to understand influences in the marine ecosystem (Waggett and Buskey 2006, 2007; Webster and Weissburg 2009). Also, trajectories of flying insects and flow around oscillating wings have been related to development of micro aerial vehicles (Reiser and Dickinson 2003; Lua *et al.* 2010). In defense-related research, understanding the flow around supercavitating projectiles has enabled further insight into their control (Rand *et al.* 1997; Vanek *et al.* 2007). Furthermore, fundamental research on flow surrounding particles and bubbles in turbulent flows has provided important physical insights for multi-phase flow applications and modeling (Balachandar and Eaton 2010).

Velocity measurement of flow around moving objects has specific challenges. Objects moving within the flow field may have undetermined shapes that change with time. For example, fish and flying insects continually change their shape and orientation for propulsion. Furthermore, moving objects can have unsteady velocity, and their trajectory is normally not known *a priori*. The complex unsteady motion of the object causes the surrounding flow to be highly three-dimensional (3D), and thus a 3D flow measurement technique is essential to analyze the flow field. Currently, the most commonly used field measurement technique capable of measuring instantaneous flow velocity is particle image velocimetry (PIV).

Recent developments in PIV have made it possible to resolve all three velocity components in three-dimensional space. These techniques include holographic PIV (Hinsch 2002), scanning PIV (Hori and Sakakibara 2004), defocussed PIV (Willert and Gharib 1992), and 3D particle tracking velocimetry (Maas *et al.* 2004). All of these methods are capable of capturing volumetric velocity fields, although each has its own

limitations. The limitations are discussed by Elsinga *et al.* (2006) in their article introducing tomographic PIV.

Tomographic PIV utilizes images of tracer particles illuminated in a fluid volume that are acquired by multiple cameras situated at different viewing angles. The images are reconstructed into intensity volumes. However, this inverse reconstruction problem is underdetermined due to the limited number of projected images. Thus, an iterative reconstruction technique, such as multiplicative algebraic reconstruction technique (MART) is used for the volume reconstruction (Herman and Lent 1976; Verhoeven 1993; Elsinga *et al.* 2006). Modified MART, such as multiplicative line-of-sight simultaneous MART (MLOS-SMART; Atkinson and Soria 2009) and motion-tracking enhanced MART (MTE-MART; Novara *et al.* 2010) have also been introduced to accelerate the reconstruction process and to mitigate the formation of ghost particles, respectively. After the volume intensities are obtained, consecutive volumes acquired at known time intervals are cross-correlated to obtain the 3-component velocity field in 3D space.

Since its development, tomographic PIV has been used in a variety of studies, including turbulent boundary layers (Elsinga 2007; Gao *et al.* 2010), cylinder wakes (Elsinga *et al.* 2006; Hain *et al.* 2008; Scarano and Poelma 2009), index-matched multi-fluid flows (Ortiz-Duenas *et al.* 2010), large-scale flows (Kuhn *et al.* 2010) and flow within a small (~1 mm) droplet using a microscopic objective (Kim *et al.* 2011). Recently, Murphy *et al.* (2011) performed tomographic PIV of flow surrounding zooplankton. Furthermore, there are ongoing efforts in software development to reduce the computational cost of tomographic PIV (Atkinson *et al.* 2008; Worth and Nickels 2008; Discetti and Astarita 2012).

For flow around moving objects in planar PIV, several masking techniques have been used to address the occurrence of these discrete objects. For tomographic PIV, however, the masking technique is less straightforward, since the location and geometry of moving objects must be identified in 3D. In the next section, previous works on object detection

and masking in planar PIV are discussed, followed by a discussion on flow around objects in volumetric PIV and three dimensional object reconstruction techniques.

3.2 Current techniques to isolate moving objects in PIV fields

3.2.1 Planar PIV fields

To detect and mask out moving objects in planar PIV, algorithmic masks are most commonly used (e.g. Kiger and Pan 2000; Khalitov and Longmire 2002; Foeth *et al.* 2006; Jeon and Sung 2010, 2011). Algorithmic masking is applied to unsteady moving objects typically by writing a program to locate the object via digital image processing. This processing sequence will "automatically" locate the boundary of the object as it moves. Algorithmic masking is applied either by detecting discrete objects within the field of view (image segmentation) or by detecting boundaries of an object which is larger than the field of view.

Image segmentation has often been applied in multi-phase flows in which discrete particles or bubbles are present within a working fluid. For example, Kiger and Pan (2000) used a median filter combined with a correlation technique to segment and track larger discrete particles in fields containing smaller tracer particles in a turbulent liquid flow. A more elaborate approach was employed by Khalitov and Longmire (2002), who used second order spatial derivatives for particle edge detection and applied two-parameter (size and brightness) phase discrimination, for segmenting PIV tracer particles and larger discrete particles. For gas-liquid flows, Foeth *et al.* (2006) applied an adaptive masking technique to separate liquid flow from the surrounding sheet cavitation on a hydrofoil. Fluorescent particles were used to minimize scattering of the illumination from the cavitation, and an adaptive mask was created to find the interface between the vapor and liquid. The mask included an elaborate sequence of digital filters and edge detection algorithms.

For large objects (larger than the field of view) or other interfacial flows, edge detection techniques have been used to identify the interface. For instance, Jeon and Sung (2010) described an algorithm for flow next to a moving or deforming surface in which they used textons to locate elements of the surface. Textons are small texture patterns that can be cross-correlated with the image to identify the boundaries. The authors noted that, for their case, the textons gave better boundary detection than other edge detection techniques. For liquid-gas interfaces, optical filtering techniques have been applied effectively in the case where optical access is available for both fluids. For example, Belden and Techet (2011) investigated flow surrounding an air-water interface using a multi-laser and multi-camera approach. In their technique, separate masking of the water and air was required such that particles were correlated only within the appropriate medium. Since the lasers illuminating the air and the water particles were of different wavelengths, optical filters was used on each camera such that particles within the desired fluid were visible only to a given camera.

3.2.2 Volumetric PIV fields

Although detection and masking of objects in planar PIV has been widely studied and applied, automated masking and reconstruction of arbitrary moving objects in volumetric PIV have not been reported. In most multi-camera volumetric PIV studies, moving (or stationary) objects did not appear completely within the field of view (e.g. Hain *et al.* 2008; Elsinga and Westerweel 2012; Flammang *et al.* 2011). As a result, most of these works address the flow on only one side of the object.

Murphy *et al.* (2011) used the Direct Linear Transform method and a manual identification technique to locate specific points on and hence orient copepods within sets of tomographic PIV images. A simplified shape, i.e. prolate spheroid, representing the copepod was then positioned within the corresponding fluid velocity field. As in the case of Murphy *et al.* (2011), measurement of 3D flow around moving objects requires reconstruction of the object. Automated object reconstruction techniques have been

applied in several disciplines. For example, in fluid dynamics, Sakakibara *et al.* (2004) carried out stereo PIV in a plane surrounding a fish, and used a shadow imaging technique with additional cameras to obtain two views of the fish "shadow". These shadow views were then used to reconstruct the fish in 3D space. A total of four cameras, two strobe lights and a laser were required along with a complex calibration procedure. In another study, Scarano and Poelma (2009) demonstrated tomographic volume reconstruction when a stationary cylinder extended across the height of the measurement volume. They noted the possibility of estimating the cylinder location within the reconstructed volume based on observation of a local absence of reconstructed particles (void region). Although the void region may potentially allow object identification, the concept requires an object with a dark surface, such that reflection from the surface does not contribute significantly to the reconstruction intensities. On the other hand, a non-reflecting surface may be impractical or impossible in many cases, for instance, in examining flow around aquatic or aerial animals. Also, if the object is moving, this would require an automated and reliable means of identifying the object boundary based on the void region.

In medical technology, computerized tomography (CT) scans have been adopted widely for 3D examination of patient organs (Hounsfield 1973). The CT scan reconstructs a detailed 3D visualization of the patient's organ using x-ray image projections from many angles. Although this technique provides high resolution reconstruction, it requires many image projections, and is typically limited to stationary objects.

In computer vision, stereo mapping using known surface textures can be used to detect 3D shapes. This requires implementing a surface texture which can be distinguished from the seeding particles in front of it through an image processing routine. Jeon and Sung (2011) demonstrated such a technique using a known texture imprinted on surfaces whose features were significantly larger than the seeding particles. The texture was then identified and located to enable reconstruction of the object surface facing the cameras. Although this technique is ideal for large and smoothly varying surfaces amenable to

application of an artificial texture, it may be impractical for the study of live animals or of many discrete objects within fluids, such as particles, bubbles, or liquid drops.

Another technique in computer vision is silhouette-based back-projection (also known as the visual hull technique), which has been used widely for object or human identification as well as tracking in 3D space (Mulayim *et al.* 2003; Matusik *et al.* 2000; Laurentini 1994). The visual hull technique, which employs multiple camera views of a single object, detects the silhouette of the object seen by each camera (see figure 3-1a). Silhouettes are then extruded to create cone-like volumes which intersect to form the object's visual hull (see figure 3-1b). This technique results in a reconstructed object (dashed lines in figure 3-1b) that is consistently larger in volume than the original object (dotted lines in figure 3-1b). Increasing the number of projected images obviously leads to a more accurate reconstruction.

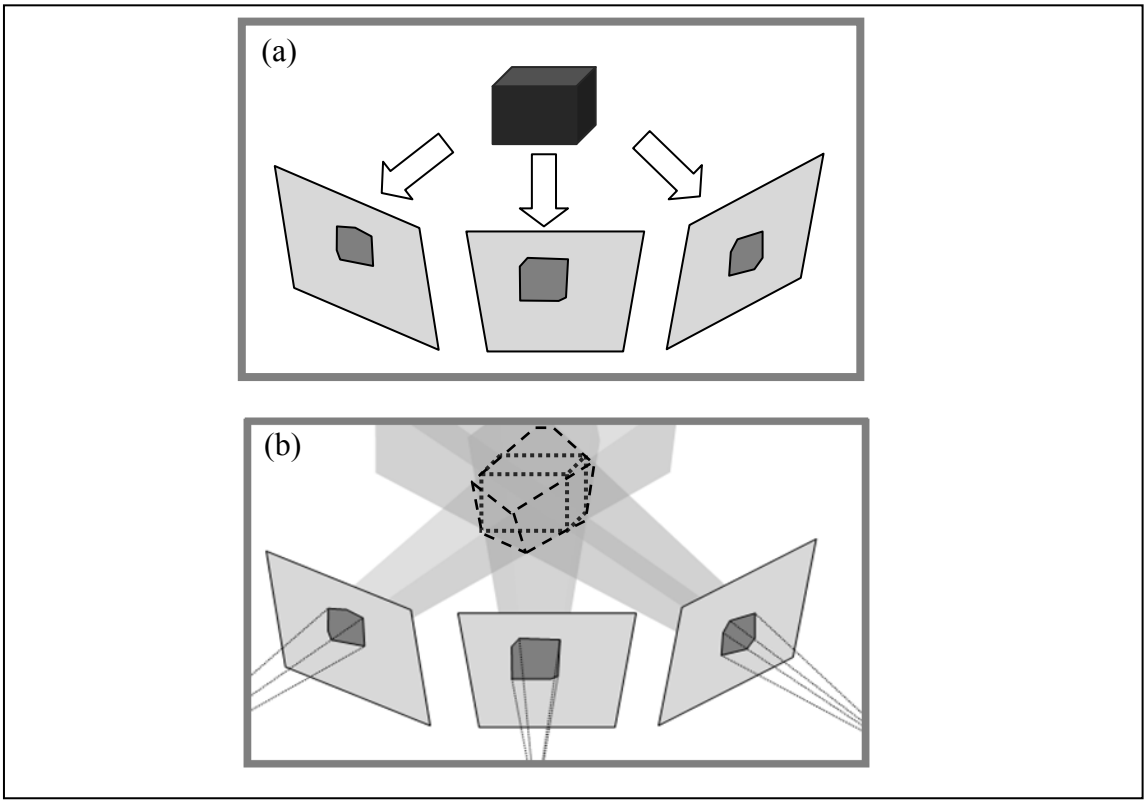

Figure 3-1: Visual hull technique. (a) Projected silhouette of an object in individual image planes. (b) Back-projection for object reconstruction. Note that the cube (dotted lines) in (b) is smaller than the intersection of back-projected volumes (dashed lines).

For tomographic PIV, reconstruction of an object within the volumetric domain requires both detecting the object amongst the tracer particles, and reconstructing it in 3D space. However, if object reconstruction and masking is not carried out, this will result in reconstruction artifacts near the object (as observed in Scarano and Poelma, 2009). These artifacts result in undesirable vectors and also hinder estimation of object location. Given the many current interests in flow around moving objects, implementing a method to remove the artifacts and automate the use of tomographic PIV in applications where the movement of the object cannot be estimated *a priori* is desirable.

In the present study, we describe a technique to identify and isolate arbitrarily moving objects and then demonstrate the method as applied to flow surrounding falling objects. This technique uses the visual hull concept for 3D object reconstruction and masking, and tomographic PIV to find the velocity around the object. It thus allows automated measurement of the volumetric velocity field surrounding a moving object while also giving an approximate shape and trajectory of the object.

3.3 Experimental Apparatus

The experimental setup was designed to demonstrate the implementation of the visual hull technique with tomographic PIV. Some solid geometric shapes were selected, and data were acquired as the objects were released and fell through a tank of water. As these objects could change orientation, speed, and trajectory while falling, they mimic objects that move arbitrarily.

3.3.1 Experimental setup

Since both the visual hull technique and tomographic PIV are photogrammetric techniques, they do not require separate hardware, calibration or independent experimental arrangements. Therefore, the conventional tomographic PIV set-up described here is also used for object reconstruction.

Experiments were performed in a Perspex tank measuring 300 mm (L) × 150 mm (W) × 205 mm (H), filled with water to a depth of 160 mm. The water was seeded with 10 µm silver-coated hollow glass spheres as tracer particles. These particles were illuminated with light from an Oxford Firefly laser with a near-infrared wavelength of 808 nm, average power of 300W, and a duty cycle of 1% (see figure 3-2). The laser emanates a thick sheet with a fan angle of 10º, and the thickness of the sheet was about 14 mm at the test section. Since near-infrared light attenuates in water, a front surface mirror was installed in an inclined position at the rear of the tank to reflect the sheet back towards the measurement domain (see figure 3-3). This increased particle illumination intensity within the volume and illuminated particles otherwise obstructed by the shadow of the solid object. The near-infrared laser was used as opposed to one with visible wavelength as it was readily available to the authors for experiments. It did not cause any significant problems with the signal to noise ratio required for tomographic PIV.

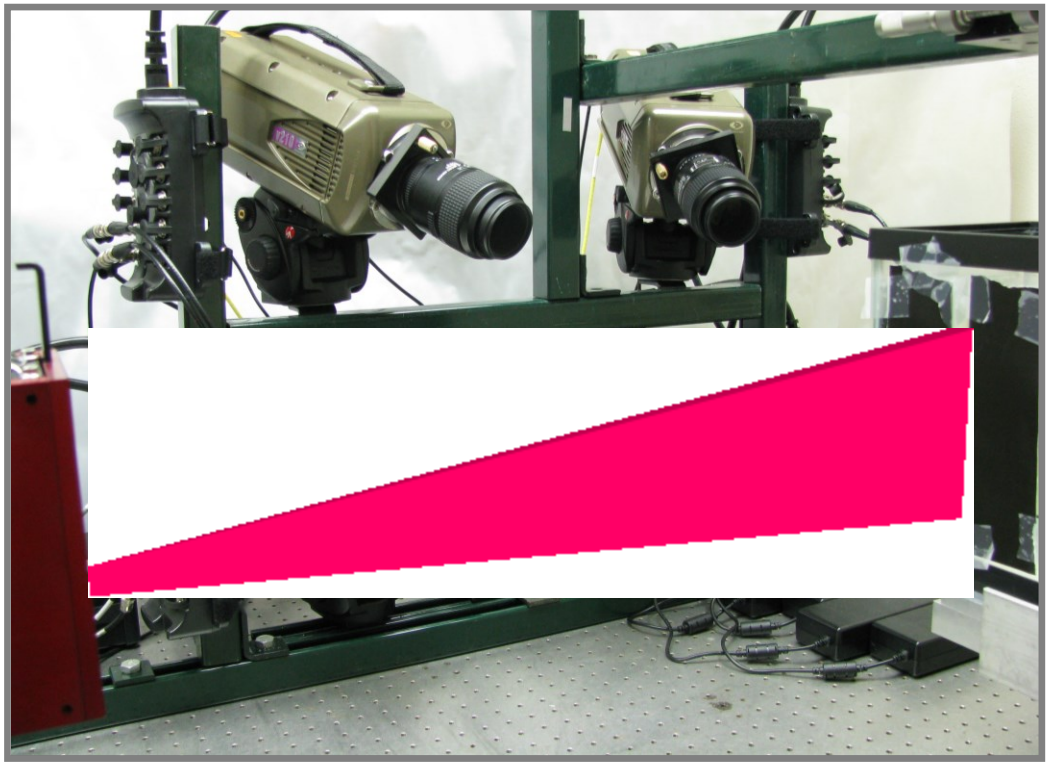

Figure 3-2: Image of the experimental setup. The light-red fan beam is a representation of the IR laser beam.

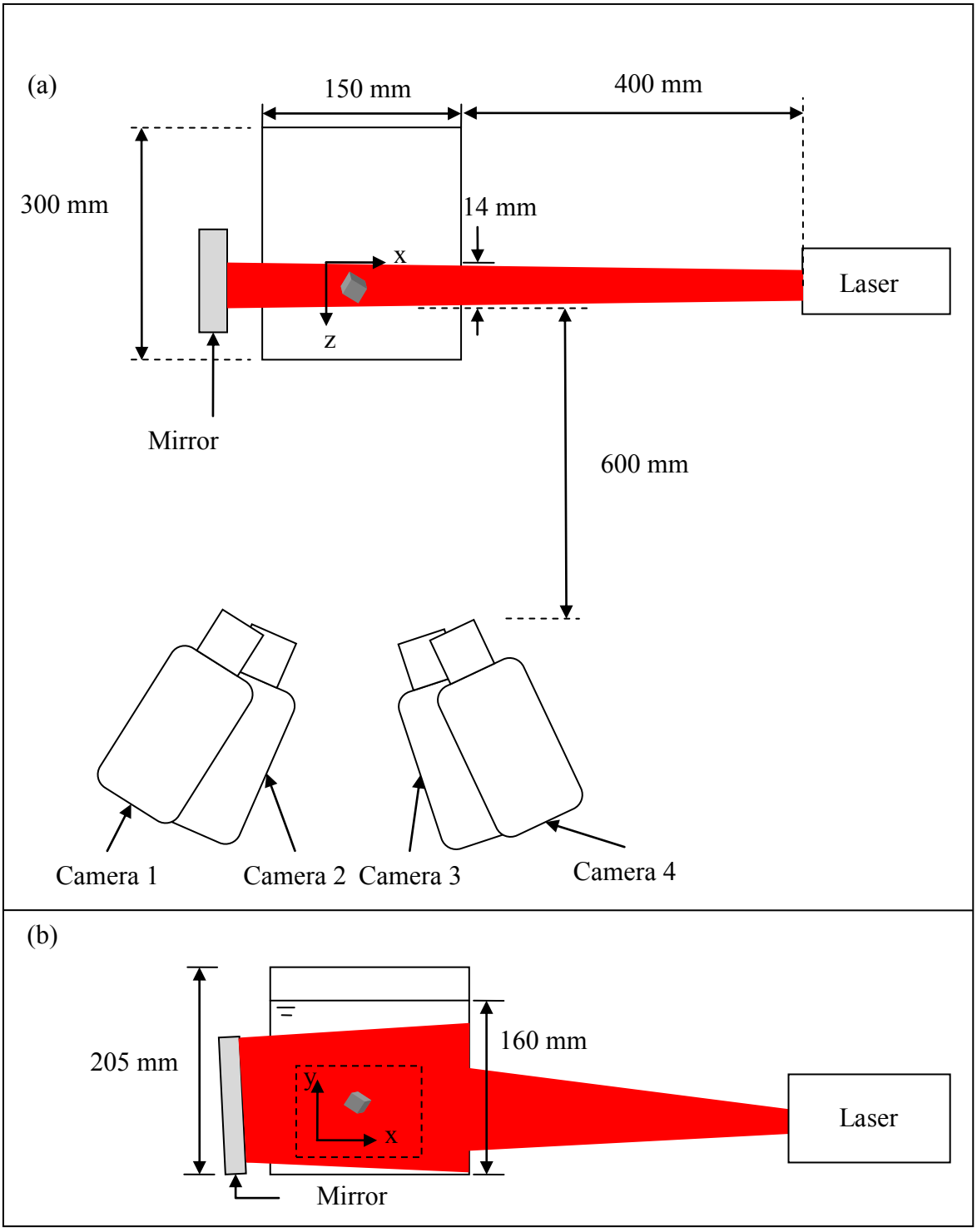

Figure 3-3: Schematic representation of the experimental setup. The plan view is shown in (a), while front view is shown in (b). The light-red fan beam is a representation of the laser illumination region. The dashed line window in (b) represents the illuminated field of view of the cameras.

The image acquisition setup included four Phantom v210 high speed cameras from Vision Research, each with a 12-bit monochrome CMOS sensor and 1280 × 800 pixel resolution. The laser modulation frequency and the camera frame rate were synchronized and set to 1000 Hz. Each camera was fitted with a Scheimpflug adapter, and angled at approximately 30° from the normal to the laser sheet. Four Nikon Micro-Nikkor lenses of focal length 105 mm were used with aperture *f*/8.

The cameras were all mounted on a steel frame on the same side of the laser sheet. The distance between the cameras and the measurement volume was approximately 600 mm. In all subsequent discussion, the x and y axes are defined parallel to the plane of the laser sheet, and the z-axis is defined positive towards the cameras with z = 0 furthest from the cameras (see figure 3-3). Image acquisition from the cameras was synchronized by supplying the frame synchronization signal from one master camera to the other three cameras and the laser.

3.3.2 Falling (Moving) objects

The falling objects investigated included a sphere, a cube, a tetrahedron and a cylinder (see figure 3-4). Their dimensions were chosen to be smaller than the thickness of the laser sheet in order for the objects to be completely within the field of view at most times during their trajectories. All objects were made of black Polyoxymethylene (delrin; density = 1.41 g/cm^3). The sphere was purchased at a desired dimension of 8 mm, while the remaining objects were machined to match the dimension of the sphere. The objects were fabricated based on material availability, and it should be noted that object surfaces need not be black or dark for successful implementation of the visual hull technique.

The experiment was carried out by initially placing an object submerged beneath the surface of water in the tank. The acquisition was started, and the object was released until it sank to the bottom of the tank due to its own weight. Acquired image sequences were then compiled for subsequent processing.

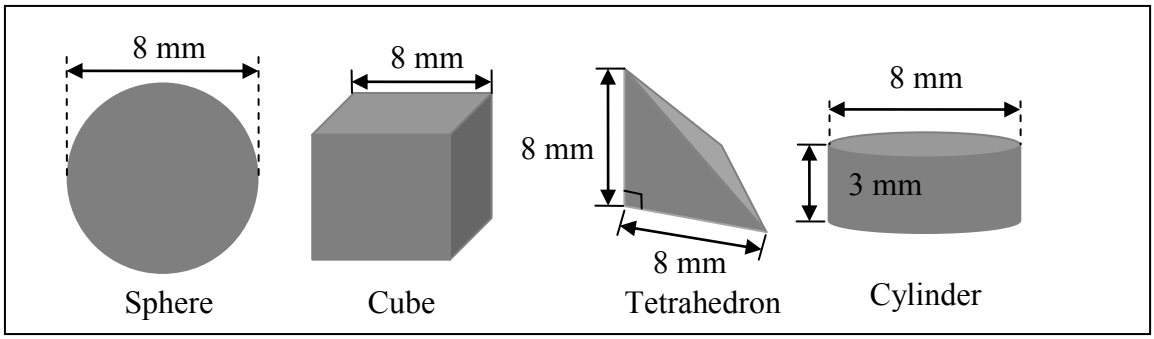

Figure 3-4: Schematic drawing of the moving objects used in the experiment to demonstrate the application of the proposed technique.

3.4 Visual hull and tomographic PIV methodology

3.4.1 Visual hull

The object reconstruction process includes two major operations: 1) detection of the object silhouette in each image, and 2) reconstruction of the object in 3D space.

3.4.1.1 Detection of silhouette

The algorithm required to detect the silhouette of the object depends mainly on the intensity of light that it scatters or reflects. For instance, if the object is highly reflective, the silhouette of the object can be detected easily based on an intensity threshold. However, a more generic approach is required for less reflective objects such as those used in this experiment. In this case, a sequence of image processing techniques was employed to recover the silhouettes (see figure 3-5). The following paragraphs describe the sequence, which employed the image processing toolbox in MATLAB®.

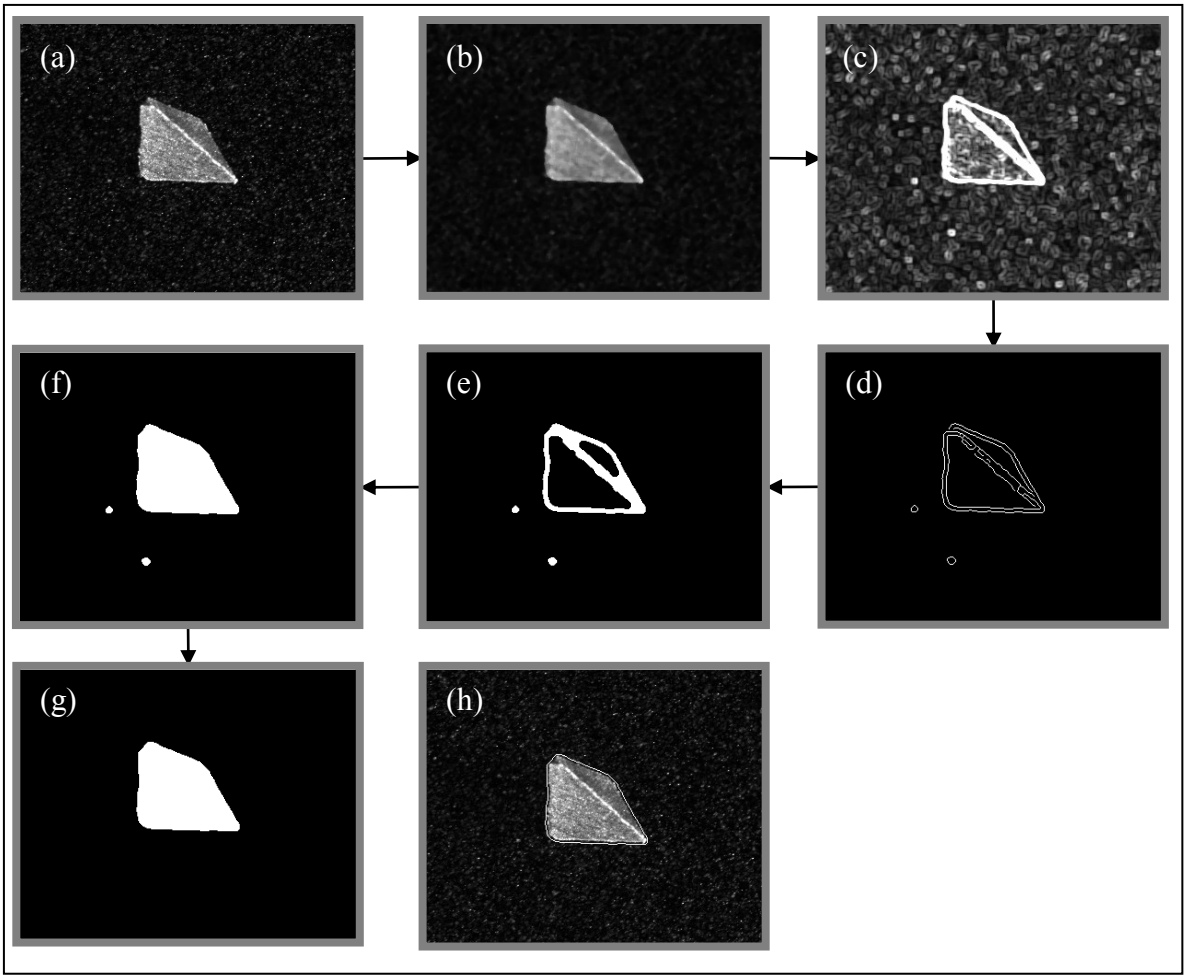

Figure 3-5: Image processing sequence to obtain the silhouette of the object with surrounding particles. The raw image is first shown in (a). The image processing sequence are as follows: (a)-(b) median filtering, (b)-(c) standard deviation filtering, (c)-(d) Canny edge detection, (d)-(e) morphological closing, (e)-(f) filling the "holes", (f)-(g) minimum object size criterion. The silhouette (g) of the object is finally obtained, and the comparison of the original object with the silhouette outline shows good agreement (h).

Figure 5a shows a raw image, which was obtained directly from the camera acquisition software and saved as an image file. In the first step, a median filter with a 5×5 pixel window was applied to filter tracer particles from the image (see figure 3-5b). The median filter replaces each pixel with the median of its neighborhood, thus significantly reducing the tracer particle intensity while preserving the intensity of the object. Since

the particles generally occupied 3×3 pixels, the window size was sufficient to suppress the intensity of the particles. A standard deviation filter with a 5×5 pixel window was then applied (see figure 3-5c). This filter replaces each pixel with the standard deviation of its neighborhood, and thus, enhances the boundaries of the object for better edge detection. Next, Canny edge detection was applied to locate the edges of the object (see figure 3-5d). Canny edge detection finds the spatial gradient in an image based on a user-defined threshold level. Upon detecting an initial edge, it tracks the connecting edges using a lower threshold level, thus, enabling it to detect weaker edges and minimizing the influence of noise or particles. At this edge detection stage, the grayscale image has been changed to binary.

Morphological operations (see Gonzalez and Woods 2002; Adrian and Westerweel 2011) were further required to close edges of the object (figure 3-5e), and to fill the object (see figure 3-5f). Morphological closing (function imclose() in MATLAB® 2008), which consists of morphological dilation followed by erosion, was applied to close the edges of the object. Morphological dilation thickens the object boundary by adding pixels to the background that neighbors the object. The object neighborhood (structuring element) was selected as a 7×7 pixel square window. In this way, it merges neighboring object lines which might not have been connected after Canny edge detection. Morphological erosion then removes pixels bounding the resulting object. Morphological filling (function imfill() in MATLAB® 2008) adds pixels to any background "holes" present within the object (see Gonzalez and Woods 2002). Figure 3-5f includes two tracer particles that were detected as objects since they were slightly brighter than other particles. Since these particles are much smaller than the object, they were removed using a minimum size criterion. Finally, the silhouette of the object was obtained (figure 3-5g), and it shows a close fit with the boundaries of the original image (see figure 3-5h).

3.4.1.2 Reconstruction of object in 3D Space

For reconstruction of the object, calibration is first required to generate a mapping function between the image coordinates (X, Y) and the physical volume coordinates (x, y,

z). The volume was calibrated using a standard black target plate of area 100 mm × 100 mm. The calibration plate had white dots located every 2.5 mm along its surface (in x and y directions). The plate was traversed in the z direction to 9 positions, spanning the volume depth of 16 mm and recorded by each camera. The resulting images were mapped into a physical space volume based on a 3rd order polynomial function using LaVision's DaVis 8.0 software.

The silhouette images obtained using MATLAB® were imported into DaVis software. After calibration, the visual hull of the object was reconstructed by back-projecting the four silhouette images from each camera into an object volume using the Multiplicative Line-of-Sight (MLOS) operation available in DaVis 8.0. In this back-projection, each image was mapped into a physical volume using the calibrated mapping function,

$$(x, y, z) = f_n (X, Y)$$

where f_n is the mapping function for camera n = 1, 2, 3, 4. The four back-projected volumes were then multiplied together. Since each silhouette image is binary, only the non-zero intersecting region of back-projected volumes remains. This reconstructed volume is known as the visual hull of the object (see figure 3-6).

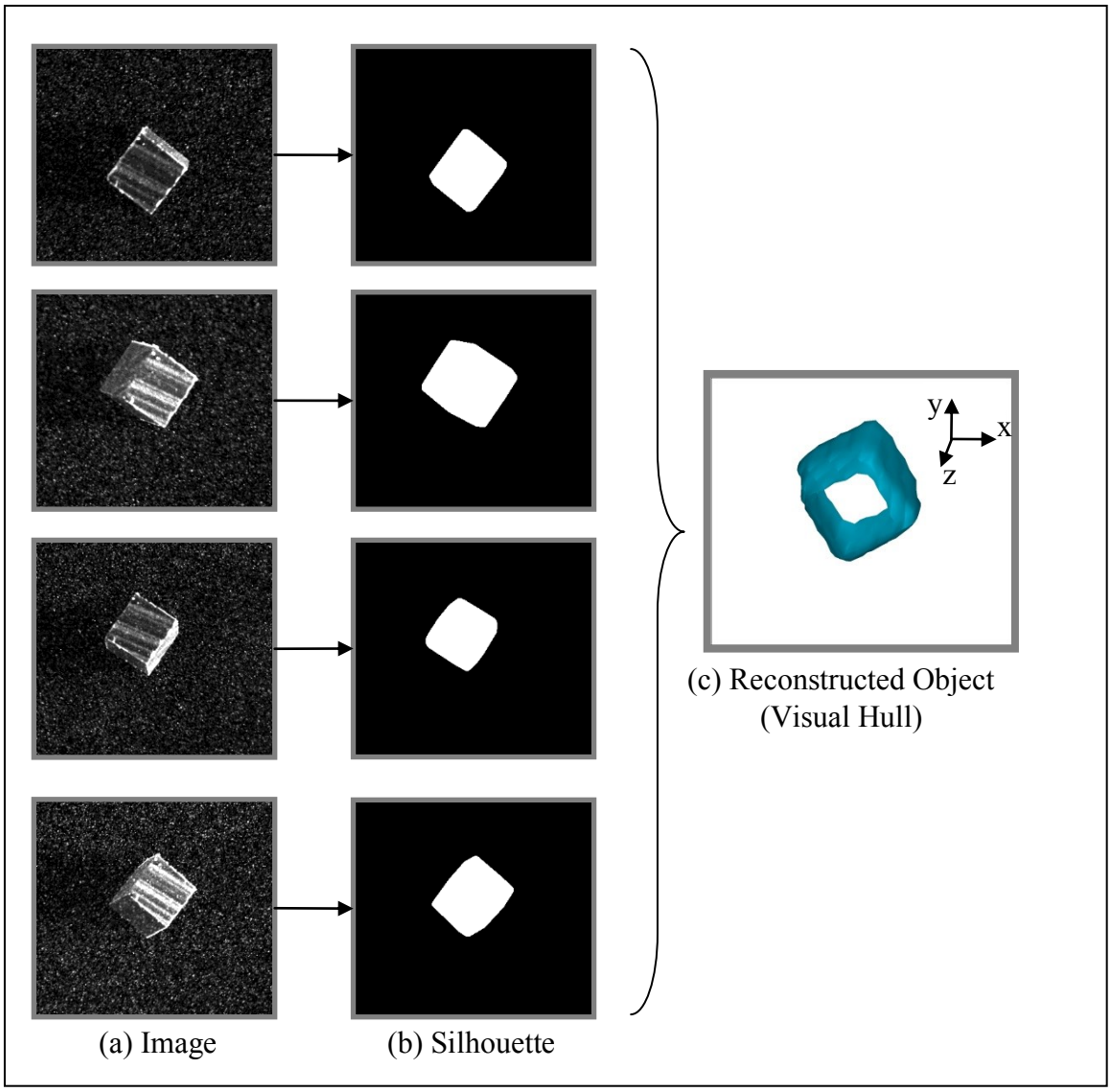

Figure 3-6: Processing sequence from (a) image to (b) silhouette and eventually to (c) visual hull of the object. (c) shows the iso-surface of the reconstructed object, which is open at two ends beyond the illuminated volume.

The visual hull technique has two predominant limitations that prevent it from reconstructing the object perfectly: (1) a limited number of cameras and (2) no ability to resolve concavities. Since there are only 4 cameras, the problem is underdetermined, and thus perfect reconstruction of the object is improbable. For instance, in figure 3-6c, the reconstructed object has an open surface in the z-direction; thus, another camera with its

optical axis aligned parallel to the x or y-direction would be required to close this surface. However, this would require additional hardware and complexity in calibration. Furthermore, a camera facing the x-direction would directly face the laser, which would be undesirable. The inability of the visual hull technique to resolve concavities is not an issue for the objects considered herein. However, interested readers may refer to Mulayim *et al.* (2003) and Laurentini (1997) with regard to concave shapes. Nonetheless, in the cases examined, the visual hull of the object appears similar to the shape of the actual object and thus gives a good estimate of the location of the object within the field of view.

The visual hull, as described above, consisted of a volume of voxels with non-zero intensity. For purposes of visualization, the voxels within the visual hull volume were placed into a Cartesian grid with sub-volumes of 12 × 12 × 12 voxels within Tecplot®. This corresponded with the velocity vector grid spacing. If 50% or more of a sub-volume was occupied, this sub-volume was included in the visual representation.

3.4.2 Tomographic PIV

Tomographic PIV includes four main steps: (1) volume calibration (including self-calibration), (2) pre-processing, (3) three-dimensional volume reconstruction, and (4) cross-correlation between volumes to obtain volumetric velocity fields which are described in more detail in the next few paragraphs.

The calibration method and procedure was described in the previous section on the visual hull. In addition, we also applied the self-calibration procedure of Wieneke (2008) to correct and improve the mapping function. This corrected mapping function ultimately was used for both back-projection and tomographic PIV. In the self-calibration procedure, we acquired 100 sets of simultaneous particle images (without objects), which were used to minimize disparity errors associated with particle triangulation. This step was also used to determine the effective volume thickness (z-dimension) over which

sufficient seeding particle intensities was available for correcting disparity errors. The x and y dimensions were determined from the overlapped camera views. The resulting volume was $-50 \text{ mm} < x < 50 \text{ mm}$, $-30 \text{ mm} < y < 30 \text{ mm}$ and $0 \text{ mm} < z < 12 \text{ mm}$, compared to the illuminated volume of 120 mm × 80 mm × 14 mm.

After self-calibration, the raw experimental images (with objects) were processed. A pre-processing step was performed to eliminate background noise, reduce the light scatter from the object surface, and compensate for intensity differences between images. In this step, a sliding minimum convolution filter was applied around a 3×3 pixel window. This eliminated the background noise and reduced the object intensity by subtracting minimum intensity values within the window, which was much smaller than the object size. Then, the images were normalized with a reference image to compensate for differences in background intensity. This pre-processing was necessary to ensure good reconstruction quality of the particles.

After pre-processing, particle intensity volumes were reconstructed from sets of four images using five iterations of the MART algorithm implemented within DaVis 8.0 software. Figure 3-7 shows x-y and x-z planes of a volume for a case without (figure 3-7a) and with pre-processing (figure 3-7b). The planes have depth of one voxel. Figure 3-7a includes reconstruction artifacts due to the presence of the object. However, the pre-processed set of images yields a better particle reconstruction quality and mostly eliminates the artifacts (figure 3-7b). Note, however, that ghost particles appear within the original object volume (figure 3-7b).

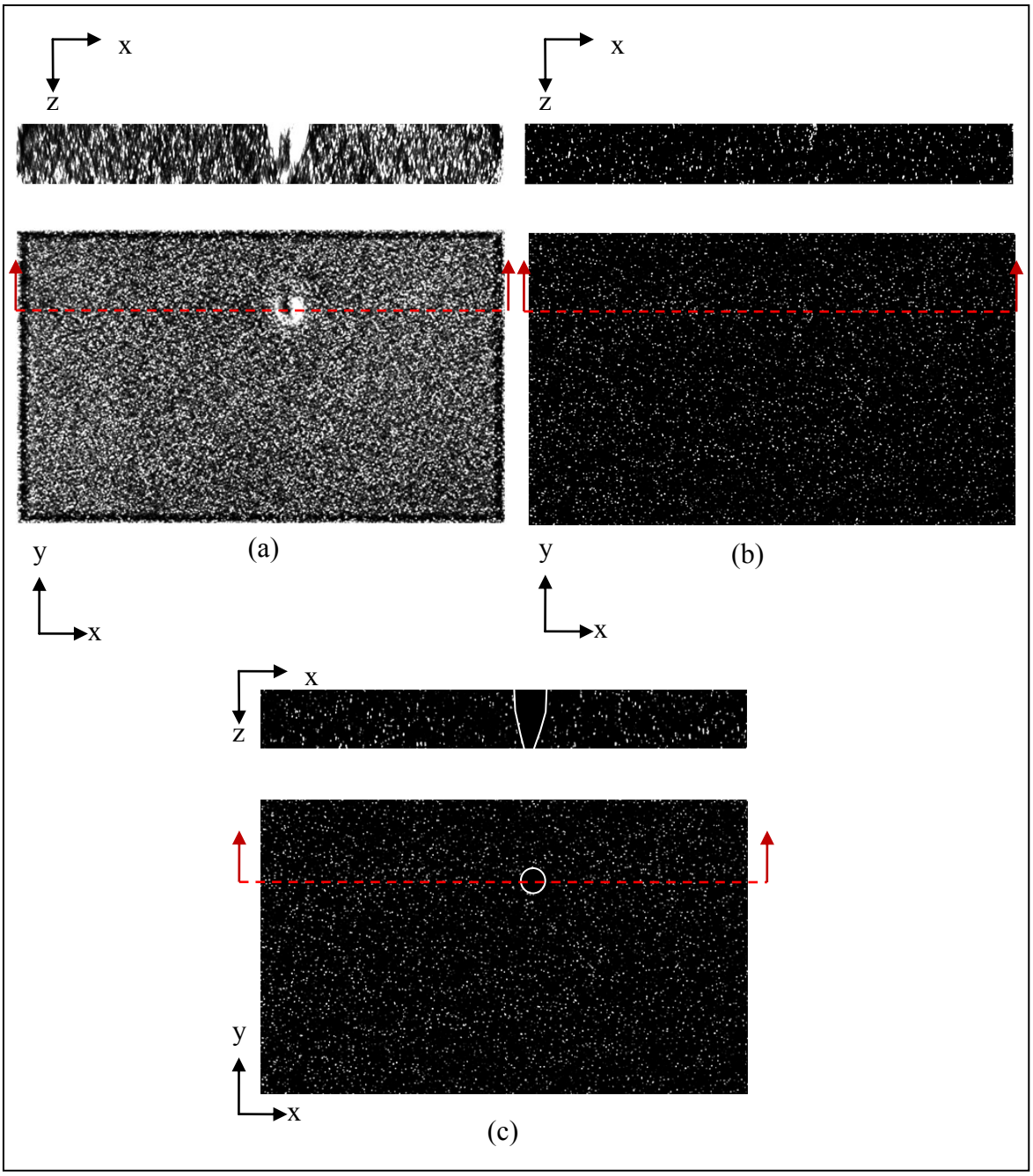

Figure 7: Reconstructed volume including a sphere where the images were (a) not pre-processed, (b) pre-processed and (c) masked. The red dashed lines represent the location of the x-z plane (situated above x-y plane). The x-y plane is extracted from middle of x-z plane. In (a), the sphere creates a reconstruction artifact, while in (b) almost no reconstruction artifact is visible. Solid white line in both views of (c) represents the masked portion of the reconstructed particle volume.

After particle reconstruction, the volume corresponding with the reconstructed object mask (visual hull) was assigned zero values, and it was multiplied with the overall reconstructed measurement volume using DaVis 8.0. This was done to remove any ghost particles appearing within the object (see e.g. figure 3-7c). Ghost particles can occur because several independent voxel intensity distributions can satisfy similar intensity projections on the cameras (Elsinga *et al.* 2006). Any ghost particles within the object could result in undesirable spurious velocity vectors after correlation or could contaminate valid vectors in the object neighborhood. We note that it would be possible to apply the mask after every MART iteration in order to redistribute any ghost intensities inside the masked volume to the real particles in the volume outside of the object and, in this way, potentially improve the reconstruction quality. This could be a good strategy when the object is dark and non-reflective. If the object is reflective, however, some of the projected intensity in the camera images is also contributed by reflections from the object surface. Completing all iterations before masking helps confine reflections to the object surface that typically would lay within the volume masked by the visual hull. By contrast, if masking is carried out after every MART iteration, the projected image intensities caused by reflection from the object would be redistributed to the volume outside of the mask, potentially increasing the number of ghost particles outside of the object. For this reason, masking after every MART iteration was not implemented.

Separate masked volumes were cross-correlated to obtain the three-dimensional tracer particle displacement. Given the minimum available $\Delta t = 1$ ms, the maximum velocity within the processed fields, and the image magnification, the smallest interrogation volume that produced relatively few spurious vectors was 32 voxel^3. A multi-pass cross-correlation was used, decreasing the interrogation box size from 48 voxel^3 initially to the final 32 voxel^3. The image particle density is 0.05 particle per pixel (ppp), and the particle density in the volume is about 7 particles per interrogation volume. The particle number density per volume was estimated after determining the average ghost particle intensity in a volume immediately outside of the illuminated region and using this value to set a minimum particle intensity threshold within the illuminated region. The

interrogation volume provided a spatial resolution in all three directions of 2.65 mm. Using a 75% overlap resulted in approximately 247,338 (151 × 91 × 18) grid points for each time step. Vectors were computed only on points located outside the reconstructed object, and any vectors centered within the object were again masked during post-processing. These steps together with the self-calibration step ensured that less than 1% of all vectors (in more than 400 volumetric vector fields) were spurious and these occurred at random locations throughout the measurement volume.

The calibration, self-calibration and pre-processing steps of tomographic PIV were carried out on a 64-bit Windows PC with 4 processors and 8 GB of memory. However, particle reconstruction and volume correlation, which were more computationally intensive (see Ortiz-Duenas *et al.* 2010), were processed in parallel on 5 similar computers.

3.5 Results

3.5.1 Reconstructed object (Visual hull)

Figure 3-8 shows examples of reconstructed object surfaces (indigo), surrounding the actual objects (red) within them. The reconstructed surfaces were determined using the visual hull technique, while the placement and orientation of the actual object within the surface was estimated manually from the raw images. These examples show that the actual objects appear to fit very closely within the reconstructed surface. Another observation is that the reconstructed shapes are generally conic-like, which is due to the intersection of lines of sight from the different camera angles on the object. Obviously, this cone-like shape will be different for other camera arrangements. It should also be noted that the actual object is always encapsulated within the visual hull, unless part of the object extends beyond the overall measurement volume (e.g. figure 3-8d). Considering the four reconstructions shown, the volume ratio between the reconstructed visual hull and its corresponding object is 1.3 for the sphere, 1.4 for the cube, 3.9 for the

tetrahedron and 1.3 for the cylinder. The tetrahedron clearly has the highest ratio because the smaller angles on its edges and vertices can create larger occlusions in the field of view for some orientations. It is also clear that significant parts of the excess volume within the hull are located in front of and behind the objects. This will be discussed further in section 6 below.

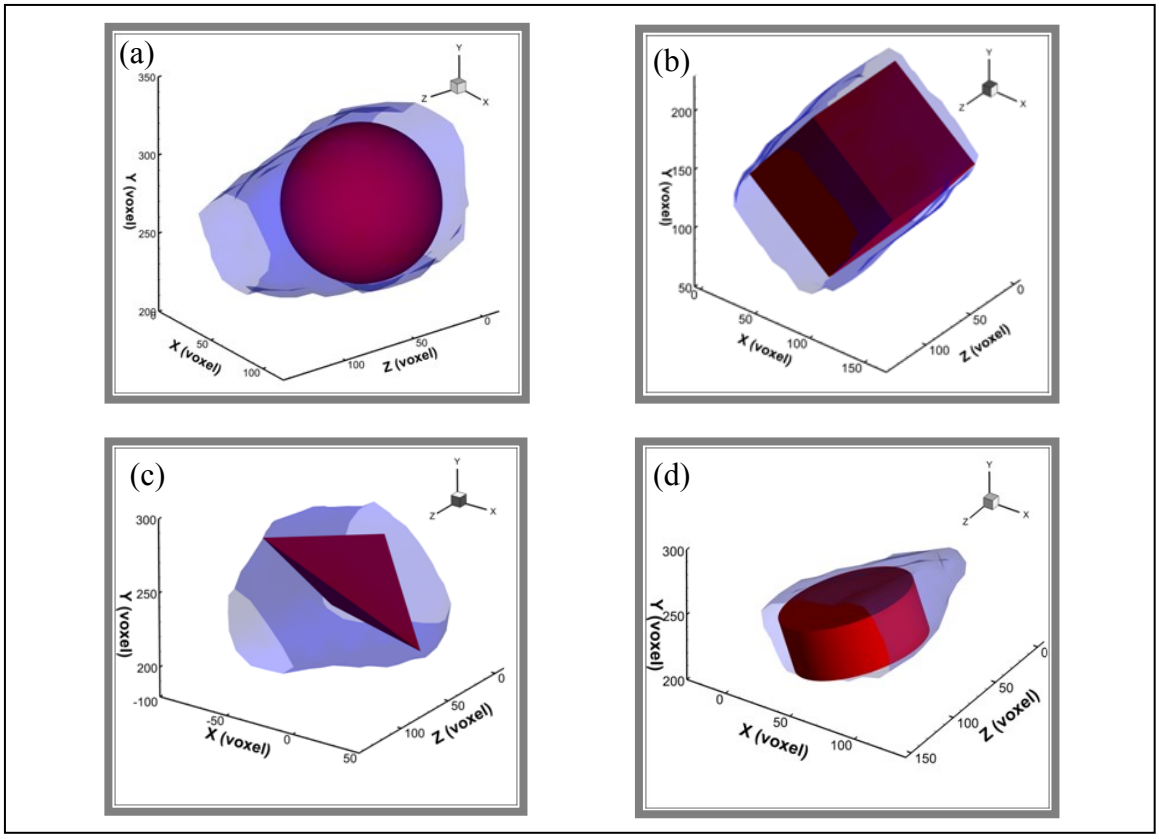

Figure 3-8: Reconstructed visual hull, shown as translucent iso-surfaces, generated from raw images of a (a) sphere, (b) cube, (c) tetrahedron and (d) cylinder. The solid objects, shown in red, were constructed manually. The location and orientation of each object was estimated from calibrated raw 2D images. These objects are placed to illustrate the fit of the reconstruction.

Figure 3-9 shows the same tetrahedron in a different orientation. As expected, a slightly different reconstructed surface is observed. Although the reconstruction shape changes with object orientation, it should be noted that the reconstruction surface consistently envelops the actual object.

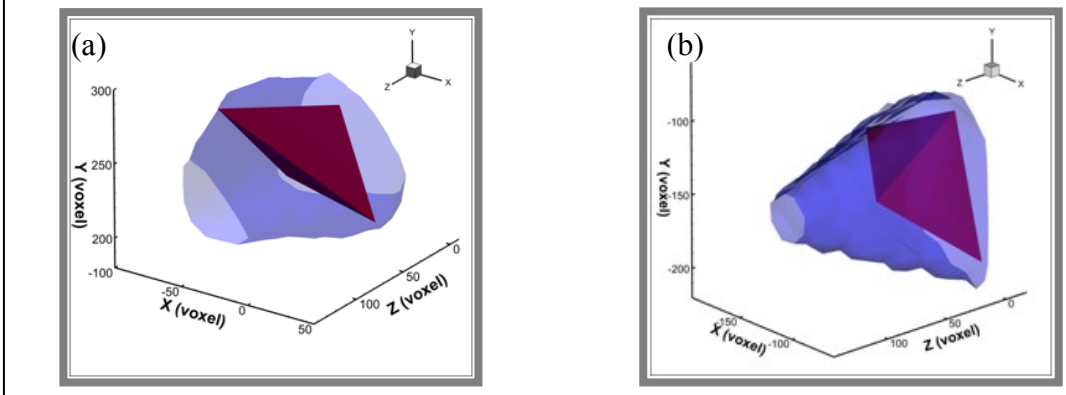

Figure 3-9: Reconstructed visual hull for multiple object orientations. Reconstructed volume in (a) is larger than in (b).

3.5.2 Vector field around the moving object

Figures 3-10 and 3-11 show velocity fields surrounding a reconstructed sphere, cube, tetrahedron, and cylinder. For clarity, vectors in only 2 planes are shown within each volume. These planes are located at z = 2 mm (blue) and 10 mm (red). Notice that vectors are computed very close to the reconstructed object (within 1.3 mm or half of an interrogation volume). No vectors appear within the reconstructed object due to particle volume masking.

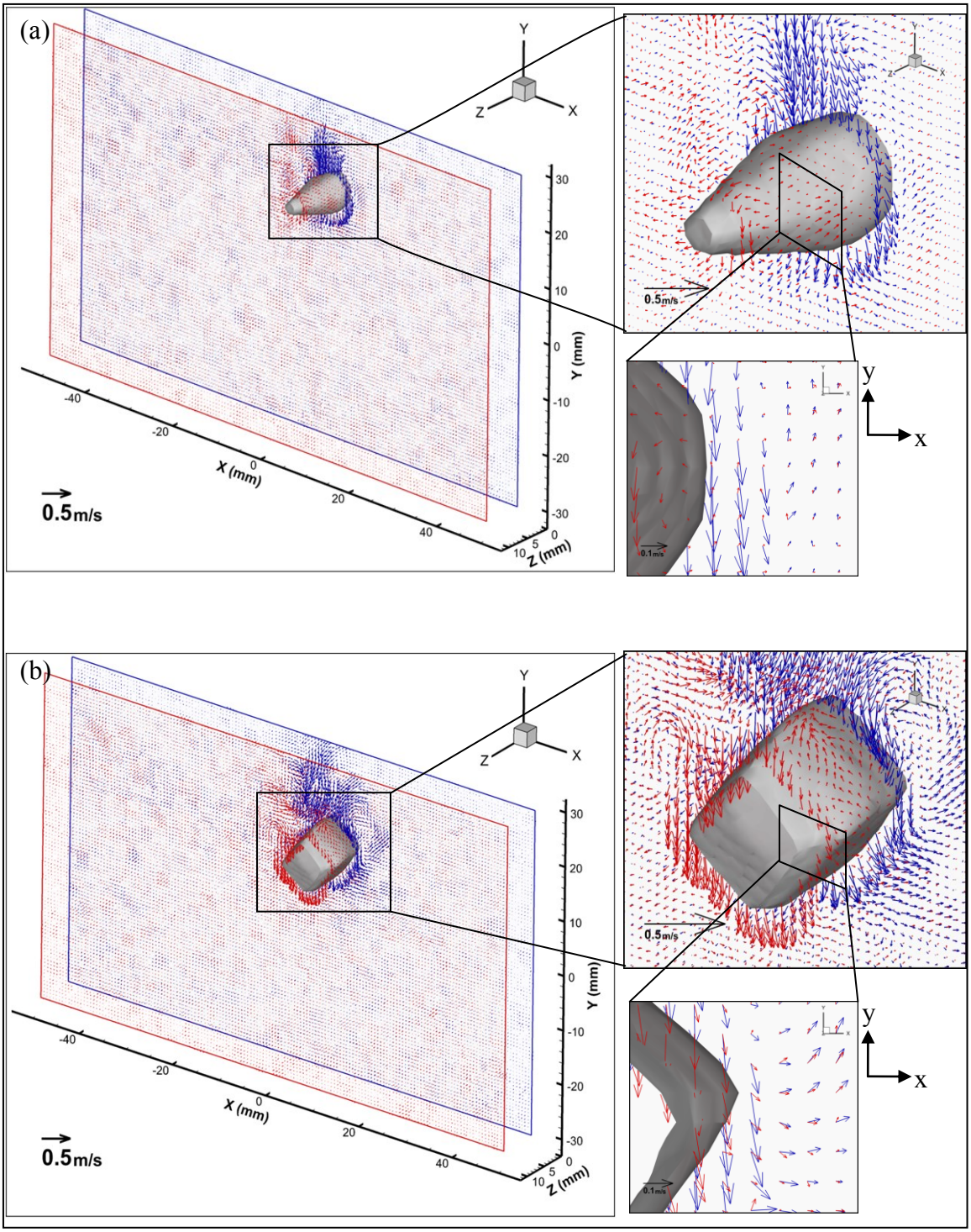

Figure 3-10: Vector fields around moving objects for (a) a sphere and (b) a cube. Only two planes at z = 2 mm (blue) and z = 10 mm (red) are shown for clarity.

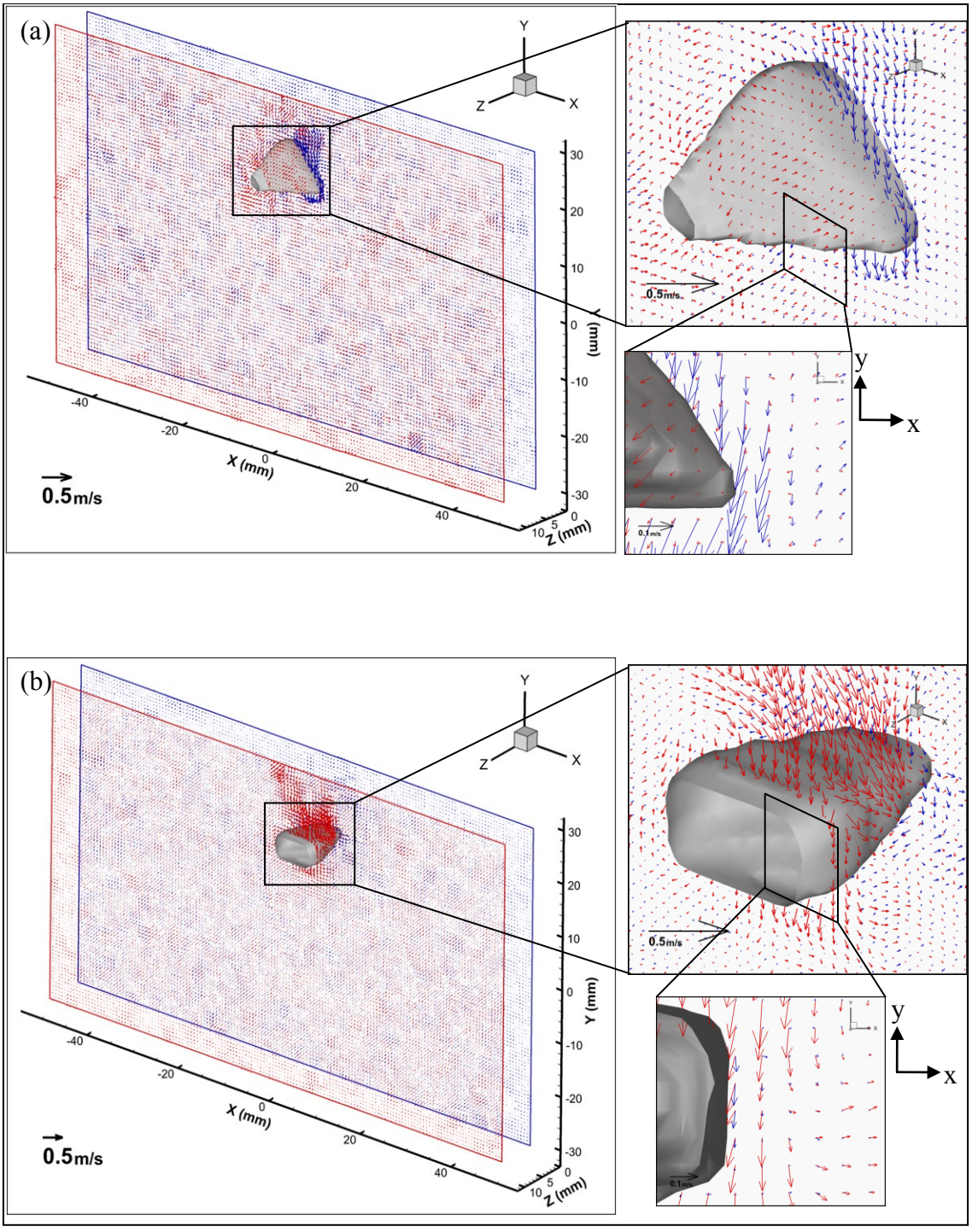

Figure 3-11: Vector field around the moving object for (a) a tetrahedron and (b) a cylinder. Only two planes at z = 2 mm (blue) and z = 10 mm (red) are shown for clarity.

In figure 3-10a, the vectors appear consistent with the motion of the sphere. The vectors in the back plane (blue) are generally higher in magnitude than those in the front plane (red). This implies that, in this instance, the sphere center is closer to the back plane. This agrees well with the reconstructed object, which appears to have a larger cross section (normal to z-axis) nearer to the back plane. Furthermore, this estimated location is also supported by fitting a sphere with the reconstructed surface (similar to that carried out in figure 3-8a), and visual inspection of the raw images. For the cube (see figure 3-10b), the vector magnitudes in both planes are comparable, which suggests that the cube lies within the volume. This agrees well with the reconstructed cube which appears to have nearly uniform cross sectional area along the two planes, and from the visual inspection of the raw images. For the tetrahedron (figure 3-11a), the back plane shows larger velocity magnitudes compared to the front plane. Again, this corresponds well with the reconstructed surface, which appears to have higher area nearer to the back plane. By contrast, the cylinder (figure 3-11b) yields higher velocity magnitudes around a larger cross section in the front plane. Another observation for the tetrahedron case is that the vector magnitudes appear generally lower than those near the sphere and cube. This is because the volume (and mass) of the tetrahedron are lower than those of the other objects, and it therefore sinks at a lower velocity.

For the results presented above, the percentage of valid vectors was examined in various regions surrounding the visual hull mask. In regions viewed by four cameras, this percentage was 99%, and any invalid vectors occurred at random locations. In regions accessible by three cameras, the percentage of valid vectors dropped to 96.5% due to reduced signal-to-noise ratio. These regions, which were limited to the rearward portion of the measurement volume beyond the leading edge of the falling object (typically $z < 8$ mm depending on the object geometry, orientation and location), surrounded the sides of the visual hull, and increased in thickness (x or y dimension) with decreasing z value (see figure 3-12a). Regions outside of the visual hull that were optically accessible by at most 2 cameras fell inside of the '3 camera' envelope, and their thickness was small (extending ~1.3 mm or about half of the interrogation spot dimension outside of the visual hull;

figure 3-12b). The percentage of valid vectors in regions viewed by two cameras was as low as 65%. This decrease in the number of valid vectors is due to the significant reduction in the particle reconstruction quality when the number of camera views decreases from 3 to 2. A parametric study of reconstruction quality against number of cameras used was carried out previously by Elsinga et al (2006) who observed a similar trend. Parametric effects on the size and location of the partially obscured regions are discussed in more detail below.

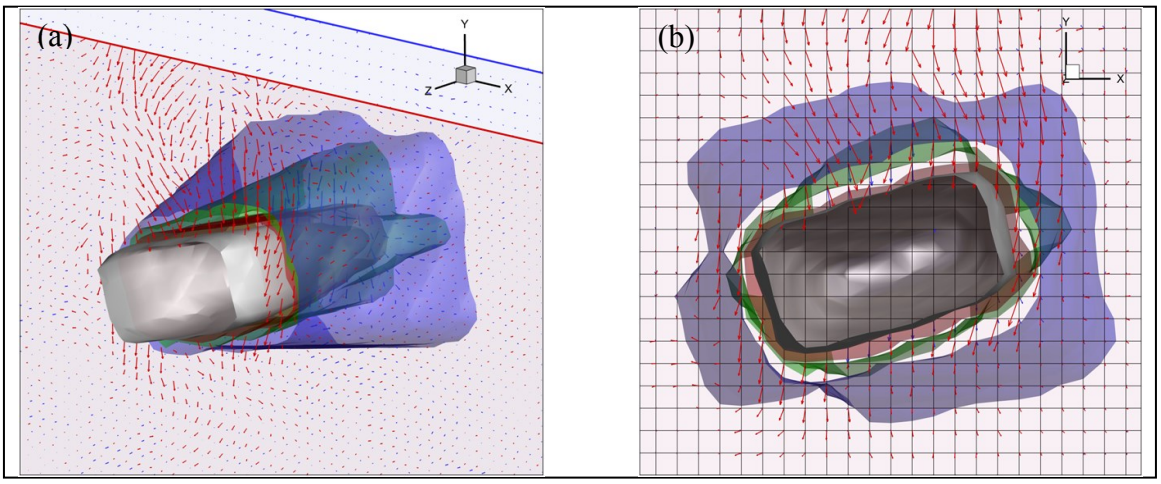

Figure 3-12: Visual hull (gray) and "envelopes" of regions optically accessible by 3 cameras (blue), 2 cameras (green), and 1 camera (red). (a) shows the increasing thickness of the region optically accessible by 3 cameras as z decreases. (b) shows x-y view and the vector grid points. Note that four grid points represent an interrogation box length for the cross-correlation with 75% overlap.

3.6 Discussion of visual hull implementation

In the preceding section, we presented results for a specific camera configuration, field of view, and relative object scale. The results for this parameter set yielded visual hull shapes that extended beyond the object dimensions, particularly in front of and behind the object. In this section, we discuss effects of variations in object size, object shape, and camera arrangement on the shape and size of the visual hull, as well as several ideas that could be employed in specific applications either to decrease the hull or mask volume

relative to the object volume or to decrease obscured regions and therefore increase the number of fluid velocity vectors obtained.

The 3D schematic diagram in figure 3-13 illustrates several sub-volumes within which simple implementation of the visual hull prevent determination of fluid velocity vectors. These regions include the partially obscured region that is accessible by less than 3 cameras (denoted by blue), the fully obscured region that is not accessible by any camera (denoted by green), and the region inherently masked by the visual hull even though it is optically accessible by all cameras (denoted by yellow). We use a criterion of less than 3 cameras for the partially obscured region based on recommendations by Elsinga et al (2006) for acceptable particle reconstruction quality. We note that in sub-volumes accessed by only 3 camera views, the reconstruction quality of tracer particles could be improved if the fourth camera image obscured by the object could be selectively excluded in the MART iteration. This idea was not carried out in the current experiments due to the limited user access to the DaVis 8.0 MART algorithm.

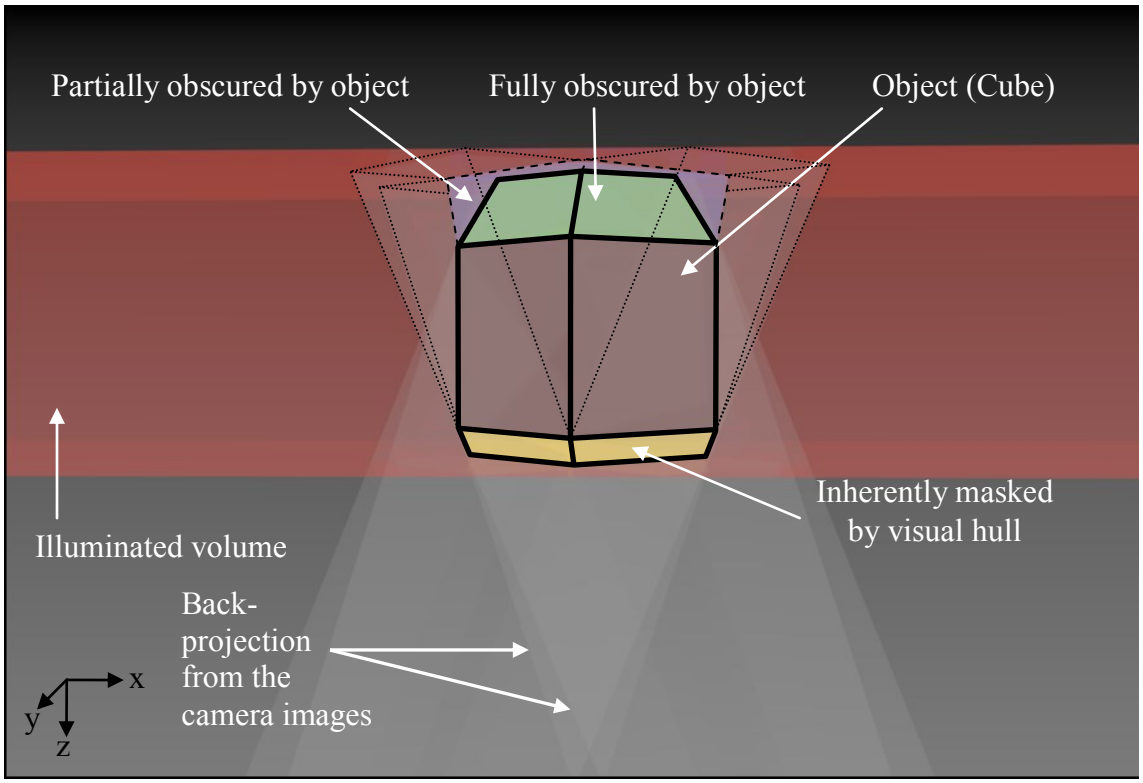

Figure 3-13: Schematic diagram of the 4 camera projections on the object (cube) which shows the obscured regions when applying the visual hull. Black solid lines represent the edges of the visual hull. Dotted lines outline regions accessible by at most three cameras. Blue (outlined by dashed lines) is accessible by less than three cameras, and green is fully obscured. The visual hull also inherently masks a non-obscured region (yellow) in front of the object. The translucent white and red regions represent the back-projections from each camera and the illuminated volume, respectively.

Ideally, particles could be reconstructed and eventually velocity vectors could be determined within the yellow region that is not obscured but nevertheless masked by the visual hull. Figure 3-14a shows an integrated x-y view of reconstructed particles located in the space in front of the spherical object (z = 65 to 140 voxels) based on the same data volume shown in Figure 3-7. The reconstruction quality in front of the sphere appears suitable for vector calculation since there are no obvious reconstruction artifacts caused by the sphere's presence. Therefore, if the front surface of the object could be determined, the yellow sub-volume could effectively be eliminated from the visual hull in

this case. However, for the general case of a moving object whose exact shape and orientation are not known *a priori*, accurate detection of this boundary may be challenging. For example, figure 3-14b(i) shows an x-z plane view with single voxel depth (reproduced from figure 3-7b) of an unmasked particle reconstruction volume that intersects the central plane of the spherical object. In the figure, the boundary of the sphere is difficult to discern even in the close up view (see insert image in figure 3-14b(i)). Figure 3-14b(ii) shows an x-z plane view for which the intensity is integrated across the center plane of the sphere over a depth of 12 voxels in the y-direction (physical dimension: 1 mm). In this figure, the greater number of reconstruction artifacts make the sphere's outline more obvious. However, the close up view of the forward sphere boundary (see insert image in figure 3-14b(ii)) reveals that it is still difficult to distinguish. Integrating over a greater voxel range in the y-direction may improve the boundary location estimate in some situations, but if the x-z boundary location varies in y, this strategy would lead to inaccuracies. This example thus illustrates that automated location of an arbitrarily shaped object boundary can be challenging at the least, and the location strategy would likely depend on the specific application considered.

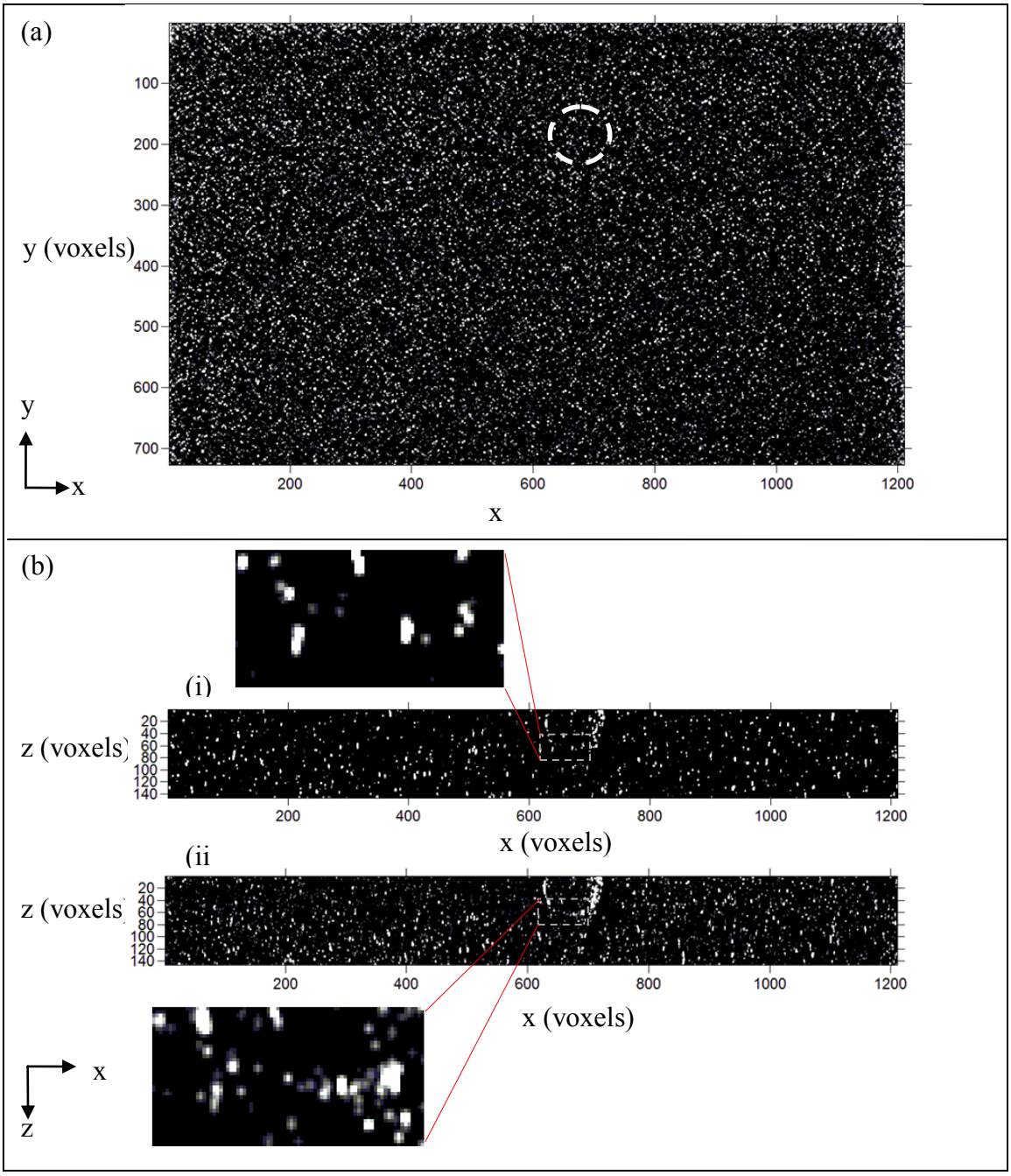

Figure 3-14: Reconstructed particle volumes where a sphere is present in the measurement volume. (a) represents the intensity integrated over the range z = 65 to 140 voxels. The dashed circle in (a) represents the location of the sphere. (b) shows the reconstructed particle volume for (i) a plane with depth of 1 voxel intersecting the center of the sphere (reproduced from figure 3-7b), and (ii) a depth of 12 voxels (physical dimension: 1 mm) in y spanning the sphere centerplane. The insert images (i) and (ii) show close up views of the sphere boundary.

While vectors in the yellow sub-volume of figure 3-13 might be resolvable through additional image processing, the fully obscured green region cannot be resolved for the given object shape and camera arrangement. On the other hand, the blue region may be resolvable, albeit with low reconstruction quality. The effects of (1) object parameters and/or (2) camera parameters on the sizes of these regions are discussed below. For ease of visualization and discussion, some 2D figures with planar projections (figures 3-15 and 3-16) as opposed to 3D figures with volumetric projections (e.g. figure 3-17) are used. In the 2D case, a partially obscured area is viewable by only one of the two cameras shown. It should also be noted that the camera sensor planes are much larger than the representations shown in figures 3-15, 3-16 and 3-17. The full sensor size was not drawn due to space constraints. Thus, we assume that every camera sensor is capable of viewing the entire illumination region in the figures.

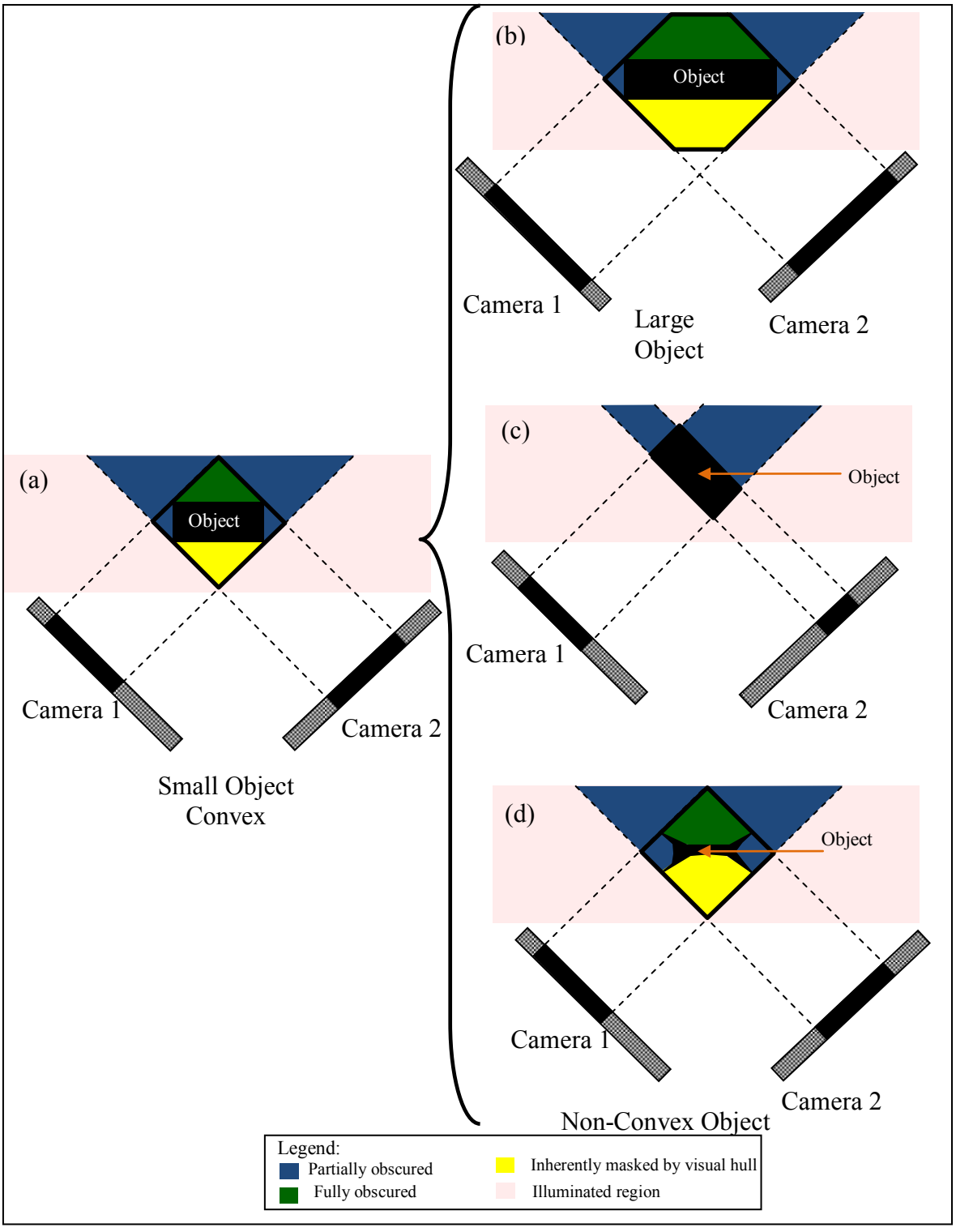

Figure 3-15: Schematic diagrams showing the variation in unresolved regions due to changes in object parameters. The (a) original object is compared with changes in its (b) size, (c) orientation, and (d) convexity. Black solid lines represent the edges of the visual hull.

Object parameters considered are size, orientation and convexity. Figures 3-15a and 3-15b compare visual hulls resulting from objects of different size within the same illumination volume. As might be expected, a larger object yields larger yellow and green regions, although the partially obscured region is not necessarily larger. Furthermore, the larger object occupies a greater area of the camera sensor, leaving a smaller area for particle reconstruction. In the projections shown, the ratio of hull area to object area is comparable for the two sizes. If an object is non-spherical, its orientation has a significant effect on the size and shape of the visual hull as well as the obscured sub-volumes (compare figures 3-15a and 3-15c). In figure 3-15c, when the object's faces are perfectly aligned with the camera image planes, the forward yellow and rearward green regions disappear completely. The partially obscured region is also smaller for this orientation. If this concept is extended to volumetric projections in three dimensions, the forward 'yellow' and rearward fully obscured regions will also be minimized when the object faces are most closely aligned with the camera image planes. Figure 3-15d shows the visual hull generated for a non-convex object. An object is considered convex if for every pair of points within the object, the straight-line segment connecting the points is also completely within the object. From the figure, all three sub-volumes (yellow, blue and green) can be enlarged by concavities in the object surface.

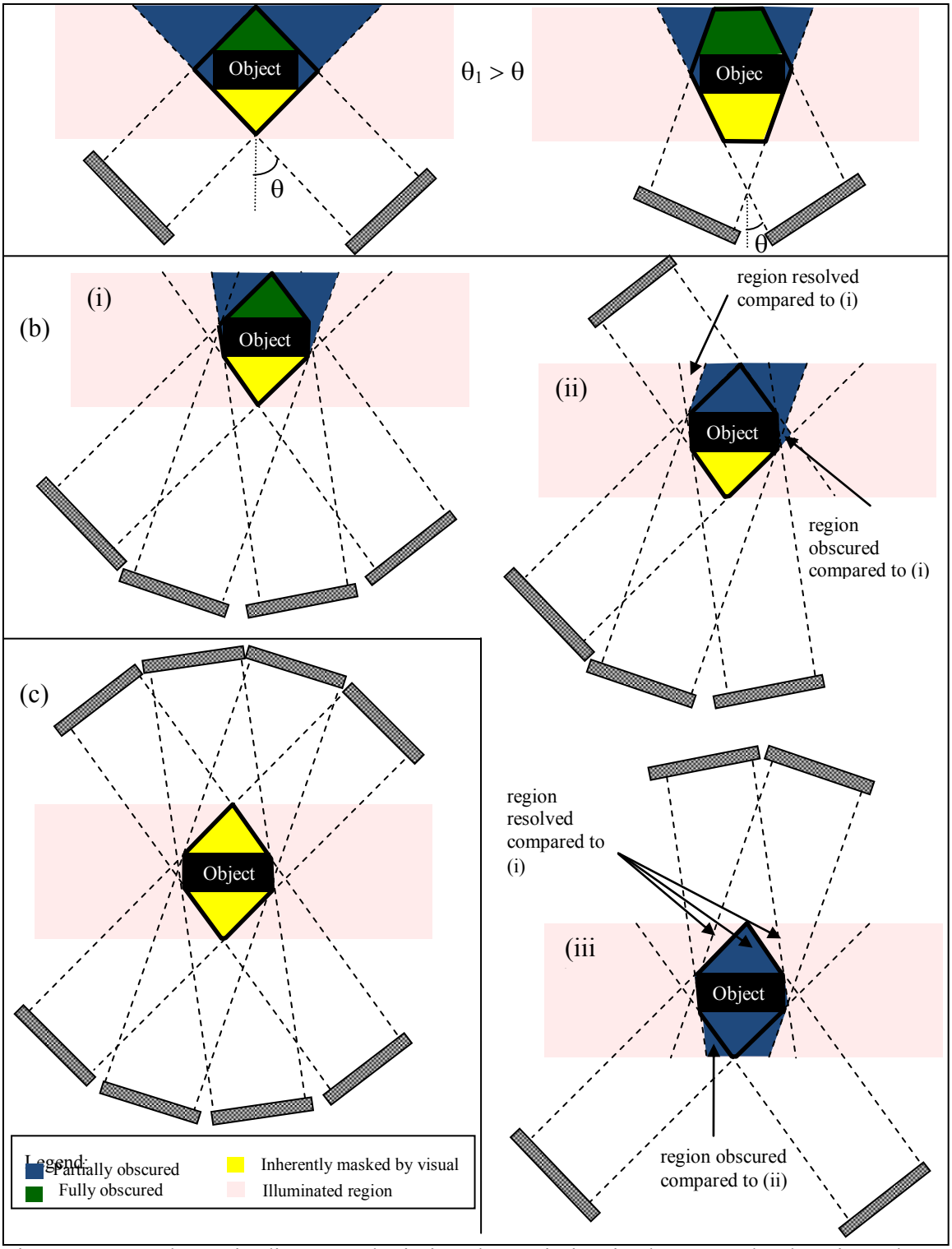

Figure 3-16: Schematic diagrams depicting the variation in the unresolved regions due to changes in camera parameters, which include (a) camera viewing angle, (b) camera arrangement, and (c) number of cameras. Black solid lines represent the edges of the visual hull.

Camera parameters, which can affect the volumes within the visual hull as well as the partially obscured volumes, include camera orientation, arrangement, and number. Figure 3-16a compares cameras inclined at larger and smaller angles, θ_1 and θ_2, to the measurement volume. It can be observed that the larger camera angle reduces the fully obscured region (green) at the expense of increasing the size of the partially obscured region (blue) and the overall obscured region blue + green. Thus, if partially obscured regions are acceptable, larger inclination angles would be desirable. However, it should be noted that Elsinga et al (2006) found an optimal regime for tomographic particle reconstruction that was limited to camera arrays with angles in the range $15^\circ < \theta < 45^\circ$.

Another parameter influencing the obscured regions is the relative positioning of cameras within an array. In the current set up, the four cameras are all placed on the same side of the laser sheet (see figure 3-16b(i)) which necessitates that some region is fully obscured. A non-planar arrangement, such as that shown in figure 3-17, generally provides better optical access to various sides of the object by reducing the blue partially obscured region. The fully obscured region can be eliminated by moving one or more cameras to the opposite side of the laser sheet as in figures 3-16b(ii) and (iii). If one camera is placed on the opposite side as in figure 3-16b(ii), the partially obscured region is shifted such that a new region is resolved while another region becomes partially obscured. If two cameras are placed on each side of the laser sheet (figure 3-16b(iii)), the partially obscured region is reduced, and the combined blue + yellow region is smaller overall. Thus, this option may be useful for specific applications. On the other hand, the camera arrangement might be optimized according to the 'side' of a given object that is of most interest.

Lastly, increasing the number of cameras can obviously reduce the masked and obscured fluid regions significantly. For example, figure 3-16c shows an eight-camera arrangement with four cameras on each side of the laser sheet. This arrangement will eliminate all obscured regions (green and blue) and provide at least four images for reconstruction of all regions outside of the visual hull.

A mathematical expression for the fully and partially obscured regions can be found for a simple object and camera arrangement. Consider a 3-D schematic of a cuboid in an illuminated volume viewed by four cameras (see figure 3-17). The inclination angles of Cameras 1-4 are α_1, α_2, α_3, and α_4 respectively. The object is represented as a simple cuboid with length *a*, width *b*, and depth *c*, where *a* and *b* are parallel to the laser sheet. The distance from the rear of the object (relative to the cameras) to the rear edge of the laser sheet is given by *t*. Based on these dimensions, the volume of the fully obscured region can be calculated as:

$$Vol_{Fully\ Obscured} = abt - \frac{t^2}{2}[a(tan(\alpha_1) + tan(\alpha_3)) + b(tan(\alpha_2) + tan(\alpha_4))] + \frac{t^3}{3}(tan(\alpha_1) + tan(\alpha_3))(tan(\alpha_2) + tan(\alpha_4)). \quad (3\text{-}1)$$

The partially obscured region, optically accessible by 2 cameras, is given by:

$$Vol_{Partially\ Obscured} = \frac{t^2}{2}[a(tan(\alpha_1) + tan(\alpha_3)) + b(tan(\alpha_2) + tan(\alpha_4))] - \frac{t^3}{3}(tan(\alpha_1) + tan(\alpha_3))(tan(\alpha_2) + tan(\alpha_4)) . \quad (3\text{-}2)$$

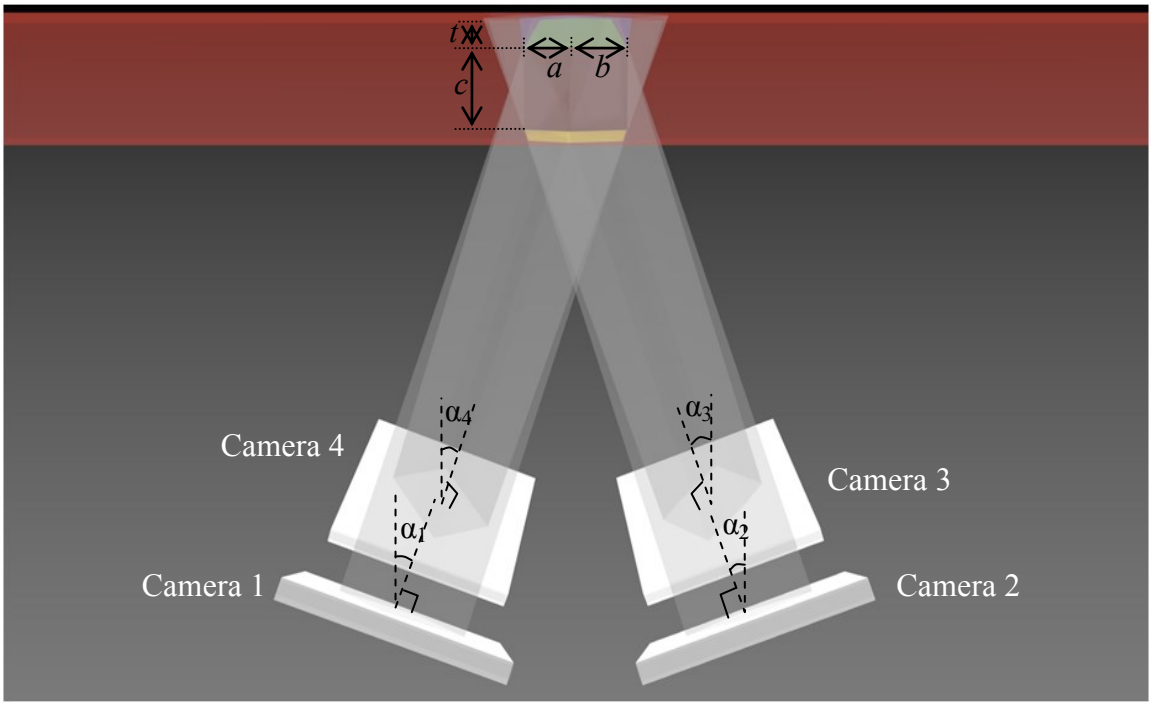

Figure 3-17: Schematic diagram of a specific "4-corners" camera arrangement. The inclination angles of cameras 1-4, with respect to the vertical direction, are α_1, α_2, α_3, and α_4 respectively. The dimensions of the cuboid are *a* (length) x *b* (width) x *c* (depth), where *a* and *b* are parallel to the laser sheet, and the side faces of the object are aligned with the camera angles. The distance from the rear of the object (relative to the cameras) to the rear edge of the laser sheet is given by *t*.

Equations (1) and (2) are valid assuming that the fully obscured volume is trapezoidal in shape (i.e. $tan(\alpha_1) + tan(\alpha_3) < b/t$ *and* $tan(\alpha_2) + tan(\alpha_4) < a/t$), and that the entire object lies within the illuminated volume. More detail is given in Appendix C. The above equations imply that the object dimensions and location within the illuminated volume, as well as the camera angles, determine the volume of these obscured regions for the example considered.

We can further simplify equations (3-1) and (3-2) by assuming a cubic object (i.e. $a = b = c$), and a symmetric camera arrangement (i.e. $\alpha_1 = \alpha_2 = \alpha_3 = \alpha_4 = \alpha$) so that the equations reduce to:

$$Vol_{Fully\ Obscured} = a^2t - 2at^2tan(\alpha) + \frac{4}{3}t^3tan^2(\alpha), \quad (3\text{-}3)$$

$$Vol_{Partially\ Obscured} = 2at^2tan(\alpha) - \frac{4}{3}t^3tan^2(\alpha), \quad (3\text{-}4)$$

and the trapezoid assumption reduces to $tan(\alpha) < a/(2t)$. Based on Equations (3-3) and (3-4), it can be shown easily that

(1) as a increases, $Vol_{Fully\ Obscured}$ and $Vol_{Partially\ Obscured}$ increase

(2) as α increases, $Vol_{Fully\ Obscured}$ decreases while $Vol_{Partially\ Obscured}$ increases

(3) as t increases, $Vol_{Fully\ Obscured}$ and $Vol_{Partially\ Obscured}$ increase

Statement (1) is consistent with the 2-D case discussed previously in figure 3-15b, while statement (2) is consistent with that discussed in figure 3-16a. Statement (3) shows explicitly how the fully and partially obscured regions increase as the object moves closer to the cameras and front edge of the laser sheet where the first term in Equation (3-3) is typically dominant such that the obscured volume scales linearly with t.

If $tan(\alpha) > a/(2t)$, however, the fully obscured region takes a shape of a pyramid, and part of the region behind the object becomes optically accessible (see Appendix C). The fully obscured volume becomes independent of t:

$$Vol_{Fully\ Obscured} = \frac{a^3}{6tan(\alpha)} \quad , \tag{3-5}$$

but the equation for the partially obscured region reduces to the same form as equation (3-4). Statements (1) and (2) are also valid for equation (3-5).

3.7 Conclusions

Volumetric velocity measurements of flow around moving objects have been demonstrated. A visual hull method was used in combination with existing tomographic PIV reconstruction software to automate identification and masking of discrete objects within the measurement volume. This technique provides information about the location of the object within the volume, while simultaneously measuring all velocity components in the 3D space surrounding the object.

The visual hull technique was implemented to locate and reconstruct the object. In this technique, each raw image underwent a sequence of image processing steps after which the object silhouette was extracted. The binary silhouette images were then reconstructed to generate the visual hull of the object. Independently, the raw images were

preprocessed, and particles were reconstructed using the MART tomographic reconstruction technique. The particle intensity fields were then masked using the reconstructed object before velocity vectors were obtained. Thus, vectors could be obtained very close to the object (within half of an interrogation window) without any contamination. Although the shape of the reconstructed object is necessarily larger than and somewhat different in shape from the actual object due to a limited number of camera projections, a reasonable estimation of the object location and orientation is nevertheless possible by observing the area distribution within the reconstructed volume. Finally, because the method described and demonstrated herein is automated, it can be used effectively to examine flows in which the body orientation and trajectory are not known *a priori*.

The current study was inspired by the need to mask aquatic organisms swimming within the measurement volume. In these applications, the object shapes are complex and variable in time. Furthermore, the object surfaces can have either no distinctive pattern or highly complicated patterns with variable scattering properties. Thus, the simplicity of the visual hull reconstruction method is especially useful. Beyond applications to aquatic, terrestrial, and aerial organisms, the issue of variable or unpredictable object size and shape extends to particle-laden, droplet-laden, bubbly, or other multiphase flow regimes where the visual hull concept could also be employed to advantage. By contrast, if the objects within the flow have known size and shape, e.g. specific solid particles or moving vehicles, and appropriate scattering signatures, then it may be possible either to reconstruct the objects accurately or otherwise locate them precisely within the measurement volume using a correlation scheme. In these cases, it would be easier to automate estimation of the location of the front surface of the object, and therefore to obtain velocity vectors within the forward (yellow) region of the visual hull.

3.8 Application: Fish

In the current work, the visual hull technique is applied to mask fish within tomographic PIV images, since the fish could introduce erroneous reconstruction artifacts. If the artifacts caused by the fish are not masked, fluid velocity vectors derived near the object may be contaminated such that they are biased or completely erroneous.

Figure 3-18 shows a schematic process employed to obtain the visual hull of a fish. Figure 3-18a includes the four images acquired from the cameras. The silhouette of the fish within each field of view (figure 3-18b) was extracted using the image processing sequence suggested in section 3.4. After that, these silhouettes were back-projected using the DaVis 8.0 multiplicative line-of-sight (MLOS) operation, to obtain the visual hull (figure 3-18c) which constituted the 3-D mask applied to the reconstructed measurement volume. Sub-volumes within pairs of masked reconstructed fields were then correlated to obtain fluid velocity vectors. For purposes of integration within plots of velocity vector fields, the voxels within the visual hull volume were placed into a Cartesian grid within Tecplot® with sub-volumes. This corresponded with the velocity vector grid spacing. If 50% or more of a sub-volume was occupied, this sub-volume was included in the visual representation of the hull. Throughout Experiments (1) and (3), an in-line arrangement (i.e. fish approaching in x and y-direction) of the food and fish was preferred, as another approach direction (e.g. negative z-direction) might result in a visual hull volume that obscured the region near the fish mouth.

The shape of the visual hull is highly dependent on the shape of the fish, orientation of the fish (i.e. direction of approach into the illuminated volume), and the camera arrangement. Since the camera arrangement and the fish shape used in the present work are constant, only the direction of approach of the fish into the illuminated volume influences the construction of the visual hull and the region where velocity vectors can be resolved. Figure 3-19 shows examples of a fish entering the illuminated volume parallel to the (a) x-y plane and (b) y-z plane. From the figure, it is observed that the fish travelling parallel to the y-z plane (figure 3-19b) creates a visual hull with a larger volume in front of the fish mouth as compared to the fish travelling parallel to the x-y

plane (figure 3-19a). Although the volume in front of the fish mouth is visible in figure 3-19b (raw image), the back-projection of the silhouette from the camera images causes the visual hull to form in front of the fish mouth. This visual hull is then used to mask the velocity vectors in that volume. The significant fluid volume masked in figure 3-19b is obviously problematic for understanding velocities near the mouth. In contrast, the visual hull created when the fish is approaching from the x-y plane (figure 3-19a) makes a tighter fit to the mouth of the fish, thus, providing more vectors in that region. Based on this observation, only results with fish trajectories orientated near the x-y plane were analyzed for this study.

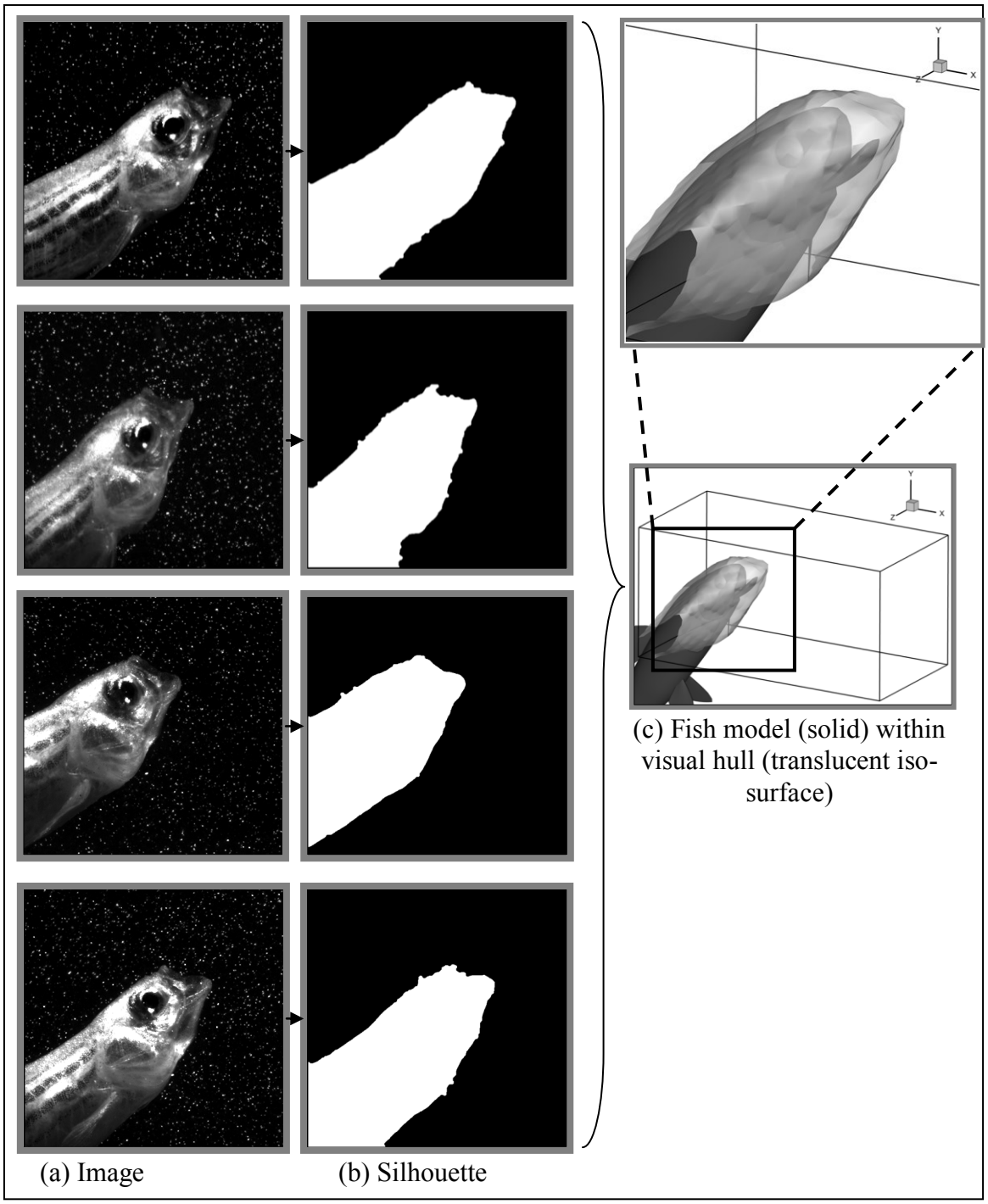

Figure 3-18 Processing sequence from (a) image to (b) silhouette to (c) visual hull of the fish (translucent iso-surface).

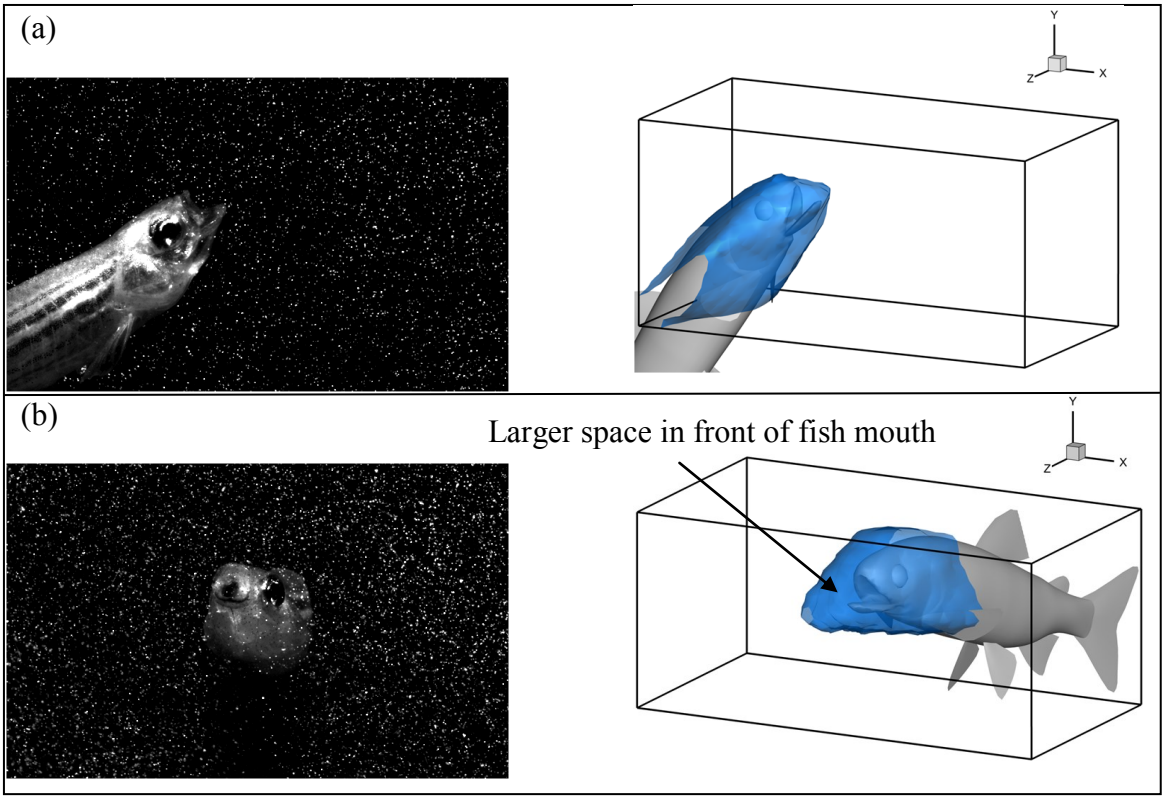

Figure 3-19: Schematic representation of the various approaches of fish into the measurement volume. (a) Fish enters from the side of the measurement volume (parallel to x-y plane); (b) fish enters the back of the volume (parallel to y-z plane).

Chapter 4

Results and Analysis

This chapter presents and discusses the results obtained for Experiment (1): Copepod interaction with wall-mounted cylinder in cross-flow, Experiment (2): Predator-prey interaction in still water, and Experiment (3): Predator-prey interaction in unsteady/turbulent flow. They will be presented in Sections 4.1, 4.2, and 4.3, respectively.

4.1 Experiment (1): Copepod interaction with wall-mounted cylinder in cross-flow

Parts of Section 4.1.2 are taken from:
Adhikari D, Hallberg M, Longmire E "Simultaneous 3D PTV and infrared tomographic PIV measurement of zooplankton distribution in unsteady flow fields" 10th Int Symp on Particle Image Velocimetry, Delft, The Netherlands (2013)

4.1.1 Upstream of cylinder

This section discusses the jumps initiated by copepods approaching a cylinder mounted on the water channel floor from upstream.

4.1.1.1 Detecting copepod jumps

Figure 4-1(a) shows an example of tracks of the copepods appearing within the field of view over a time sequence of 40 seconds with $U_0 = 0.77$ m/s. The copepods are observed to move steadily and at uniform velocity upstream of the cylinder, but their tracks are disorganized downstream of the cylinder due to the wake flow. An end-on observation upstream of the cylinder reveals multiple copepods executing high-speed jumps (see insert 4-1a). This shows that copepods initiate a jump as they approach the cylinder. The copepods jump with a z-direction velocity away from the cylinder (denoted by dotted ellipses). These jumps are identified based on the spacing of neighboring spheres in the plotted tracks.

Each copepod was identified and tracked, and an identity (ID) number corresponding to each copepod track was generated by using an open-source code (adapted from Blair and Dufresne 2013). In figure 4-1(b), a given contour shade on the spheres represents the ID number for each copepod.

Based on tracks such as those in figure 4-1(b), an algorithm was developed to detect instances of copepod jumps. This detection was carried out using speed thresholds where a change in copepod speed of more than 15% between consecutive time steps (Δt = 6.06 or 9.09 ms) was considered a jump. Figure 4-1c shows all of the tracks that contain jumps, and the location where the jump was initiated is denoted by a circle. In some cases, a copepod executed more than one jump within the track upstream of the cylinder. Tracks downstream of the cylinder were not analyzed in this section.

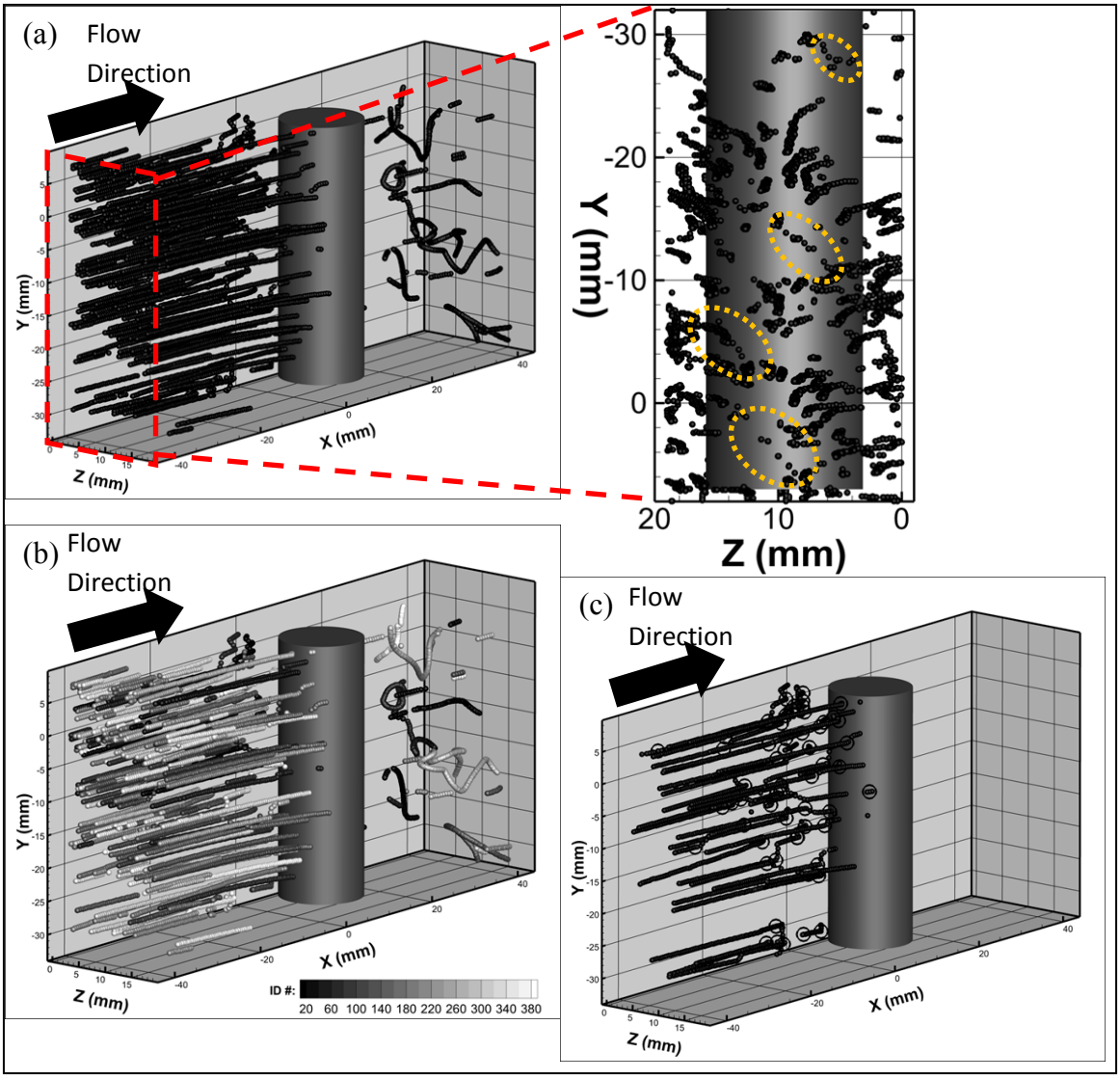

Figure 4-1: Copepod tracks upstream and downstream of the cylinder where U_0 = 0.77 m/s. (a) shows the original tracks where the copepods are observed to execute high-speed jumps upstream of the cylinder (insert), (b) shows the contours on the tracks depicting the ID number of the copepod, and (c) shows only those upstream tracks that include jumps. The circles in (c) represent the locations where the jumps were initiated.

Upstream interactions were investigated for the four cases tabulated in table 4-1. Cases 1 and 2 have the same free stream velocity, but different cylinder diameters. Cases 2, 3, and 4 have different free stream velocities, but the same cylinder diameter. Note that

Reynolds number, based on cylinder diameter and free stream velocity, progressively increases from Case 1 to 4.

Table 4-1: Experimental cases carried out for copepod interaction with cylinder (upstream)

Case	Cylinder diameter, d_c (mm)	Free stream velocity, U_0 (m/s)	Reynolds number, $Re = U_0 d_c/\upsilon$
1	6.35	0.038	230
2	12.7	0.038	460
3	12.7	0.077	930
4	12.7	0.115	1460

4.1.1.2 Copepod 'jump' locations

Figure 4-2 shows the distribution (in x-z projection) of jump locations upstream of the cylinder. Figures 4-2 (a), (b), (c) and (d) correspond to Cases 1, 2, 3 and 4 (see table 4-1), respectively. The origins for these figures are situated at the center of the cylinder. It should be noted that spanwise distributions are overlapped about z = 0 mm (considering symmetry of flow upstream of the cylinder), so that the z-axis represents a magnitude of spanwise offset.

The total number of tracks obtained for Cases 1 – 4 was 166, 91, 323, and 397, respectively. Not every copepod (or 'particle') approaching the cylinder executed an escape response (as observed in figure 4-1c). For the copepods that jumped, the total number counted for Cases 1 – 4 was 75, 39, 156, and 178, respectively

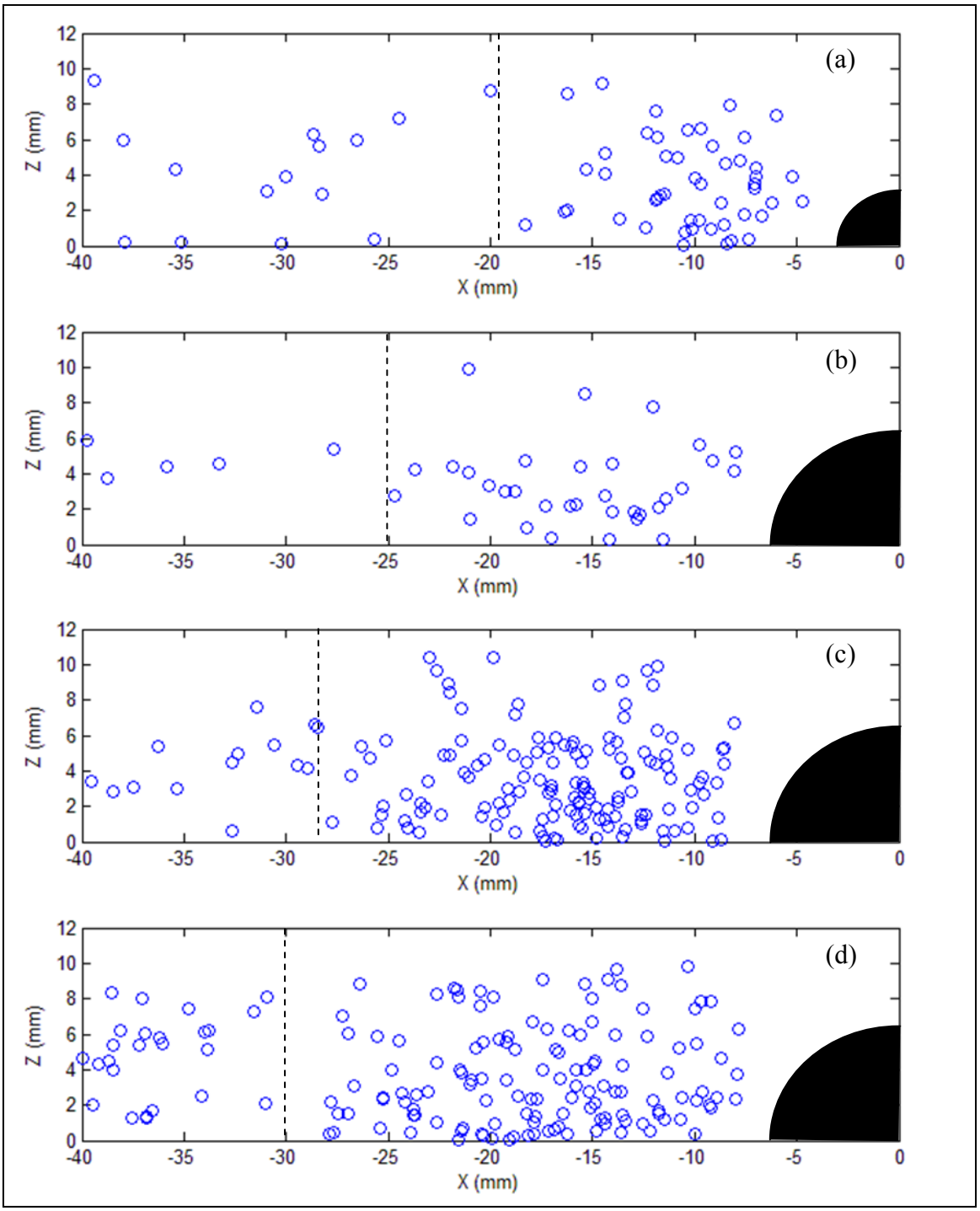

Figure 4-2: Locations where high-speed jumps were initiated. (a)-(d) represent Cases 1 – 4 (see table 4-1). The dashed line represents the cut-off location upstream of which behavior was not included for further analysis.

From figure 4-2, more copepod jumps are observed as the copepods get close to the cylinder. This suggests that copepods do respond to the flow disturbance upstream of the cylinder. At larger upstream distances, x < ~ -20 mm, jump locations appear scattered and less frequent for all cases. Since these jump locations are sporadic, it is assumed that these copepod jumps were not caused by the cylinder or related flow disturbances. Thus, upstream cut-off locations at x = -19 mm, -25 mm, -28 mm, -30 mm were established for cases 1 – 4, respectively (see dashed lines). Only jump locations downstream of the dashed lines are assumed as possible responses to the cylinder. After these cut-offs, the number of jumps counted for cases 1 – 4 was 49, 33, 138, and 130, respectively. Table 4-2 summarizes the number of copepod tracks, total number of jumps and the number of jumps after cut-off.

Table 4-2: Summary of the number of copepod tracks, total number of jumps and number of jumps after cut-off for cases 1 – 4.

Case	Total number of tracks	Total number of jumps	Number of jumps after cut-off
1	166	75	49
2	91	39	33
3	323	156	138
4	397	178	130

4.1.1.3 Copepod sensing

Velocity Gradients

Copepods are thought to respond to fluid velocity gradients (e.g. Kiørboe *et al.* 1999). For time-resolved volumetric velocity fields, velocity gradients can be expressed as a complete velocity gradient tensor ($\nabla \boldsymbol{u}$) or Lagrangian acceleration ($d\boldsymbol{u}/dt$).

The velocity gradient tensor is a 2nd order tensor, which can be divided into a symmetric deformation tensor ($0.5(\nabla \boldsymbol{u} + (\nabla \boldsymbol{u})^T$) and anti-symmetric rotation tensor ($0.5(\nabla \boldsymbol{u} - (\nabla \boldsymbol{u})^T$).

The derivation of an invariant quantity, maximum principal strain rate (or MPSR), from the deformation tensor has been described in Section 1.2.1.1.

For the anti-symmetric rotation tensor, $\boldsymbol{\Omega}$, the expression is given as:

$$\boldsymbol{\Omega} = 0.5(\nabla \boldsymbol{u} - (\nabla \boldsymbol{u})^T) = \begin{bmatrix} 0 & \frac{1}{2}\left(\frac{\partial u}{\partial y} - \frac{\partial v}{\partial x}\right) & \frac{1}{2}\left(\frac{\partial u}{\partial z} - \frac{\partial w}{\partial x}\right) \\ \frac{1}{2}\left(\frac{\partial v}{\partial x} - \frac{\partial u}{\partial y}\right) & 0 & \frac{1}{2}\left(\frac{\partial v}{\partial z} - \frac{\partial w}{\partial y}\right) \\ \frac{1}{2}\left(\frac{\partial w}{\partial x} - \frac{\partial u}{\partial z}\right) & \frac{1}{2}\left(\frac{\partial w}{\partial y} - \frac{\partial v}{\partial z}\right) & 0 \end{bmatrix}$$

$$= \frac{1}{2}\begin{bmatrix} 0 & -\omega_z & \omega_y \\ \omega_z & 0 & -\omega_x \\ -\omega_y & \omega_x & 0 \end{bmatrix} \quad (4\text{-}1)$$

where ω_x, ω_y, ω_z are the x, y, z components of vorticity, respectively. The magnitude of vorticity, given by

$$\|\omega\| = \sqrt{{\omega_x}^2 + {\omega_y}^2 + {\omega_z}^2} \quad (4\text{-}2)$$

is also invariant to the coordinate system.

Assuming the copepod drifts with a fluid element, the temporal velocity gradient of the flow field affecting the copepod is the Lagrangian acceleration. The equation for this acceleration, along the path of the copepod, is given as:

$$\frac{d\boldsymbol{u}}{dt} = \frac{\partial \boldsymbol{u}}{\partial t} + \boldsymbol{u} \cdot \nabla \boldsymbol{u} \quad (4\text{-}3)$$

where $\boldsymbol{u}$ is the local velocity of the fluid.

Thus, the effects on copepod sensing due to MPSR, vorticity, and acceleration can be investigated. Each of these quantities can be obtained at the location of the copepod jump using the Taylor-series least-square method (described in Section 2.3.2.5).

Results and Discussion

Figure 4-3 shows the probability distribution of MPSR at copepod jump locations for Cases 1 – 4 (see table 4-1). Figure 4-4 shows the corresponding probability distribution of MPSR in the entire fluid field upstream of the cylinder. It can be observed that the MPSR distributions in figure 4-3 appear different to those figure 4-4. For instance, figure 4-4 shows that MPSR values the fluid fall mostly in the range 0 – 0.15 s^{-1} (up to 90% for figure 4-4a), but figure 4-3 shows that copepods do not respond to smaller MPSR values (noted by the gap in the bar graph near the origin).

From figure 4-3, the distribution of MPSR appears similar for Cases 1 and 2 (different cylinder diameter), with a few isolated instances of MPSR > 5 s^{-1} observed for Case 1. However, the range of MPSR increases from Cases 2 – 4 (increasing free stream velocity), which suggests that the copepods respond to a larger range of MPSR as the velocity of the free stream increases and the distribution of MPSR broadens. Cases 2 – 4 also show that the minimum value at which the copepods respond to MPSR increases with free stream velocity. Nevertheless, the dominant values of MPSR remain < 5 s^{-1} for all cases. A few instances of copepods responding to high values > 10 s^{-1} are observed in Cases 1, 3, and 4.

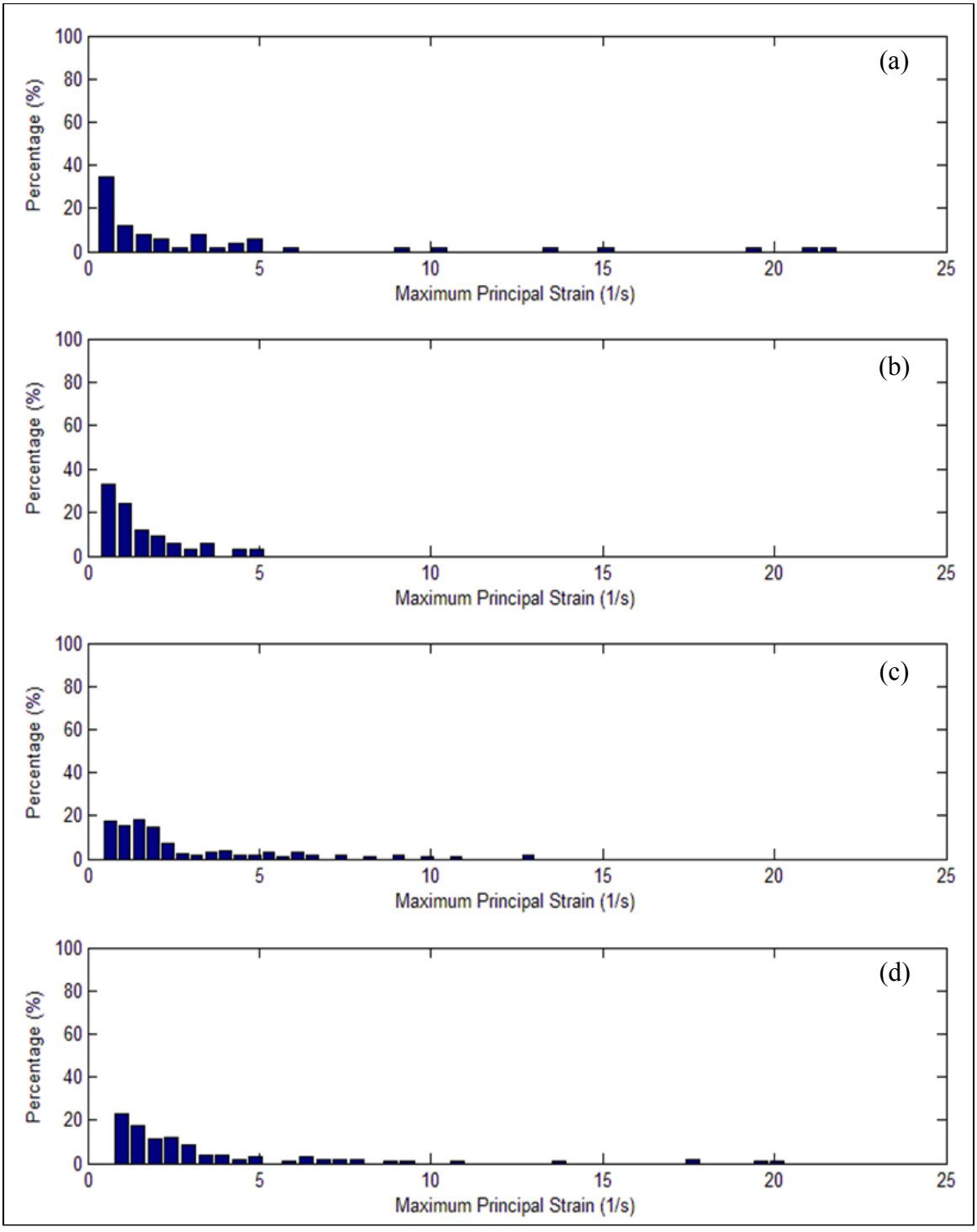

Figure 4-3:Probability distribution of the maximum principal strain rate (MPSR) of fluid at the location where a copepod jump was initiated. (a)-(d) represent cases 1 – 4 (see table 4-1)

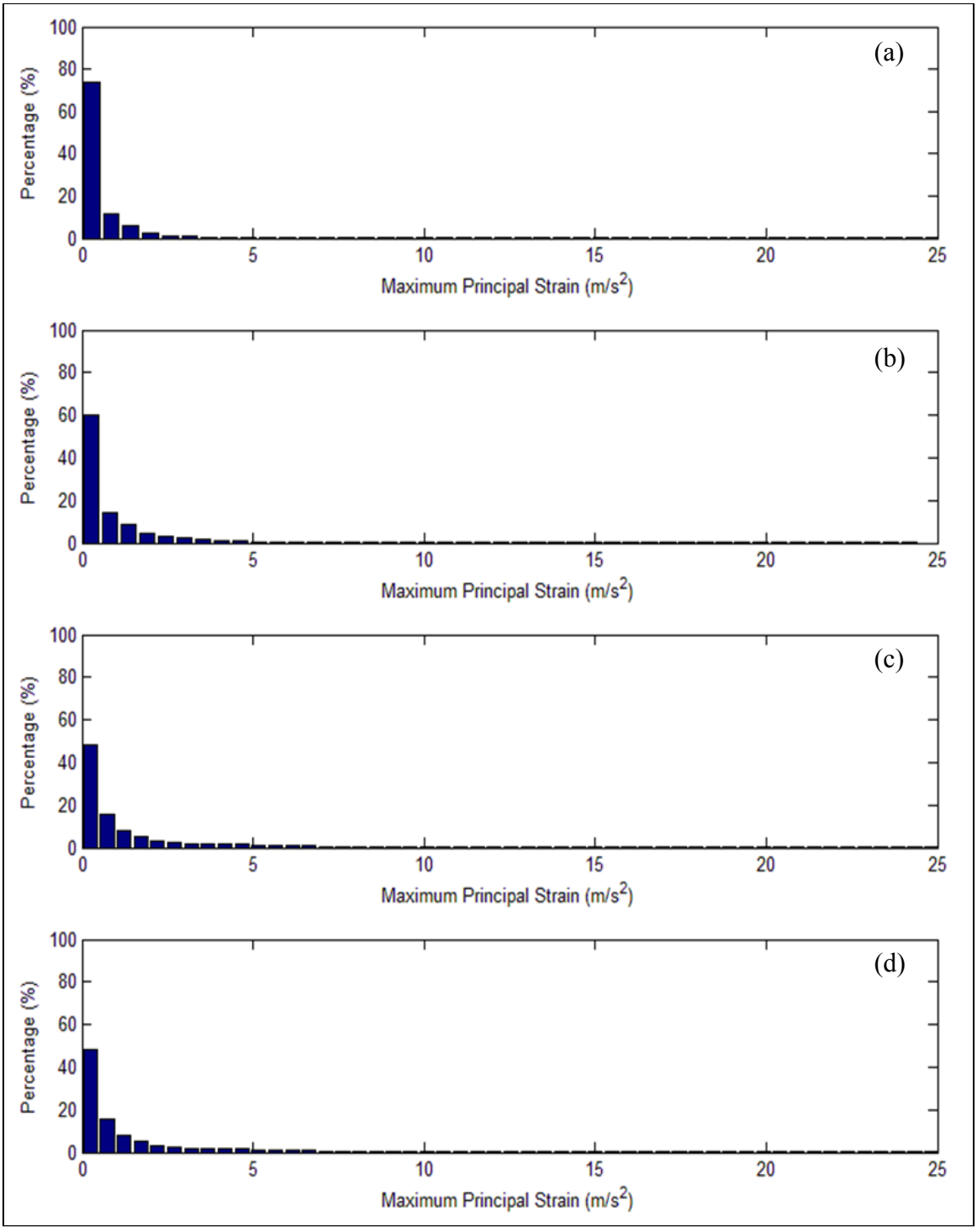

Figure 4-4: Probability distribution of MPSR of fluid upstream of the cylinder. (a)-(d) represents cases 1 – 4 (see table 4-1).

In figure 4-3, the range of values for MPSR at jump locations appears similar to that reported by Kiørboe *et al.* (1999), where they reported minimum possible values of strain rate ranging from 0.5 – 5 s^{-1}. However, a few instances of copepods responding to MPSR > 10 s^{-1} observed herein are consistent with existence of higher ranges of strain rate values reported by Buskey *et al.* (2002) (0.4 - 12 s^{-1}) and Fields and Yen (1996, 1997) (1.5 - 51.5 s^{-1}). From figure 4-3, the probability of copepods responding to MPSR values > 10 s^{-1} is 10%, 0%, 2%, and 4.5% for Cases 1, 2, 3 and 4, respectively. This shows that, although MPSR values > 10 s^{-1} may occur, the probability of copepods responding to these values is relatively low for the cases studied.

Vorticity magnitude distributions are shown in figure 4-5. The peak value of the distribution is 60 – 80% for vorticity values ranging from 0 – 0.3 s^{-1} for all cases. The distribution does not vary significantly in all cases, thus results do not appear to show a trend or thresholds for copepods to jump. Furthermore, the dominant values of vorticity (0 – 0.3 s^{-1}) are generally less than MPSR (0.5 – 5 s^{-1}) (figure 4-5).

Figure 4-6 shows the vorticity distribution of the entire volumetric fluid velocity field upstream of the cylinder for the four cases. The peak value of the distribution is 60 – 90% for vorticity values ranging from 0 – 0.3 s^{-1} for all cases. It can be observed that the vorticity distribution in figure 4-6 appears similar to 4-5. This shows that vorticity magnitude distribution at the location of the copepods in figure 4-5 may just be a sample measurement of the flow field upstream of the cylinder. In addition, it should be noted that the vorticity magnitude values are relatively low upstream of the cylinder. Thus, any response of copepods to vorticity magnitude is not conclusive from the current results, although Kiørboe *et al.* (1999) have suggested that copepods do not elicit escape responses based on vorticity magnitude.

Figure 4-7 shows the distribution of the Lagrangian acceleration at the location of copepods for Cases 1 – 4, and figure 4-8 shows the Lagrangian acceleration for the entire volumetric flow velocity field upstream of the cylinder. Like the MPSR distributions (figure 4-3 and 4-4), the acceleration of the flow at the location of the copepods (figure 4-

7) has a different distribution compared to the entire fluid field upstream (figure 4-8). This difference is especially evident with the gap in the bar graph near the origin in figure 4-7(b), (c), and (d). In figure 4-7, the acceleration probability distribution is observed to be similar for Cases 1 and 2, and the distribution range increases with the free stream velocity for Cases 2 – 4. Furthermore, the peak value of the distribution shifts from 0.02 to 1.6 m/s^2 as the free stream velocity increases from 0.038 to 0.115 m/s. In addition as the free stream velocity increases, the probability of dominant acceleration value decreases from 30-40% for Cases 1 and 2, to 13% for Case 4.

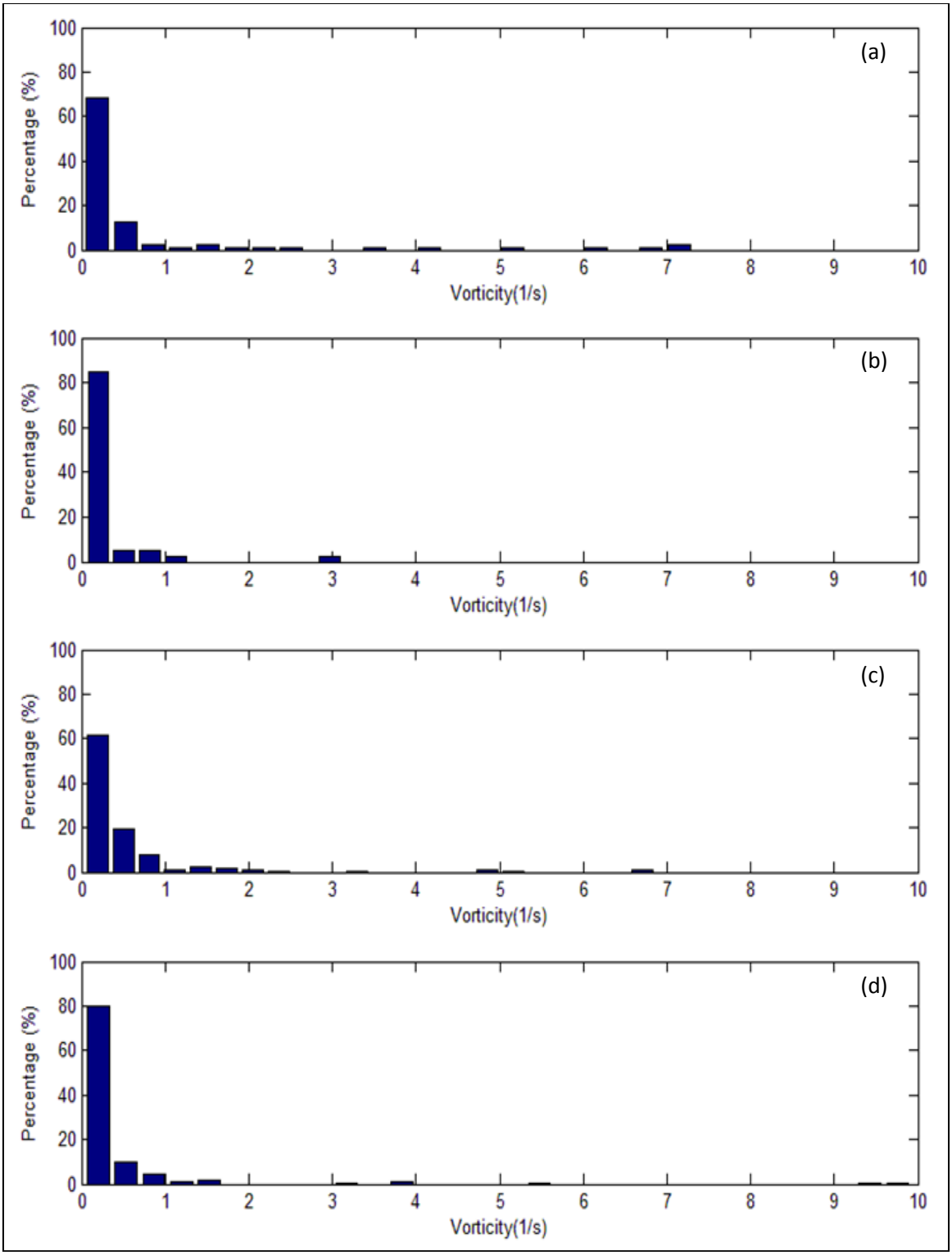

Figure 4-5: Probability distribution of vorticity of fluid at the location where copepod jump was initiated. (a)-(d) represents cases 1 – 4 (see table 4-1)

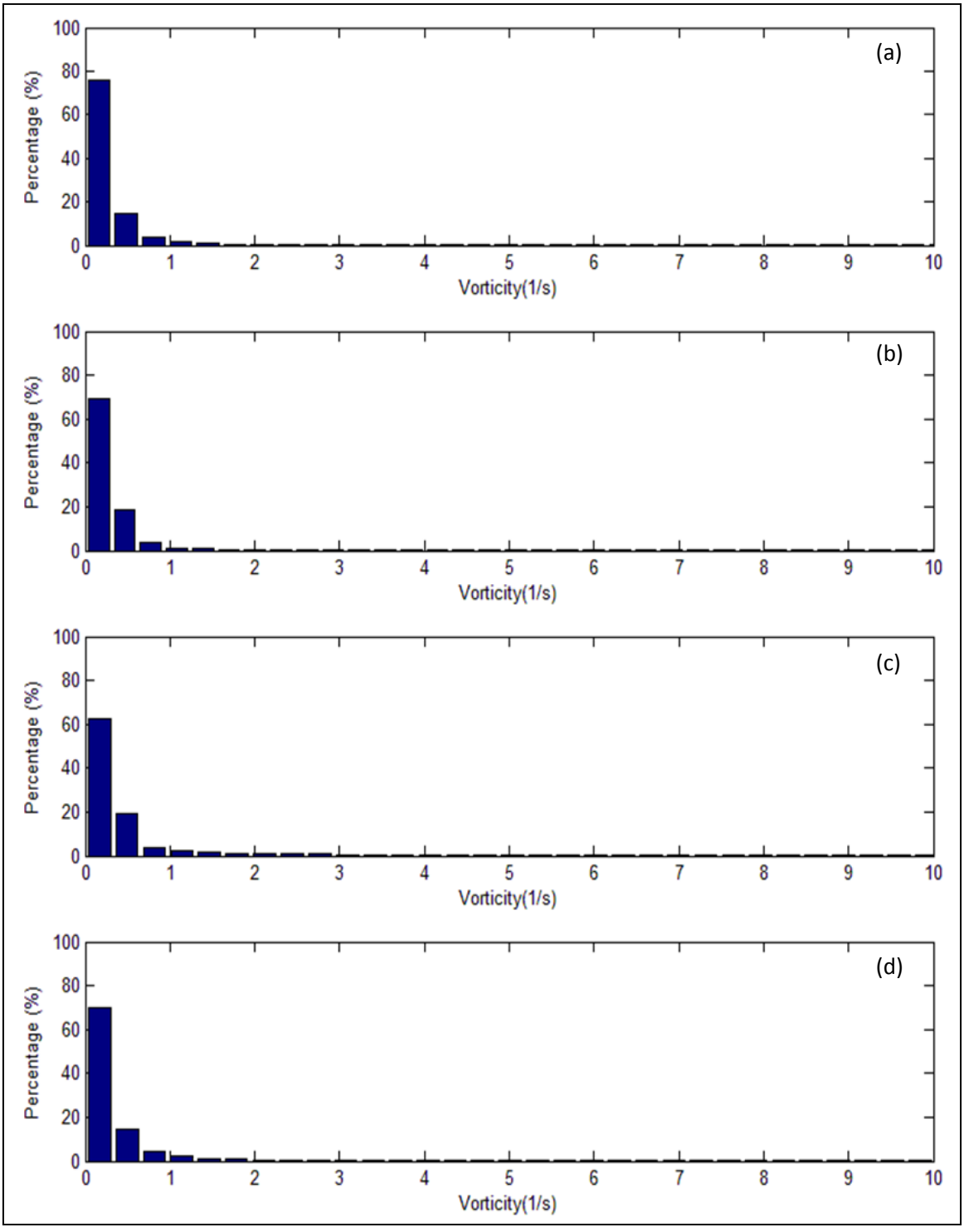

Figure 4-6: Probability distribution of vorticity of fluid upstream of the cylinder. (a)-(d) represents cases 1 – 4 (see table 4-1).

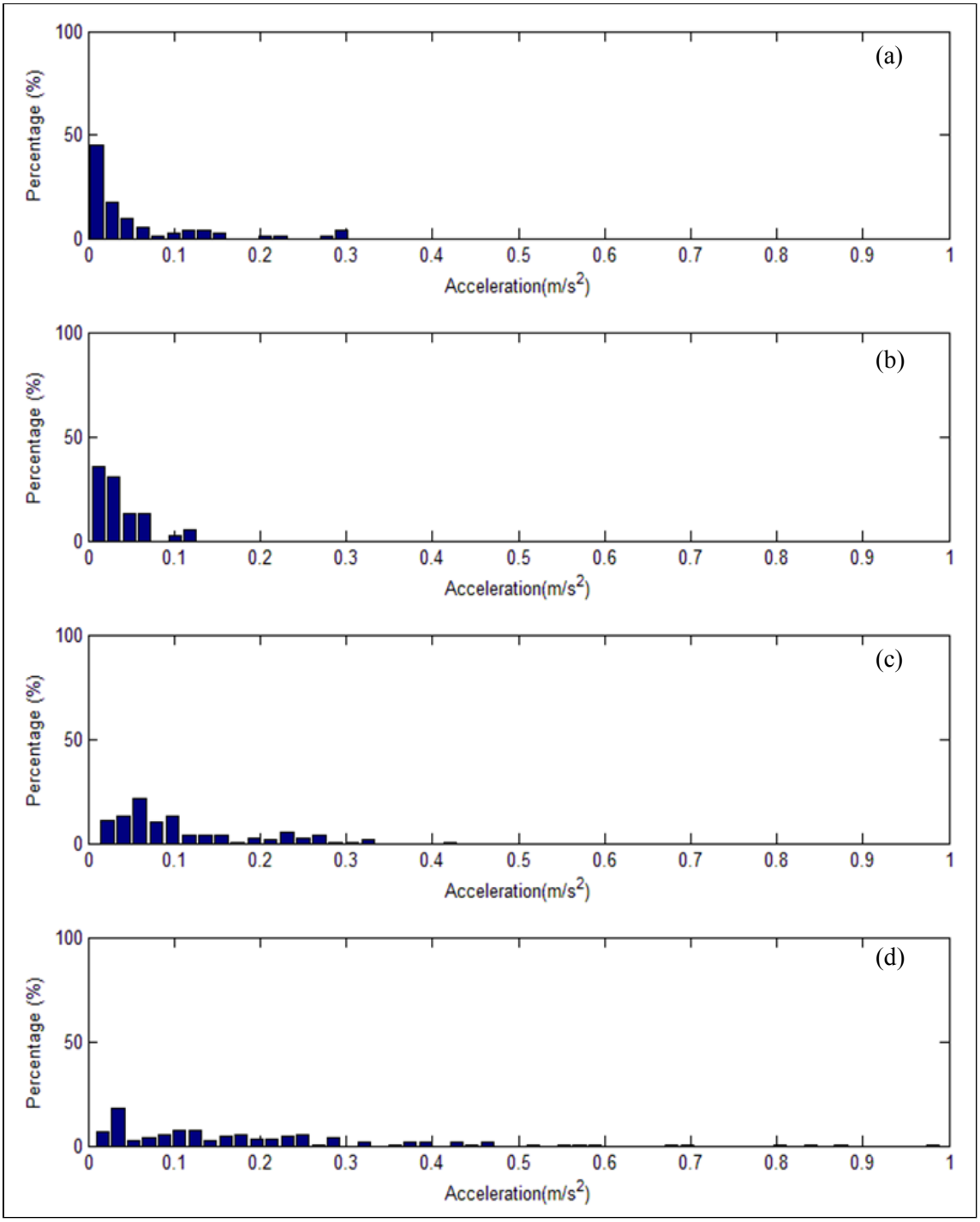

Figure 4-7: Probability distribution of the Lagrangian acceleration of fluid (following the copepod) at the location where copepod jump was initiated. (a)-(d) represents cases 1 – 4 (see table 4-1)

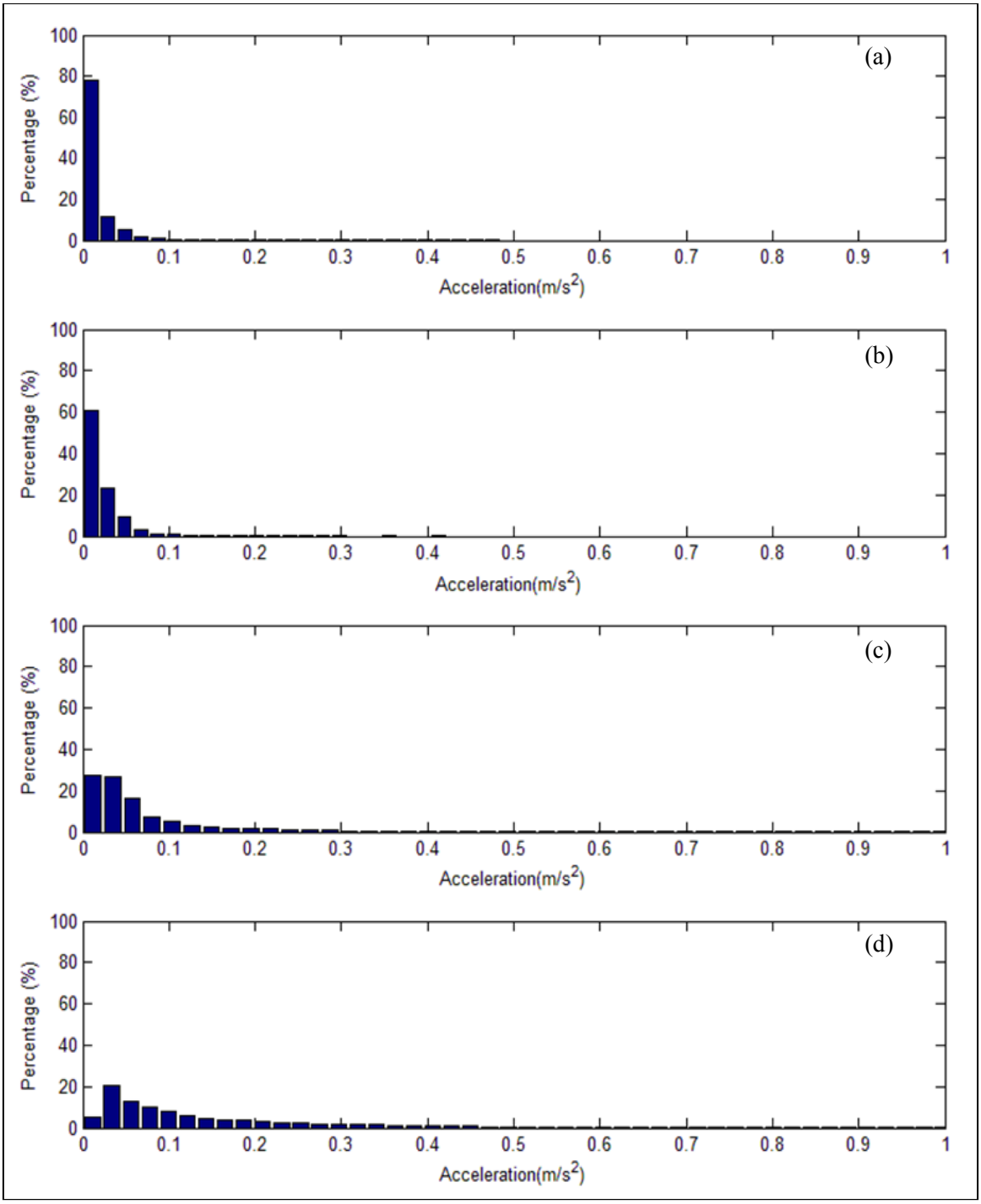

Figure 4-8: Probability distribution of Lagrangian acceleration of fluid upstream of the cylinder. (a)-(d) represents cases 1 – 4 (see table 4-1).

Figures 4-3, 4-5, and 4-7 suggest that MPSR or acceleration is found to trigger copepods to execute a high-speed jump. Copepods respond to increasing range of MPSR and acceleration when the free stream velocity increases. In addition, at higher free stream velocities, copepods appear to be less sensitive to acceleration. However, probability distributions of MPSR and acceleration remain the same when copepods interact with different cylinder sizes.

To understand the current experimental data better, we consider a model of two-dimensional potential flow upstream of a cylinder. The maximum principal strain rate derived for this model ($MPSR_{potential}$) is easily obtained in polar coordinates as:

$$MPSR_{potential} = \frac{2U_0 a^2}{r^3} \tag{4-4}$$

where U_0 is the free stream velocity, a is the radius of cylinder, and r is the radial coordinate from the center of the cylinder. Note that $MPSR_{potential}$ is independent of angular coordinate, θ. Consider a threshold value of $MPSR_{potential}$ required for copepods to initiate a jump, as γ_{max}. Thus, the reaction distance of copepods from the center of the cylinder, $r = r_d$, can be represented in potential flow by manipulating equation 4-4:

$$r_d = \sqrt[3]{\frac{2U_0 a^2}{\gamma_{max}}} \tag{4-5}$$

Equation (4-5) can be used to plot r_d against U_0 (for constant a; figure 4-9a), and r_d against a (for constant U_0; figure 4-9b). Figure 4-9(a) shows curves plotted for γ_{max} = 0.4, 1, 5, and 50 s^{-1}. The reaction distance based on experimental data for Cases 2 – 4 is shown as scatter plots at free stream velocities, U_0 = 0.0384, 0.77, and 0.115 m/s, respectively (see figure 4-9a). The scatter points appear predominantly within γ_{max} = 0.4 – 5 s^{-1}, and this range agrees well with Kiørboe *et al.* (1999). However, figure 4-9(a) also shows that at lower free stream velocities, scatter points are observed to cross the lower threshold bound of γ_{max} (i.e. $\gamma_{max} < 0.4$ s^{-1}), while at higher free stream velocities, the points cross the upper bound (i.e. $\gamma_{max} > 5$ s^{-1}).

Figure 4-9(b) shows equation (4-5) plotted as reaction distance, r_d, against cylinder radius, a, at γ_{max} = 0.15, 0.4, 1, 5, and 50 s^{-1}. The experimental data from Cases 1 – 2 are shown as scatter plots for cylinder radius, a = 3.175 mm and 6.35 mm, respectively. From the figure, for both experimental cases, the scatter points appear within γ_{max} = 0.15 – 5 s^{-1}. The lower bound of this range is lower than that obtained for figure 4-9(a).

The results show many instances where copepods jump at very low MPSR values (below those reported by Kiørboe *et al.* 1999) corresponding with significant distances away from the cylinder. Also, in some cases, copepods come very close to the cylinder (where γ_{max} is large) before attempting to escape. From figure 4-9, the reaction distances of the copepods appear to deviate from the potential flow model of MPSR.

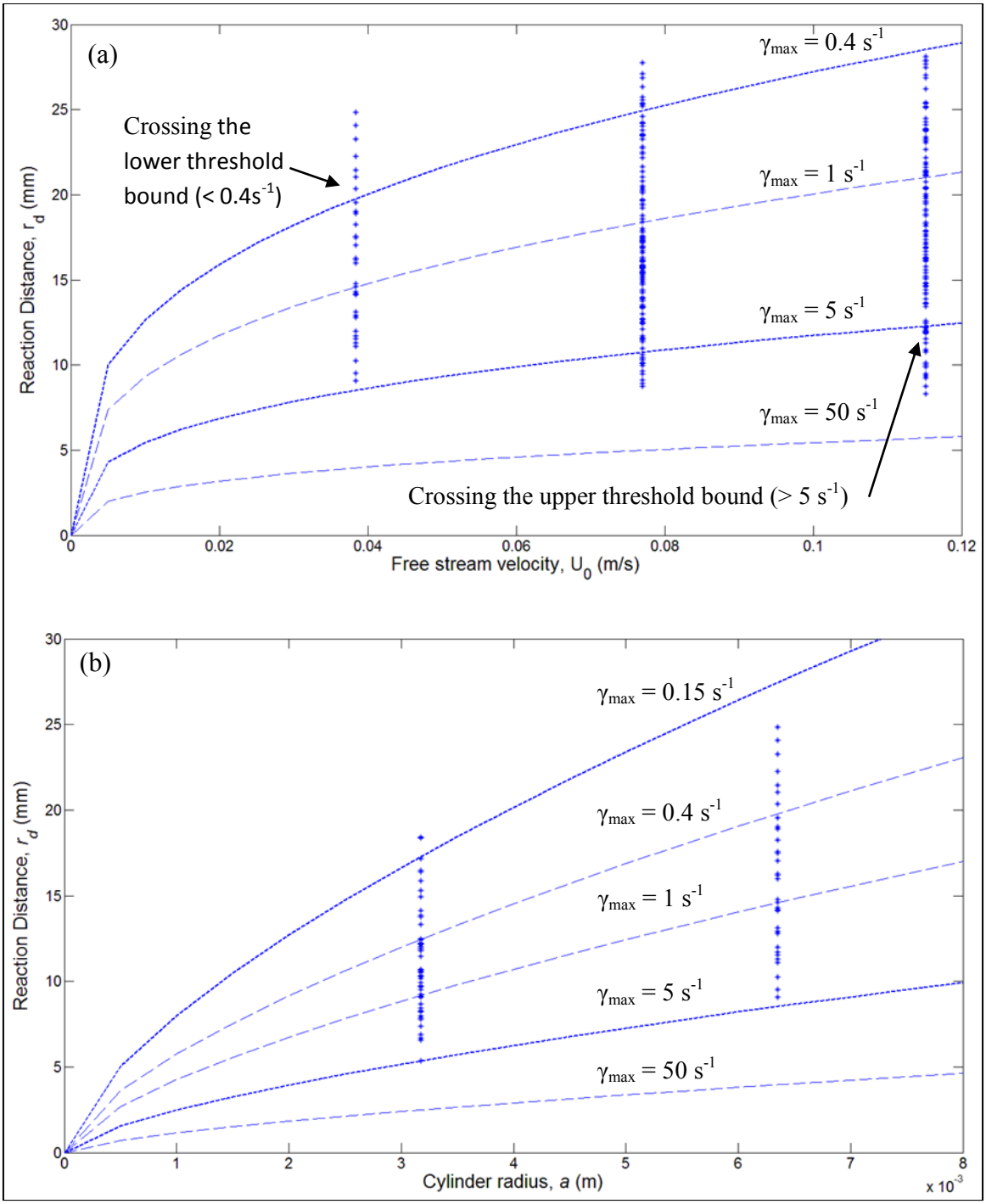

Figure 4-9: Graphs of reaction distance against (a) free stream velocity (cylinder radius maintained at 6.35 mm), and (b) cylinder radius (free stream velocity maintained at 0.0384 m/s). Dashed line curves represent 2D potential flow model, and scatter points represent the experimental values.

Considering a potential flow upstream of the cylinder, the Langrangian acceleration following the copepod path is provided in equation (4-3). Since 2D potential flow upstream of the cylinder is at steady state, $\partial \boldsymbol{u}/\partial t = 0$, the acceleration in equation (4-3) is reduced to:

$$\frac{d\boldsymbol{u}}{dt}_{potential} = \boldsymbol{u} \cdot \boldsymbol{\nabla u} \tag{4-6}$$

where **u** is the local velocity of the fluid. The magnitude of acceleration in equation 4-6 can be derived to give:

$$\left\|\frac{d\boldsymbol{u}}{dt}\right\|_{potential} = \|\boldsymbol{u}\| \frac{2U_0 a^2}{r^3} = \|\boldsymbol{u}\| \times MPSR_{potential} \tag{4-7}$$

where $\|\bullet\|$ is an absolute magnitude of a vector (or l^2 norm). Equation (4-7) shows that for potential flow past a cylinder, the local flow acceleration magnitude is a product of $MPSR_{potential}$ and the magnitude of local flow/copepod velocity, $\|\mathbf{u}\|$. Figure 4-10 shows the graph of acceleration, $\|d\boldsymbol{u}/dt\|$, against $\|\mathbf{u}\| \times$ MPSR. The dashed line in the graph depicts equation (4-7). A scatter plot of the experimental data from Cases 1 – 4 is superposed in the figure.

Although it was discussed earlier that copepods may respond to MPSR or acceleration, this model shows that MPSR and acceleration may not be independent for some conditions. From figure 4-10, at lower accelerations ($\|d\boldsymbol{u}/dt\| < 0.1\ m/s^2$), experimental data points show good agreement with the potential flow model (equation 4-7). At higher accelerations ($\|d\boldsymbol{u}/dt\| > 0.3\ m/s^2$), however, a larger percentage of the experimental data deviates from the dashed line in figure 4-10. The deviation mainly occurs below the dashed line since $\|d\boldsymbol{u}/dt\| \leq \|\boldsymbol{u}\| \times MPSR$ for steady state and irrotational flow (see proof: Appendix D). It is noted that the deviation is more apparent for higher free stream speeds. The deviation in the experimental data from the dashed line (2D potential flow) is a result of different directions of fluid velocity and acceleration. This difference can be due to three-dimensionality of the flow.

For complex, rotational and unsteady flows, this relationship between MPSR and acceleration does not apply, and can bring further complexity to copepod sensing. Copepod distribution and sensing downstream of the wake is discussed in Section 4.1.2.

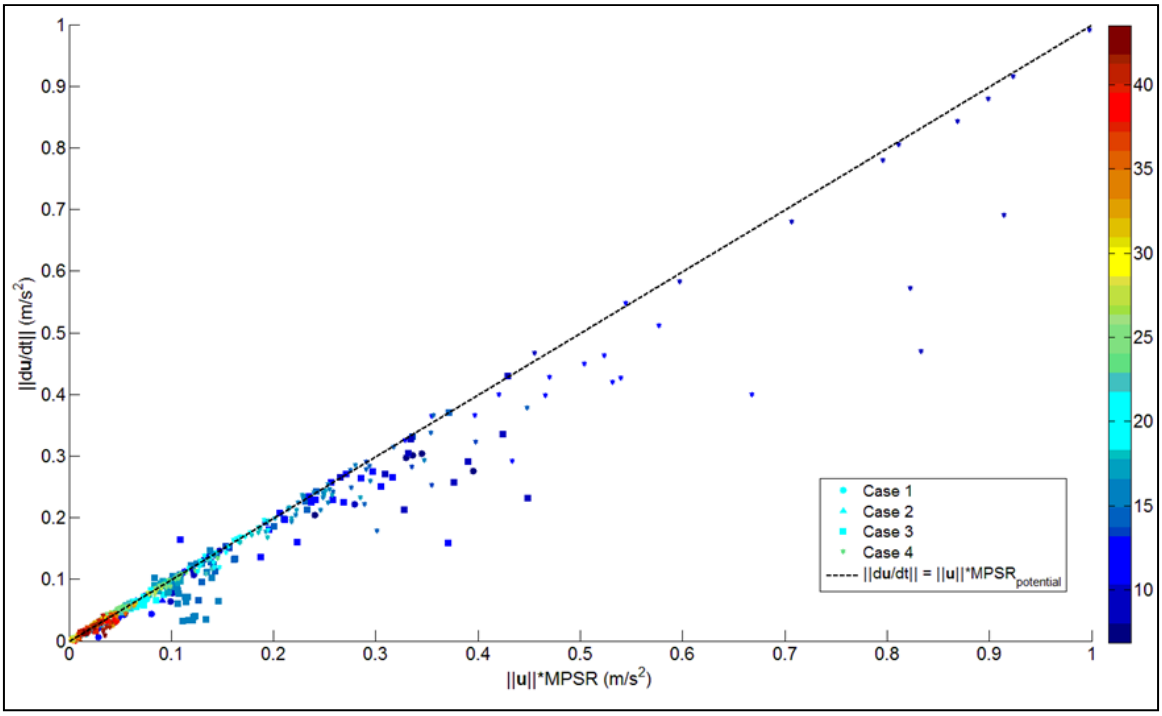

Figure 4-10: Graph of acceleration ($\|d\boldsymbol{u}/dt\|$) against ($\|\boldsymbol{u}\| \times MPSR$). The dashed line is linear relationship derived from 2D potential flow model $\|d\boldsymbol{u}/dt\| = \|\boldsymbol{v}\| \times MPSR_{potential}$. The scattered points represent experimental data: cases 1(●), 2(▲), 3(■), and 4(*). The color contour represents the distance of the copepod from the center of the cylinder in mm.

4.1.1.4 Copepod locomotion

After sensing flow disturbances, copepods execute a high-speed jump. Based on the copepod tracks (see figure 4-1c), the speed-time profiles, maximum speeds and directions of copepod jumps were determined. The speeds and directions of copepod jumps from a fixed frame of reference were obtained by subtracting the local flow velocity at the initial position of the copepod.

Figure 4-11(a) shows speed-time profiles of all copepod jumps obtained in Cases 1 − 4. Although figure 4-11(a) is generally messy due to the myriad of speed-time profiles, a dominant profile is apparent. An approximate dominant speed-time profile is shown in figure 4-11(a) as a thick dashed curve. Most copepods appear to follow this profile. The dominant speed-time profile is schematically represented in figure 4-11b. When copepods execute a high-speed jump, they first accelerate until a maximum speed is reached. This is followed by a rapid deceleration due to drag forces by the surrounding fluid (see figure 4-11b). Two important variables characterizing the speed-time profile of a copepod jump are the total time of jump, t_{jump}, and the maximum speed, v_{max}. Based on the dashed line in figure 4-11(a), the time of jump is t_{jump} = 25-30 ms, and the maximum velocity is v_{max} = 0.065 m/s.

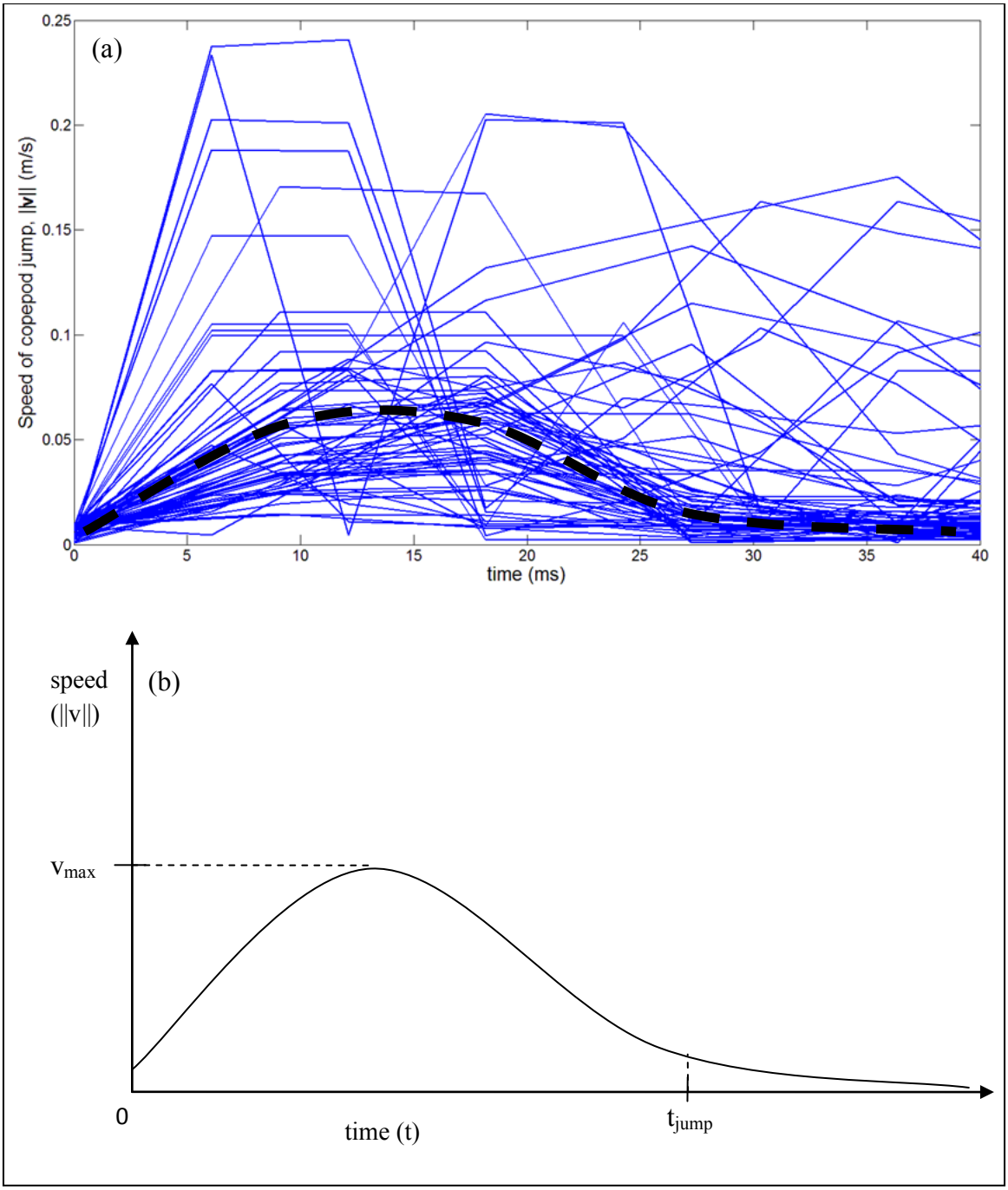

Figure 4-11: Speed relative to the local flow velocity. (a) Experimental and (b) schematic speed-time graph of copepod jump. Dashed curve in (a) represents the outline of the dominant experimental speed-time profile.

Figure 4-12 shows the distributions of maximum speed during the copepod jumps. The dominant maximum speed appears to be 0.06 – 0.07 m/s for all cases. This is consistent with the estimated dominant v_{max} observed in figure 4-11. Furthermore, isolated instances of very high speeds, up to 0.32 m/s are observed in figure 4-12c. The average speed for figures 4-12(a) to (d) is 0.074 m/s, 0.072 m/s, 0.093 m/s, and 0.107 m/s, respectively. On average, the maximum speeds increase with the free stream flow velocity (Cases 2 – 4), while there is no significant difference in the range of jump speeds when the cylinder diameter changes (Cases 1 – 2). These results indicate that copepods may have tendencies to jump at higher speeds when subject to higher free stream velocities.

Buskey *et al.* (2002) reported copepods attaining speeds of up to 0.4 m/s, while Yen (2000) pointed out that copepods can even reach speeds of up to 1 m/s. The current result provides evidence of copepods moving at speeds up to 0.32 m/s (see figure 4-12c). However, these high speeds appear as isolated incidents of copepod response for the cases studied. The results suggest that copepods jump at a broader range of velocities when the free stream velocity increases.

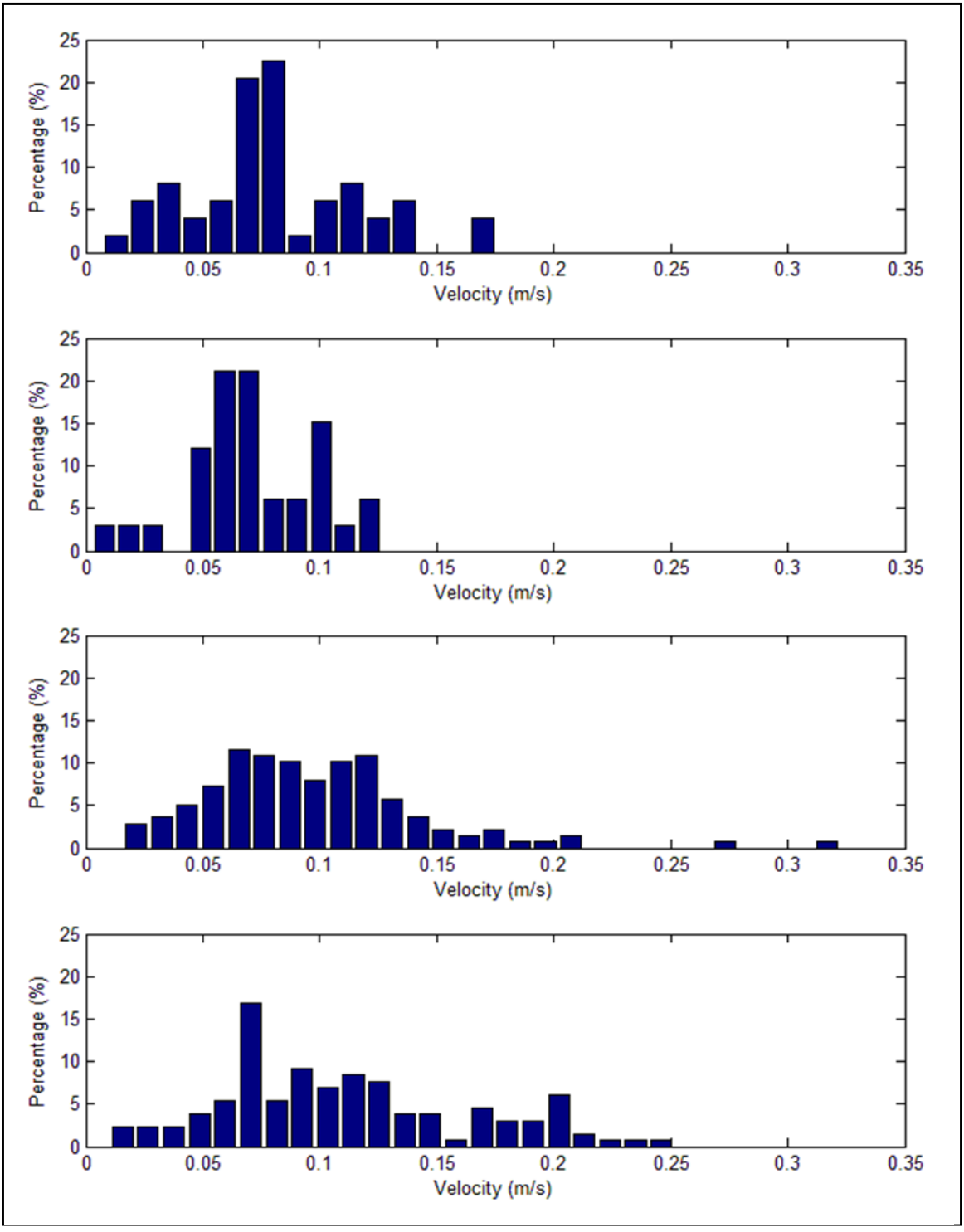

Figure 4-12: Probability distribution of maximum copepod speed during jumps. Speeds are relative to local flow velocity. (a)-(d) represents cases 1 – 4 (see table 4-1)

Next, copepod jump direction is examined. Figures 4-13 and 4-14 show angle histogram plots of the direction of escape from x-y, and x-z perspectives. In figure 4-14, the distribution assumes symmetry about z =0 mm, so that all values are mapped into a 180º range. A schematic representation of the cylinder perspective is shown in the center of each figure. Composite histograms based on all copepods jumps for figures 4-13 (a) – (d) and 4-14 (a) – (d) are provided in figures 4-13(e) and 4-14(e), respectively.

In figure 4-13, copepods are observed to avoid jumping towards the cylinder, since 70% of all copepods are observed to jump in the range of 90˚ – 270˚ (based on total number of copepods in figure 4-13e). Most of the copepods jumping towards the cylinder occur for Case 1 (figure 4-13a), where the size of the cylinder is relatively small. Figure 4-13(e) also shows most copepods jump upwards (i.e. 0˚ – 180˚). Figure 4-14 also shows that about 70% of the copepods are observed to jump to the side and back with angles 90˚ – 150˚ away from the x-axis. This suggests that copepods appear to detect the presence of an object and move away from it at a lateral angle of 90˚ – 150˚ (see figure 4-14).

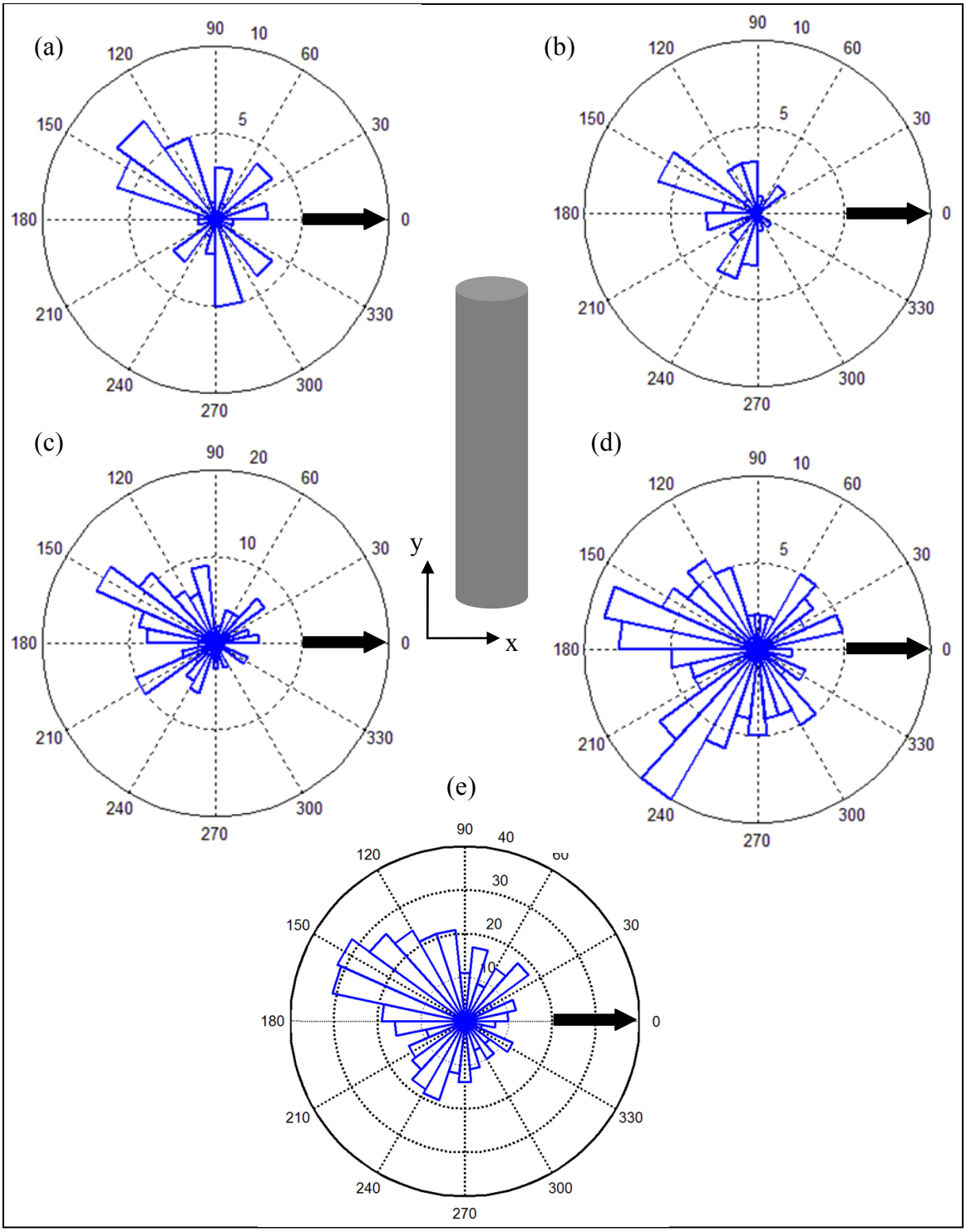

Figure 4-13: Angle histogram (x-y plane) of jump direction of copepod upstream of the cylinder. The cylinder in the middle represents the orientation of the cylinder in this plane. Thick arrows in the plot represent the direction flow. (a)-(d) represent cases 1 – 4 (see table 4-1), (e) represents the total number of copepods from (a)-(d).

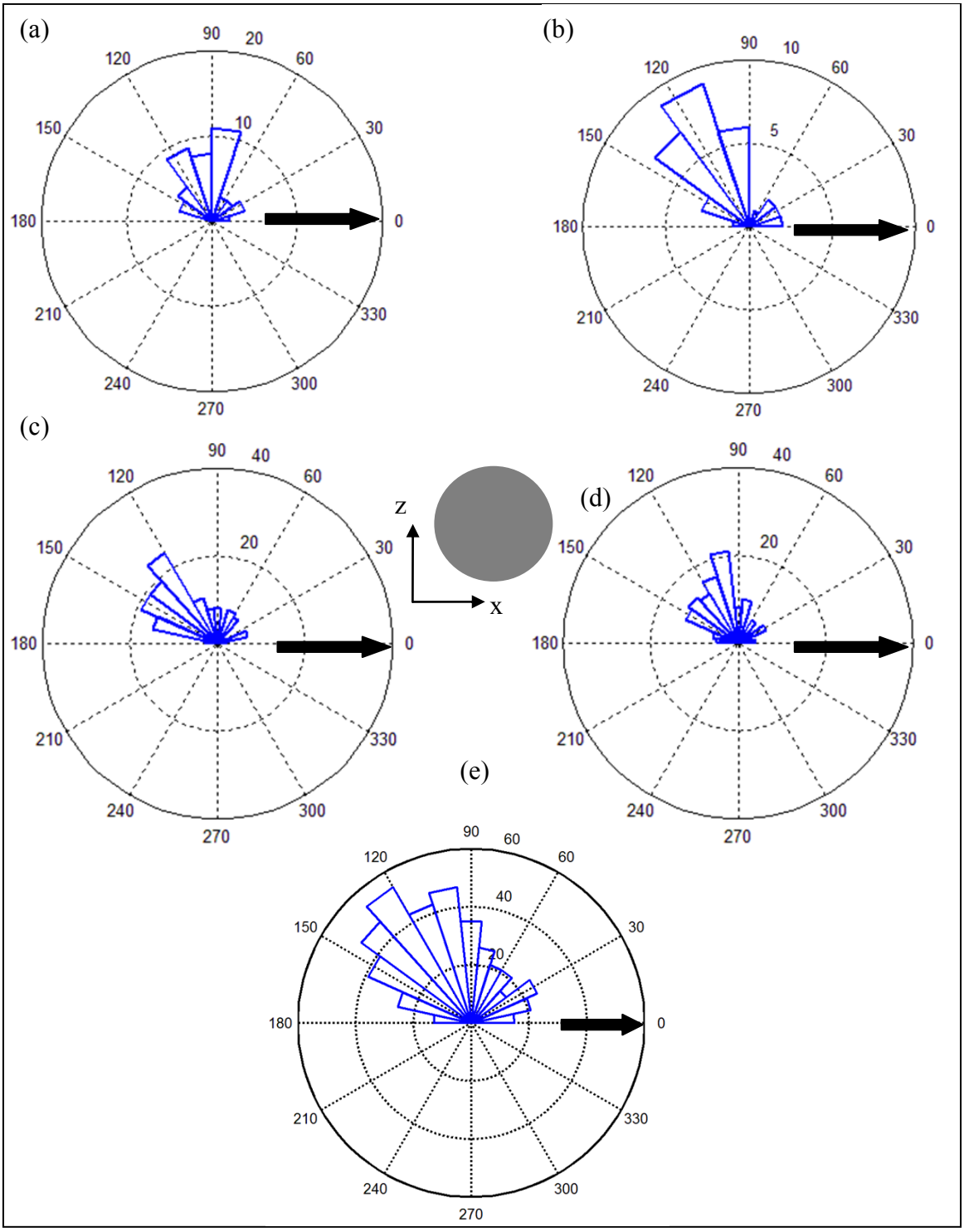

Figure 4-14: Angle histogram (x-z plane) of jump direction of copepod upstream of the cylinder. The cylinder in the middle represents the orientation of the cylinder in this plane. Thick arrows in the plot represent the direction flow.(a)-(d) represents cases 1 – 4 (see table 4-1), (e) represents the total number of copepods from (a)-(d).

4.1.2 Copepod distributions downstream of cylinder

Figure 4-15 shows an example of instantaneous copepod locations amid a surrounding velocity field downstream of the cylinder. The volumetric field includes an iso-surface of vorticity magnitude ($\|\boldsymbol{\omega}\| = 25\ s^{-1}$) with color contours representing total velocity magnitude. The spheres represent copepods. The wake of the cylinder is highly unsteady and is observed to contain coherent flow structures which may influence copepod response.

Conditions with free stream velocity, U_0 = 0.77m/s, and cylinder diameter, d_c = 12.7 mm (same as Case 3), were considered in the study of the influence of wake structures on copepods downstream of the cylinder. Measurements were taken at three different locations in the z-direction: (1) measurement volume directly behind the cylinder (as shown in figure 4-15), (2) volume offset from cylinder axis by 1.5cm in positive z-direction, and (3) volume offset from cylinder axis by 3.0 cm in positive z-direction. Each volume spanned the range of -40 mm < x < 40 mm, -32 mm < y < 8 mm, 0 < z < 19 mm, where the cylinder center is located at x = -80 mm, z = 9.5 mm, and the wall where the cylinder is mounted is located at y = -32 mm. The cylinder spans the entire y-axis. Independent realizations of data (495 datasets) were sampled from time-series image sequences with time interval, Δt = 7.69 ms. Since an instance was considered independent when more than half of the zooplankton in the preceding images moved out of the field of view, every 25th image from a sequence was considered independent (time between independent instances: 192 ms). From the image sets, the positions of all the copepods were recorded. For comparison brine shrimp, which are incapable of executing a high-speed jump, were also investigated, and the distributions are compared.

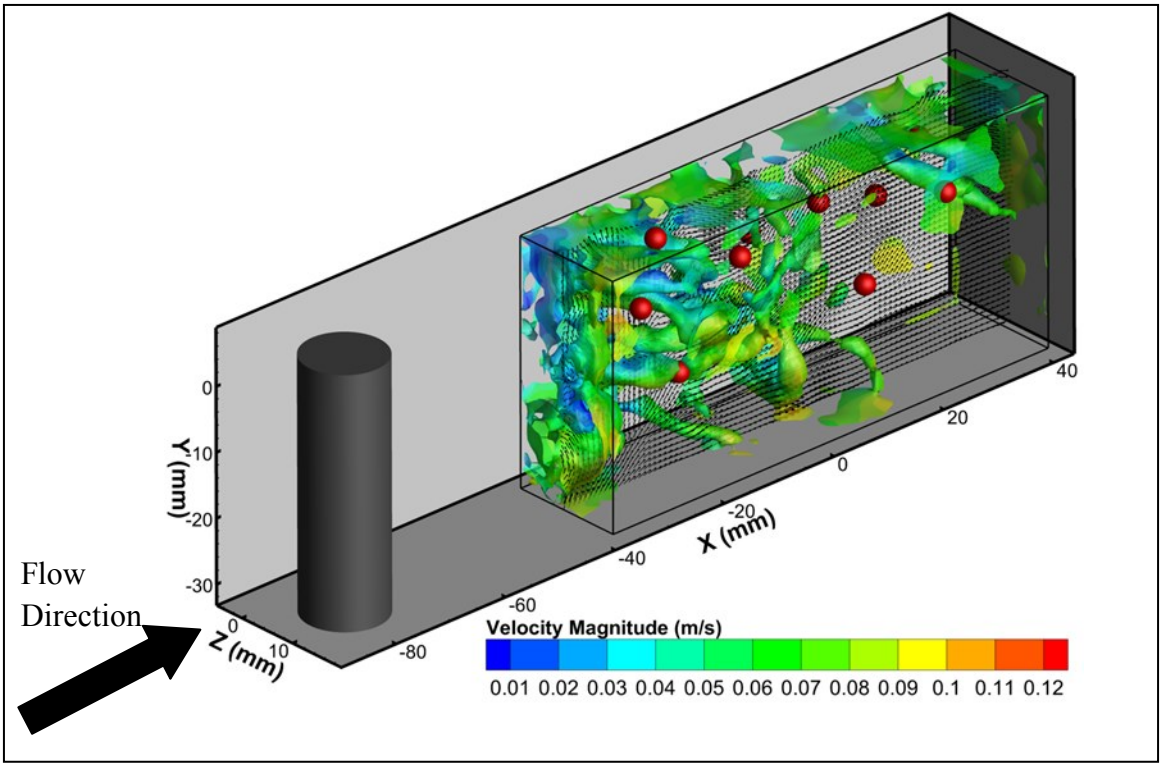

Figure 4-15: Volumetric flow field and copepod distribution behind a vertically mounted cylinder located at x = -80 mm, z = 9.5mm. Height of the cylinder has been truncated for clarity. The vorticity iso-surface is $\|\omega\| = 25\ s^{-1}$.

4.1.2.1 Stokes number and hypothesis

The inertial Stokes number for both copepods and brine shrimp (when not actively moving) was estimated as $Sk \sim 0.3$ with respect to the largest estimated eddy behind the cylinder. Without active motion, both zooplankton were therefore influenced in a similar manner by eddies. Here, the Stokes number is defined as:

$$Sk = \frac{\tau_p}{\tau_f}\ ; \tau_p = \frac{\rho_p {d_p}^2}{18\rho_f \upsilon_f};\ \tau_f = \frac{d_c}{U_0}, \tag{4-9}$$

where ρ_p is the density of the zooplankton, ρ_f is the density of the fluid, d_p is the length of the zooplankton, v_f is the kinematic viscosity of the fluid, d_c is the diameter of the cylinder and U_0 is the free stream velocity.

The Stokes number above indicates that passive motions of both species can be influenced significantly by the largest eddies. However, previous work and findings from Section 4.1.1 suggest that when a copepod senses certain local velocity gradient characteristics, it can respond actively with high acceleration and slip velocity. Thus, we hypothesize that the spatial distribution of copepods downstream of the cylinder may differ from that of the brine shrimp.

4.1.2.2 Copepod spatial distribution and sensing

Figure 4-16 shows graphs of zooplankton count against z-direction based on all of the independent data sets. A total of 4916 brine shrimp and 9215 copepods were counted. Thus, for better comparison, the count was normalized using the average number density of each zooplankton across the z-direction. From figure 4-16(a), the brine shrimp appear to be distributed evenly across the z-direction even with the presence of the cylinder. However, there are ~14% fewer copepods (figure 4-16b) present directly behind the cylinder as compared to away from the cylinder. This must be due to 'active' behavior of copepods and could be caused by strong velocity gradients either upstream of the cylinder or downstream in the wake of the cylinder.

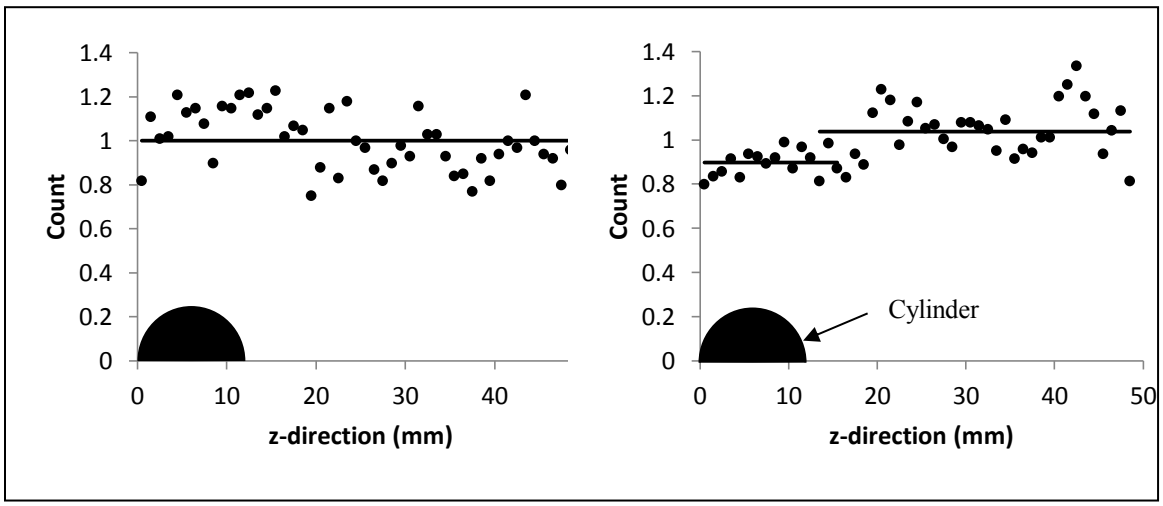

Figure 4-16: Zooplankton count against z-direction for (a) brine shrimp and (b) copepods. The count has been normalized with the average value of the respective zooplankton for clarity in comparison. Counts at each z location include all x and y locations within the field of view (i.e. -40 mm < x < 40 mm; -32 mm < y < 8 mm).

Figures 4-17 show the distribution of local maximum principal strain rate at the location of brine shrimp, and copepods, respectively. The measurements were taken directly behind the cylinder (over z = 0 mm to 19 mm; figures 4-17a), 15 mm offset from cylinder axis (over z = 15 mm to 34 mm; figures 4-17b), and 30 mm offset from cylinder axis (over z = 34 mm to 53 mm; figures 4-17c). From the figures, the distributions of both brine shrimp and copepods are very similar. Directly behind the cylinder (figures 4-17a), the MPSR value ranges from 0 to ~25 s^{-1} with a peak at ~8 s^{-1}. Moreover a very high percentage of the distribution is higher than γ_{max} = 0.4 s^{-1}, the predominant jumping threshold obtained upstream of the cylinder (see Section 4.1.1). Thus, in the cylinder wake the copepods appear to stay within these high strain rate regions rather than move toward lower strain regions. Time series video based on 3D PTV as well as direct observation showed that very few of the copepods exhibited jumps while in the wake of the cylinder. This suggests that the maximum principal strain rate downstream of the cylinder is probably not responsible for the uneven distribution of copepods shown in figure 4-16. Thus, the cause of the uneven distribution likely results from their behavior upstream of the cylinder.

Figure 4-18 shows tracks of the (a) brine shrimp and (b) copepods upstream and downstream of the cylinder as determined from time sequences. Both zooplanktons appear to move steadily with the upstream flow, while their paths are disorganized in the wake of the cylinder. However, the end-on views of the upstream paths for brine shrimp and copepods show a difference. In figure 4-18(a) insert, the brine shrimp appear to move steadily with the flow upstream. However, in figure 4-18(b) (also observed previously in figure 4-1) some copepods are observed to jump in the z-direction as they near the cylinder (marked by dotted ellipses). These copepod escape responses have higher spanwise velocity based on the spacing of neighboring spheres in the plotted tracks, which is also documented in Section 4.1.1. We believe that some of these escaping copepods move far enough in the spanwise direction that they are not re-circulated into the fluid directly behind the cylinder. Therefore, the lower number

density in the wake is most likely caused by the copepods responding to the sudden deceleration upstream of the cylinder.

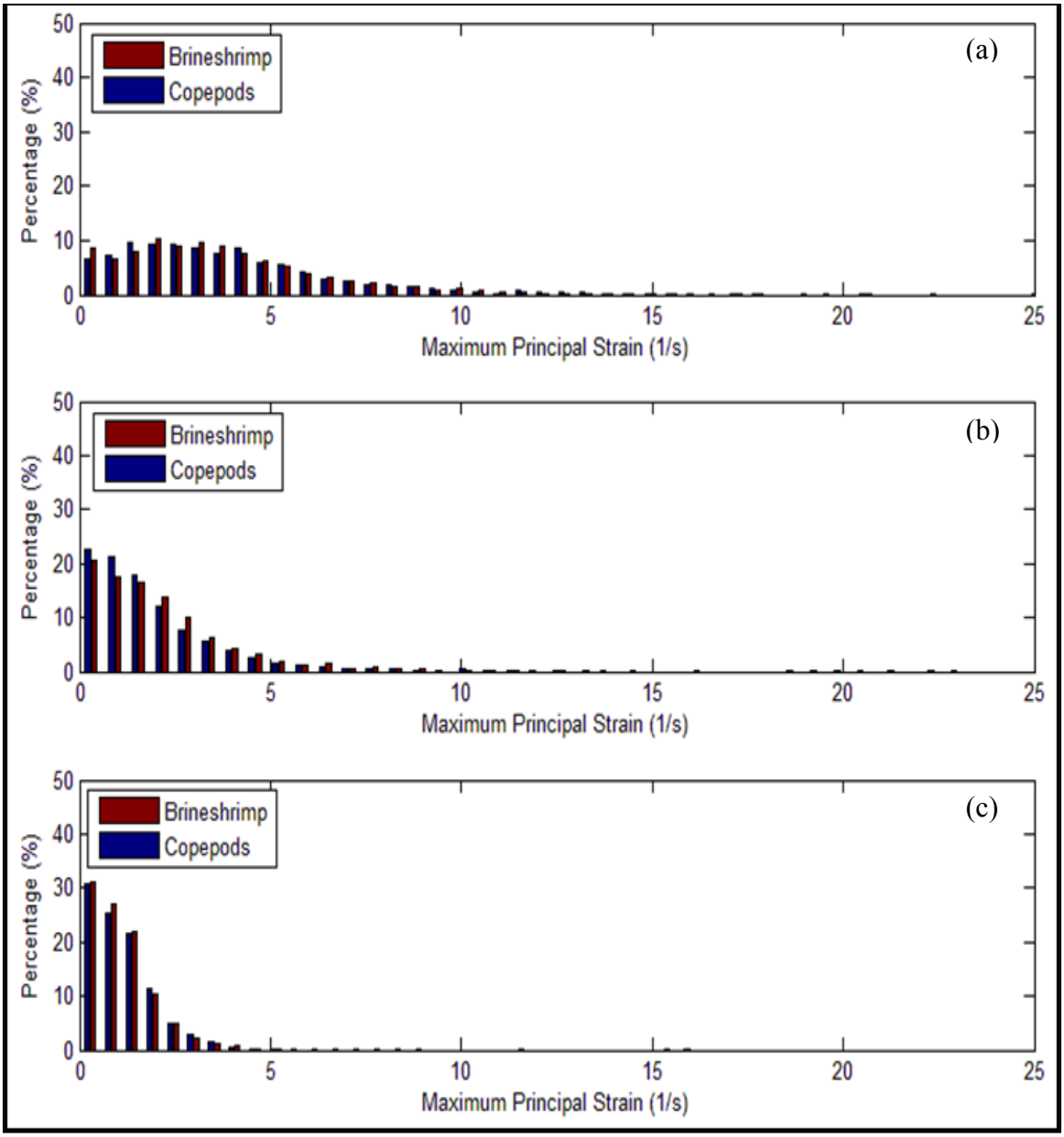

Figure 4-17: Probability distribution of the maximum principal strain rate (MPSR) of fluid at the location of brinshrimp (red) and copepods (blue) downstream of cylinder. The x-y plane for all cases was -40 mm < x < 40 mm, -32 mm < y < 8 mm. The z-locations of the measurement volume were (a) directly behind the cylinder (0 < z < 19 mm), (b) offset from cylinder axis 1.5 cm in positive z-direction, (c) offset from cylinder axis by 3.0 cm in positive z-direction.

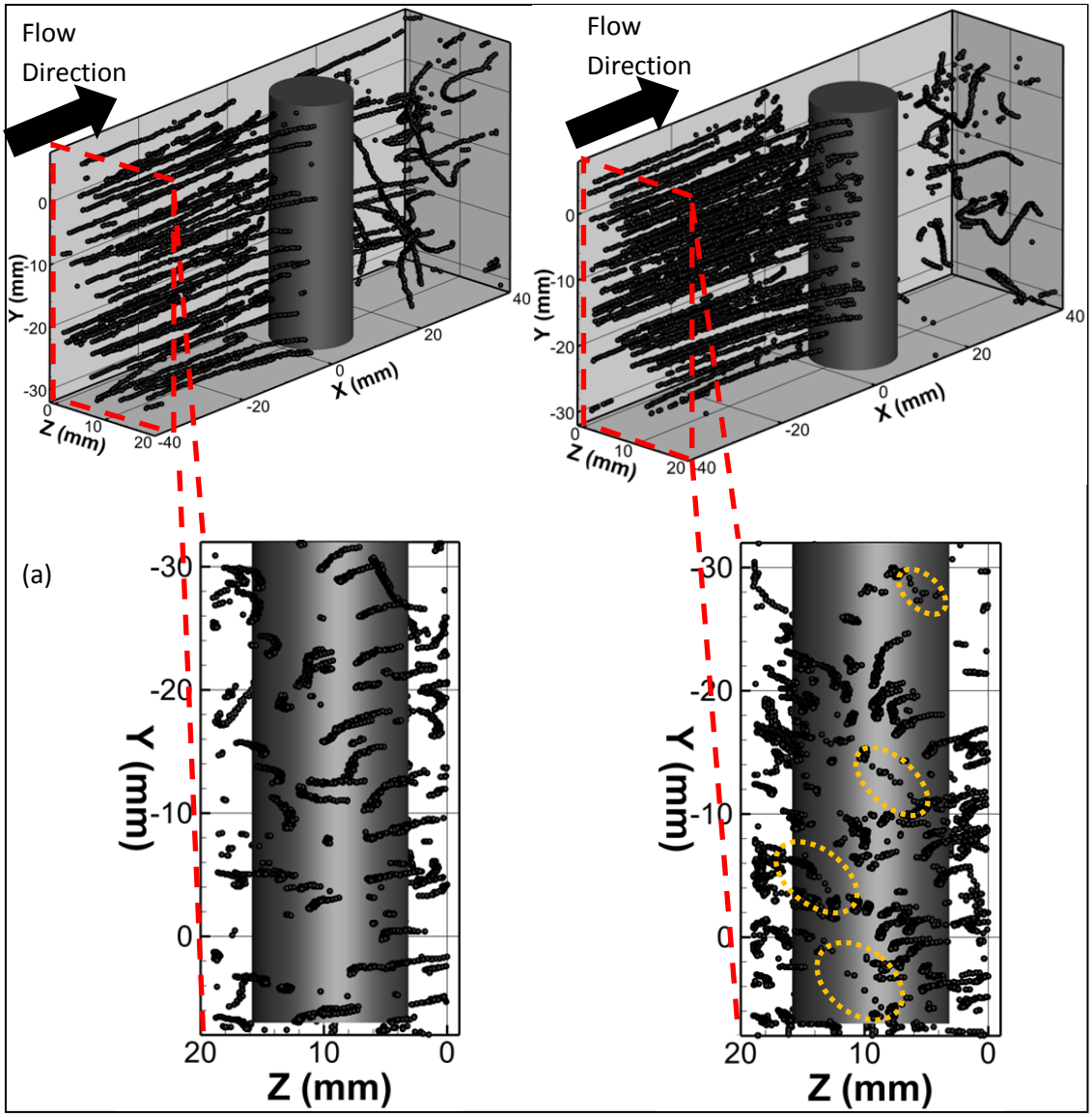

Figure 4-18: (a) Brine shrimp and (b) copepods showing their time series tracks (12 seconds) upstream and downstream of the cylinder with end-on views. Dotted ellipses show some instances of escape response by copepods when nearing the cylinder.

4.2 Experiment (2): Predator-prey interactions in still water

Sections 4.2.1 − 4.2.3 is taken from:
Adhikari, D. & Longmire, E. K. (2013) "Infrared tomographic PIV and 3-D motion tracking system applied to aquatic predator-prey interaction" Meas. Sci. Tech.(Special issue: Advances in 3D Velocimetry) Vol. 24 (2), 024011

Section 4.2.4 is taken from:
Adhikari D, Longmire E, Gemmell B "Infrared tomographic PIV measurement of aquatic predator-prey interaction" 16th Int Symp on Applications of Laser Techniques to Fluid Mechanics, Lisbon, Portugal (2012)

Zebrafish predation on non-evasive and evasive prey is discussed in the context of fish motion, the flow disturbance generated by the fish, and resulting copepod trajectories.

4.2.1 Free-swimming zebrafish

Figure 4-19a shows a time sequence of images for a free-swimming zebrafish. It is expected that fluid in front of the fish will be pushed forward, similar to a bow wave. The fish Reynolds number Re for this case is about 3200, using the fish width in the sagittal plane (here x-y plane) as the characteristic length. Tomographic PIV provides a fully resolved mapping of the associated velocity field. For example, the volumetric field at one instance (t = 20 ms) is shown in figure 4-19b. Closer observation of the x-y plane (sagittal plane) of the fish (see insert in figure 4-19b) shows velocity vectors diverging, as if from a point, ahead of the fish nose. By contrast, a portion of the corresponding x-z plane shows a set of velocity vectors that are relatively parallel across ~4 mm in the z-direction, demonstrating that the fluid motion ahead of the fish is clearly three-dimensional. Thus, the overall motion can only be captured by a volumetric method.

Figure 4-19b also demonstrates the application of the visual hull method within a reconstructed vector field. Specifically the visual hull (white iso-surface) acts as an

effective mask around the fish to avoid contamination of the local fluid vectors (see Chapter 3). In addition, the location of the fish mouth (denoted by white '+' in figure 4-19b) can be estimated from the iso-surface of the visual hull. Because the visual hull is a mask, however, and not a direct identifier, it does not provide a systematic means of tracking the fish, as opposed to the eye tracking mechanism based on the Circular Hough Transform and 3-D PTV (see Chapter 2). The grey sphere within the visual hull (see figure 4-19b) represents the measured location of the fish eye. This location and its trajectory over time give a more accurate estimate of the fish translation and velocity. Based on examination of the reconstructed volumes and organism tracks from t = 0 - 28 ms, the average velocity of the free-swimming fish was 0.07 m/s compared to the fluid velocity at a point ~1 mm in front of the fish, which was only 0.01 m/s. This indicates that the fluid velocity in front of the fish mouth was significantly less than the fish translation velocity and suggests that the large difference between the velocity of the fish and the flow in front of it may be due to the relatively streamlined body of the fish.

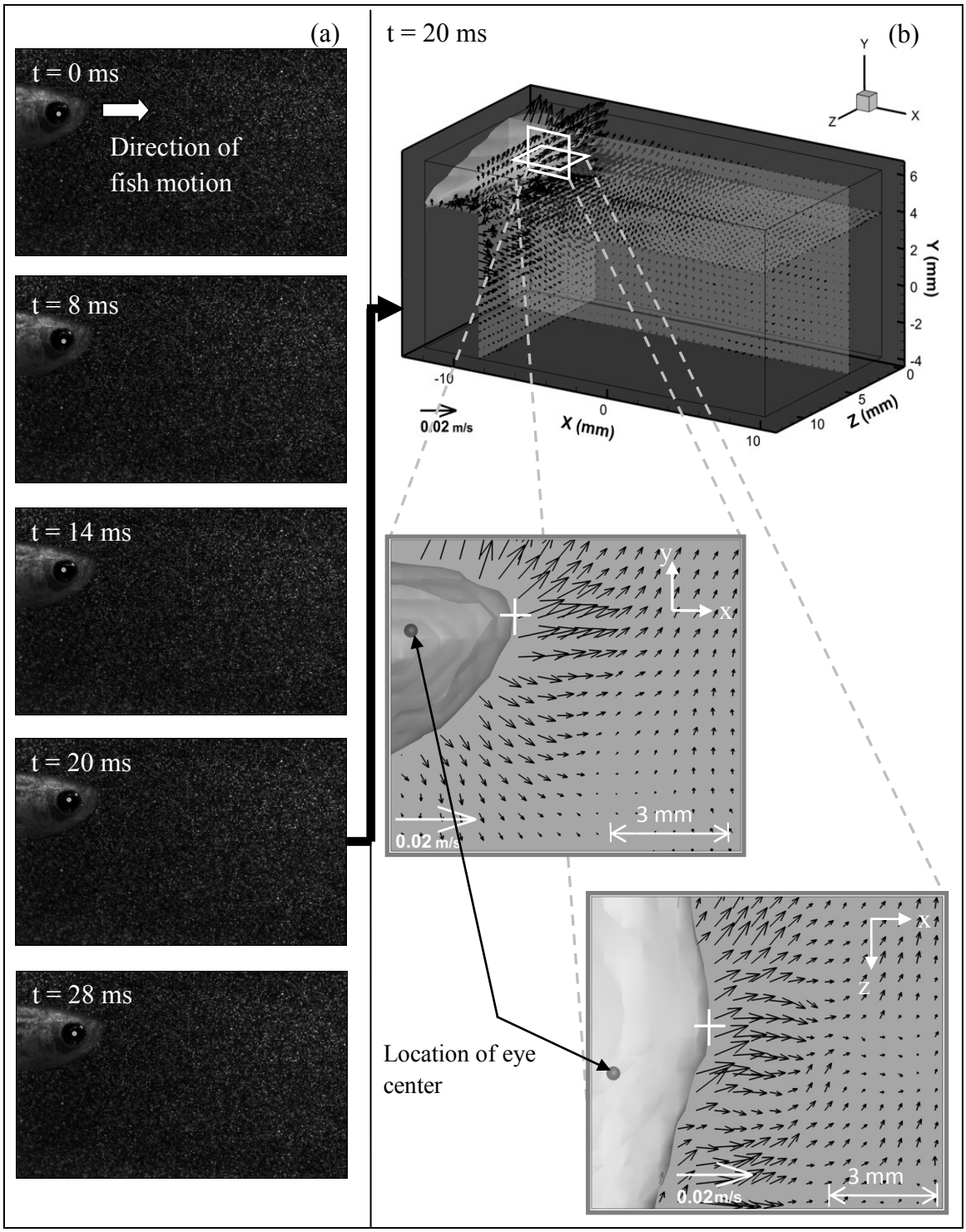

Figure 4-19: (a) Selected image sequences of a fish executing free swimming. Grey dot depicts the center of the eye used to track the fish motion. (b) Volumetric velocity field of fluid in absolute frame at a selected time (t = 20ms). Eye center is marked as a grey sphere within the visual hull. White '+' is the estimated location of the fish mouth.

4.2.2 Zebrafish feeding on non-evasive prey

Figure 4-20 shows a time sequence of images and corresponding vector fields of the zebrafish feeding on a non-evasive prey (water flea). In figure 4-20a, the white dot represents the location of the prey, and the grey dot is the center of the fish eye. In the figure, the fish is observed to approach the prey from below (t = 0 ms). The fish then lifts its head (t = 10 ms) before sucking in the prey (t = 20 ms), and eventually dropping its head (t = 36 ms). The action of sucking the fluid into the mouth for feeding is known as suction feeding. Figure 4-20b shows velocity vectors only in the sagittal plane of the fish for clarity. At t = 10 ms, it is observed that lifting of the head causes a local divergence in the fluid velocity. Then, at t = 20 ms, the local vectors become directed toward the fish mouth as the prey is sucked in.

A more detailed view extracted from this sequence is given in figure 4-21, which shows a perspective view of suction feeding as well as close up views of x-y and y-z planes located near the fish mouth at the time immediately before the prey is captured. The direction of the fluid velocity near capture is thus indicated. The fish Reynolds number at this time is 4200, which is obviously higher than in the free-swimming case. It can be observed from the close up views that the flow field associated with the suction is three-dimensional and non-axisymmetric, which reiterates the need for volumetric measurements in this type of study. The white and grey spheres within the vector field represent the volumetric location of the prey and fish eye, respectively, at t = 20 ms. The black sphere gives the initial location of the prey at t = 0 ms. The marked prey locations show that the fish suction counteracts any bow wave effect that might push the prey away. Instead, the prey is observed to be sucked downward a distance of about 1 mm by the fish as part of the successful predation. Furthermore, a z-component vorticity plot (see figure 4-22) shows a large vortex near the fish head as the suction feeding is executed. Based on the frame-by-frame sequence, it was observed that this vortex sustains itself from t = 14 to 30 ms, initiating before and lasting well beyond ingestion of the prey. This may suggest that the vortex helps entrain the prey before the fish ingests it. The flow field relative to the moving fish may provide additional insight on the capture

of the prey. Such a velocity field is plotted in figure 4-23 for t = 20 ms. In this reference frame, the region in front of the fish mouth has the highest velocity magnitude in the field, with the velocity direction toward the mouth.

Figure 4-24 plots the translational speeds of the fish and prey as well as the local fluid velocity at the prey location through t = 24 ms. The predator and prey speeds were obtained from 3-D tracking sequences, while the local fluid velocity was obtained from the tomographic PIV vector fields. The local fluid velocity was measured at the grid point nearest to the head of the prey. The measured fish speed increases significantly between t = 8 and 10 ms, which corresponds partially to the lift of the fish head prior to suction feeding. Note that this approximate speed is then maintained until after predation occurs at t = 18 - 20 ms. The local fluid velocity near the prey matches the tracked prey velocity closely for t = 0 - 14 ms as would be expected. After t = 14 ms, the local fluid velocity at the prey location could not be measured since the prey was partially obstructed by the fish mouth. However, the prey tracking velocity increases sharply as the prey is sucked into the fish mouth.

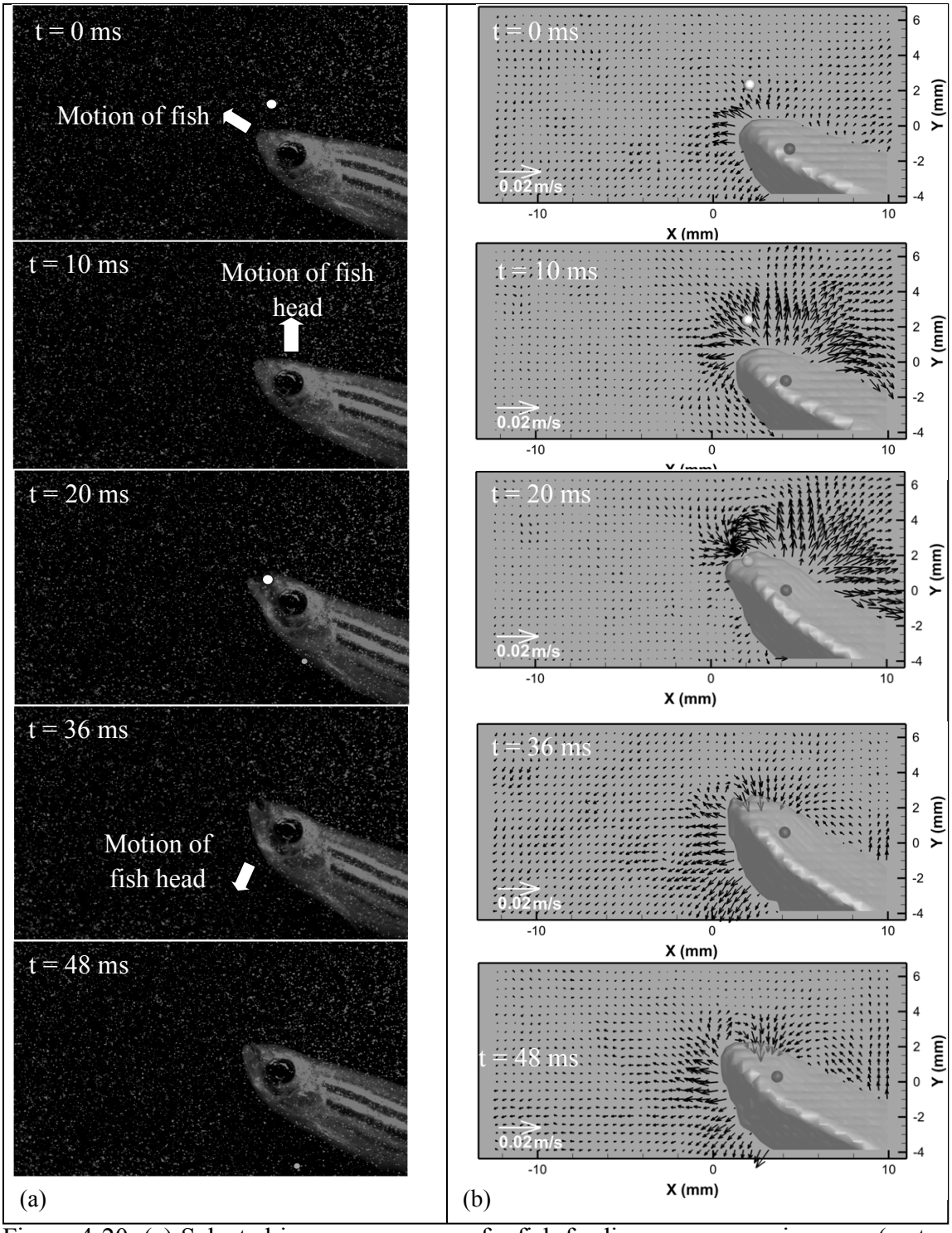

Figure 4-20: (a) Selected image sequences of a fish feeding on non-evasive prey (water flea). White dot depicts the location of the prey. Grey dot is location of eye center. (b) Corresponding fluid velocity fields in absolute frame. Only vectors in the sagittal plane of the fish are shown.

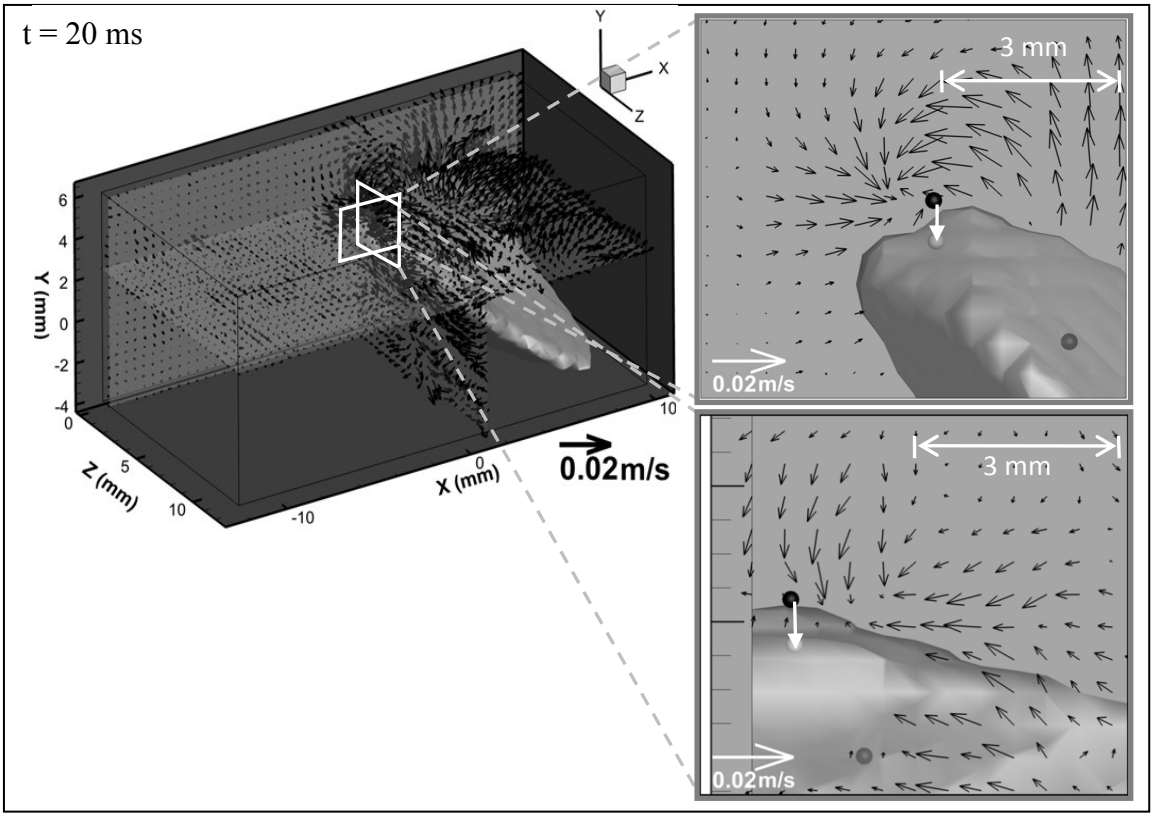

Figure 4-21: Absolute velocity of fluid as fish captures non-evasive prey, t = 20 ms. The black dot gives the location of the prey at t = 0 ms, white dot depicts the location of the prey, and grey dot is location of eye center.

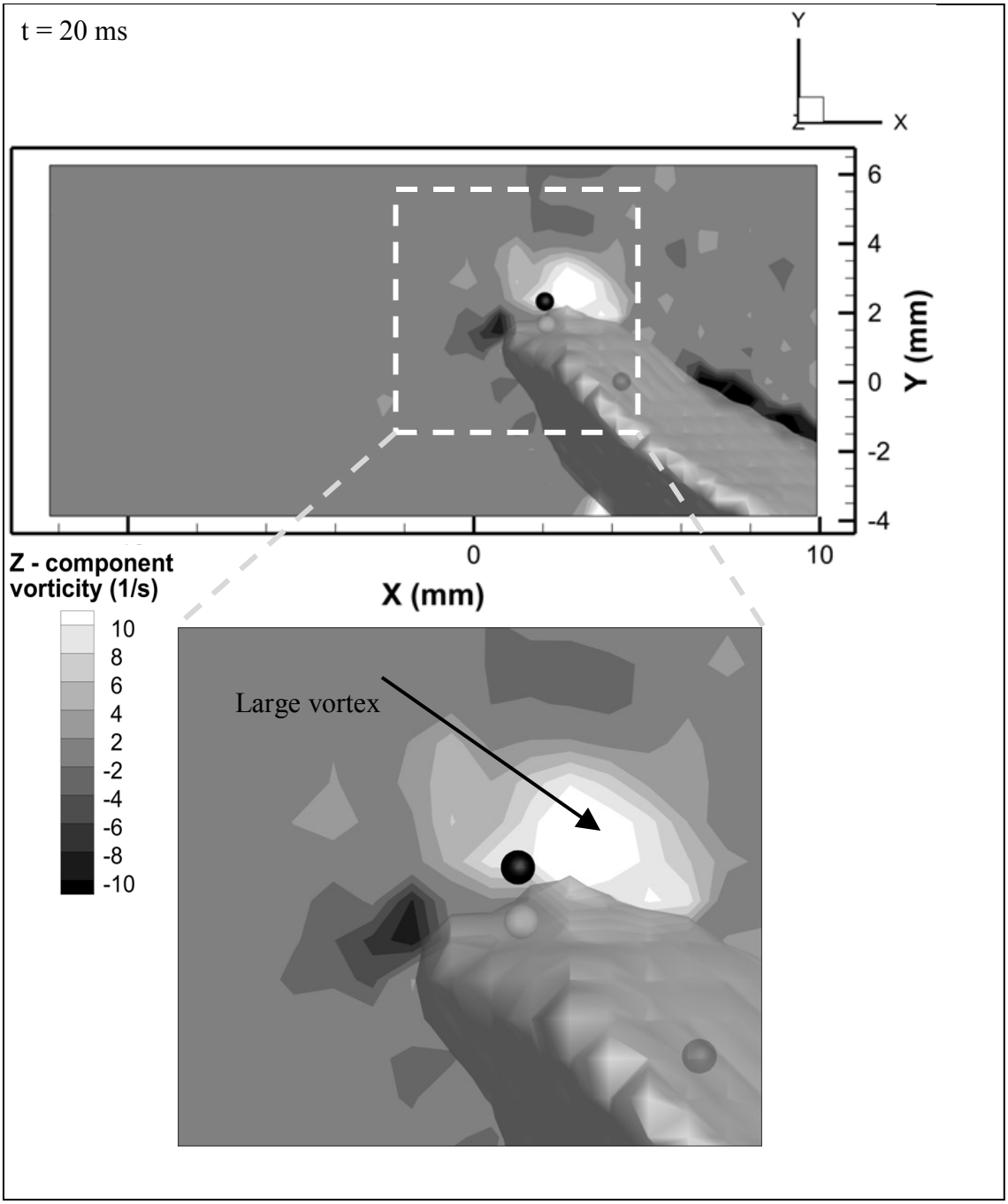

Figure 4-22: Z-component vorticity contours as the fish captures non-evasive prey at t = 20 ms. Only the contours in the sagittal plane of the fish are shown. A large vortex is sustained near the head of the fish during suction feeding from t = 14 - 30 ms. The black dot gives the location of the prey at t = 0 ms, white dot depicts the location of the prey, and grey dot is location of eye center.

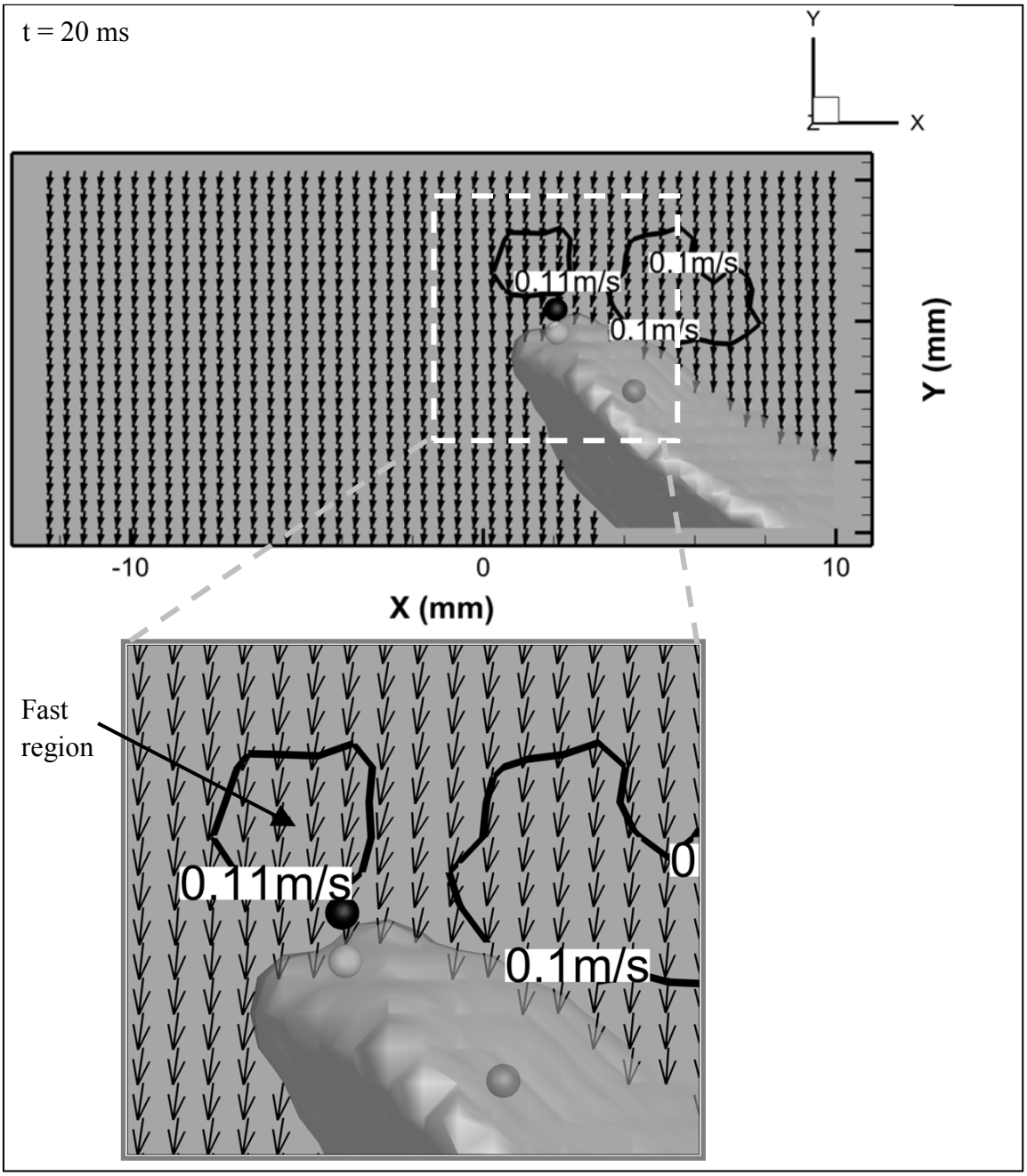

Figure 4-23: Velocity field relative to the fish. t = 20 ms. Projections of vectors in the sagittal plane of the fish are shown. Color/contour gives magnitude of 3-component vectors. The black dot gives the location of the prey at t = 0 ms, white dot depicts the location of the prey, and grey dot is location of eye center.

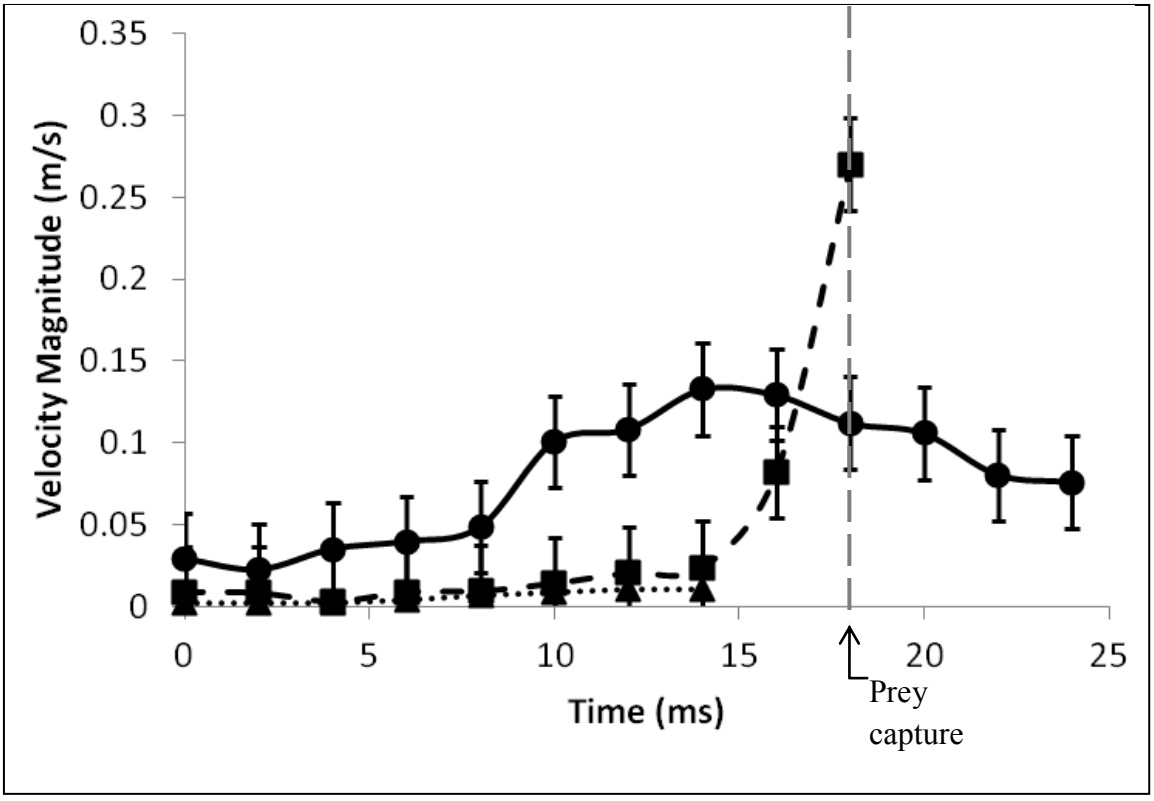

Figure 4-24: The velocity magnitude of predator (solid line; ●), prey (dashed line; ■), and local fluid velocity at the location of prey (dotted line; ▲).

4.2.3 Zebrafish feeding on evasive prey

Figure 4-25 shows a time sequence of images and vector fields for a zebrafish feeding on an evasive prey (copepod). For evasive prey, the fish is observed to execute a sudden acceleration to capture the prey instead of applying only suction feeding. In figure 4-25a, before t = 0 ms, the fish locates and moves slowly towards the prey. The time, t = 0 ms was selected as the time just before the sudden acceleration of the fish. The copepod (prey) initiates its escape response sometime between t = 0 and 2 ms. At t = 6 ms, the fish is already lunging forward to capture the evasive prey (known as ram feeding), instead of simply lifting its head, which is in clear contrast to the suction feeding shown in figure 4-20. Due to the sudden acceleration, a diverging velocity field is observed at t = 6 ms (figure 4-25b). Note, however, that the velocity vectors between the prey and the fish mouth are relatively shorter than those in the surrounding zones. This may be caused

by the fish sucking in fluid both to minimize warning to the prey and to prevent the bow wave from pushing the prey away. After the prey is captured at t = 22 ms, velocity vectors are generally diverging near the fish mouth, and greater in magnitude as compared with t = 6 ms. The sudden acceleration of the fish, along with the relatively lower velocity generated between the fish and prey, suggests that the fish changes its strategy when feeding on evasive prey, as compared to non-evasive prey.

Figure 4-26 gives a perspective view during this ram feeding event with zoomed views of x-y and y-z planes, which again illustrate the three-dimensionality of the flow field. As before, this figure corresponds to the time just before the prey is captured, thus giving the local direction of the fluid velocity near capture. The white and grey spheres within the vector field mark the volumetric location of the prey and fish eye, respectively. The black sphere represents the initial location of the prey at t = 0 ms. The prey track shows the escape response of the copepod as it attempts to move away from the attacking fish. This is in contrast to figure 4-21 where the passive prey was drawn into the fish mouth. The escape direction of the copepod shows that it moves across local streamlines such that its velocity direction is different from the direction of the local fluid velocity. The z-vorticity field at the time of capture (see figure 4-27) appears more complex than in the suction feeding case, partly because the fish is moving much more rapidly and generating a stronger 'bow' disturbance. Nevertheless, the concurrent suction through the fish mouth generates a strong reverse vorticity pattern over t = 8-14 ms (the prey is captured just after 12 ms). At the time shown, a 'reverse' vortex pair is observed in front of the fish mouth. The sudden acceleration of the fish as well as the opening and closing of its mouth and associated suction accelerations must also add to the complexity of the vorticity pattern.

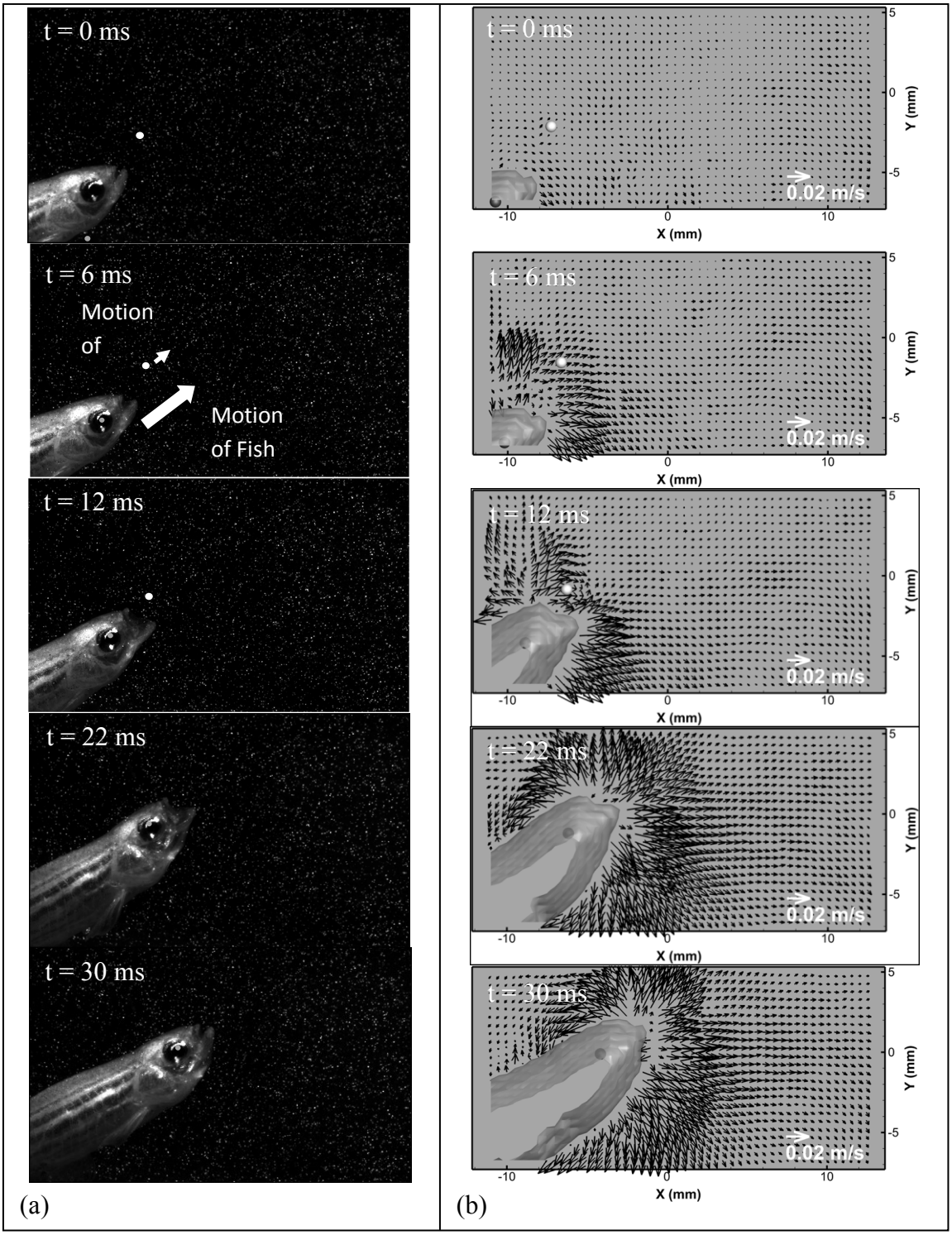

Figure 4-25: (a) Selected image sequence of a fish feeding on evasive prey (copepod). White dot depicts the location of the prey. Grey dot depicts fish eye center. (b) Corresponding fluid velocity fields in absolute frame. Only vectors in the sagittal plane of the fish are shown.

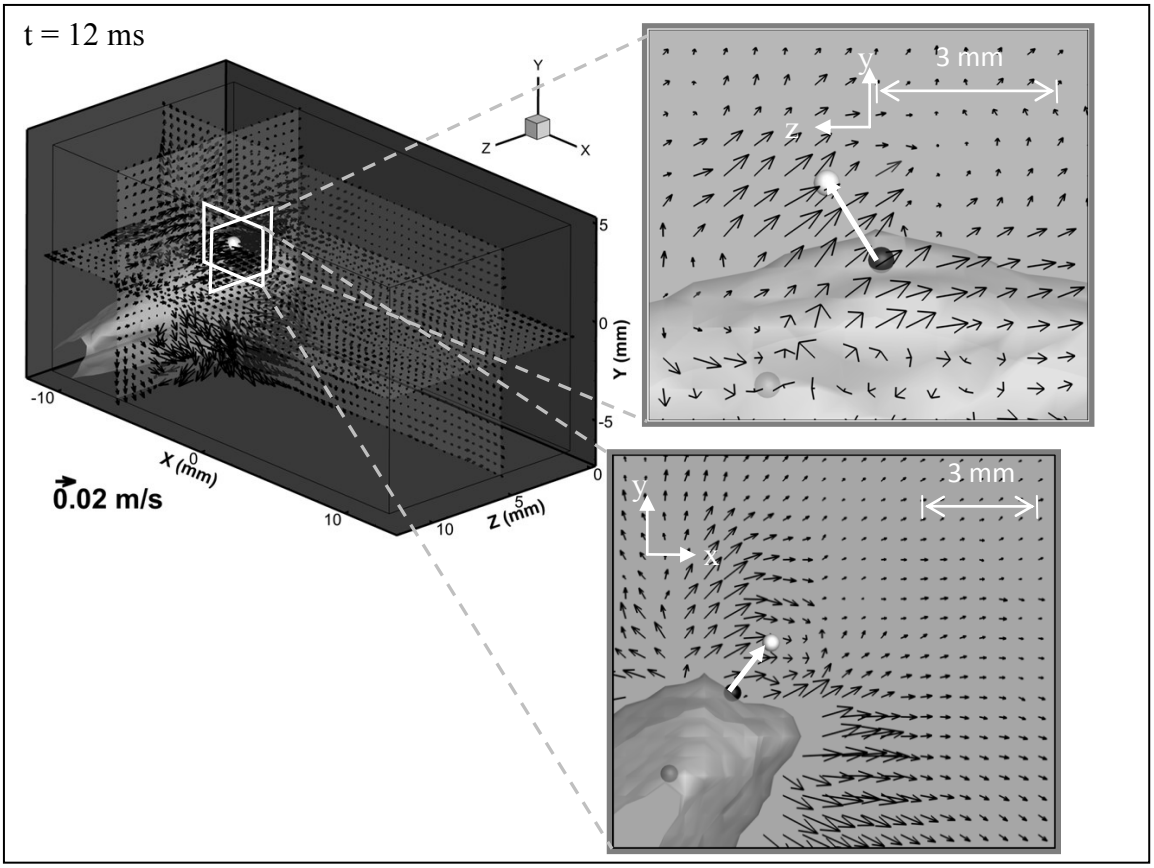

Figure 4-26: Absolute velocity of fluid surrounding fish capturing evasive prey at t = 12 ms. The black dot gives the location of the prey at t = 0 ms, white dot depicts the location of the prey, and grey dot is location of eye center.

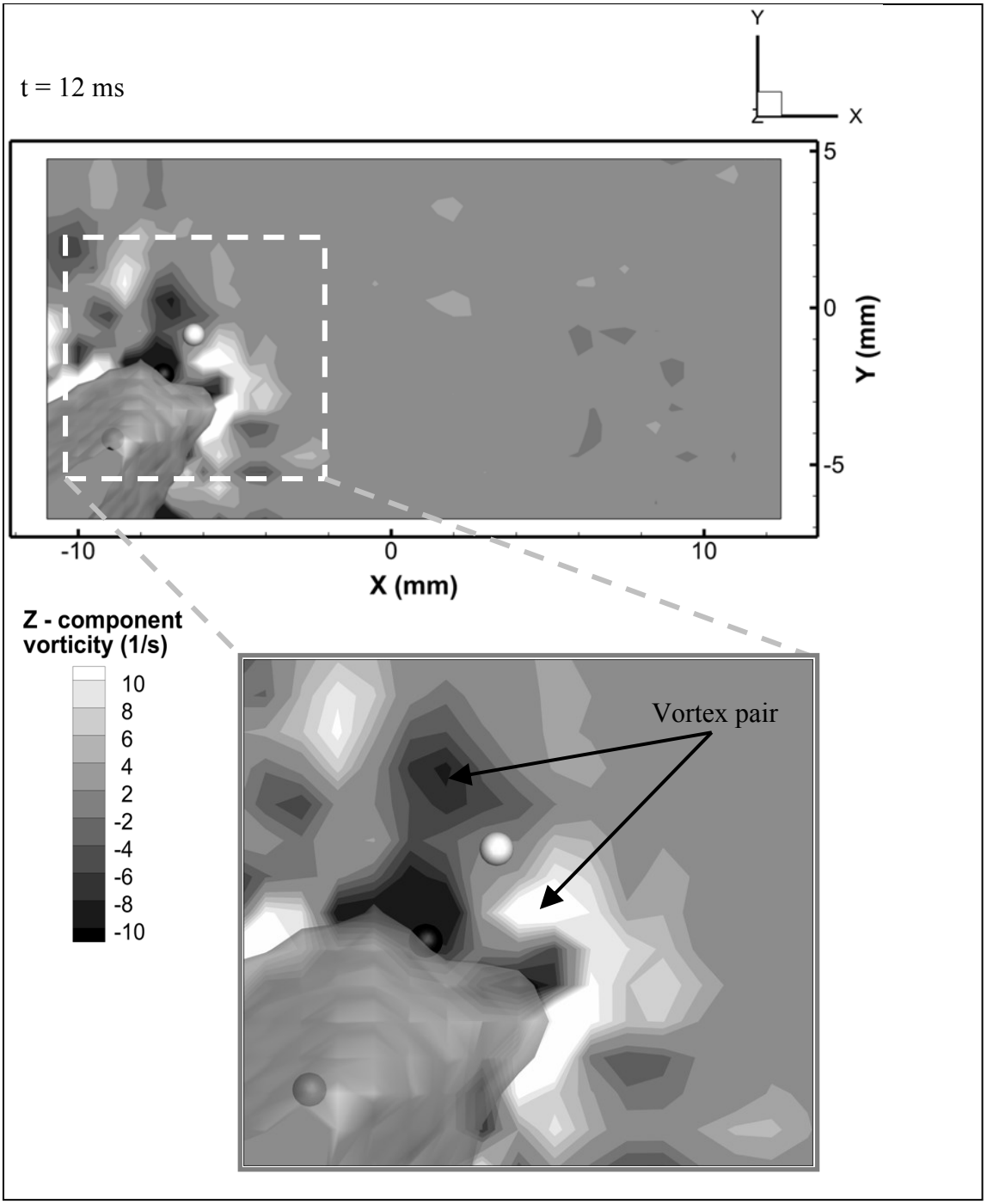

Figure 4-27: Z-component vorticity contours as fish captures evasive prey at t = 12 ms. Only the contours in the sagittal plane of the fish are shown. The black dot gives the location of the prey at t = 0 ms, white dot depicts the location of the prey, and grey dot is location of eye center.

Figure 4-28 shows the fluid velocity relative to the fish. In this reference frame, it is again clear that the relative velocity is larger immediately in front of the fish mouth compared with the regions immediately surrounding the mouth. Thus, this reiterates our observation that the fish is allowing fluid to enter its mouth as it approaches the prey allowing the fish to move forward without pushing the prey away. The trajectories taken by the fish and copepod during the ram feeding from t = 0 - 12 ms, at which point the copepod is captured, are plotted in Figure 4-29. It should be noted that the track of the fish eye has a clear offset from the trajectory of the prey since the eye is a fixed distance away from the mouth of the fish. The directions of the fish and copepod velocities can be inferred easily from the respective trajectory directions. A close observation of the trajectories shows that their directions are somewhat misaligned in that the copepod travels ~1 mm in the +z-direction, while the fish stays aligned with a single x-y plane. The fish nevertheless captures the copepod because the copepod actually moves *toward* the z-location of the fish mouth. If the copepod had chosen to move in a different direction, it may have escaped (discussed later in Section 4.2.4). In addition, while the direction of prey translation may be important for escaping the predator, the prey may also need either to respond faster or move faster to escape the approaching predator.

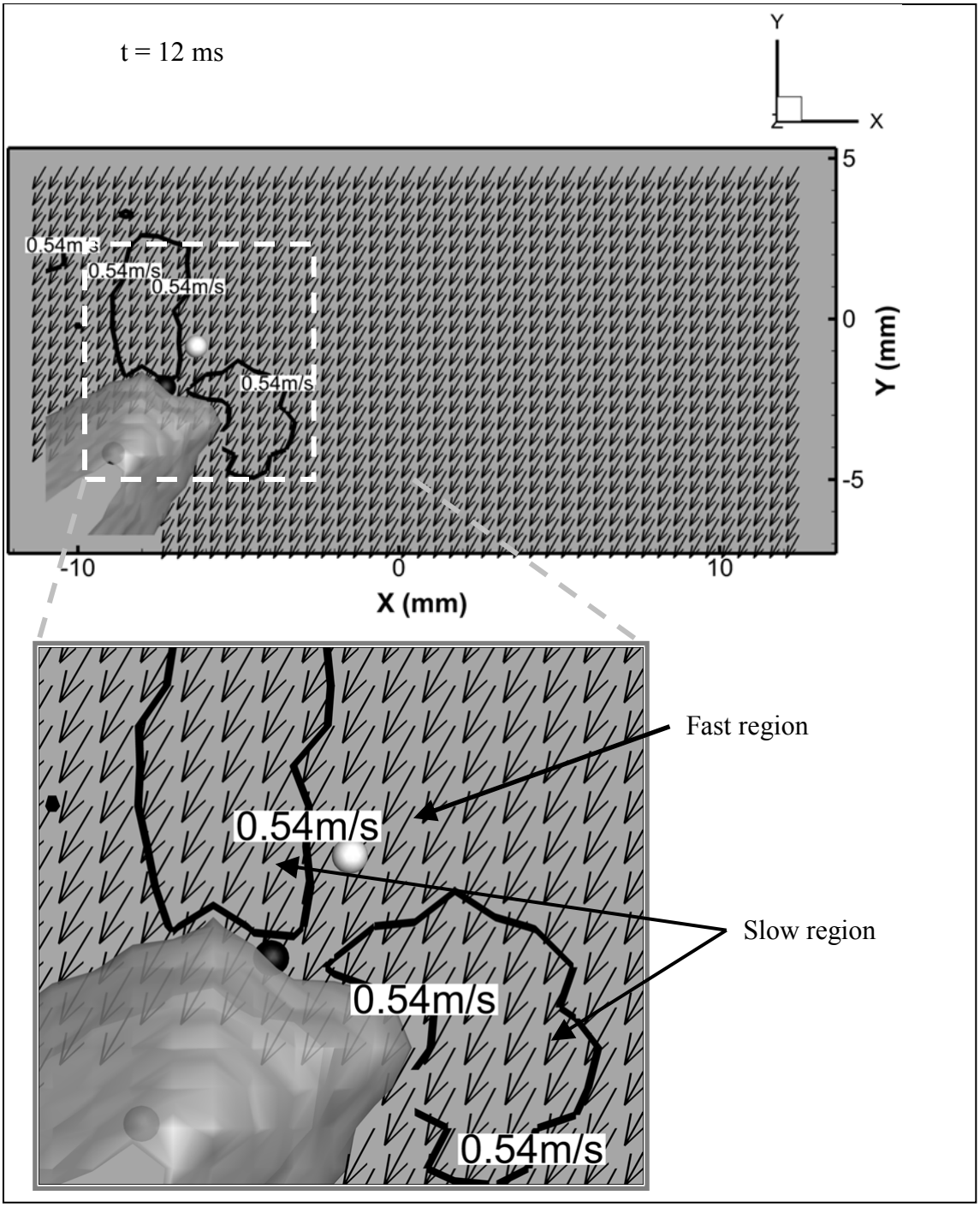

Figure 4-28: Velocity field relative to the fish. t = 12 ms. Projections of vectors in the sagittal plane of the fish are shown. Color/contour gives magnitude of 3-component vectors. The black dot gives the location of the prey at t = 0 ms, white dot depicts the location of the prey, and grey dot is location of eye center.

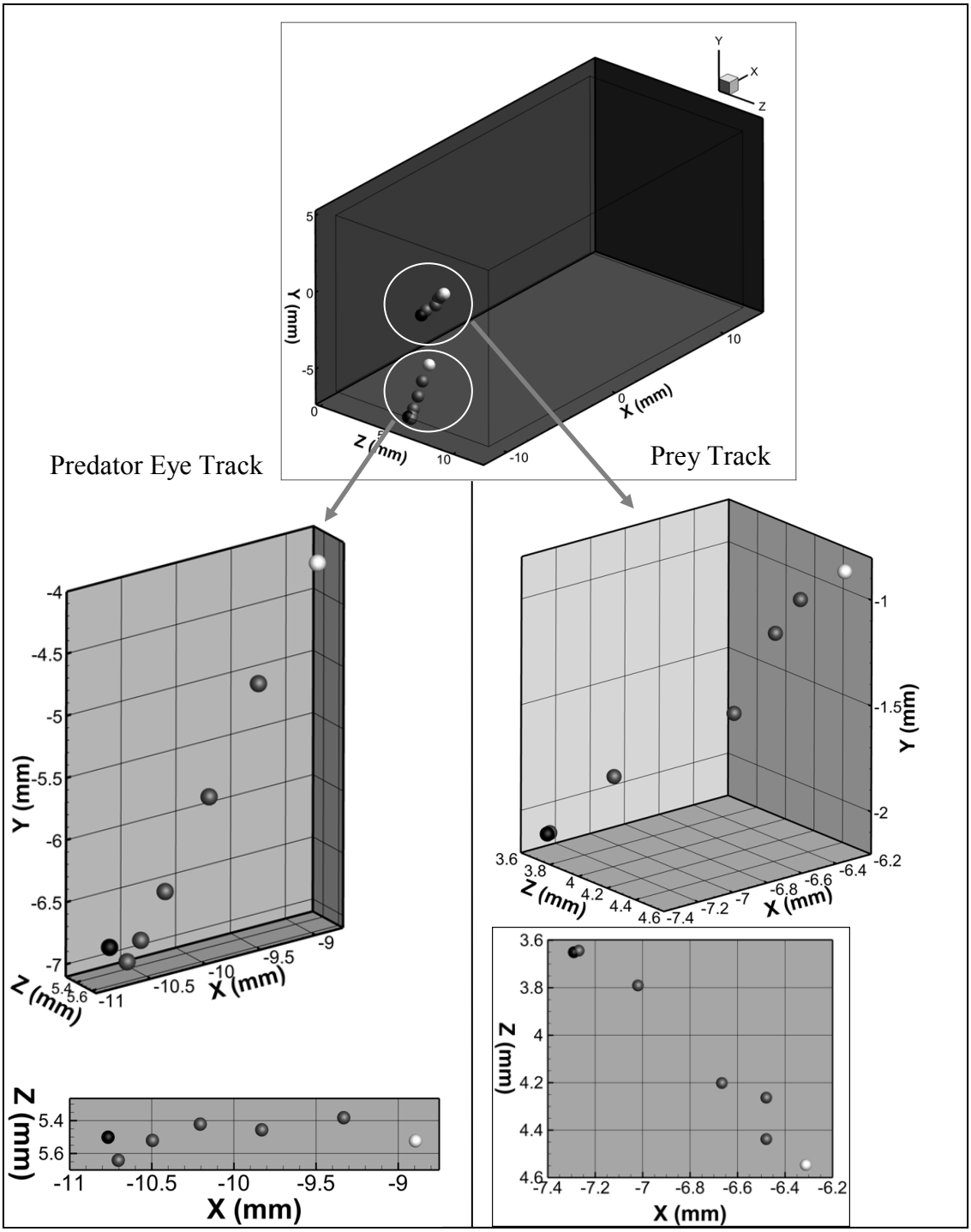

Figure 4-29: Predator eye and prey tracks for time sequence from t = 0 ms to 12 ms. Final (t = 12 ms) location of the predator and prey is shown by the white sphere. The initial (t = 0 ms) location of both predator eye and prey is given by the black sphere.

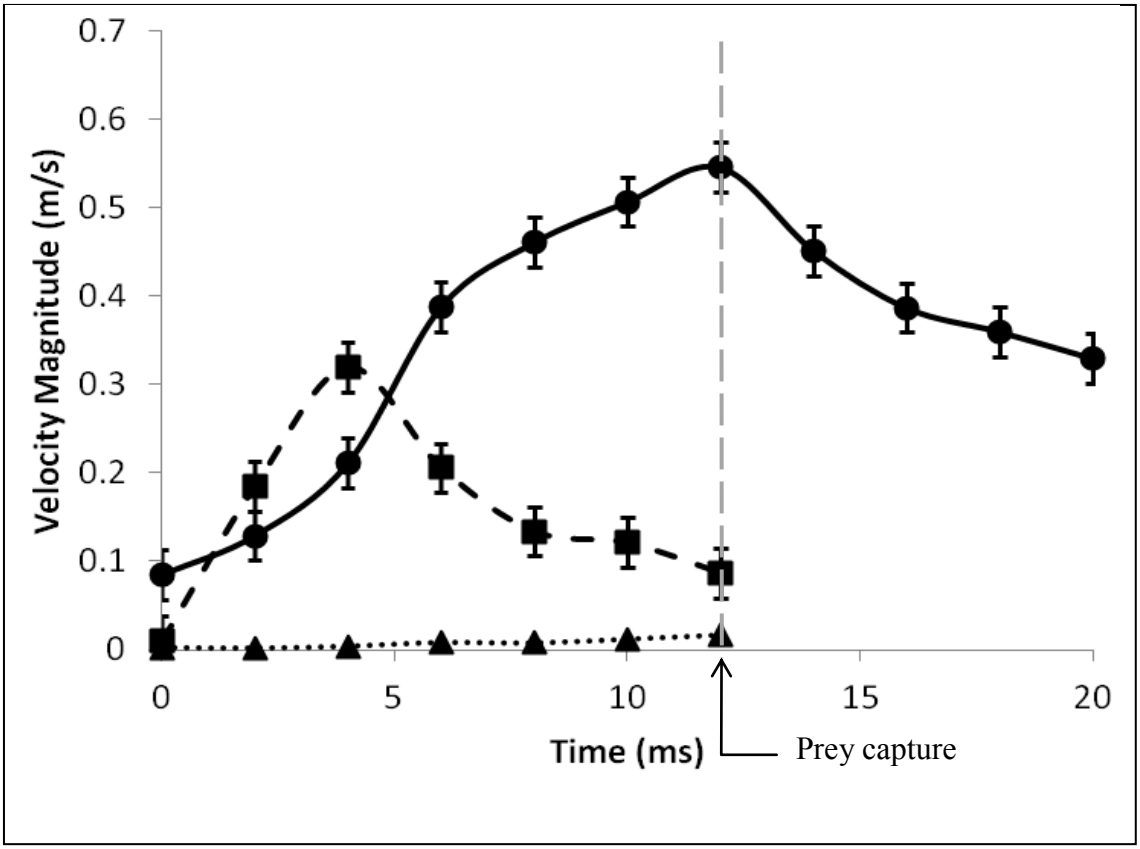

Figure 4-30: The velocity magnitude of predator (solid line; ●), prey (dashed line; ■), and local fluid velocity at the location of prey (dotted line; ▲).

Figure 4-30 gives a time record of the velocity magnitude for the fish, the copepod, and the local flow at the copepod location. The local fluid velocity was measured at the grid point nearest to the head of the copepod. The fish clearly accelerates during its lunge, and decelerates more gradually after capturing the copepod at t = 12 ms. In attempting to escape, the more nimble copepod accelerates more quickly than the fish, initially exceeding the fish velocity. However, the copepod does not maintain its maximum speed (measured at t = 4 ms), and it slows down significantly before it is eventually captured. The velocity of the fluid near the copepod is very low compared to the speed of either organism, and may help explain the decrease in copepod speed after its initial acceleration. The maximum fish Reynolds number in this case was 22000, which is much higher than the value attained while capturing a non-evasive prey. The maximum Reynolds number of the copepod during the entire escape sequence was found to be

~320. Thus, inertia is very important in characterizing the motion of both species. We note that, when the copepod is moving at its maximum speed (in this case, ~0.33 m/s) and Reynolds number, it must experience significant drag from the surrounding fluid. Thus, unless it continues to exert a significant forward thrust, the drag will lead it to decelerate.

4.2.4 Capture and escape of evasive prey

Figure 4-31 (reproduced from figure 4-25 and 4-27) shows a raw image (figure 4-31a) from one of the cameras and the corresponding volumetric vector field (figure 4-31b) of the zebrafish, as it is about to capture a copepod successfully at t = 12 ms. In the entire image sequence (not shown in the figure), the fish is observed to first approach the prey, and then execute a sudden acceleration to capture it (ram feeding). Figure 4-31 shows only an instance of the ram feeding just before the copepod was captured. The vector field around the mouth of the fish during ram feeding is generally diverging (see figure 4-31b). This high velocity lunge causes the flow around the mouth of the fish to attain velocity of about ~0.014 - 0.02 m/s, mainly directed away from the fish mouth. From the initial and final location of the prey (see black and while spheres in figure 4-31b), it is observed that the prey moves away from the mouth of the predator (see x-y plane), and the direction of motion does not follow the direction of the fluid velocity (see y-z plane). Thus, the evasive copepod is observed to move away from the fish mouth independent to the direction and magnitude of the flow field. This observation is possible due to the capability of the system to measure 3-D flow field and location of the organism.

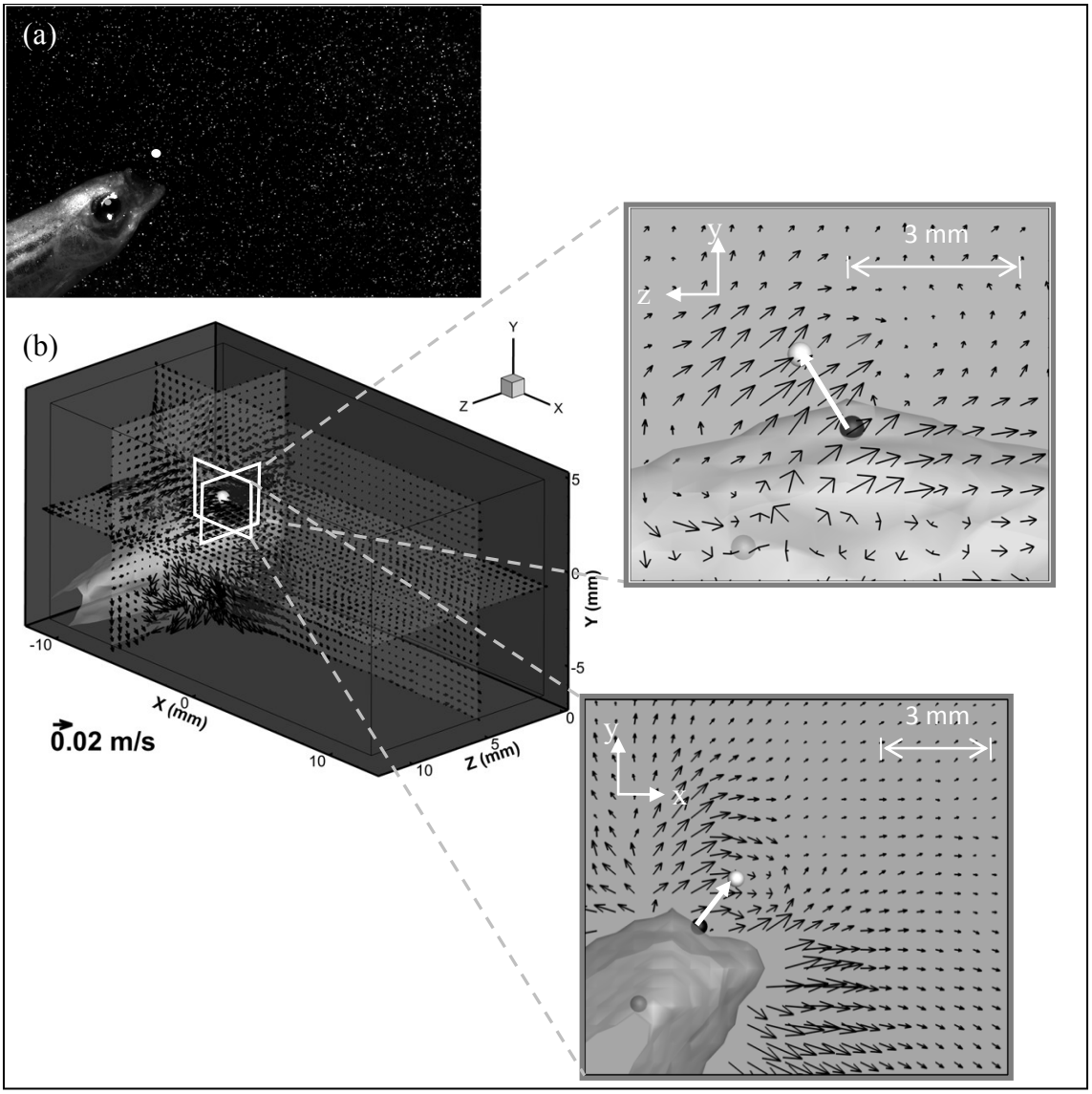

Figure 4-31: Volumetric velocity field of the fish capturing evasive prey (copepod) at t = 12 ms. (a) Image and (b) volumetric vector field. White dot depicts the location of the prey, and grey dot depicts the center of the fish eye used track its motion. Black dot depicts the initial (t = 0 ms) location of the prey.

Figure 4-32 shows a result from a case where the zebrafish fails to capture the copepod. Figure 4-32a shows an image, and figure 4-33b shows the corresponding velocity field when the fish forages on the copepod. This instance corresponds to the same time, t = 12 ms, as the successful prey capture in figure 4-31, and it is also the time that the fish mouth comes closest to the copepod. For this case, the velocity field around the mouth of

the fish is also generally diverging. The magnitude of the velocity field around the fish is about ~0.014 - 0.02 m/s, and mainly directed away from the mouth of the fish. This velocity field magnitude is similar to that observed in figure 4-31. The prey trajectory (figure 4-32b) shows that the prey moves away from the fish in both x-y and y-z planes. This suggests that, while volumetric velocity vectors may provide the flow field around the interaction, no obvious difference in the field is observed for predation success and failure (figures 4-32 and 4-33).

The velocity magnitudes of the predator, prey, and the fluid velocity at the location of the prey are shown in figure 4-33(a) and (b) for predation success and failure, respectively. For both cases, t = 0 ms is designated as the time when the copepod first starts to move, which is less than 2 ms (or one data frame) after the initial acceleration of the fish. Note that the velocities of the fish and copepod are much higher than the local flow velocity.

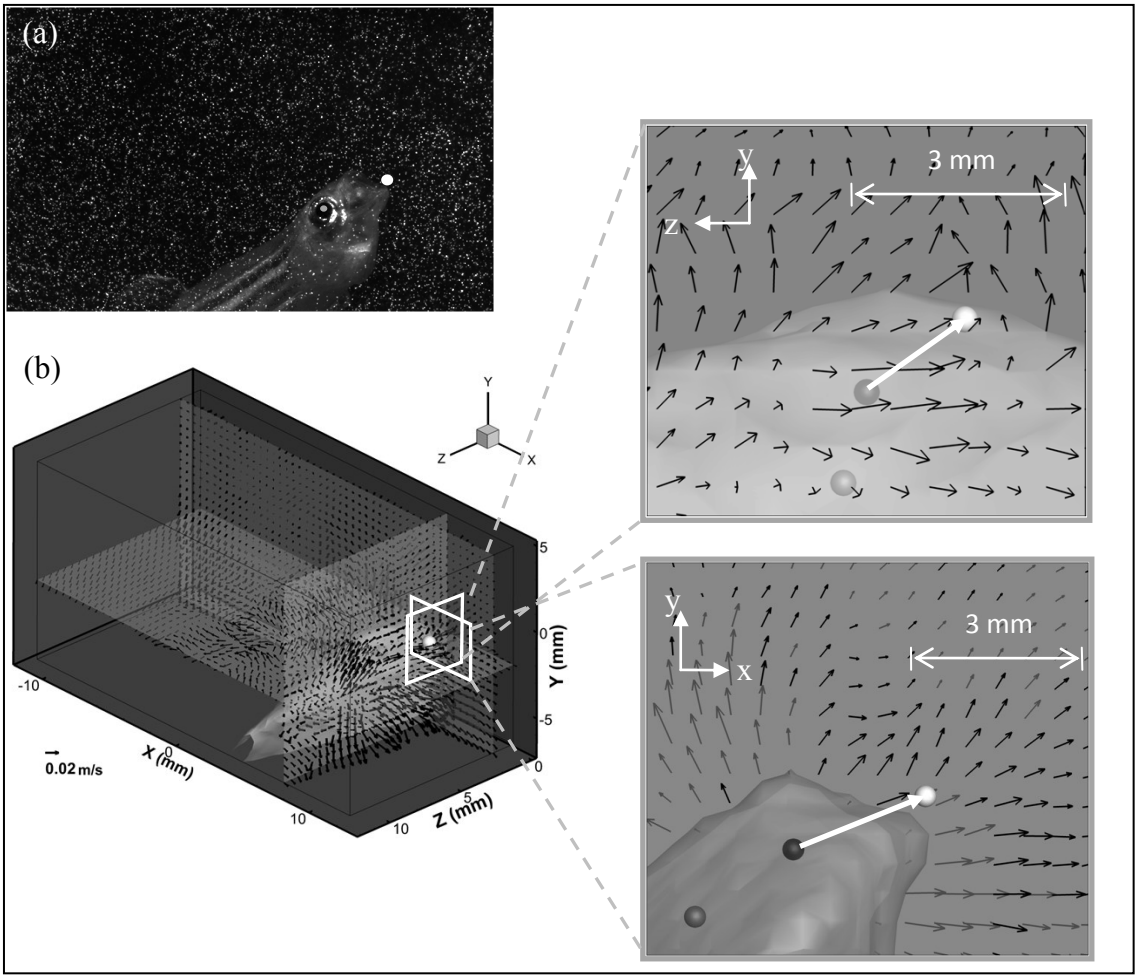

Figure 4-32: An instance of volumetric velocity field of the fish failing to capture evasive prey (copepod) at t = 12 ms. (a) Image and (b) volumetric vector field. White dot depicts the location of the prey, and grey dot depicts the center of the fish eye used track its motion. Black dot depicts the initial location of the prey.

For the case of predation success (figure 4-33a), the maximum velocity of the fish is ~0.55 m/s, while the maximum velocity of the copepod occurs earlier with a magnitude of ~0.32 m/s. In the same figure, it is also noted that the copepod is captured when the velocity of the fish is maximum. On the contrary, in the case of predation failure, the maximum velocity of the copepod is ~0.5 m/s, which is approximately the same as the maximum velocity of the fish (figure 4-33b). Also, the copepod velocity at the time of closest approach (dashed green line) is larger than when the other copepod was captured. This may intuitively suggest that higher prey velocity can lead to predation failure.

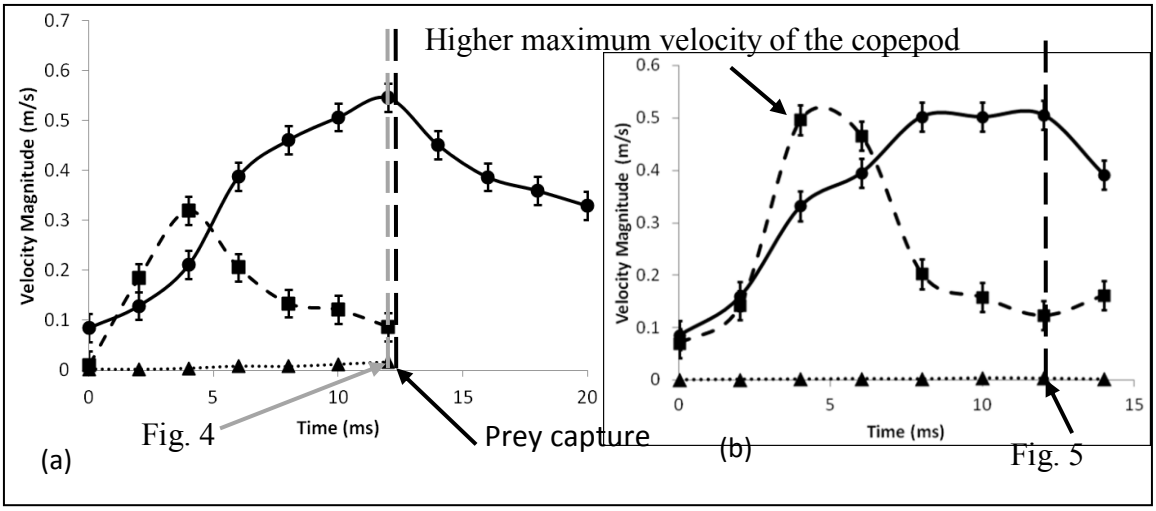

Figure 4-33: The velocity magnitude of predator (solid line; ●), prey (dashed line; ■), and local flow velocity at the location of prey (dotted line; ▲). (a) Predation success, (b) Predation failure.

Trajectories of the fish and copepod are shown in figures 4-34 (t = 0 - 12 ms) and 4-35 (t = 0 - 14 ms) for the cases of predation success and failure, respectively. From figure 4-34, we observe that the fish trajectory is mainly in the x-y plane with limited displacement in the z-direction. However, the copepod moves with a positive z-displacement component towards the fish. Although the copepod maximum velocity is higher than fish at t = 2 - 5 ms (as observed in figure 4-33a), its motion towards the z-location of the fish contributes to the predation success.

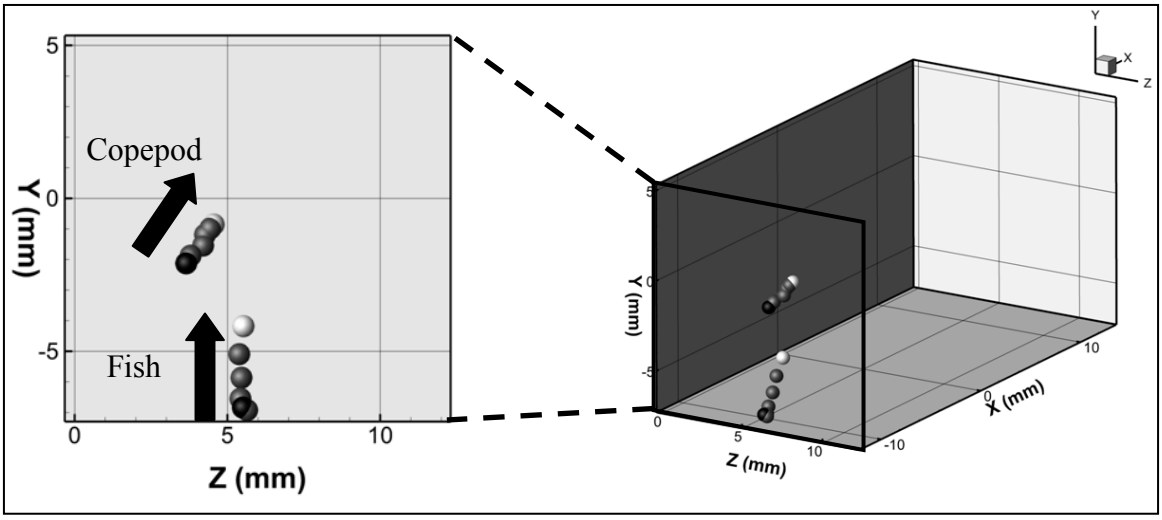

Figure 4-34: Predator and prey tracks with $\Delta t = 2$ ms time intervals for successful prey capture by ram feeding. The white sphere shows final location of the prey and predator, while the black sphere gives the initial locations.

Figure 4-35 shows a different trajectory of the fish and copepod as compared to figure 4-34. In figure 4-35, the fish moves in the positive z direction (+ ~1 mm), while the copepod moves in the negative z direction (- ~2 mm). This trajectory combination, combined with the higher maximum velocity of the copepod suggests that predation failure in this case may be due to strategic combination of the maximum velocity of the copepod and the direction at which it escapes relative to the fish. The copepod is able to jump away from the fish by choosing a better escape direction.

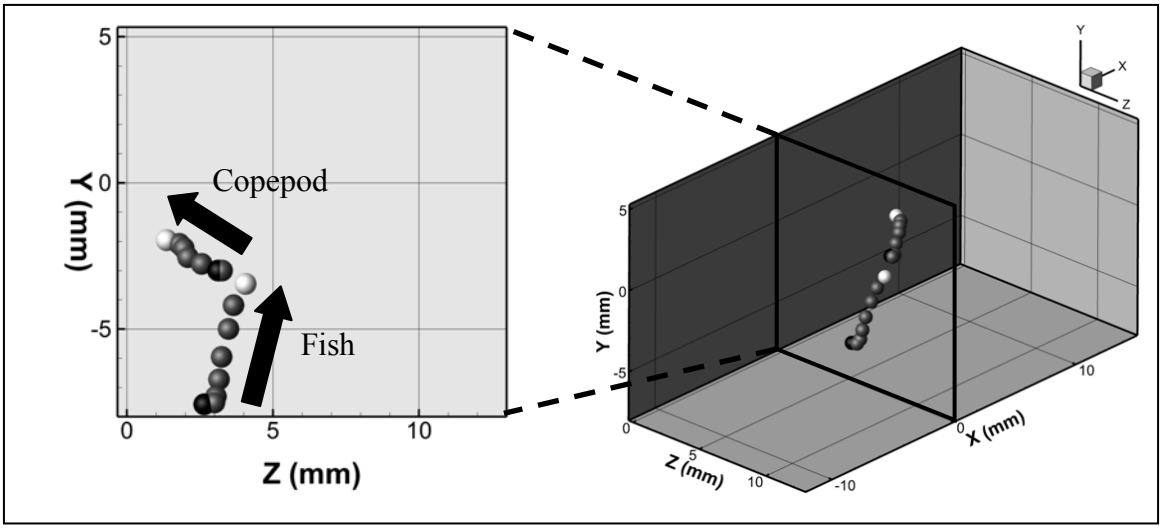

Figure 4-35: Predator and prey tracks with $\Delta t = 2$ ms time intervals for failed prey capture by ram feeding. The white sphere shows final location of the prey and predator, while the black sphere gives the initial locations.

4.3 Experiment (3): Predator-prey interaction unsteady/turbulent flow

This section explores flow fields and organism trajectories when predator-prey interactions occur in unsteady/turbulent flow. Section 4.3.1 describes the various stages of predator-prey interaction in uniform cross flow. Next, the instantaneous flow field when the predator (fish) strikes the prey (copepod) in cross flow is examined (Section 4.3.2), followed by discussion on local flow quantities detected by copepods for escape (Section 4.3.3). The velocity profile and trajectory of the fish and copepods are discussed in Section 4.3.4. Finally, the predator-prey interaction in unsteady cross-flow is analyzed and compared with previous findings (Section 4.3.5).

4.3.1 Predator-prey interaction in cross-flow

Predator-prey (blenny-copepod) interactions in uniform cross flow (U_0 = 0.0384 and 0.077 m/s) were observed for more than 20 events. In most cases, the blenny moved out of the measurement volume when attempting to capture the copepod. However, their behavior could be observed visually from the 3D PTV cameras. Based on the visual analysis of all recorded images, the blenny was able to capture the copepod in only one event at U_0 = 0.077 m/s. This suggests that copepods are able to escape more than 95% of the time in uniform flow, for both U_0 = 0.0384 m/s and 0.077m/s. Detailed measurement and analysis on four events (3 predation failures; 1 predation success) are elaborated.

Figure 4-36 shows a time sequence of images and vector fields for a blenny feeding on a copepod in a uniform cross flow. The time, t = 0 ms was selected as the time when the fish begins to move from its housing towards the prey. From t = 0 − 169 ms (figure 4-36), the fish moves relatively slowly (based on the magnitude of the velocity vectors in front of the fish head) towards the prey. During this slow approach, the Reynolds number based on fish velocity is about 150. At t = 183 ms, the fish is already lunging forward to capture the copepod by ram feeding (fish initiates acceleration at t = 176 ms). Due to the sudden acceleration, a larger magnitude diverging velocity field is observed at t = 183 ms (figure 4-36b). At this time, the fish Reynolds number is about 750, which is

much higher than that during the initial exit of the fish from the housing. As with the zebrafish predation on copepods discussed in Section 4.2, the blenny is observed to execute a sudden acceleration to capture the prey instead of applying only suction feeding. In the event shown in figure 4-36, the prey escapes by moving away (starting t = 176 ms) when the fish lunges (t = 176 ms − 281 ms). The copepod appears to jump at the same time as the start of the fish lunge. This suggests that response latency of the copepod is within the time interval of recording (2 ms). Upon failing to capture the copepod at t = 183 ms, the fish starts to retreat to its housing (from t = 197 ms). The slow approach to prey (t = 0 − 169 ms), followed by a sudden acceleration (or lunge) (t = 183 ms), and retreat (t = 197 − 281 ms) was observed consistently for every blenny-copepod interaction event recorded.

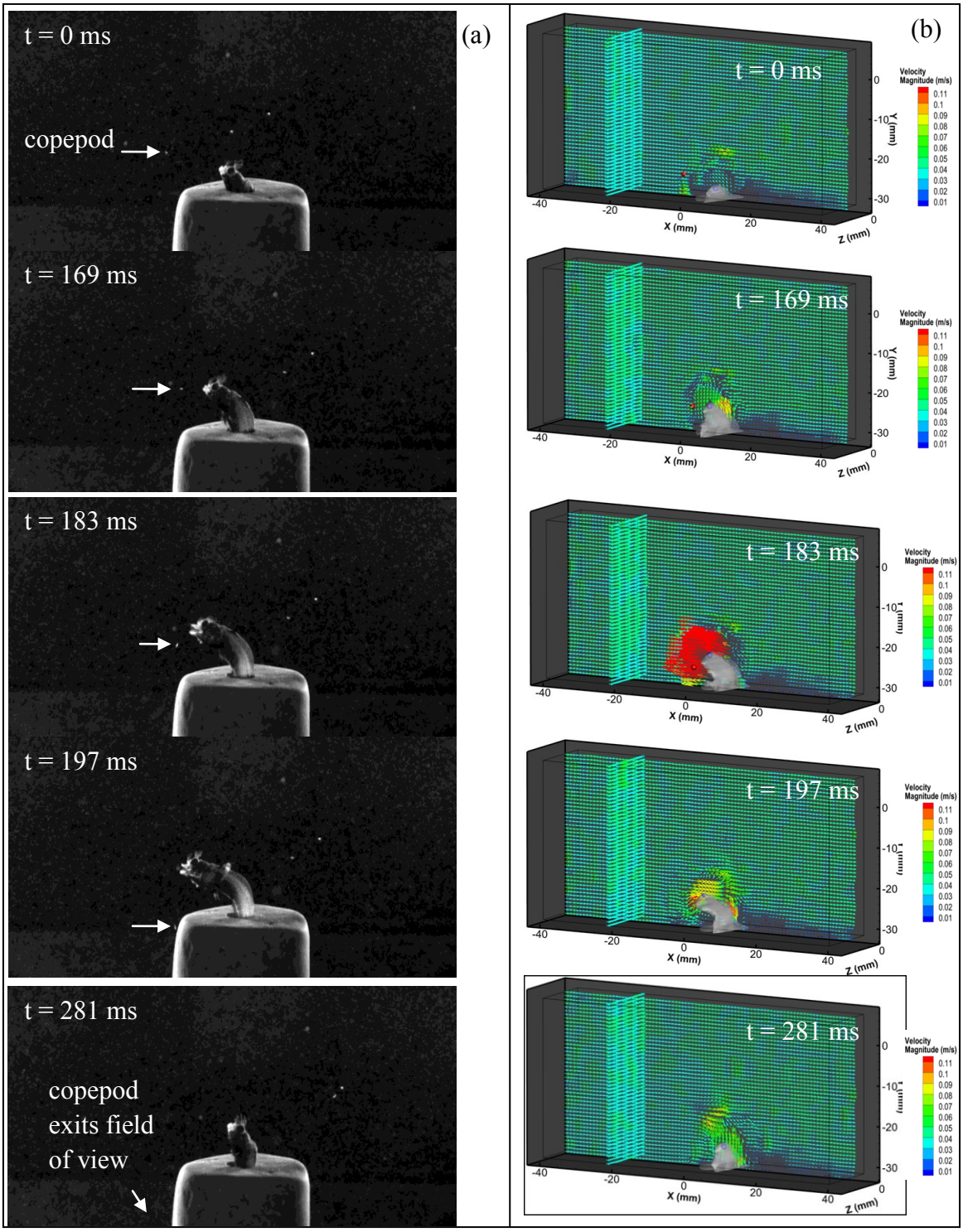

Figure 4-36: (a) Selected images from sequence of a fish feeding on copepod in a uniform cross-flow. Red dot depicts the location of the prey. Blue dot is location of eye center. (b) Corresponding fluid velocity fields in absolute frame. Only vectors in the x-y plane intersecting the location of the copepod are shown.

4.3.2 Flow field surrounding feeding fish in cross-flow

Detailed close up views of x-y and y-z planes located near the fish mouth just before (t = 169 ms) and at the time of sudden acceleration (t = 183 ms) are shown in figures 4-37(a) and (b), respectively. It can be observed from the views that the flow field associated with the fish motion is three-dimensional and non-axisymmetric (see inserts of figure 4-37). The red and blue spheres within the vector field represent the volumetric location of the prey and fish eye, respectively. For figure 4-37(b), the green sphere gives the previous location of prey at t = 169 ms. Note that the location of the fish eye has a clear offset from the trajectory of the prey since the eye is a fixed distance away from the mouth of the fish.

In figure 4-37(a), the approach of the fish is observed to cause a diverging disturbance region in front of the fish head (bounded by dashed line in figure 4-39a insert). This region can be estimated by outlining the boundary where the vector direction changes suddenly from positive streamwise (caused by the free stream velocity) to negative (caused by the fish motion). Analysis of several events showed that copepods could sense this disturbance region, and escape. In order to prevent the copepod escape, the fish first approaches the copepod slowly and then executes the lunge just before the copepod enters the region of disturbance. This allows the fish to be at a close distance, without triggering the copepod to escape, before it suddenly accelerates (i.e. ram feeding mode). The closest distance, before sudden acceleration of the fish, was 4 − 5 mm. During ram feeding (see figure 4-37b), the disturbance region extends over a larger distance, enveloping the copepod. The forward extent of the disturbance region during the sudden acceleration was about 8 − 10 mm. At this time, the copepod senses the disturbance and attempts to escape. The response latency of the copepod is estimated as 2 ms (see Lenz and Hartline 1999; Chapter 4.2), which is within the repetition time of the current PIV measurement sequence (Δt = 7 ms). Since the copepod responds almost immediately to the sudden acceleration by the fish, the predation success now depends on the jump acceleration and velocity of the copepod, lunge velocity of the fish, and their directions. For example, predation success may occur if the copepod jumps towards the

fish mouth, but predation failure occurs if the copepod jumps away or perpendicular to direction of fish approach. In figure 4-37, the directions of the fish and copepod trajectories can be inferred easily. A close observation of the trajectories shows that their directions are misaligned such that the copepod travels ~2 mm in the negative y-direction, while the fish lunges predominantly in the negative x-direction. Thus, the copepod escapes in this particular interaction.

Figure 4-38 shows the fluid velocity relative to the fish. In this reference frame, the relative velocity in front of the fish mouth and regions immediately surrounding the mouth appear similar. Thus, there is no evidence of fluid entering the mouth of the blenny during its ram feeding. This velocity field thus appears different from that associated with the zebrafish during ram feeding (see figure 4-38). In that case, the zebrafish ingested fluid into its mouth as it approached the prey, allowing it to move forward without pushing the prey away (also see Gemmell *et al*. 2014). However, for the current results, no observation of suction may be attributed to a smaller head size of the blenny (2 mm), compared to 4 mm of the zebrafish, such that any fluid intake might not be resolvable by the spatial resolution (~3 mm) of the tomographic PIV measurement in the current work.

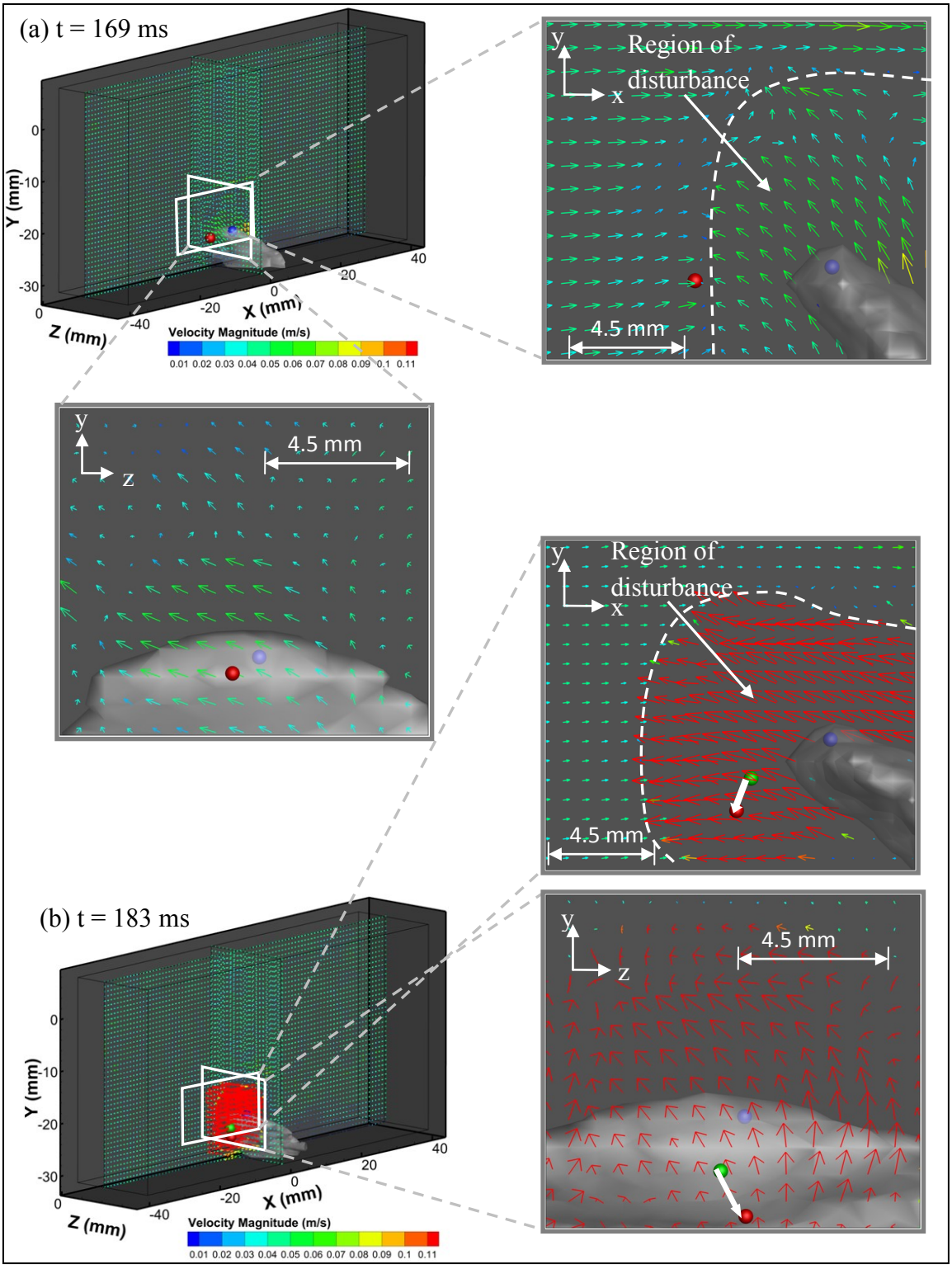

Figure 4-37: Absolute velocity of fluid as blenny attempts to capture copepod at (a) t = 169 and (b) t = 183 ms. The red dot depicts the location of the prey, and blue dot is location of eye center. The green dot in (b) gives the location of the prey at t = 169 ms.

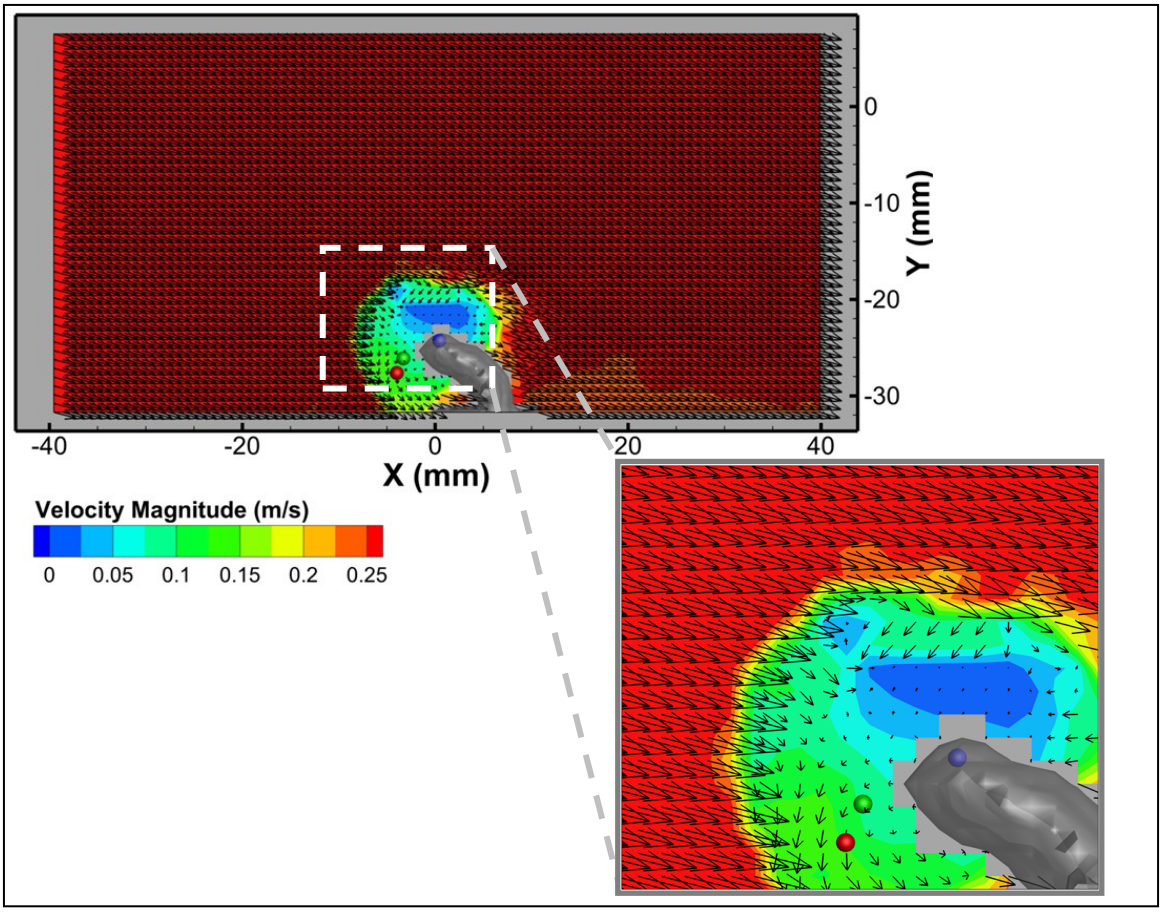

Figure 4-38: Velocity field relative to the fish, at t = 183 ms. Projections of vectors in the x-y plane where copepod is located are shown. Color/contour gives magnitude of 3-component vectors. The green dot gives the location of the prey at t = 169 ms, red dot depicts the location of the prey, and blue dot is location of eye center.

4.3.3 Local flow quantities when copepod escapes

Figures 4-39 to 4-42 show (a) copepod trajectories and (b) graphs of local velocity gradients (maximum principal strain rate, vorticity magnitude, total acceleration) against time. The velocity gradients were measured at the location of the copepod for four different predator-prey interaction events in uniform cross-flow. The local velocity gradient values at the copepod location immediately before its sudden acceleration (or high-speed jump) are marked by dotted circles in the figures. The predator-prey interaction events were carried out in a uniform cross flow with velocity U_0 = 0.0384 for

figures 4-39 and 4-40, and 0.077 m/s for figures 4-41 and 4-42, respectively. The copepod was captured by the blenny in figure 4-40, while it escaped in the other events.

Figures 4-39, 4-41, and 4-42 show more than one jump executed by the copepod. Observation of the vector field sequences showed that the first jump (1) was executed when the copepod entered the region of disturbance generated by the fish during its slow approach (discussed in the preceding section). The second jump (2) was executed when the fish lunged to feed on the copepod. In figure 4-42, a third jump (3) was observed, which occurred after the copepod escaped.

Figure 4-39(a) shows the trajectory of the copepod in the x-y projection. The location of the jump can be identified by a sudden change in direction from streamwise. Figure 4-39(b) shows the local values of maximum principal strain rate (MPSR), vorticity magnitude and total acceleration of the flow at the location of the copepod. Considering the jump locations (1) and (2) in figure 4-39, it appears that the copepod responds to an increase in MPSR for the first jump and then responds again when MPSR increases to over 4.5 s^{-1} for the second jump. For the second jump, which is caused by the fish lunge, the copepod also experiences significant increases in vorticity magnitude and total acceleration (locations denoted by dotted circle).

Figures 4-40 and 4-41 show events with one and two jumps respectively. For figure 4-40, the single jump coincides with the fish lunge and local increase in MPSR. Furthermore, like figure 4-39, the copepod at that location also experienced increases in vorticity magnitude and total acceleration. In figure 4-41, both the first and second jump correspond with increases in MPSR. For this event, however, the corresponding local flow quantities showed that copepod initiates its second jump with increase in MPSR, while acceleration and vorticity show minimal increase.

Figure 4-42 shows three jumps. The first jump does not appear to be a consequence of an increase in MPSR. This could be due to the disturbance occurring at sub-scale resolution of tomographic PIV, since visual observations of the vector field confirmed that the copepod was very close to the disturbance region when it executed the first jump. The

second jump appears to result from increases in MPSR and total acceleration, which corresponded to the fish lunge. Finally, the third jump, which occurred after the copepod escaped the fish, shows an increase in MPSR. However, the third jump is relatively weak, as apparent later in speed-time graph (see figure 4-44b).

For all four events studied (figures 4-39 to 4-42), the MPSR value was $< 4.5s^{-1}$ at the location of the copepod in the first jump (1). The first jump was mainly due to copepod sensing the disturbance region generated by the slow approach of the fish. For the second jump, the MPSR value was $> 7.5s^{-1}$ when the fish lunged to feed on the copepod. The value when fish lunge was generally larger than at time of first jump.

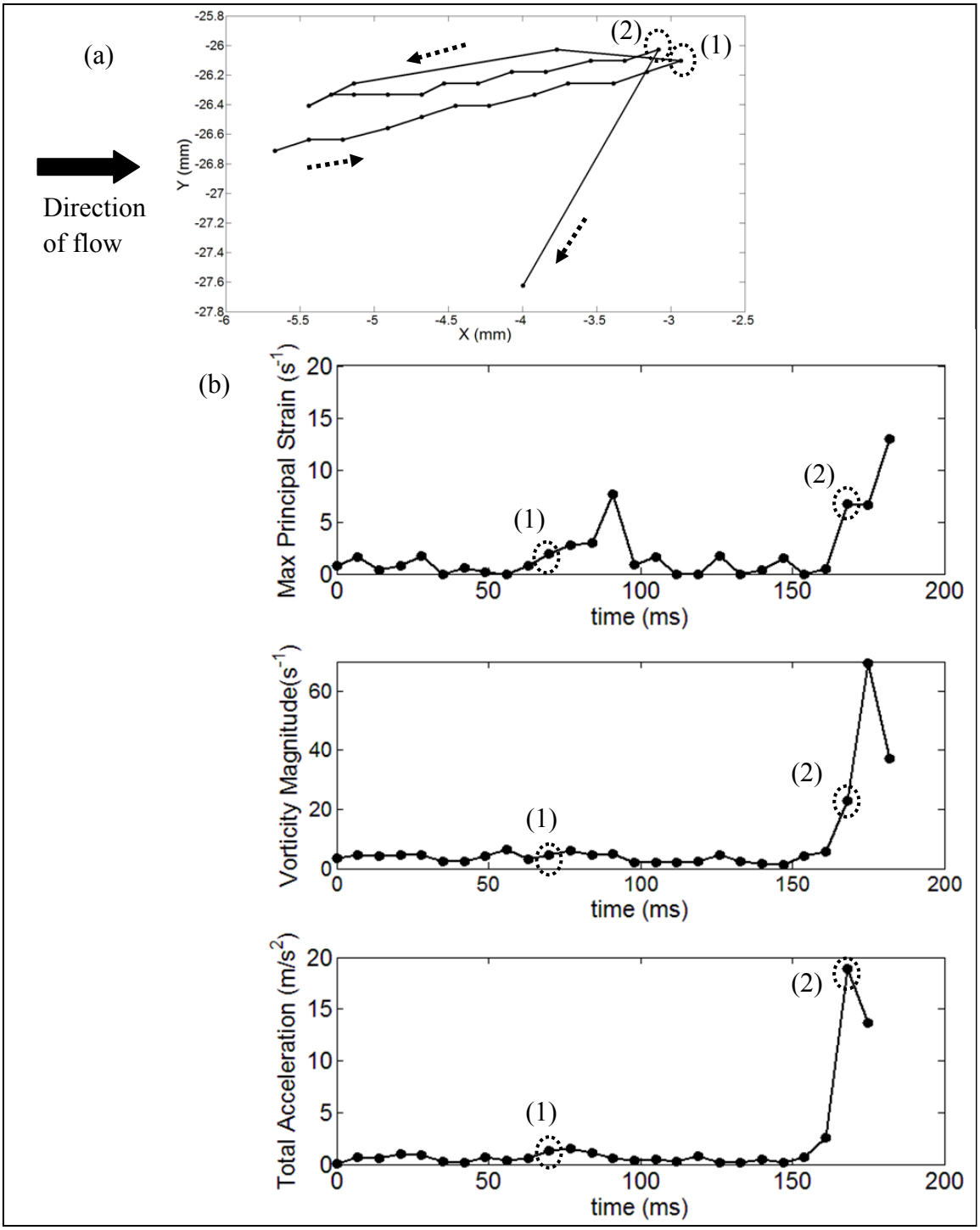

Figure 4-39: (a) Trajectory of copepod from x-y perspective. (b) Velocity gradient values (MPSR, vorticity magnitude, total acceleration) against time graph of the fluid at the location of the copepod as it moves in the trajectory shown in (a). Event corresponds with figure 4-38. $U_0 = 0.0384$

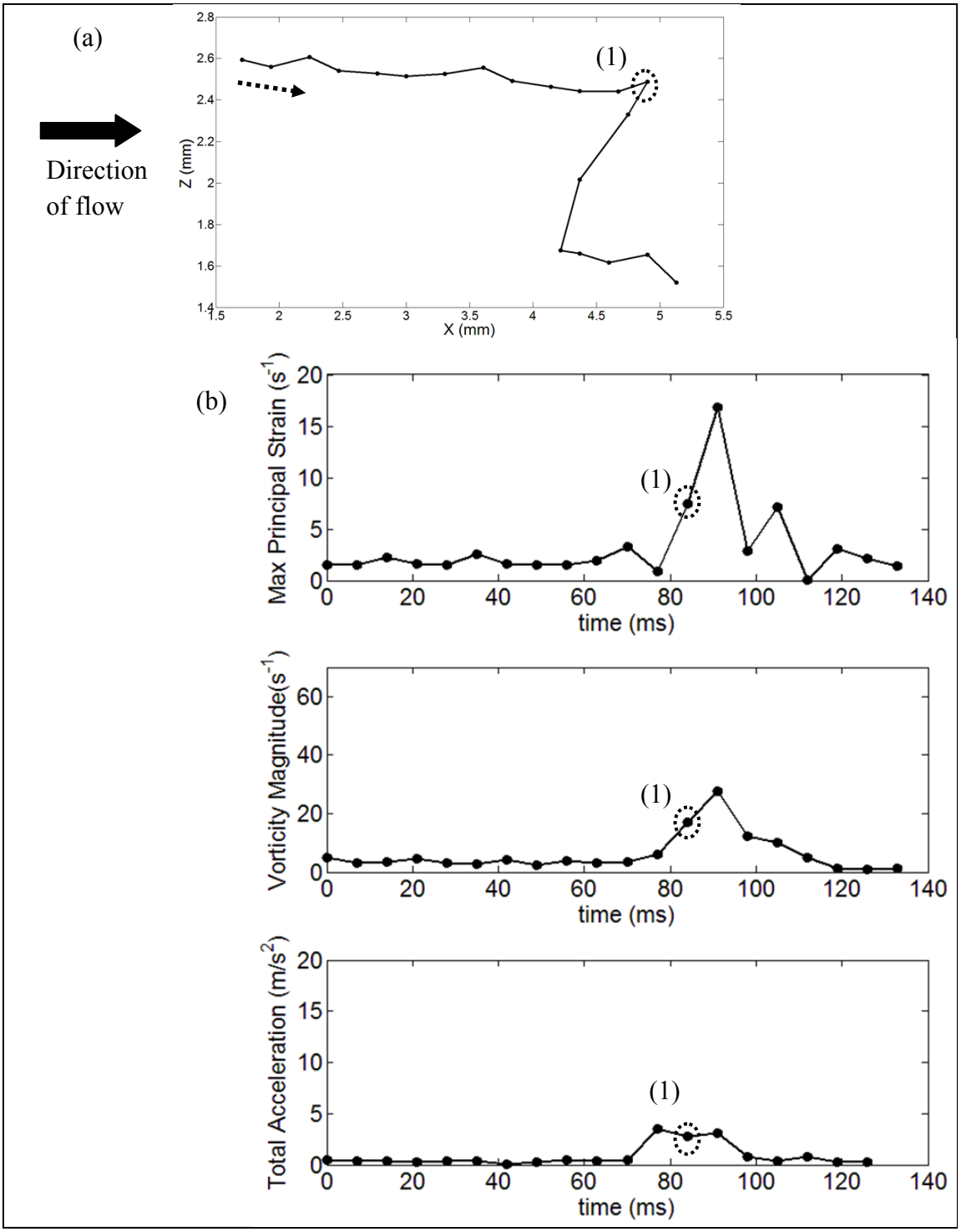

Figure 4-40: (a) Trajectory of copepod from x-z perspective. (b) Velocity gradient values (MPSR, vorticity magnitude, total acceleration) against time graph of the fluid at the location of the copepod as it moves in the trajectory shown in (a). $U_0 = 0.0384$

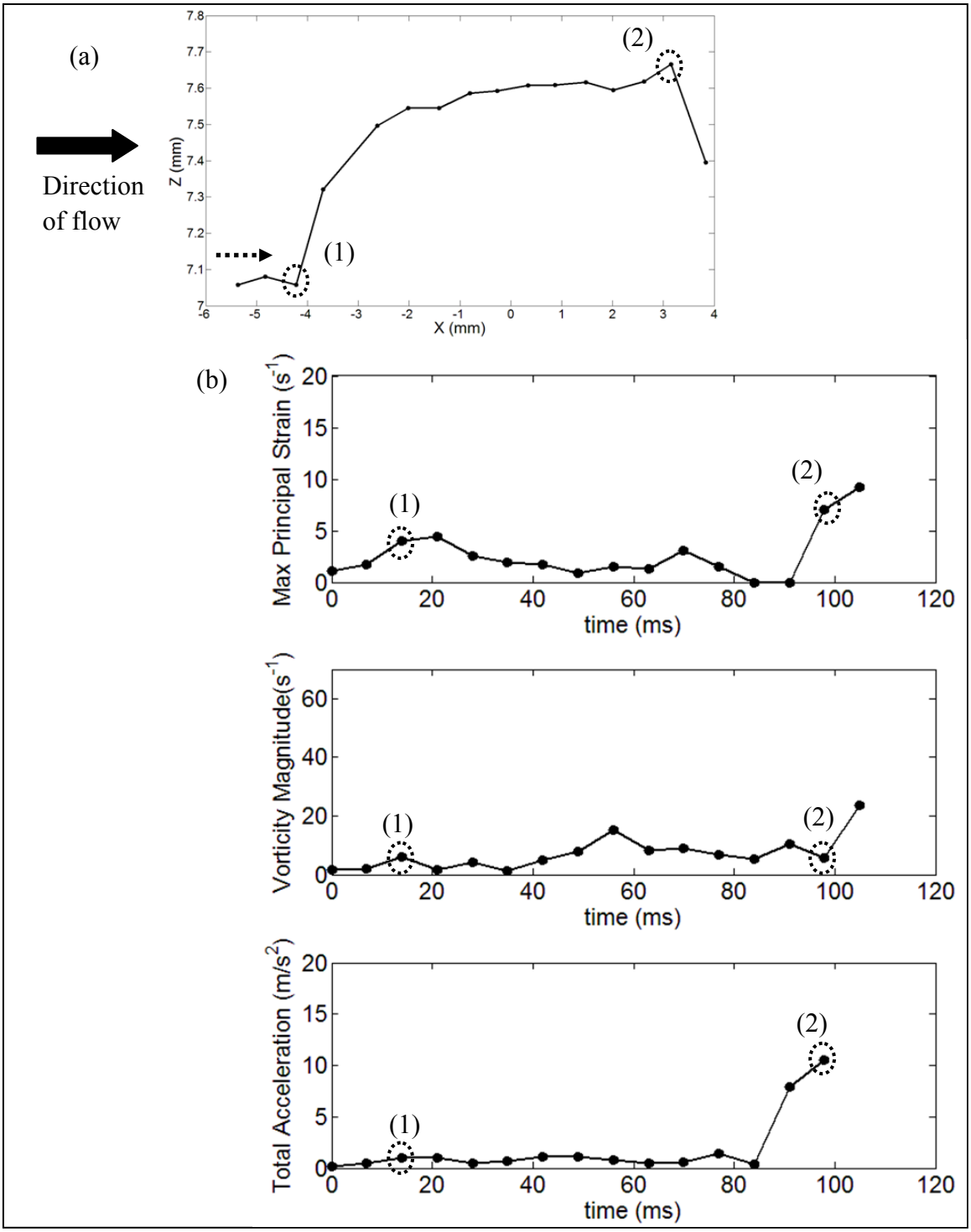

Figure 4-41: (a) Trajectory of copepod from x-z perspective. (b) Velocity gradient values (MPSR, vorticity magnitude, total acceleration) against time graph of the fluid at the location of the copepod as it moves in the trajectory shown in (a). $U_0 = 0.077$

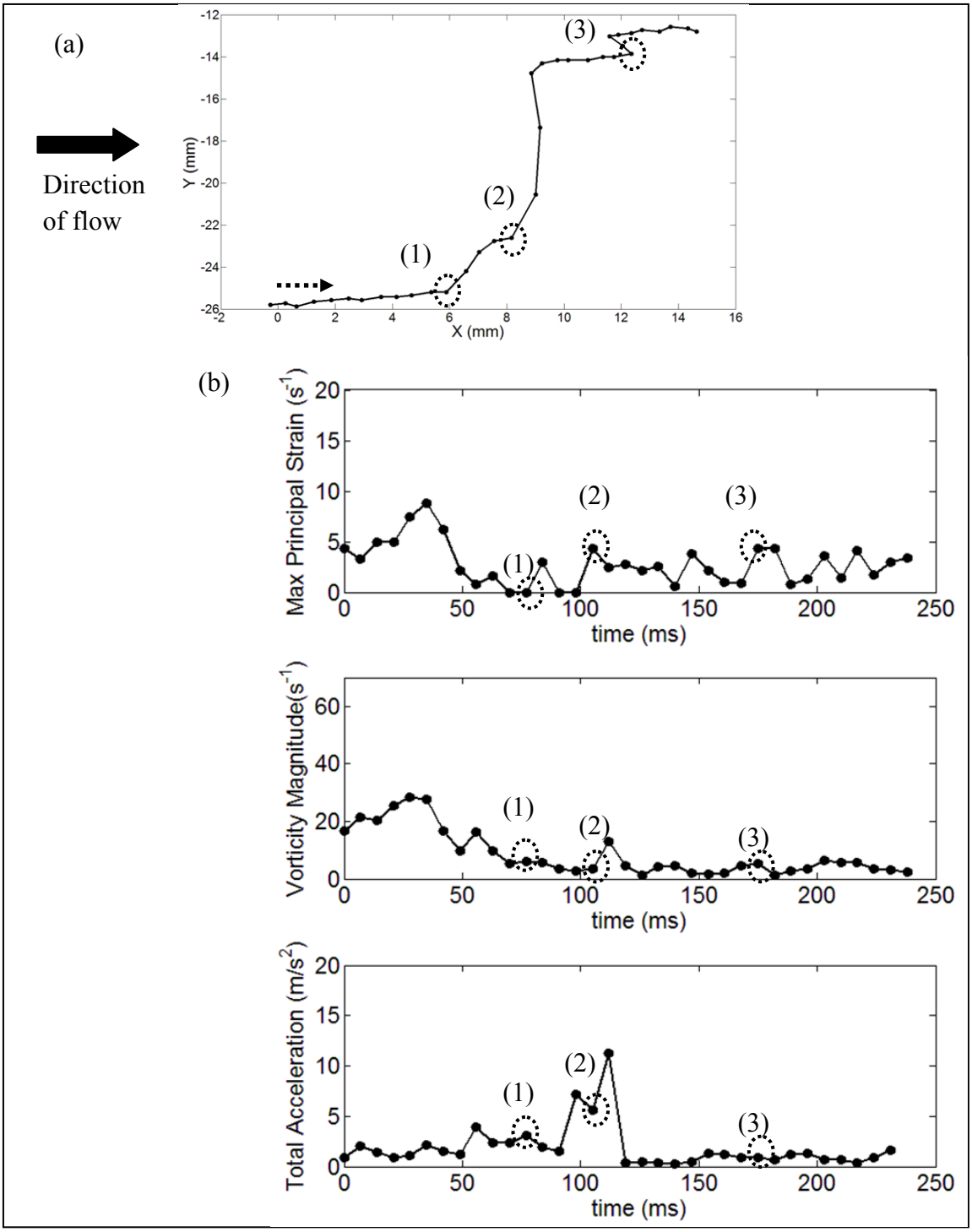

Figure 4-42: (a) Trajectory of copepod from x-y perspective. (b) Velocity gradient values (MPSR, vorticity magnitude, total acceleration) against time graph of the fluid at the location of the copepod as it moves in the trajectory shown in (a). $U_0 = 0.077$

4.3.4 Velocity profile of fish and copepod

Figures 4-43 and 4-44 show speed-time profiles of the fish and copepod for different events with uniform cross flow velocities U_0 = 0.0384 m/s and 0.077 m/s, respectively. Figures 4-43(a), (b), and 4-44(a), (b) correspond to figures 4-39 to 4-42, respectively. In figure 4-43 (b), the fish captured the copepod, while it failed to capture in the other events.

Figure 4-43(a) plots the translational speeds of the fish and copepod through t = 294 ms. The slow approach of the fish (t = 0 − 169 ms) is observed to be relatively constant at ~0.038 m/s, and this speed is similar to the drift speed of the copepod, albeit in a different direction. The measured fish speed increases significantly between t = 169 and 183 ms, during its sudden acceleration. This is followed immediately by a sudden deceleration from t = 183 to 189 ms to a speed ~0.1m/s, which corresponds to the fish retreat until t = 294 ms. Note that the retreat speed (~0.1 m/s) is consistently greater than the approach speed (0.04 m/s), in figures 4-43(a) and (b). This is consistent with the idea that the blenny approaches the copepod slowly to prevent the copepod from escaping. The overall speed-time profile of the fish appears similar for both figures 4-43(a) and (b), with a maximum fish velocity of 0.25 m/s.

The copepod speed-time profile in figure 4-43 shows the copepod drift velocity of 0.038m/s, which matches the free stream cross flow velocity. The copepod escaped in figure 4-43(a), and was captured in figure 4-45(b). In figure 4-43(a), the copepod executes two jumps (starting at t = 70 ms, and t = 169 ms), where the maximum speed of first jump was recorded at 0.2 m/s, and second jump at 0.5 m/s. The acceleration of the copepod and fish appear to be similar in both jumps, but they are not well resolved in this sequence as compared to Experiment (2). The latter jump corresponds to the fish predation and is much higher than the fish speed, while the initial jump corresponds to the copepod entering the region of disturbance during slow approach of the blenny. After the second jump, the speed of the copepod was not recorded since it was captured. In figure 4-43(b), only one jump is observed (starting at t = 154 ms) with maximum speed at

0.15m/s, but at that point, the copepod was captured. The maximum speed of copepod jump is lower than the fish speed in figure 4-43(b).

At higher cross flow velocity (U_0 = 0.077 m/s; see figure 4-44), the speed-time profile of the fish is different. The fish is observed to accelerate slowly up to 0.1 m/s (see figure 4-44a). After which, it accelerates strongly to a speed of ~0.25m/s, and then decelerates back to 0.1 m/s. This sudden acceleration and deceleration is similar to that observed in figure 4-43. Finally, the fish retreats into its housing at speeds of 0.1 m/s. The speed-time profile of the fish is similar for figures 4-44(a) and (b), with a maximum fish velocity of 0.25 m/s.

In figure 4-44(a), the copepod executes two jumps (starting at t = 70 ms, and t = 169 ms). Three jumps are executed in figure 4-44(b); however, the third jump is not apparent from the speed-time graph since the jump is relatively weak. The two jumps observed start at t = 28 ms and t = 56 ms, respectively. For both events, the second jump corresponds to the fish lunge, while the first jump corresponds to the copepod entering the region of disturbance during slow approach of blenny. For figure 4-44(a), the speed of the copepods is not recorded after t = 98 ms since the copepod escaped the field of view of measurement. The maximum speed of the copepod is much higher than the fish in figure 4-44(b), while the speed of the copepod is lower for figure 4-44(a). However, unlike figure 4-43, the copepod escapes the fish predation even when the maximum copepod speed is lower than the fish speed (as shown in figure 4-44a).

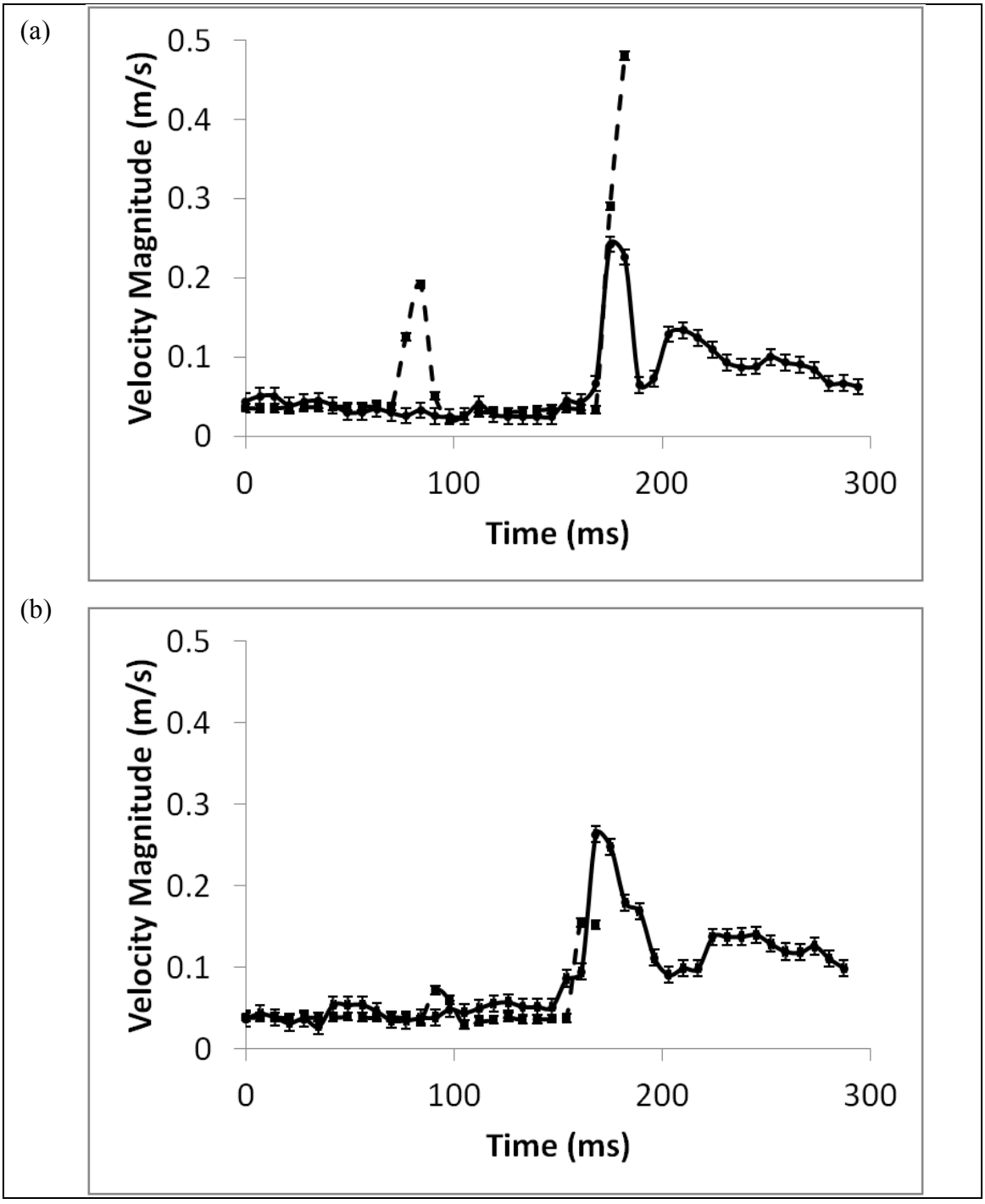

Figure 4-43(a) and (b): The speed-time graph of two different predator-prey interaction events with uniform cross flow velocity, U_0 = 0.0384 m/s. Predator (solid line; ●) and prey (dashed line; ■).

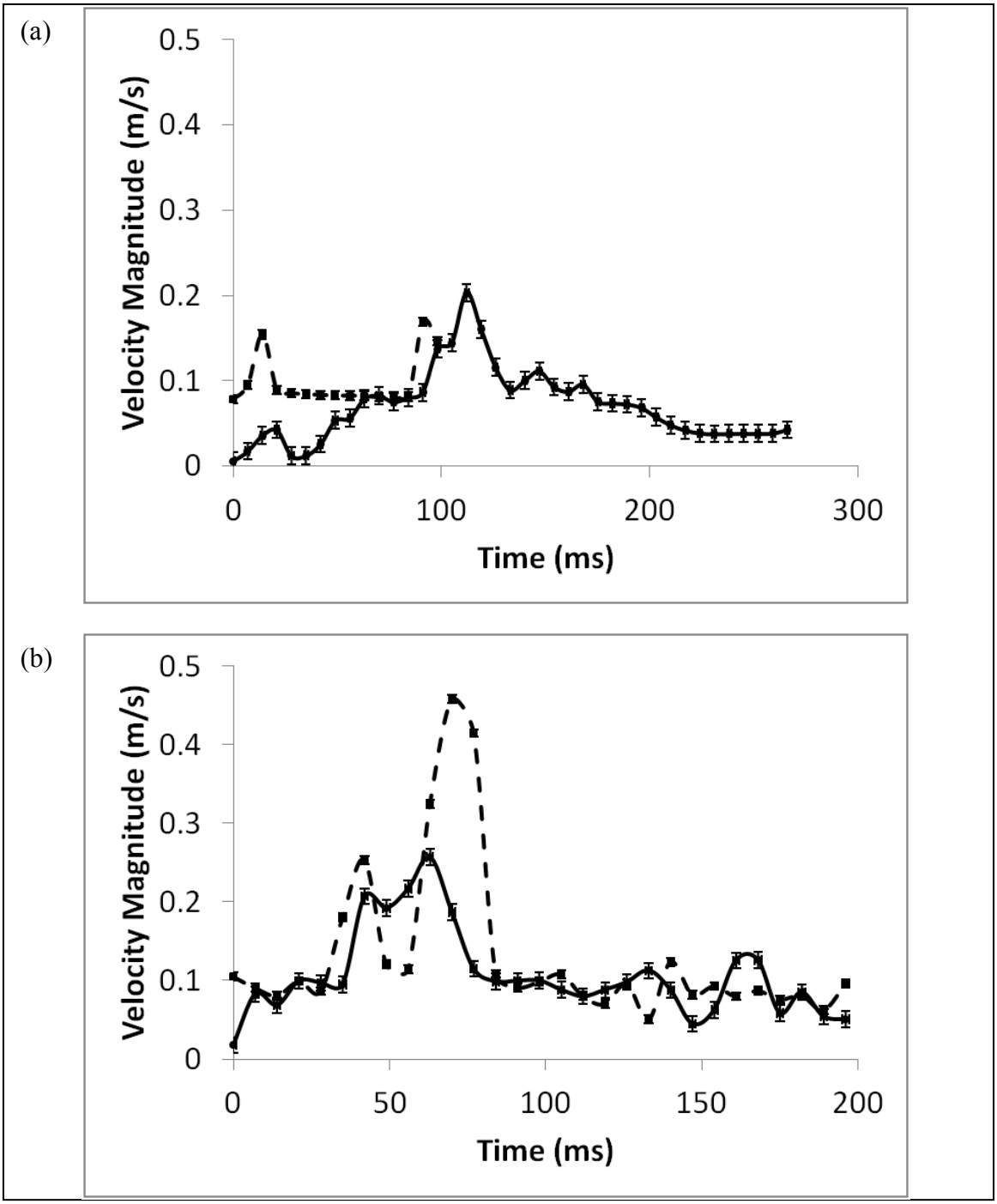

Figure 4-44(a) and (b): The speed-time graph of two different predator-prey interaction events with uniform cross flow velocity, U_0 = 0.077 m/s. Predator (solid line; ●) and prey (dashed line; ■).

Trajectories of the fish and copepod are shown in figures 4-45 (t = 0 - 169 ms) and 4-46 (t = 0 - 98 ms) for the events of predation success (figure 4-45b) and failure (figure 4-46a), respectively. From figure 4-45, we observe that the copepod moves in the positive x-direction due to the drift by the cross flow. Upon sensing the approaching fish moving in positive y-direction, the copepod executes a jump (depicted by a kink in the trajectory) in the same direction. Thus, the direction of the copepod jump towards positive y contributes to the predation success, although the maximum speed of the copepod was higher than the fish.

By comparison, figure 4-46 shows a different trajectory of the fish and copepod. In figure 4-46, the fish moves in the positive y-direction, while the copepod moves in the negative y-direction. This trajectory combination suggests that predation failure in this case may simply depend on the direction of copepod escape, although the maximum speed of the copepod is lower than the fish.

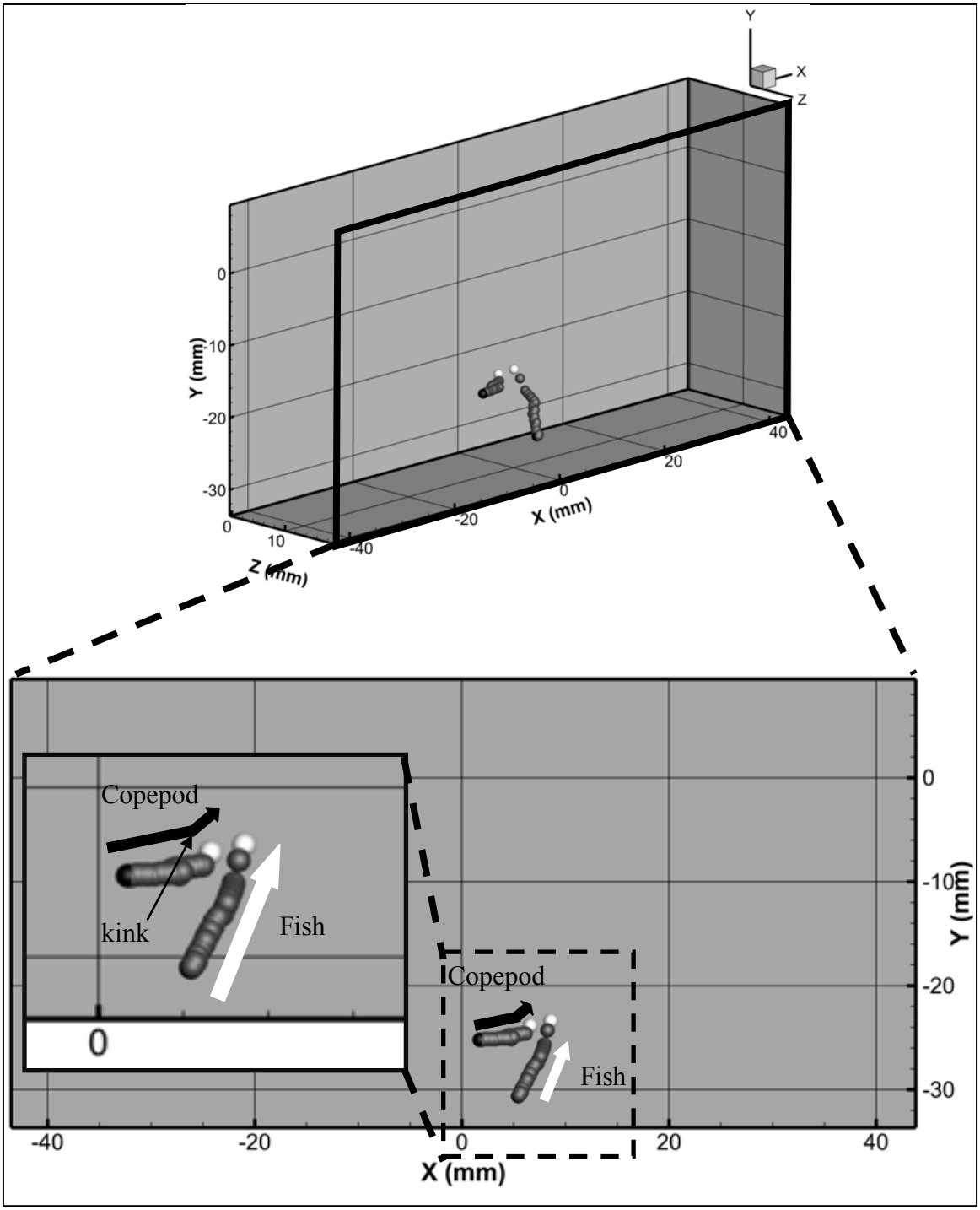

Figure 4-45: Predator and prey tracks with Δt = 7 ms time intervals for success prey capture event of figure 4-41(b). The white sphere shows final location of the prey and predator, while the black sphere gives the initial locations.

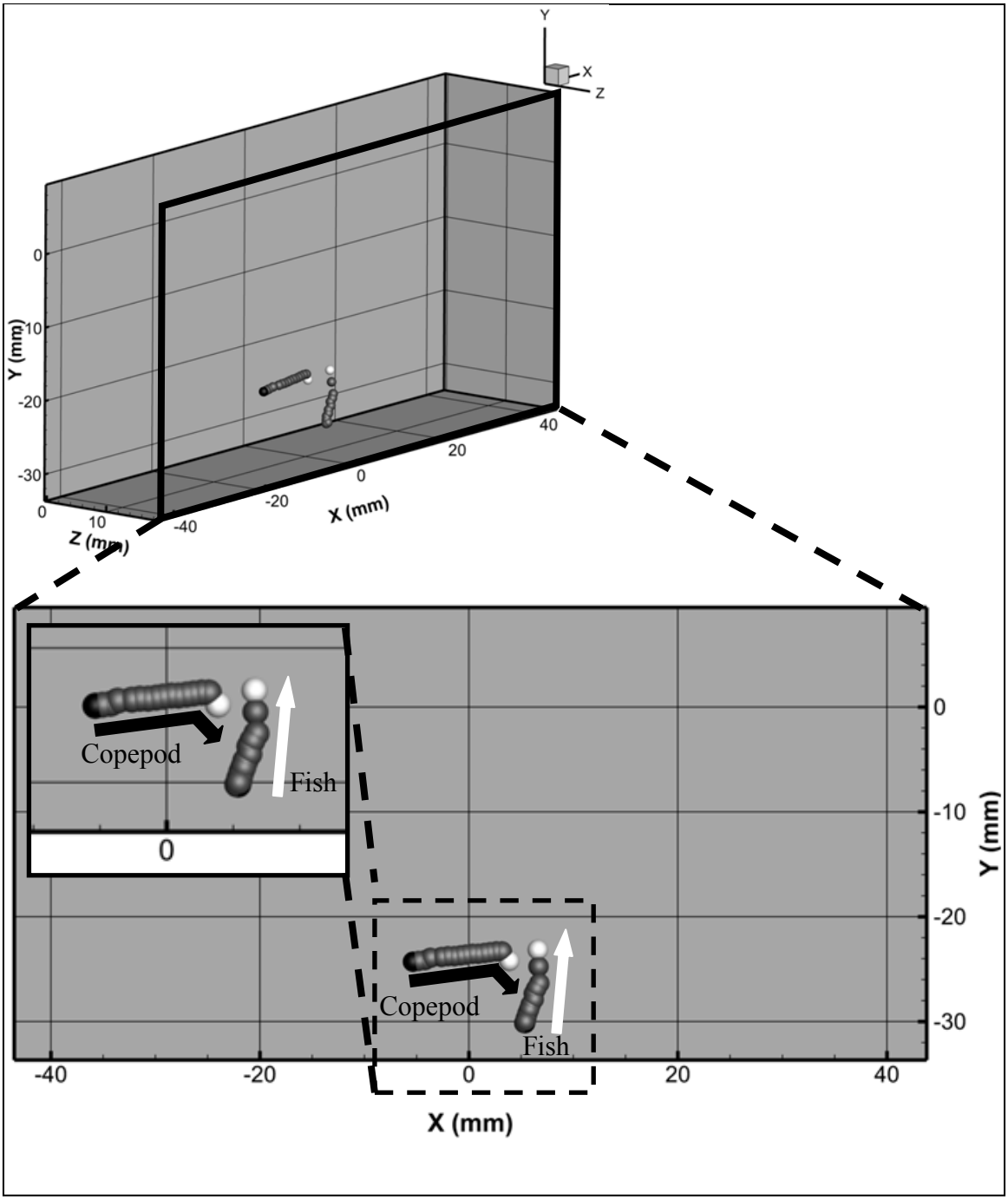

Figure 4-46: Predator and prey tracks with Δt = 7 ms time intervals for failed prey capture event of figure 4-42(a). The white sphere shows location at of the prey and predator immediately after the prey successfully escapes predation, while the black sphere gives the initial locations.

4.3.5 Flow field caused by feeding fish in cylinder wake

Predator-prey (blenny-copepod) interactions in unsteady cross flow (U_0 = 0.077 m/s) in a cylinder wake (d_c = 12.7 mm) were observed for many events. The fish housing was placed direction (1) behind the cylinder, at an offset of (2) 15 mm, and (3) 30 mm in the z-direction to the cylinder. These three conditions were made by placing the cylinder upstream of the housing at x = -80 mm, and z = (1) 9.5 mm, (2) -5.5 mm, and (3) -20.5 mm, respectively. In some cases, the blennies moved out of the measurement volume when attempting to capture the copepod, thus the flow field could not be measured for all events. However, their behavior was observed visually from the 3D PTV cameras. The goal was to create enough turbulence from the cylinder wake such that fish successfully captures most of the copepods. However, based on the visual analysis of all recorded images, the blenny was never able to capture any copepods. General observation showed that the blenny approached the copepod even closer than in the uniform cross flow, before the blenny executed a sudden acceleration. Detailed measurement and analysis of two specific events (an event directly behind the cylinder; and an event with cylinder offset of z = 15 mm) are elaborated.

Figure 4-47 shows a time sequence of (a) images and (b) vector fields for a blenny-copepod interaction behind a cylinder (i.e. unsteady cross-flow). The unsteady flow can be observed from variation in color contours of vector magnitude (see figure 4-47b). In figure 4-47a, from t = 0 – 133 ms, the fish locates and starts to move slowly towards the prey. At t = 140 ms, the fish is already lunging forward to capture the evasive prey (i.e. ram feeding). Due to the sudden acceleration, a larger magnitude, diverging velocity field is observed at t = 140 ms (figure 4-47b). The copepod is observed to escape by moving away when the fish lunges (t = 140 ms). Upon failing to capture the copepod, the fish immediately starts to retreat to its housing (from t = 154 ms). This predation sequence is similar to that of predator-prey interaction in uniform cross-flow (see figure 4-36).

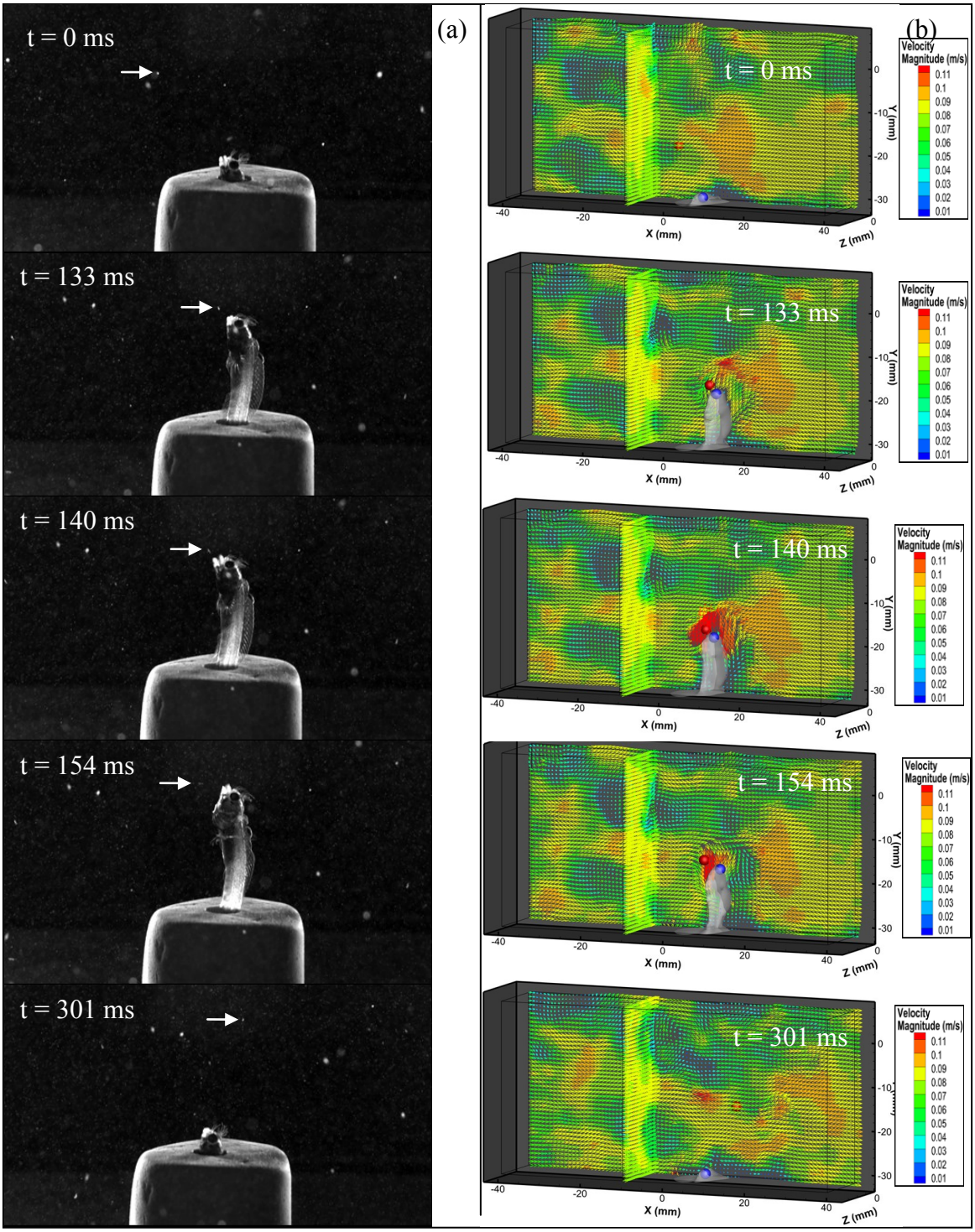

Figure 4-47: (a) Selected image sequences of a fish feeding on copepod behind a cylinder (cylinder location: x = -80 mm, z = -5.5 mm). Red dot depicts the location of the prey. Blue dot is location of eye center. (b) Corresponding fluid velocity fields in absolute frame. Vectors in x-y plane intersect the location of the copepod at t = 140 ms. Free stream velocity, U_0 = 0.077 m/s, and cylinder diameter, d_c = 12.7 mm.

Figure 4-48 shows the detailed views at (a) t = 133 ms and (b) t = 140 ms, just before and during the lunge executed by the fish to feed on the copepod, respectively. In figure 4-48a, the x-y plane shows the unsteady flow field caused by the cylinder wake and the fish. In figure 4-37a (Section 4.3.2), we observed a distinct region of disturbance generated by the fish motion in a uniform cross-flow. However, in figure 4-48a, a distinct region of disturbance is not discernible. Furthermore, the fish in figure 4-48a appears to be very close (~2mm compared to 4 − 5 mm in figure 4-37a) to the copepod before it lunges to feed. This suggests that the unsteady flow field may aid the fish during predation by masking the distinct region of disturbance it creates during its slow approach.

In figure 4-48(b), a distinct disturbance region does appear due to the strong fish acceleration. The velocity magnitude in front of the fish head is much higher than that due to any unsteady flow fluctuations. After a very short latency (~ 2ms), the copepod escapes away from the disturbance region. This suggests that, although the fish may get very close to the copepod during slow approach in unsteady field, the copepod still escapes the fish predation successfully.

Figure 4-49 and 4-50 show (a) trajectories and (b) velocity gradient characteristics of the flow at the location of the copepod in two events in unsteady flow. Figure 4-49 is the same event shown in figure 4-47, while figure 4-50 is measured with the fish housing placed directly behind the cylinder located at x = -80 mm and z = 9.5 mm. For both events, only one jump is observed. This jump corresponds to the time when the fish suddenly accelerates. The local flow characteristics reveal small fluctuations in MPSR, vorticity magnitude and total acceleration while the copepod is drifting with the flow. However, distinct rises in the MPSR (figure 4-50) and acceleration (figure 4-49) values when the fish approaches the copepod are still evident at the location of the copepod jump. Since the cylinder wake includes higher absolute MPSR and acceleration values than the uniform flow cases, the value in MPSR at which the copepod responds appears higher for wakes than for uniform flow. Thus, this indicates that copepods sense a larger increase in MPSR (figure 4-50) and acceleration (figure 4-49) during fish lunge, instead

of merely sensing a simple threshold in an unsteady flow field. This local flow "signal" causes the copepod to execute an escape response from the predator.

Figure 4-51 shows the speed-time profile of the fish and copepod directly behind a cylinder wake with free stream velocity, U_0 = 0.77 m/s. The graph shows the fish approaching the copepod with increasing speed (t = 0 to 21 ms), after which, the fish executes a lunge (maximum speed = 0.25 m/s) at t = 28 ms. Upon sensing the disturbance caused by the lunge, the copepod executes a jump to escape from the fish. Upon unsuccessful predation, the fish retreats to its housing with a speed of 0.1 m/s. The maximum lunge speed of the fish and the retreat speed are both similar to those discussed in figure 4-45.

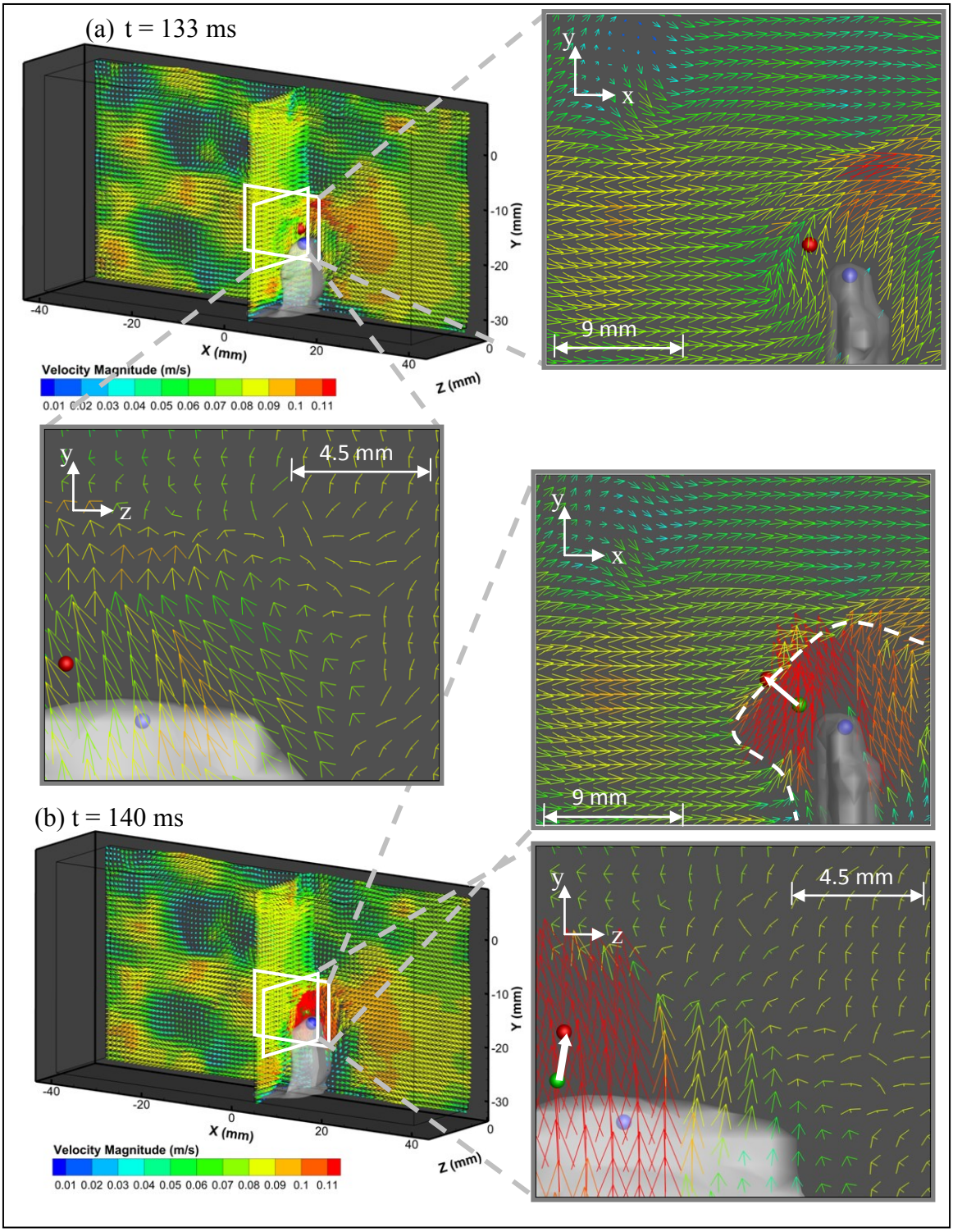

Figure 4-48: Absolute velocity of fluid (a) just before (t = 133 ms), and (b) when (t = 140 ms) the blenny attempts to capture copepod. The green dot gives the location of the prey at t = 0 ms, red dot depicts the location of the prey, and blue dot is location of eye center.

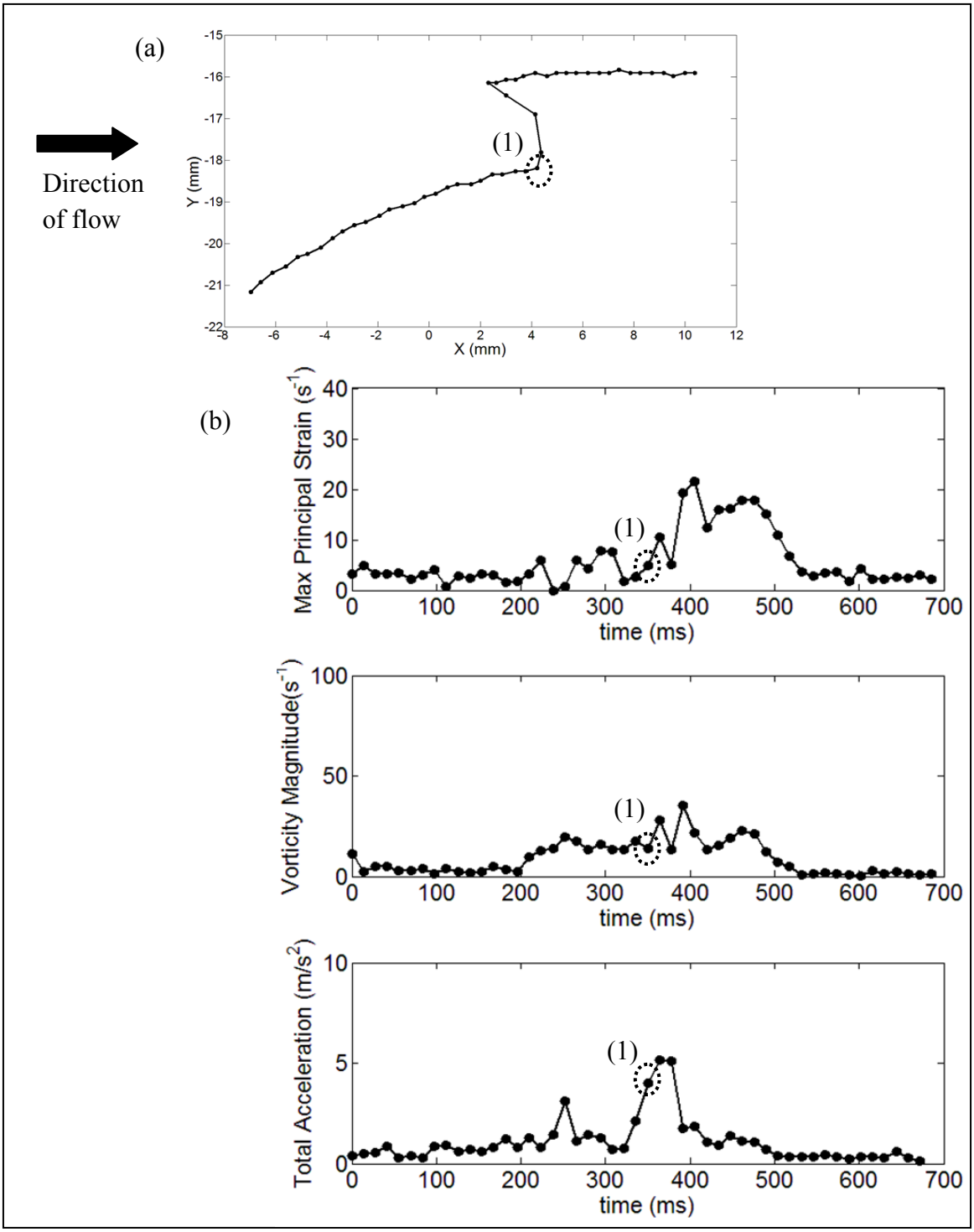

Figure 4-49: (a) Trajectory of copepod from x-y perspective. (b) Velocity gradient values (MPSR, vorticity magnitude, total acceleration) against time graph of the fluid at the location of the copepod as it moves in the trajectory shown in (a). Event corresponds with figure 4-45, $U_0 = 0.077$ m/s

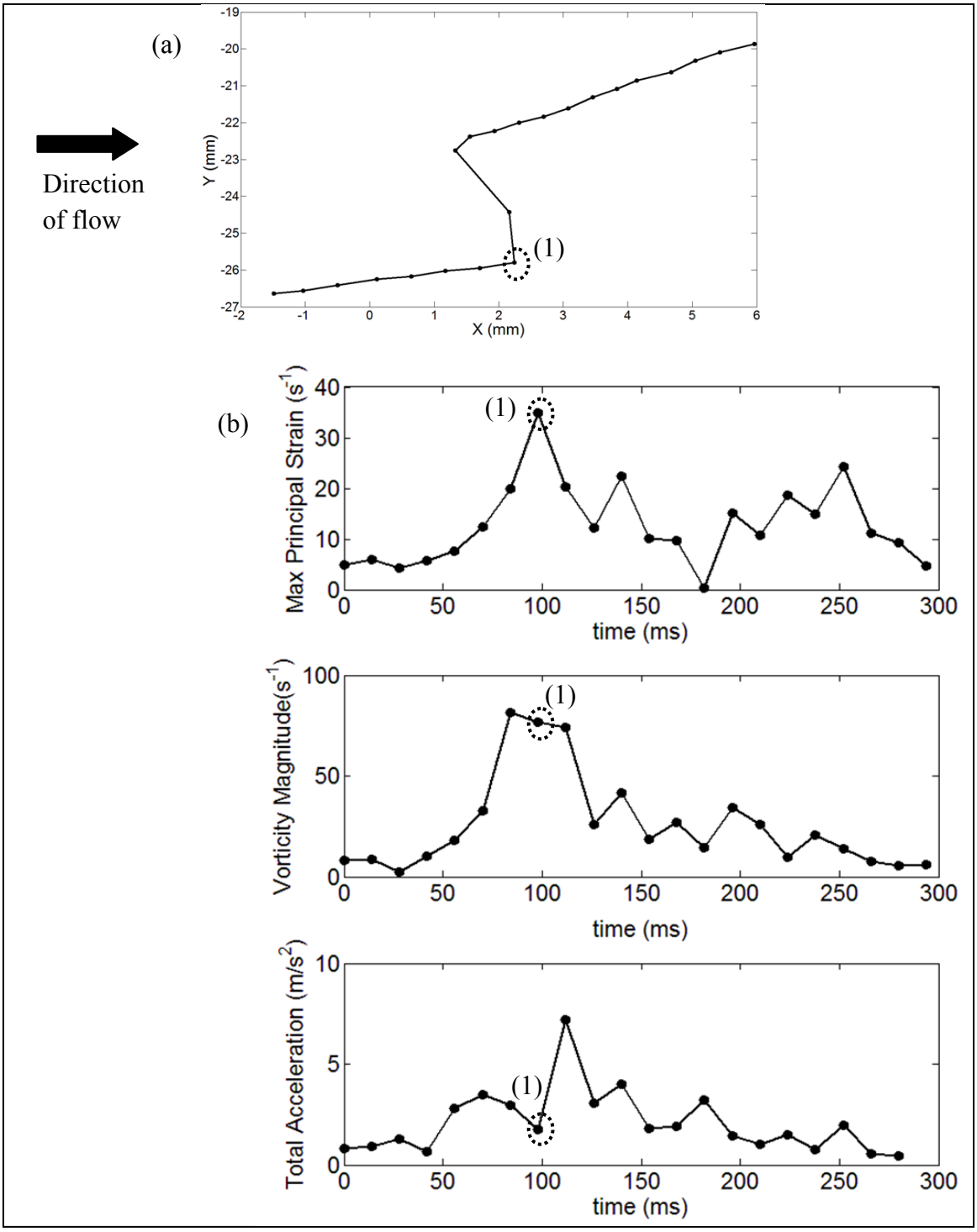

Figure 4-50: (a) Trajectory of copepod from x-y perspective. (b) Velocity gradient values (MPSR, vorticity magnitude, total acceleration) against time graph of the fluid at the location of the copepod as it moves in the trajectory shown in (a). Event carried out with fish housing placed in the cylinder wake (cylinder location: x = -80 mm, y = 9.5 mm), U_0 = 0.077 m/s.

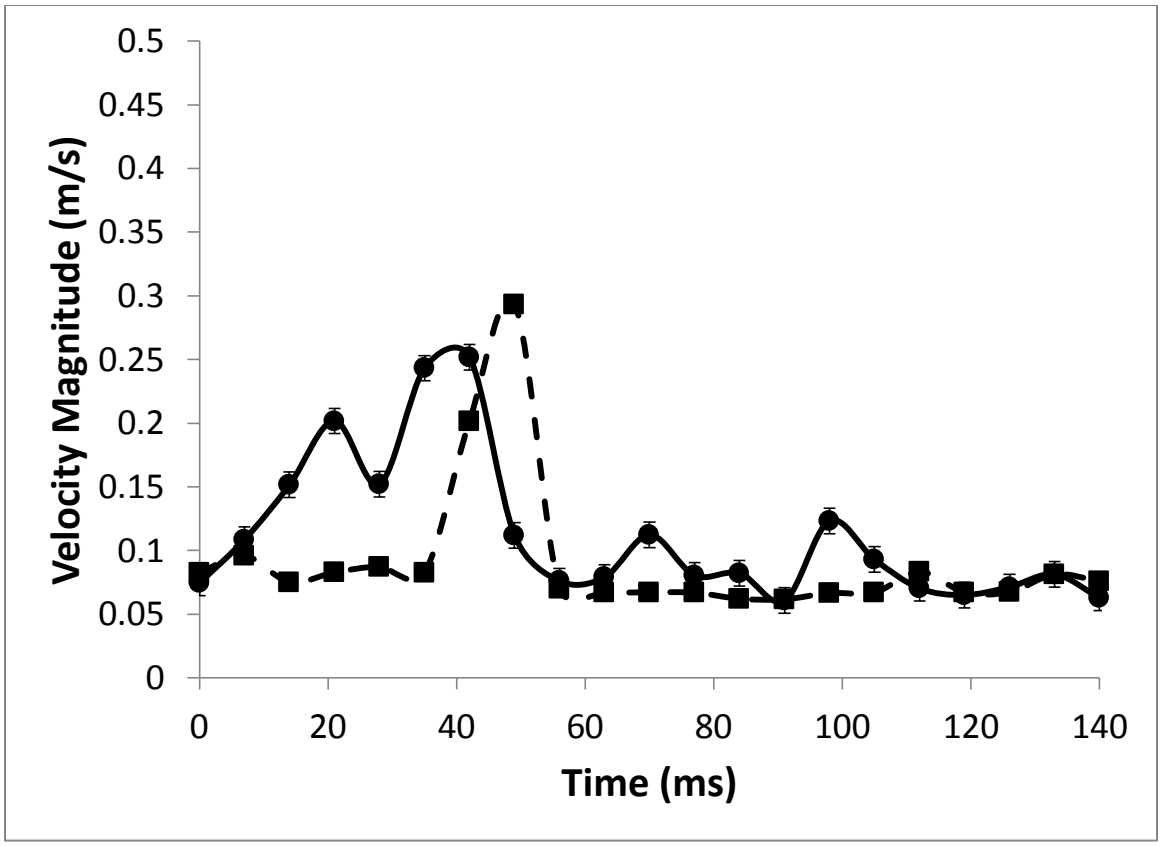

Figure 4-51: The speed-time graph of predator (solid line; ●) and prey (dashed line; ■) with unsteady cross flow velocity within the cylinder (cylinder location x = -80, y = 9.5 mm), U_0 = 0.077 m/s.

Chapter 5

Discussion and Conclusions

The objective of this thesis was to develop a measurement system, and to provide quantitative answers to various biological questions surrounding aquatic predator-prey interactions. Three separate experiments (Experiments (1), (2) and (3); see Chapter 4) were conducted to provide insights into predator-prey (fish-copepod) interactions. A novel measurement system was developed and its applications are discussed in Section 5.1. Specific questions relating to copepod sensing and locomotion are in Section 5.2. Finally, in Section 5.3, the motion and predation techniques of fish on evasive and non-evasive zooplanktons in still and moving/unsteady fluid, are discussed.

5.1 Applications of measurement technique

5.1.1 Infrared tomographic PIV + 3D PTV

Infrared tomographic PIV + 3D PTV was developed and demonstrated to study the fluid dynamics of predator-prey interaction in aquatic environments. Tomographic PIV was used to obtain the volumetric velocity field of the fluid, while 3D PTV tracked the prey, and the eye of the predator. A Circular Hough transform (CHT) algorithm located the eye of the predator automatically in the camera images. An infrared wavelength (808 nm) laser, which is invisible to aquatic organisms but detectable by camera sensors, was used for illumination. This wavelength ensured that organisms maintained their natural behavior during the experiment.

For tomographic PIV, the flow field around the fish and the copepod had an interrogation volume of (3 × 3 × 3) mm and a measurement volume of (80 × 40 × 19) mm for Experiments (1) and (3), while the interrogation volume was (2 × 2 × 2) mm, and measurement volume was (22.5 × 10.5 × 12) mm for Experiment (2). These

measurement specifications show that spatial resolution decreases when the measurement volume increases (provided the number of voxels per interrogation volume remains constant). This means that for a given camera with a finite sensor size, we can increase the measurement volume at the expense of coarser spatial resolution. In the current work, the measurement volume was large enough to study flow around the fish, but the PIV resolution was not sufficient to resolve the details of copepod motion. Thus, 3D PTV was applied to find the trajectory and velocity of the copepods. The 3D PTV was applied to measurement volumes of (80 × 40 × 19) mm for Experiments (1) and (3), and (22.5 × 10.5 × 12) mm for Experiment (2). For Experiments (1) and (3), the 3D PTV could provide location and velocity of the smaller scale copepods with a spatial and velocity uncertainty of 0.04 mm and 0.006 m/s, respectively. For Experiment (2), however, additional cameras were not used for PTV, thus the spatial and velocity uncertainty was 0.02 mm and 0.03 m/s, respectively. However, the current system still lacks the capability to resolve small-scale flow structures around the copepods.

Beyond the experiments carried out, the combined tomographic PIV + 3D PTV technique could also be used to measure particle motions and volumetric velocity fields of carrier fluids in dispersed multi-phase flow (including particle-laden flows), simultaneously. This could provide new insights to behaviors of particles and carrier fluid, which have been studied mainly using photographic techniques, hot-wire anemometry, laser-Doppler anemometry and planar PIV + PTV measurement (Balachandar and Eaton 2010). However, the drawback of this technique is the relatively coarse spatial resolution of the tomographic PIV, which may prevent resolving the smallest eddies and velocity variations surrounding the dispersed particles.

5.1.2 Visual hull method for tomographic PIV

A visual hull technique was implemented to mask out discrete objects (such as fish) appearing within the reconstructed volume in tomographic PIV. Application of the visual hull technique ensured that velocity vectors near the object/fish were not contaminated

during cross-correlation. This was done by masking the volume occupied by the fish using back-projection of the fish silhouette from the images. It was noted that the visual hull is dependent on the number of cameras, arrangement of cameras, object orientation, and the depth of the measurement volume.

Potential applications of the visual hull technique include its use as a masking technique for various multi-camera PIV methods. Mendelson and Techet (2013) have applied the visual hull technique for synthetic aperture PIV, while Murphy (2012) applied it for tomographic PIV with a smaller field of view. Furthermore, visual hull can be applied to facilitate the study of flow around an aerial or aquatic body, or to mask particles in various dispersed multi-phase flows.

The visual hull is a first approach to object reconstruction in three-dimensional space, where the reconstructed volume generally encapsulates the original object. Although visual hull may provide an estimate of an object location or orientation, it does not accurately define it. Thus, the visual hull technique for moving objects in volumetric PIV may promote further research on accurate object reconstruction, which can be useful for flow problems where the object location, orientation and shape are not known *a priori*.

5.2 Copepod sensing and locomotion

5.2.1 What local flow characteristics do copepods sense before they jump?

Local velocity gradients are thought to trigger copepod jumps. In the current work, velocity gradients were divided into three coordinate-invariant quantities (maximum principal strain rate, vorticity magnitude, and Lagrangian acceleration), and the copepod sensing was investigated based on copepods' response and their location.

Previous studies claim that copepods respond to a so-called minimum "strain rate" threshold, which are given by various values including 0.5 – 5 s^{-1} (Kiørboe *et al.* 1999), 1.5 s^{-1} (Fields and Yen 1997), and 0.4 – 12 s^{-1} (Buskey *et al.* 2002). In order to

investigate the variability in these threshold quantities, in Chapter 4.1 (Experiment 1), copepod interaction with a wall-mounted cylinder in cross-flow was analyzed. Experimental measurements and a 2D potential flow model indicated that copepods predominantly responded to MPSR ranging from $0.4 - 5s^{-1}$ upstream of the cylinder. However, it was also found that the lower bound of this range decreased to $0.15\ s^{-1}$ at lower free stream velocity (U_0 = 0.0384 m/s), although minimum MPSR threshold did not vary with different cylinder diameters. Instances of copepods responding to MPSR > $10\ s^{-1}$ were also observed, although the probability of such occurrences was relatively low (< 10 %). Since a range of "threshold" quantities exists and they depend on free stream velocity, it suggests that a simple minimum MPSR threshold may not be the cue that triggers copepod response.

Amongst the invariant quantities obtained within the temporal and spatial velocity gradients, copepods appear to respond to MPSR and Lagrangian acceleration values upstream of the cylinder. Based on 2D potential flow around a cylinder, the Lagrangian acceleration of the fluid, $||d\boldsymbol{u}/dt||$, was found to be related directly to MPSR such that, $||d\boldsymbol{u}/dt|| = ||\boldsymbol{u}|| \times MPSR_{potential.}$ It was also noted that for any steady and irrotational flow, Lagrangian acceleration and MPSR are related by an inequality $||d\boldsymbol{u}/dt|| \leq ||\boldsymbol{u}|| \times MPSR$, and this inequality was satisfied by the experimental results. This suggested that the Lagrangian acceleration can be related to MPSR upstream of the cylinder. Vorticity values upstream of the cylinder, however, were generally small, and copepods did not appear to respond to these vorticity values. Thus, in the current work, copepods appear to be influenced predominantly by MPSR.

While copepods were found to respond to relatively low MPSR values upstream of the cylinder, the copepods appeared at locations with MPSR exceeding $20s^{-1}$ downstream of the cylinder. Furthermore, downstream of the cylinder, the distribution of MPSR at copepod locations was no different from that for non-evasive brineshrimp, which are not known to respond to MPSR. In addition, visual observation showed that copepods rarely jumped within the wake of the cylinder. Thus, this further illustrated that the

hydrodynamic cue triggering the copepods' response is more complex than a simple MPSR threshold value.

In Experiment (3) a fish approaching a copepod in a cross flow was studied. When a fish approached a copepod, the local MPSR at the location of the copepod was found to increase in most events. It was found that the increase in MPSR triggered the copepod to execute a jump. In most cases, copepods escaped the fish in still and moving water. Some copepods, however, did not manage to escape the fish successfully. This was due to inappropriate direction of copepod jumps. Instances of copepod capture were discussed in Experiment (2) and (3) where copepods jumped in the direction of the fish mouth as the fish was moving towards the copepod. This allowed the fish to feed successfully on the prey. If the copepod had jumped in the different direction to the direction of approach by the predator, its escape would have been successful.

Results based on Experiments (1), (2) and (3) suggest that copepods respond to a large and sudden increase in MPSR, instead of a simple MPSR threshold quantity.

5.2.2 What is the direction and maximum speed of copepod jumps?

Based on the interaction of copepods with a wall-mounted cylinder in cross-flow it was found that, as the copepods approached the cylinder, most jumped away from it. This showed that copepods have some ability to sense the direction of an approaching cylinder, and suggests that they can also sense and jump away from an approaching predator.

The copepods were found to jump predominantly at a maximum speed (slip velocity) of $0.06 - 0.07$ m/s when approaching a wall mounted cylinder. However, the range of maximum speeds increased with the free stream velocity. This may suggest that jumping characteristics (e.g. maximum speed) of the copepod may be dependent on the sensing characteristics (e.g. increase in MPSR or acceleration).

5.3 Fish motion and predation

5.3.1 What is the strategy for successful fish predation on copepods?

In Experiments (2) and (3), we observed that the fish first executed (1) a slow approach towards the prey, followed by (2) a sudden acceleration (ram feeding mode) to capture the copepod, successfully. How slow should the fish move towards the copepod? How close should the fish get before executing the ram feeding? Does this strategy always result in predation success? Although answers to these questions are not obvious from the experimental observations, we can apply a potential flow to model the fish motion and predict strategic outcome of the "slow approach, sudden acceleration" - type feeding executed by the fish. Before attempting to understand the successful predation strategy, we first attempt to model the flow field around free-swimming fish.

During its free swimming, the flow field in front of a fish head appears to diverge. Heuch *et al.* (2007) measured the flow field using planar PIV, and their results suggested a diverging flow field in front of the fish head. In Experiment (2), similar diverging flow was observed in front of the zebrafish head during free swimming, although the flow field was not strictly axisymmetric. A similar flow field was also observed for a blenny (Experiment 1) when it approached to feed on the copepod. Since the Reynolds number of fish swimming was relatively high (Re > 100), a simple approach to model fish swimming is a diverging potential flow.

We apply a potential flow Rankine fore-body model, which consists of a uniform flow and a three-dimensional source, to mimic flow around a fish head (see figure 5-1). The streamfunction of this model is given as (Panton 1996):

$$\psi(r,\theta,\phi) = \frac{1}{2}U_0 r^2 sin^2\theta - \frac{m}{4\pi}(1 + cos\theta) \qquad (5\text{-}1)$$

where $m = 4\pi U_0 R^2$; R is the distance from the source to the stagnation point (R is related to the size of the fish head); U_0 is the free stream velocity, $\theta = 0^\circ$ for the configuration in figure 5-1(a); r is the distance from the source. Considering a reference frame of a fish moving at $U_{fish} = U_0$ (see figure 5-1b), the first term in equation 5-1 can be removed.

This results in a simple moving source term (as depicted in figure 5-1c), where the streamfunction and radial velocity, respectively, are given by

$$\psi(r,\theta,\phi) = -\frac{m}{4\pi}(1+cos\theta) \tag{5-2}$$

$$v_r = \frac{1}{r^2 sin\theta}\frac{\partial\psi}{\partial\theta} = \frac{m}{4\pi r^2}\,, \tag{5-3}$$

where the source is moving at velocity U_{fish} from right to left. Since potential flow is Laplacian, changes to the flow field are felt immediately throughout the domain as the source moves.

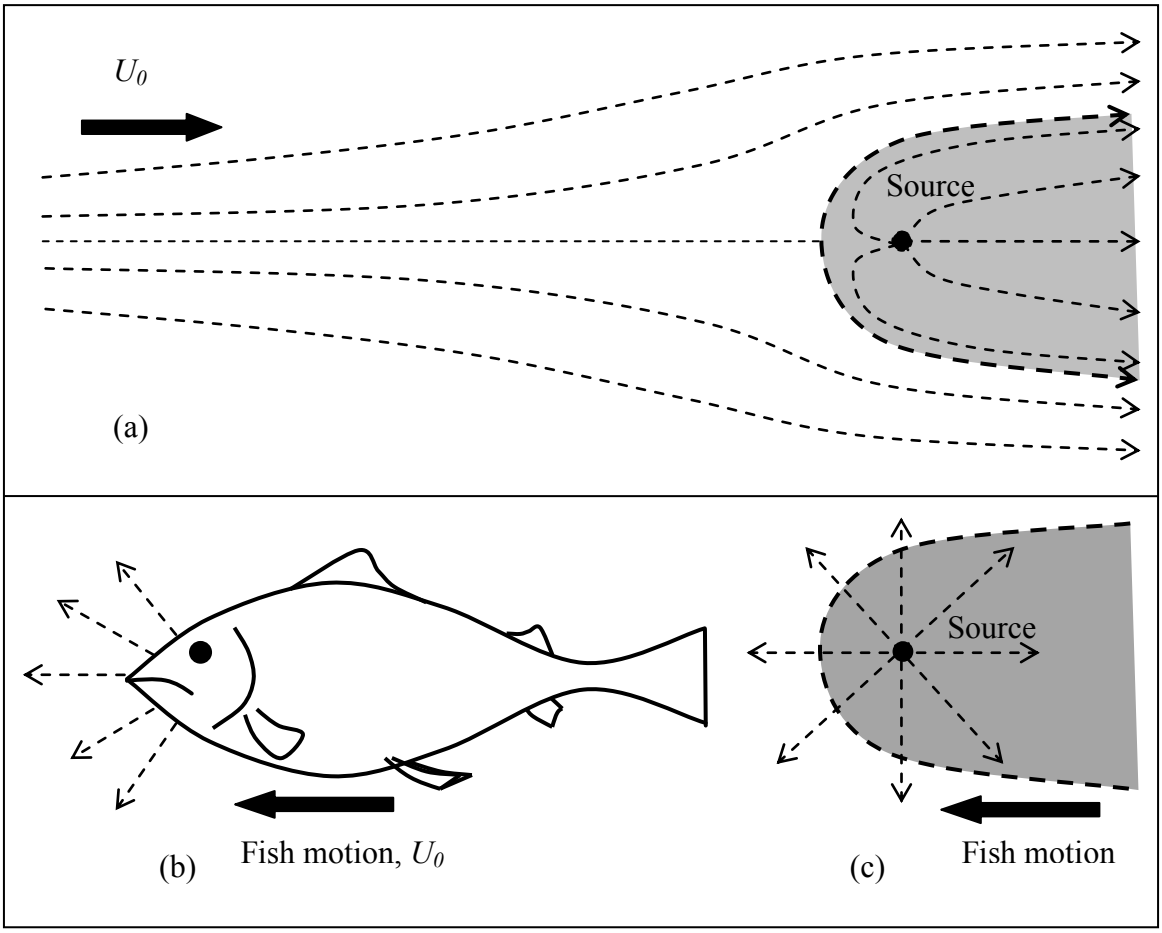

Figure 5-1: (a) Schematic representation of axisymmetric Rankine body model. (b) Schematic representation of the diverging flow generated by the fish during its motion, and the (c) moving source based on the Rankine body model.

In steady flow upstream of the cylinder (Experiment 1), copepods responded predominantly to local MPSR within 0.5 - $5s^{-1}$. In a uniform flow or quiescent fluid, we assume that the fish moves slowly towards the copepod until the local MPSR at the location of the copepod increases to $5s^{-1}$. Beyond this value, we assume the copepods jump, since the probability of the copepod escaping when MPSR > $5s^{-1}$ is high in steady or quiescent fluid. For the axisymmetric moving source fish model (equation 5-2), the MPSR value at the location of the copepod is given by MPSR = $2U_{fish}R^2/r^3$, where r is the distance of the source away from the copepod; R is the distance from the source to the estimated "mouth of the fish" which is assumed to be 2 mm for this study. The cubic dependence on r shows that the fish disturbance drops off very rapidly with increasing distance from the fish head.

Consider an initial location of a copepod 40 mm away from the fish model (see figure 5-2). First, the fish slowly approaches the copepod with a given U_{fish} until the MPSR value at the location of the copepod reaches $5s^{-1.}$ Based on observations in Experiment (3), the velocity of the fish during slow approach was U_{fish} = 0.03 m/s, and the maximum speed attained by the fish, during ram feeding, was 0.25 m/s. In Experiment (2), the maximum value attained by a zebrafish during ram feeding was 0.5 m/s. In figure 5-3, the graph of MPSR against distance of fish from the copepod for fish approach velocities, U_{fish} = 0.03 m/s, 0.25 m/s, and 0.5 m/s, is plotted. The fish model approaches closest to the copepod when its velocity is lowest. Thus, this suggests that the initial slow approach of the fish aids in letting it get closer to the copepod without incurring MPSR > $5s^{-1}$ at the location of the copepod. Although velocity slower than 0.03 m/s could lead to even closer approach to the copepod, more time may be required for the fish to reach that location. By that time, the copepod may have already moved away due to other factors (e.g. disturbance from ambient flow, attacks from other predators).

From figure 5-3, the closest distance to the copepod such that U_{fish} = 0.03 m/s and MPSR $\leq 5s^{-1}$, is 3.63 mm. Since the zebrafish mouth is assumed to be R = 2 mm (R is expected to be even smaller for blenny) away from the source, the distance between the fish mouth and the copepod is 1.63 mm. For cases studied in Experiment (2), experimental results of

zebrafish showed larger approach distances. Starting at this approach distance, the fish accelerates and executes ram feeding.

During ram feeding, the copepod typically senses the flow disturbance caused by the sudden acceleration of the fish and jumps. The response latency of the copepod after sensing the local flow disturbance is assumed to be $t_{latency}$ = 2 ms based on our experimental observations (also noted by Lenz and Hartline 1999). The time required for the fish to catch the copepod is given by $t_{ram} = s_{close} / U_{ram}$, where U_{ram} is the average velocity of the fish during ram feeding, and s_{close} is the closest distance from the fish mouth to the copepod before ram feeding. We assume the value of U_{ram} = 0.25 m/s based on the maximum ram velocity measured in Experiment (3). The time taken for the fish to capture the copepod is $t_{ram} = s_{close}/U_{ram}$ = 6.5 ms which is obviously greater than $t_{latency}$. This result suggests that the fish might not be able to capture the copepod before it escapes even after utilizing the "slow approach, sudden acceleration" technique. This is consistent with the results of the zebrafish feeding on copepods, where the copepods escape if the fish does not execute other flow manipulation techniques (such as suction).

Although the theoretical model shows that the "slow approach, sudden acceleration" technique applied by the fish may not be sufficient for predation success, some events of predation success were observed experimentally. Both Experiments (1) and (2) suggested that successful predation could be attributed to the copepod jumping in a direction in line with the fish ram trajectory. Furthermore, evidence of fluid suction during ram feeding observed in zebrafish (see Chapter 4.1; Gemmell *et al.* 2014) would decrease the extent of the disturbance zone and facilitate hydrodynamic stealth during ram feeding. In addition, for unsteady flows, copepods were found to respond to large increases in MPSR, thus, the s_{close} value could decrease sufficiently since MPSR values 'suddenly' increase only when fish the is very close to the copepod. When s_{close} decreases, t_{ram} also decreases allowing the fish to increase probability of capture before the copepod escapes.

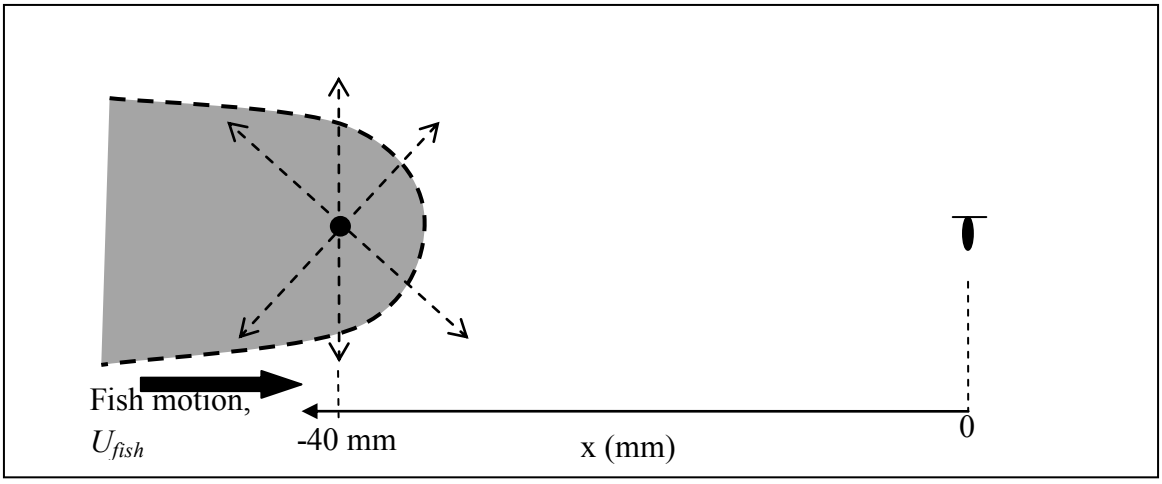

Figure 5-2: Schematic representation of the fish model (i.e. moving source) moving towards a copepod. The distance from the source to the nose is R = 2 mm.

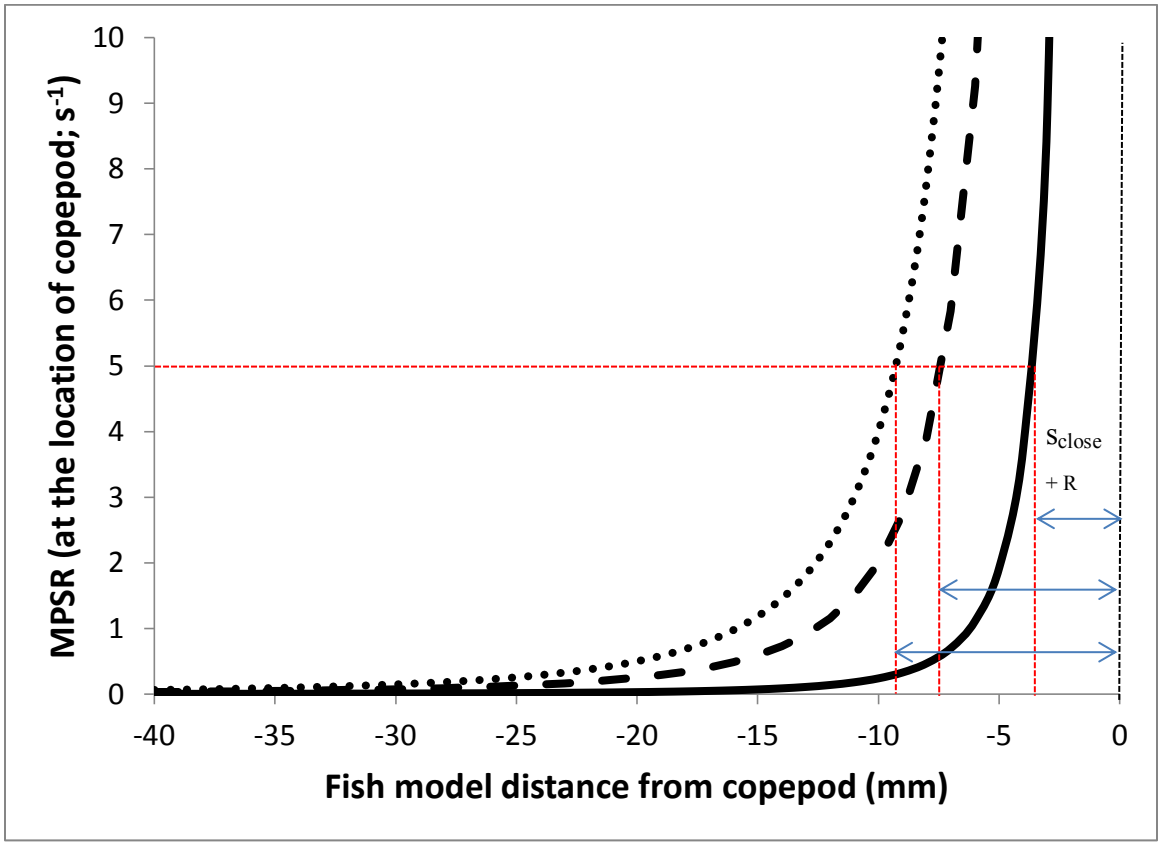

Figure 5-3: Graph of MPSR at the location of the copepod against the distance of zebrafish model from the copepod. The graphs are plotted for U_{fish} = 0.03 m/s (solid line; —), 0.25 m/s (dashed line; - -), 0.5 m/s (dotted line; · ·).

5.3.2 How do fish capture non-evasive and evasive prey?

Fish capturing non-evasive (e.g. water flea) and evasive (e.g. copepods) prey was investigated in Experiment (2). For capturing non-evasive prey, a zebrafish lifts its head and executes suction feeding to draw the prey into its mouth (see figure 5-4). Since a free swimming fish creates a diverging flow in front of its mouth (as explained in Section 5.3.1), the flow may push the prey away as the fish attempts to feed on it. Suction feeding helps to draw the prey towards the fish as it approaches. During suction feeding, a vortex was formed near the head of the fish. The possible mechanism for the vortex generation is shown in figure 5-4. The combination of fluid being pushed by the impulsive head motion, and drawn by suction feeding can result in formation of a rotational flow field (or a vortex) as depicted in figure 5-4.

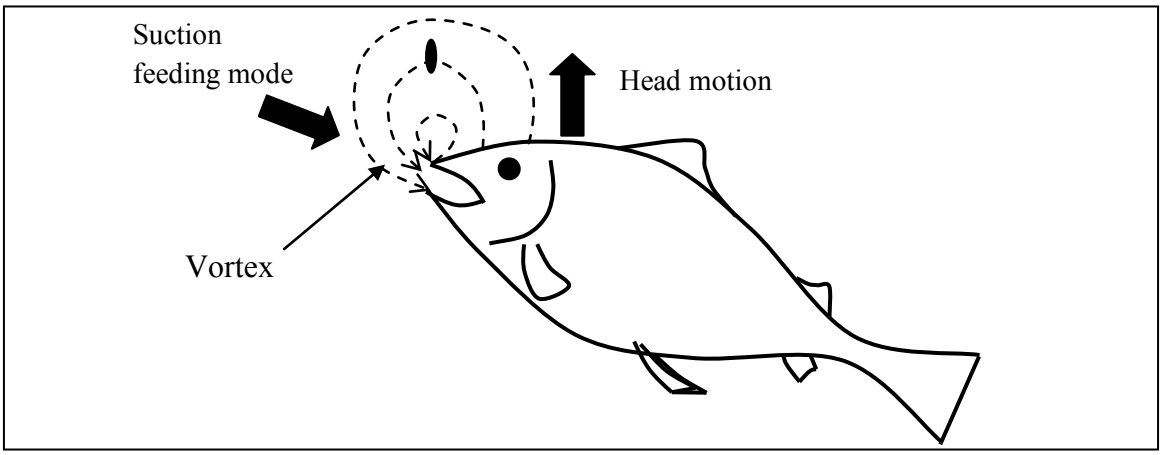

Figure 5-4: Schematic representation of suction feeding on non-evasive prey. The generation of a vortex near the fish head is shown as a result of head motion and suction.

For capturing evasive prey, Experiments (2) and (3) showed that a fish generally applies a two-step strategic approach. First, the fish slowly approaches a prey (step 1), and then makes a sudden acceleration (i.e. ram feeding; step 2) in an attempt to capture it (see figure 5-5). The prey, a copepod for example, will be able to sense a flow disturbance generated by the fish and attempts to escape. The response latency of the copepod after sensing the flow disturbance has been found to be shorter than 2 ms (estimated by

visually observing recordings at 500 fps; also see Lenz and Hartline 1999). From Experiments (2) and (3), it was found that predation success depends on the direction and velocity of the fish predation and copepod escape. Section 5.3.1 provided a simple model that suggested that "slow approach, fast acceleration" technique alone does not provide enough time for the fish to capture copepods. Instead, flow manipulation (such as suction by the fish or external turbulence) is necessary to ensure higher predation success rate.

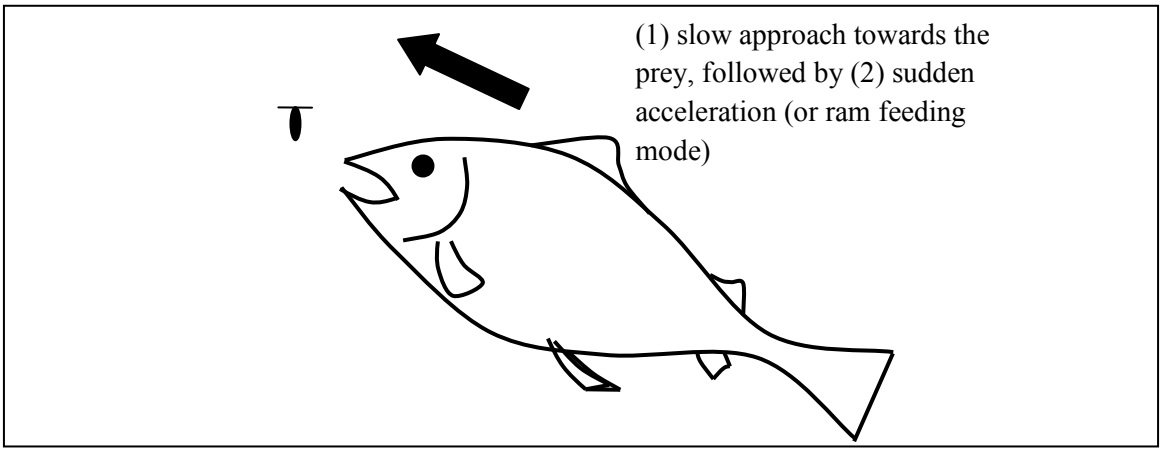

Figure 5-5: Schematic representation of feeding on evasive prey. This feeding technique occurs in a two-step process. (1) Initial slow approach towards the prey, followed by (2) a sudden acceleration (ram feeding mode) to capture the prey.

Similar to capture of evasive prey in still water, in a uniform cross-flow, the fish approached an evasive prey (e.g. a copepod) slowly, and executed ram feeding when it was sufficiently near the prey. During its motion, the fish generated a disturbance region (depicted in figure 5-6) such that MPSR increased rapidly when the copepod entered this disturbance region. In Experiment (3), we observed the presence of this disturbance region during both slow approach and sudden acceleration (or ram feeding). However, the forward extent of the disturbance region was shorter during slow approach as compared to ram feeding.

When the cross-flow is unsteady, the disturbance region is not distinct during slow approach. This suggests that the copepod did not experience a sudden increase in strain rate even when the copepod was very close to the fish mouth. However, when the fish

executed a sudden acceleration to feed on the copepod, a distinct disturbance region formed, which triggered the copepod to jump and escape. It can be extrapolated from this observation that if fluctuations in the ambient velocity field are high enough, no obvious disturbance region would be present during ram feeding, and thus, the likelihood of the copepod capture would increase. This is likely the reason behind the observation of Buskey *et al.* (2002), Clarke *et al.* (2005), and Clarke *et al.* (2009) that capture rates increases in turbulence compared with laminar conditions.

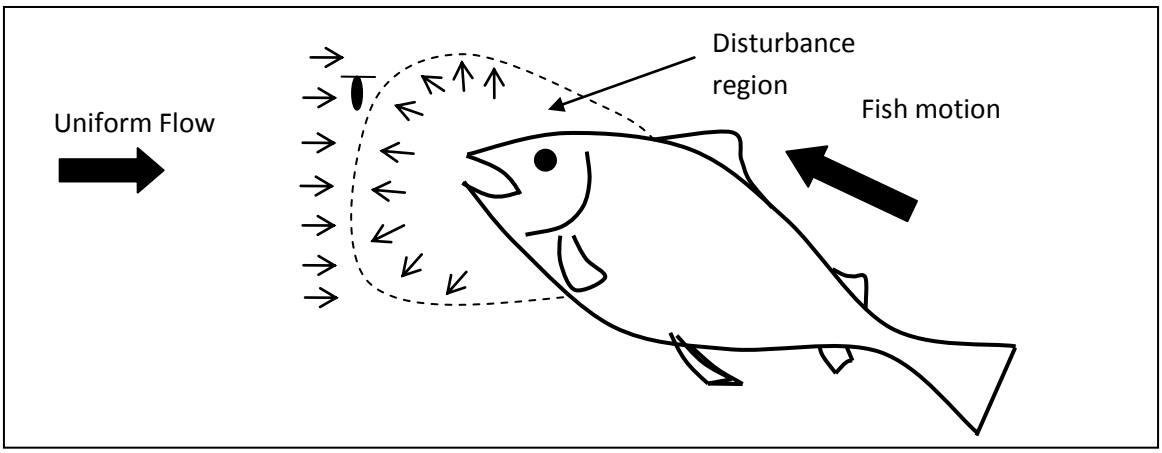

Figure 5-6: Schematic representation of the flow field in front of the fish in a uniform cross-flow. A disturbance region is generated in front of the fish head. The boundary of this region is depicted by a large change in velocity direction within a small length. The forward extent of the disturbance region increases with the fish motion.

Chapter 6

Future Work

While the thesis has provided answers to various biological questions, it has created more avenues for future work that potentially can lead to additional insights on predator-prey interaction. Suggested future work includes advancing the measurement system for multi-scale flows (Section 6.1), modeling copepod sensing and locomotion (Section 6.2), and understanding the universality of fish feeding strategy on evasive copepods (Section 6.3).

6.1 Towards advancing measurement system for multi-scale flows

The infrared tomographic PIV + 3D PTV system implemented in this work is capable of obtaining a time-resolved volumetric velocity field, and measuring fish and copepod trajectories and velocities. While a spatially resolved velocity around both the fish and the copepod is desired, the current system limits this capability since it has a trade-off between obtaining both high spatial resolution and large field of view.

As a future work, a system capable of resolving the larger scale flow structures around the fish and the small-scale structures around the copepod is proposed. This may be carried out by assembling a set of two volumetric measurement techniques - a larger field of view (and larger spatial resolution), and a smaller field of view (and smaller spatial resolution). The smaller field of view can be measured within the larger domain at the location of the copepod. The velocity vector fields of both measurement techniques can be superposed into a multi-grid vector field (shown schematically in figure 6-1). This would allow analysis of both large and smaller scale flow structures generated by fish and copepod during aquatic predator-prey interaction. While getting the copepod to stay within the smaller field of view can be challenging, this may be overcome by using a pipette to place the copepod at the specific location, and waiting for the fish to feed.

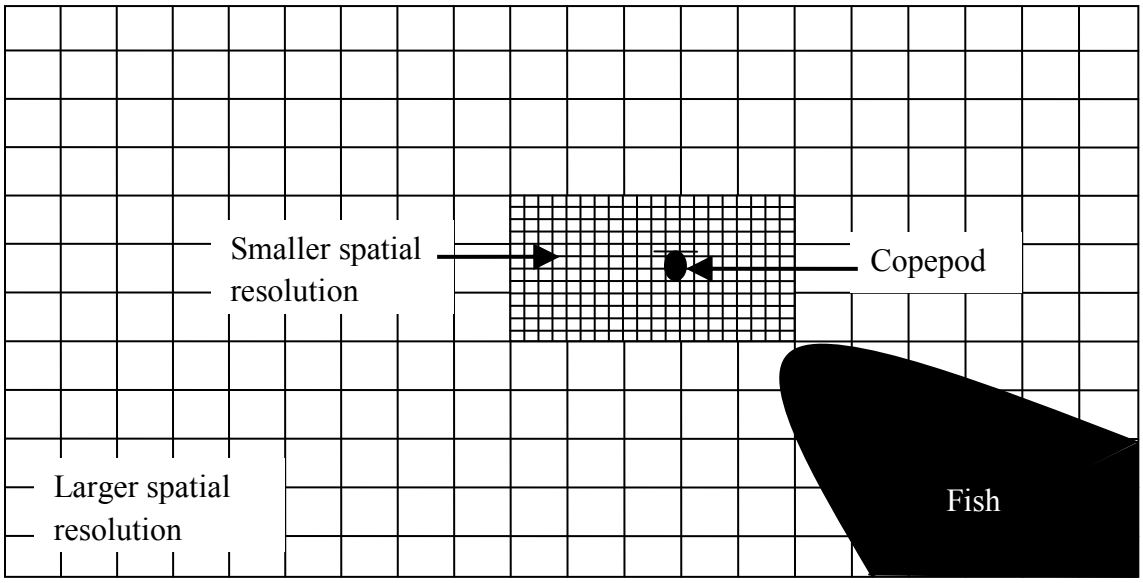

Figure 6-1: Schematic representation of a proposed multi-grid measurement system. Two separate volumetric measurement system is used to measure at large and small spatial resolution.

6.2 Towards modeling copepod sensing and locomotion

6.2.1 Sensing

A sudden increase in MPSR has been found to trigger jumps by the copepods upstream of cylinder and during ram feeding of fish. However, the relationship between copepod orientation and MPSR is still unknown. Finding this relationship may provide a better understanding of how the local normal and shear strain rates play a role in bending the setae of the copepod which are thought to trigger the escape. Furthermore, the role of Lagrangian acceleration and vorticity could also be investigated based on the orientation of the copepod.

The current measurement system does not provide the orientation of the copepod due to a large field of view. Thus, a smaller field of view with higher spatial resolution is required to obtain the orientation of copepods. The orientation of the copepod and its relationship to the various strain rate components within the velocity gradient tensor could provide a more accurate probabilistic model for copepod response to various magnitudes of strain rate and copepod orientation.

6.2.2 Locomotion

The acceleration, *dv/dt* of the copepods from an inertial frame of reference can be obtained directly from the results, together with other flow related quantities. This acceleration is a result of various forces action on the copepods, including propulsive force generated by copepods swimming which cannot be measured directly. However, the propulsion, $\boldsymbol{F_c}$, could be estimated using a modified Maxey-Riley equation discussed in Chapter 1 (Section 1.2.1.2):

$$\left(2\rho_p + \rho_f\right)\frac{d\boldsymbol{v}}{dt} = \frac{9\mu\phi(Re_p)}{a^2}(\boldsymbol{v}-\boldsymbol{u}) + 3\rho_f\frac{D\boldsymbol{u}}{Dt} + \left(\rho_p - \rho_f\right)\boldsymbol{g} + \boldsymbol{F}_{\boldsymbol{c}} \quad (6\text{-}8)$$

where $\phi(Re_p) = 1 + 0.1935\mathrm{Re}^{0.6305}$ for $20 < \mathrm{Re_p} \leq 260$ (Clift *et al*. 1978); **v** is the velocity of the particle (i.e. copepod); $\boldsymbol{u}$ is the local velocity of the fluid; ρ_p and a are the density and radius of the particle, respectively; ρ_f and μ are the density and kinematic viscosity of the fluid, respectively; $\nu = \mu / \rho_f$; $\boldsymbol{g}$ is gravitational acceleration; and $\boldsymbol{F_c} = \rho_p\boldsymbol{a_c}$ is the propulsive force generated by the copepod swimming ($\boldsymbol{F_c} = 0$ when not jumping; $\boldsymbol{a_c}$ is the acceleration due to propulsion). *D/Dt* is the material derivative following the fluid particle, while *d/dt* is the total derivative following copepod.

To find $\boldsymbol{a_c}$, equation 6-8 can be written as:

$$\boldsymbol{a}_{\boldsymbol{c}} = \frac{1}{\rho_p}\left(\left(2\rho_p + \rho_f\right)\frac{d\boldsymbol{v}}{dt} - \frac{9\mu\phi(Re_p)}{a^2}(\boldsymbol{v}-\boldsymbol{u}) - 3\rho_f\frac{D\boldsymbol{u}}{Dt} - \left(\rho_p - \rho_f\right)\boldsymbol{g}\right) \quad (6\text{-}9)$$

Solving eqation (6-9) can provide the rate of change of momentum of the copepods by their swimming propulsion. This can allow calculation of forces and impulse generated during their swimming, and can be used to find out if it is proportional to the local flow disturbances. These quantities are of great interest to biologists.

6.3 Universality of fish feeding on evasive prey

Zebrafish and blennies have shown similar feeding techniques on copepods (evasive prey). For both fish species, they approach the copepod slowly, and execute sudden

acceleration (ram feeding) to feed on the copepod. Is the slow approach, followed by sudden acceleration common to other fish and living organisms? Are there other approaches used by fish? A proposed future work is to answer these questions by studying additional marine organisms.

Bibliography

Adhikari D, Longmire EK (2012) Visual hull method for tomographic PIV measurement of flow around moving objects. *Exp Fluids.* **53**(4): 943-964

Adhikari D, Longmire E, Gemmell B (2012) Infrared tomographic PIV measurement of aquatic predator-prey interaction. *16th Int Symp on Applications of Laser Techniques to Fluid Mechanics*. Lisbon, Portugal.

Adhikari D, Longmire EK (2013) Infrared tomographic PIV and 3-D motion tracking system applied to aquatic predator-prey interaction. *Meas. Sci. Tech.* **24**(2) 024011

Adhikari D, Hallberg M, Longmire E (2013) Simulataneous 3D PTV and infrared tomographic PIV measurement of zooplankton distribution in unsteady flow fields. *10th International Symposium on Particle Image Velocimetry*, Delft, The Netherlands.

Adrian RJ, Westerweel J (2011) Particle Image Velocimetry. *Cambridge University Press*, New York, USA

Atkinson CH, Dillon-Gibbons CJ, Herpin H, Soria J (2008) Reconstruction Techniques for Tomographic PIV (Tomo-PIV) of a Turbulent Boundary Layer. *14th Int Symp on Applications of Laser Techniques to Fluid Mechanics*. Lisbon, Portugal

Atkinson C, Soria J (2009) An efficient simultaneous reconstruction technique for tomographic particle image velocimetry. *Exp Fluids.* **47**:553-568

Balachandar S, Eaton JK (2010) Turbulent Dispersed Multiphase Flow *Annu. Rev. Fluid. Mech.* **40**: 111-133

Bandyopadhyay PR (2005) Trends in biorobotic autonomous undersea vehicles *IEEE J Ocean Eng.* **30**: 109-139

Belden J, Techet AH (2011) Simultaneous quantitative flow measurement using PIV on both sides of the air-water interface for breaking waves. *Exp Fluids.* **50**:149-161

Blair D, Dufresne, E. "Matlab Particle Tracking." *Matlab Particle Tracking*. Georgetown University, n.d. Web. 21 Oct. 2013. <http://physics.georgetown.edu/matlab/>.

Buskey EJ, Lenz PH and Hartline DK (2002) Escape behavior of planktonic copepods in response to hydrodynamic disturbances: high speed video analysis" *Mar Ecol Prog Ser.* **235**: 135-146

Catton KB, Webster DR, Brown J, Yen J (2006) Quantitative analysis of tethered and free-swimming copepodid flow fields. *J Exp Biol.* **210**:299-310

Catton KB, Webster DR and Yen J (2012) The effect of fluid viscosity, habitat temperature, and body size on the flow disturbance of *Euchaeta*. *L&O:F&E.* **2**: 80-92

Clarke RD, Buskey EJ, Marsden KC (2005) Effects of water motion and prey behavior on zooplankton capture by two coral reef fishes. *Mar Biol.* **146**: 1145-1155

Clarke RD, Finelli CM, Buskey EJ (2009) Water flow controls distribution and feeding behavior of two co-occuring coral reef fishes: II. Laboratory experiments. *Coral Reefs* **28**(2): 475-488

Clift R, Grace JR, Weber ME (1978) Bubbles, drops and particles. *Academic Press*, New York.

Colin SP, Costello JH, Hansson LJ, Titelman J, Dabiri JO (2010) Stealth predation and predatory sucess of the invasive ctenophore *Mnemiopsis leidyi*. *Proc Natl Acad Sci USA*. **107**(40):17223-17227

Dabiri JO (2005) Unsteady fluid mechanics of starting-flow vortex generators with time-dependent boundary conditions. *PhD Thesis*. California Institute of Technology, Pasadena, California, USA.

Dabiri JO, Colin SP, Katija K, Costello JH (2010) A wake-based correlation of swimming performance and foraging behavior in seven co-occurring jellyfish species. *J Exp Biol*. **213**: 1217-1225

Day SW, Higham TE, Cheer AY, Wainwright PC (2005) Spatial and temporal patterns of water flow geenrated by suction feeding bluegill sunfish Lepomis macrochirus resolved by Particle Image Velocimetry. *J Exp Biol.* **208**: 2661-2671

Discetti S, Astarita T (2012) A fast multi-resolution approach to tomographic PIV. *Exp Fluids*. **52**(3): 765-777

Elsinga GE (2007) Tomographic particle image velocimetry and its application to turbulent boundary layers. *Dissertation*, Delft University of Technology

Elsinga GE, Scarano F, Wieneke B, van Oudheusden BW (2006) Tomographic particle image velocimetry. *Exp Fluids.* **41**: 933-947

Elsinga GE, Westerweel J (2012) Tomographic-PIV measurement of the flow around a zigzag boundary layer trip. *Exp Fluids.* **52**(4): 865-876

Epps BP, Techet AH (2007) Impulse Forces Generated During Unsteady Maneuvering of Swimming Fish. *Exp Fluids.* **43**(5): 691-700

Fields DM and Yen J (1996) The escape behavior of *Pleuromamma xiphias* from a quantifiable fluid mechanical disturbance. *Zooplankton: sensory ecology and physiology.* Ed. Lenz PH, Hartline DK, Purcell JE, Macmillan DL. pp 323-339

Fields DM and Yen J (1997) The escape behavior of marine copepods in response to a quantifiable fluid mechanical disturbance. *J. Plankton Res.* **19**: 1289-1304

Finelli CM, Clarke RD, Robinson HE, Buskey EJ (2009) Water flow controls distribution and feeding behavior of two co-occuring coral reef fishes: I. Field measurements. *Coral Reefs.* **28**: 461-473

Fish FE and Lauder GV (2006) Passive and active flow control by swimming fishes and mammals. *Annu. Rev. Fluid. Mech.* **38**: 193-224

Flammang BE, Lauder GV, Troolin DR, Strand TE (2011a) Volumetric imaging of fish locomotion. *Biol Lett* DOI:10.1098/rsbl.2011.0282

Flammang BE, Lauder GV, Troolin DR, Strand T (2011b) Volumetric imaging of shark tail hydrodynamics reveals a three-dimensional dual-ring vortex wake structure. *Proc R Soc B* **278**(1725): 3670-3678

Foeth EJ, van Doorne CWH, van Terwisga T, Wieneke B (2006) Time resolved PIV and flow visualization of 3D sheet cavitation. *Exp Fluids.* **40**:503-513

Gao Q, Ortiz-Duenas C, Longmire EK (2010) Eddy structure in turbulent boundary layers based on tomographic PIV. *15th Int Symp on Applications of Laser Techniques to Fluid Mechanics*. Lisbon, Portugal

Gemmell BJ, Adhikari D, Longmire EK (2014) Volumetric quantification of fluid flow reveals fish's use of hydrodynamic stealth to capture evasive prey. *J R Soc Interface* **11**: 20130880

Gonzalez RC, Woods RE (2002) Digital Image Processing. *Prentice-Hall*, New Jersey

Granata TC and Dickey TD (1991) The fluid mechanics of copepod feeding in a turbulent flow: A theoretical approach. *Prog. Oceanogr.* **26**: 243-261

Guasto JS, Rusconi R, Stocker R (2012) Fluid Mechanics of Planktonic Microorganisms. *Annu. Rev. Fluid. Mech*. **44**:373-400

Hain R, Kahler CJ, Michaelis D (2008) Tomographic and time resolved PIV measurements in on a finite cylinder mounted on a flat plate. *Exp Fluids.* **45**(4): 715-724

Hale GM, Querry MR (1973) Optical Constants of Water in the 200-nm to 200-µm Wavelength Region. *Appl Opt.* **12**(3):555-563

Herman GT, Lent A (1976) Iterative reconstruction algorithms. *Comput Biol Med.* **6**:273–294

Heuch PA, Doall MH, Yen J (2007) Water flow around a fish mimic attracts a parasitic and deters a planktonic copepod. *J. Plankton Res.* **29**(1) 3 – 16

Higham TE, Day SW, Wainwright PC (2005) Sucking while swimming: evaluating the effects of ram speed on suction generation in bluegill sunfish *Lepomis macrochirus* using digital particle image velocimetry. *J Exp Biol.* **208**(14): 2653-2660

Hinsch KD (2002) Holographic particle image velocimetry. *Meas Sci Technol.* **13**:61-72

Holzman R, Wainwright PC (2009) How to surprise a copepod: Strike kinematics reduce hydrodynamic disturbance and increase stealth of suction-feeding fish. *Limnol Oceanogr.* **54**(6): 2201-2212

Hook SE, Fisher NS (2001) Sublethal effects of silver in zooplankton: importance of exposure pathways and implications for toxicity testing. *Environ Toxicol Chem.* **20**:568-74

Hori T, Sakakibara J (2004) High Speed Scanning Stereoscopic PIV for 3D Vorticity Measurement in Liquids. *Meas Sci Technol.* **15**:1067-1078

Hounsfield GN (1973) Computerized transverse axial scanning (tomography): Part 1. Description of system. *Br Inst Radiology.* **46**:1016-1022

Jeon YJ, Sung HJ (2010) PIV measurement of flow around an arbitrarily moving body. *Exp Fluids*. **50**:787-798

Jeon YJ, Sung HJ (2011) Simultaneous PIV measurement of flow around a moving body. *9th Int Symp on Particle Image Velocimetry*. Kobe, Japan.

Jiang H and Kiørboe T (2011) The fluid dynamics of swimming by jumping in copepods. *J R Soc Interface*. **8**: 1090-1103

Jiang H and Osborn TR (2004) Hydrodynamics of copepods: a review. *Surveys in Geophysics* **25**: 339-370

Jumars PA, Trowbridge JH, Boss E, Karp-Boss L (2009) Turbulence-plankton interaction: a new cartoon. *Mar. Ecol.* **30**: 133-150

Khalitov DA, Longmire EK (2002) Simultaneous two-phase PIV by two-parameter phase discrimination. *Exp Fluids*. **32**: 252-268

Kiger KT, Pan C (2000) PIV Technique for the Simultaneous Measurement of Dilute Two-phase Flows. *J Fluids Eng*. **122**: 811-818

Kim H, Groβe S, Elsinga GE, Westerweel J (2011) Full 3D-3C velocity measurement inside a liquid immersion droplet. *Exp Fluids.* **51**(2): 395-405

Kiørboe T, Saiz E and Visser A (1999) Hydrodynamic signal perception in the copepod *Acartia tonsa*" *Mar Ecol Prog Ser.* **179**: 97-111

Kiørboe T, Jiang H, Colin SP (2010) Danger of zooplankton feeding: The fluid signal generated by ambush feeding copepods. *Proc R Soc B*. **277**: 3229-3237

Kiørboe T and Visser AW (1999) Predator and prey perception in copepods due to hydromechanical signals. *Mar Ecol Prog Ser*. **179**: 81-95

Khun M, Ehrenfried K, Bosbach J, Wagner C (2010) Large-scale tomographic particle image velocimetry using helium-filled soap bubbles. *Exp Fluids.* **50**:929-948

Lauder GV and Clark BD (1984) Water flow patterns during prey capture by teleost fishes. *J. Exp Biol.* **113**: 143-150

Lauder GV and Drucker EG (2004)Morphology and experimental hydrodynamics of fish fin control surfaces. *IEEE J Ocean Eng*. **29**: 556-571

Laurentini A (1994) The Visual Hull Concept for Silhouette-Based Image Understanding. *IEEE Trans Pattern Anal machine Intell* **16**:150-162

Laurentini A (1997) How Many 2D Silhouettes Does it Take to Reconstruct a 3D Object? *Comput. Vision and Image Understanding* **67**:81-87

Laws EM and Livesey JL (1978) Flow Through Screens. *Annu. Rev. Fluid. Mech*. **10**: 247 - 266

Lenz PH and Hartline DK (1999) Reaction times and force production during escape behavior of a calanoid copepod, *Undinula vulgaris*. *Mar Biol.* **133**:249-258

Lenz PH and Yen J (1993) Distal setal mechanoreceptors of the first antennae of marine copepods. *Bull Mar Sci.* **53**: 170-179

Lua KB, Lai KC, Lim TT, Yeo KS (2010) On the aerodynamic characteristics of hovering rigid and flexible hawkmoth-like wings. *Exp Fluids.* **49**: 1263-1291

Lythogoe JN, Partridge JC (1989) Visual pigments and the acquisition of visual information. *J Exp Biol.* **146**: 1-20

Maas HG, Gruen A, Papantoniou D (1993) Particle tracking velocimetry in three-dimensional flows. Part 1. Photogrammetric determination of particle coordinates. *Exp Fluids*. **15**:133–146

Malkiel E, Sheng J, Katz J, Strickler JR (2003) The three-dimensional flow field generated by a feeding calanoid copepod measured using digital holography. *J. Exp. Biol.* **206**: 3657-3666

Matusik W, Buehler C, Raskar R, Gortler SJ, McMillan L (2000) Image-Based Visual Hulls. *SIGGRAPH '00 Proceedings of the 27th annual conference on Computer graphics and interactive techniques*. New Orleans, Louisiana USA

Mauchline J (1998) The Biology of Calanoid Copepods. San Diego, CA. *Academic Press.*

Mehta RD and Bradshaw P (1979) Design Rules for Small Low Speed Wind Tunnels. *Aeronautical Journal*, **83**(827): 443-449

Mulayim AY, Yilmaz U, Atalay V (2003) Silhouette-Based 3-D Model Reconstruction From Multiple Images. *IEEE Trans Syst Man Cybern B* **33**:582-591

Maxey MR and Riley JJ (1983) Equation of motion for a small rigid sphere in a nonuniform flow. *Phy Fluids.* **26**(4): 883-889

Mei R (1996) Velocity fidelity of flow tracer particles. *Exp Fluids.* **22**: 1-13

Melling A (1997) Tracer particles and seeding for particle image velocimetry. *Meas. Sci. Tech.* **8**(12): 1406:1416

Mendelson and Techet (2013) 3D Synthetic Aperture PIV of Swimming Fish. *10th Int Symp on Particle Image Velocimetry*, Delft, The Netherlands

Michaelides EE (1997) Review – The Transient Equation of Motion for Particles, Bubbles and Droplets. *J. Fluids Eng.* **119**: 233-247

Murphy DW (2012) Planktonic propulsion: The hydrodynamics, kinematics, and design of metachrony. *PhD Thesis*. Gerogia Institute of Technology, Atlanta, Georgia, USA.

Murphy DW, Webster DR, Yen J (2011) A High-Speed Tomographic PIV Investigation of Plankton-Turbulence Interaction. *9th Int Symp on Particle Image Velocimetry*. Kobe, Japan

Murphy DW, Webster DR and Yen J (2012) A High Speed Tomographic PIV System for Measuring Zooplankton Flow. *L&O: Methods* **10**: 1096-1112

Novara M, Batenburg KJ, Scarano F (2010) Motion tracking-enhanced MART for tomographic PIV. *Meas Sci Tech.* **21**:035401

Ortiz-Duenas C, Kim J, Longmire EK (2010) Investigation of liquid-liquid drop coalescence using tomographic PIV. *Exp Fluids*. **49**:111-129

Peng J and Dabiri JO (2009) Transport of inertial particles by Lagrangian coherent structures: application to predator-prey interaction in jellyfish feeding. *J Fluid Mech.* **63**: 75-84

Pope SB (2000) Turbulent Flows. *Cambridge University Press*, Cambridge, UK.

Prairie JC, Sutherland KR, Nickols KJ, Kaltenberg AM (2012) Biophysical interactions in the plankton: A cross-scale review. *L&O: F&E* **2**: 121-145

Raffel M, Willert CE, Wereley ST, Kompenhans J (1993) Particle Image Velocimetry: A practical guide. *Springer-Verlag Berlin Heidelberg*, New York.

Ramamurthy AS, Han SS, Biron PM (2013) Three-Dimensional Simulation Parameters for 90˚ Open Channel Bend Flows. *J Comp Civil Eng.* **27**(3):282-291

Rand R, Pratap R, Ramani D, Cipolla J, Kirschner I (1997) Impact dynamics of a supercavitating underwater projectile. *DETC ASME Des Eng Tech Conf*

Reiser MB, Dickinson MH (2003). A test bed for insect-inspired robotic control. *Phil Trans R Soc Lond A* **361**: 2267–2285

Robinson HE, Christopher MF, Buskey, EJ (2007) The turbulent life of copepods: effects of water flow over coral reef on their ability to detect and evade predators. *Mar Ecol Prog Ser.* **349**: 171-181

Ruiz LA, Whittlesey RW, Dabiri JO (2011) Vortex-enhanced propulsion. *J Fluid Mech* **668**: 5-32.

Sakakibara J, Nakagawa M, Yoshida M (2004) Stereo-PIV study of flow around a maneuvering fish. *Exp Fluids.* **36**:282-293

Scarano F, Poelma C (2009) Three-dimensional vorticity patterns of cylinder wakes. *Exp Fluids*. **47**:69-83

Schreiner A (2011) Eye Tracking Program. *Research Report*. Department of Aerospace Engineering & Mechanics, University of Minnesota.

Siddiqui MHK (2007) Velocity measurements around a freely swimming fish using PIV. *Meas Sci Technol* **18**:96-105

Strickler JR and Bal AK (1973) Setae of the first antennae of the copepod *Cyclops scutifer* (Sars): Their structure and importance. *Proc Nat Acad Sci*. **70**: 2656-2659

Sutherland KR, Madin LP (2010) Comparative jet wake structure and swimming performance of salps. *J Exp Biol.* **213**: 2967-2975

Sutherland KR, Dabiri JO, Koehl MAR (2011) Simultaneous field measurements of ostracod swimming behavior and background flow. *L&O: F&E.* **1**: 135-146.

Talapatra S and Katz J (2013) Three-dimensional velocity measurements in a roughness sublayer using microscopic digital in-line holography and optical index matching. *Meas Sci Technol.* **24**: 024004

Triantafyllou MS, Triantafyllou GS, Yue DKP (2000) Hydrodynamics of fishlike swimming. *Annu. Rev. Fluid. Mech.* **32**: 33-53

Tytell ED, Lauder GV (2004) The hydrodynamics of eel swimming. I. Wake structure. *J Exp Biol.* **207**: 1825-1841

Vanek B, Bokor J, Balas GJ, Arndt REA (2007) Longitudinal motion control of a high-speed supercavitation vehicle. *J Vib Control.* **13**: 159-184

Verhoeven D (1993) Limited-data computed tomography algorithms for physical sciences. *Appl Opt.* **32**:3736-3754

Viitasalo M, Kiørboe T, Flinkman J, Pedersen LW, Visser AW (1998) Predation vulnerability of planktonic copepods: consequences of predator foraging strategies and prey sensory abilities. *Mar Ecol Prog Ser.* **175**: 129-142

Waggett RJ, Buskey EJ (2006) Copepod sensitivity to flow fields: detection by copepods of predatory ctenopores. *Mar Ecol Prog Ser*. **323**: 205-211

Waggett RJ, Buskey EJ. (2007) Copepod escape behavior in non-turbulent and turbulent hydrodynamic regimes. *Mar Ecol Prog Ser.* **334**:193-198

Webster DR, Weissburg MJ (2009) The Hydrodynamics of Chemical Cues among Aquatic Organisms. *Annu Rev Fluid Mech.* **41**: 73-90

White FM (2003) Fluid Mechanics. *McGraw-Hill*. New York, USA.

Wieneke B (2008) Volume self-calibration for 3D particle image velocimetry. *Exp Fluids.* **45**:549-556

Wilga CD, Lauder GV (2004) Hydrodynamic function of the shark's tail. *Nature* **430**: 850.

Willert CE, Gharib M (1992) Three-dimensional particle imaging with a single camera. *Exp Fluids*. **12**: 353-358.

Woodson CB, Webster DR, Weissburg MJ and Yen J (2005) Response of copepods to physical gradients associated with structure in the ocean. *Limnol. Oceanogr.* **50**: 1552-1564

Worth NA, Nickels TB (2008) Acceleration of Tomo-PIV by estimating the initial volume intensity distribution. *Exp Fluids.* **45**:847-856.

Yamazaki H and Squires KD (1996) Comparison of oceanic turbulence and copepod swimming". *Mar Ecol Prog Ser.* **144**: 299-301

Yu J, Hu Y, Huo J, Wang L (2009) Dolphin-like propulsive mechanism based on an adjustable Scotch yoke. *Mech Mach Theory.* **44**:603-614

Yen J and Fields D (1992) Escape reponses of Acartia hudsonica nauplii from the flow field of Temora longicornis. *Arch. Hydrobiol. Beih. Ergebn. Limnol.* **36**: 123-134

Yen J, Lenz PH, Gassie DG and Hartline DK (1992) Mechanoreception in marine copepods: electrophysiological studies on the first antennae. *J Plankton Res.* **14**: 495-512

Yen J (2000) Life in Transition: Balancing Inertial and Viscous Forces by Planktonic Copepods. *Biol Bull.* **198**: 213-224

Appendix A: Head loss calculation and motor power requirement for the channel

Head loss is energy loss in bulk fluid, which is normalized by the velocity of the fluid and its density. Head loss of the fluid flow consists of friction loss (or major loss) and minor losses. Friction loss is the dissipation in energy of the fluid due to viscous effects generated at the surface of the channel. Minor losses are energy losses due to various obstructions that may be present in a water channel or pipe (e.g. channel entrance, exit, expansion, contraction, bends, etc).

Total head loss in a channel, Δh_{total}, is given by the following expression (White 2003):

$$\Delta h_{total} = \Delta h_{friction} + \sum \Delta h_{minor} = \frac{U^2}{2g}\left(\frac{fL}{D_H} + \sum K\right) \quad \text{(A-1)}$$

where $\Delta h_{friction}$ is friction loss, Δh_{minor} is minor losses, U is velocity of fluid, g is gravitational constant, L is the length of channel, D_H is the hydraulic diameter, f is the Darcy friction factor, and K is the loss coefficient of various obstructions within the channel.

For the current water channel, the friction losses (major loss) consist of losses through straight and corners sections. The minor losses includes the bends at the corners, flow through screens and honeycombs. The friction factor was obtained from Moody diagram, and the minor losses due to bends were approximates from White (2003). The minor losses due to porous screens and honeycombs was estimated from Laws and Livesey (1978).

From equation (A-1), the total head loss is a quadratic function of the fluid velocity. In order to drive the flow in the channel, a motor capable of driving a paddlewheel that can compensate the energy loss is desired. After considering a 30% efficiency of the motor and paddlewheel system, the relationship between the power of the motor and the velocity of the water channel is provided in figure A-1.

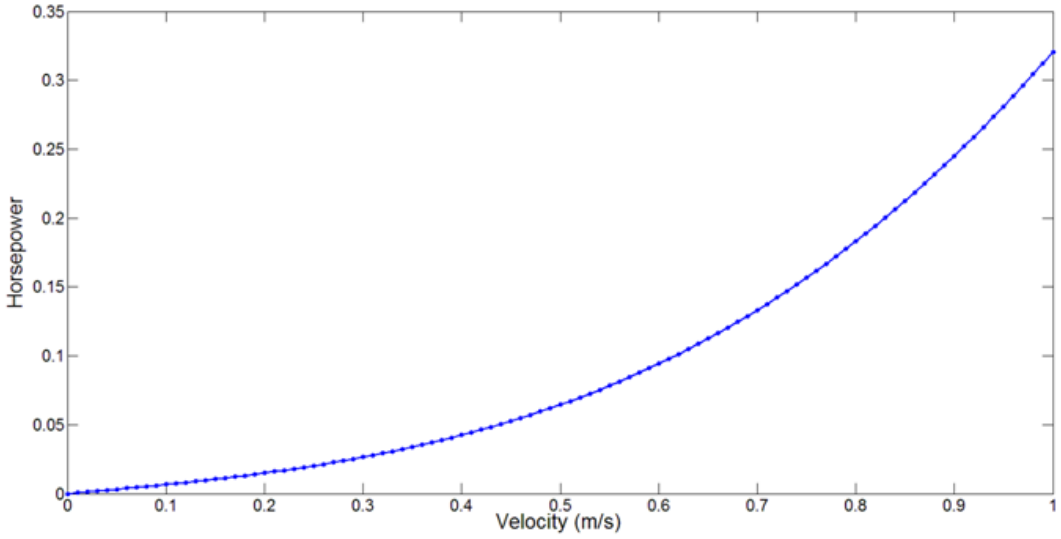

Figure A-1: Graph of horsepower needed to drive the paddlewheel against the velocity of the fluid.

The maximum flow velocity desired for the experiment was 0.3 m/s. This translates to a ~0.03 hp from figure A-1. Considering experiments succeeding the current experiment may require higher speeds, and motor availability, a 0.25 hp permanent magnet motor was chosen. A high torque and low revolution speed motor was desired due to the size of the paddlewheel. Thus, the permanent magnet motor fitted with a gear assemby was purchased.

Appendix B: Circular Hough Transform

Circular Hough Transform (CHT) is a feature detection technique utilized in digital image processing. The purpose of this technique is to find circles within a picture using a voting procedure. This procedure is a carried out in a parameter space (also known as accumulator space) by identifying the local maximum points. CHT is derived from the conventional Hough transform, which is used to identify straight lines.

CHT is performed by first transforming the image space to the accumulator space. After which, the maximum point in the accumulator is detected (or "voted") and provides the location of the circle in the image. These two stages of CHT are described below.

(1) Transform image to accumulator

The equation of a circle is given as:

$$x = a + R\cos\theta$$
$$y = b + R\sin\theta, \quad \text{(B-1)}$$

where *(x, y)* are the image coordinates, R is a known radius of the circle with center at unknown (a , b), and θ varies from 0 to 2π. For the current work, the radius is assumed constant. Equation B-1 is reformulated to the following parametric equations:

$$a = x - R\cos\theta$$
$$b = y - R\sin\theta \quad \text{(B-2)}$$

Equations B-2 transform the given image (x, y) to an accumulator space (a, b). For example, consider four points in the image along the circumference of a circle (see figure B-1a). The points are mapped into the accumulator using equation B-2 (see figure B-1b). It should be noted that from the figure, and equations B-1 and B-2 that each point in the image maps to a circle in the accumulator.

(2) Selecting the peak and locating the circle

Now, consider an image with coordinates *(x, y)*, where every pixel intensity is mapped to the accumulator in *(a,b)* space. When every pixel is transformed from image to accumulator, the peak value in the parameter space is identified. The peak value corresponds to local maximum number of "votes" that occurred in the accumulator. For example, the peak location in figure B-2 is at (a_1, b_1). This coordinate provides the center of a circle in the image.

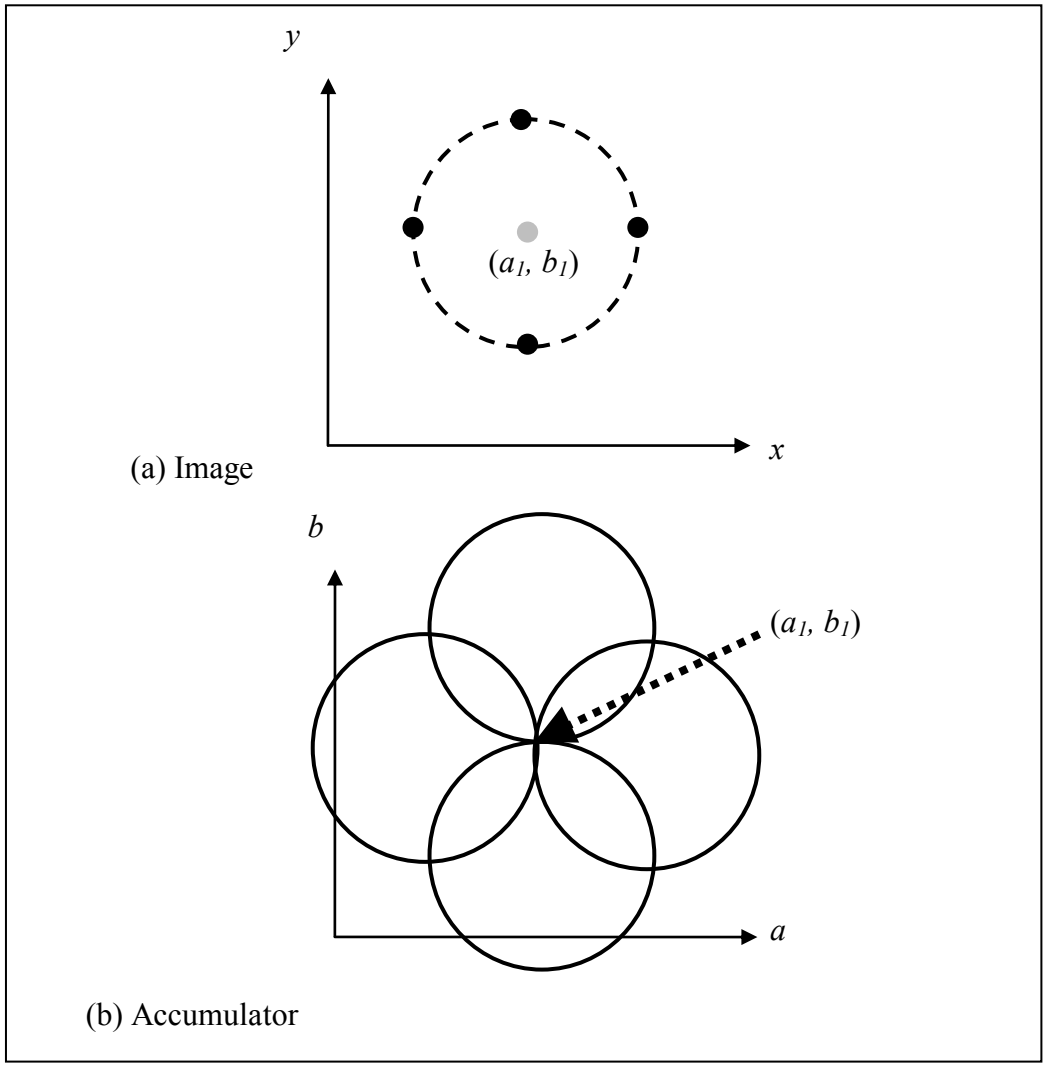

Figure B2-2: (a) Image space showing 4 points representing a circle. (b) Accumulator space with four circles corresponding to the 4 points in the image. The peak location (a_1, b_1) in the accumulator represents the center of the circle in the image.

Appendix C: Formulae derivations for obscured regions of a simple object shape and standard four-camera configuration

Consider the camera arrangement and object orientation shown in figure C-1. We assume the lines of sight are parallel for each camera, and the object is a cuboid. The inclination angles of Cameras 1-4 are α_1, α_2, α_3, and α_4 respectively. The dimensions of the cuboid are *a* (length) x *b* (width) x *c* (depth), where *a* and *b* are parallel to the laser sheet, and the side faces of the object are aligned with the camera angles. The distance from the rear of the object (relative to the cameras) to the rear edge of the laser sheet is given by *t*.

The fully obscured region (green in figure C-1) is not optically accessible by any camera. For the given object orientation, this region can be either trapezoidal or pyramidal in shape, depending on the laser sheet thickness, object location, and object dimension. Mathematically, the following relations must be satisfied for a trapezoidal-shaped fully obscured region:

$$tan(\alpha_1) + tan(\alpha_3) < \frac{b}{t} \quad \text{(C-1)}$$

$$tan(\alpha_2) + tan(\alpha_4) < \frac{a}{t} \quad \text{(C-2)}$$

Otherwise, the fully obscured region is pyramidal.

The partially obscured region (blue in figure C-1), which is accessible by less than 3 cameras, can be calculated by subtracting the fully obscured volume from the object "shadow" (i.e. $a \times b \times t$).

Trapezoidal Fully Obscured Region

First, we consider the trapezoidal fully obscured volume (figure C-2) which can be split into a cuboid (blue), 4 half – cuboids (red) and 4 pyramids (green). We can obtain the total volume by summing the 9 parts (figure C-3).

$$a' = a - t \times tan(\alpha_2) - t \times tan(\alpha_4) \quad \text{(C-3)}$$

$$b' = a - t \times tan(\alpha_1) - t \times tan(\alpha_3) \quad \text{(C-4)}$$

(1) Cuboid

$$Volume(Cuboid) = a' \times b' \times t = abt - t^2\left[a\big(tan(\alpha_1) + tan(\alpha_3)\big) + b\big(tan(\alpha_2) + tan(\alpha_4)\big)\right] + t^3\big(tan(\alpha_1) + tan(\alpha_3)\big)\big(tan(\alpha_2) + tan(\alpha_4)\big) \quad \text{(C-5)}$$

(2) Total Volume of 4 Half Cuboids

$$Volume(Half\ Cuboids) = \frac{1}{2}\Big[a't\Big(\big(tan(\alpha_1) + tan(\alpha_3)\big) + b't\big(tan(\alpha_2) + tan(\alpha_4)\big)\Big)\Big] = \frac{t^2}{2}[a(tan(\alpha_1) + tan(\alpha_3)) + b(tan(\alpha_2) + tan(\alpha_4))] - t^3(tan(\alpha_1) + tan(\alpha_3))(tan(\alpha_2) + tan(\alpha_4)) \quad \text{(C-6)}$$

(3) Total Volume of 4 Pyramids

$$Volume(Pyramids) = \frac{1}{3} \times t \times [t \times (tan(\alpha_2) \times tan(\alpha_4) + tan(\alpha_4) \times tan(\alpha_3) + tan(\alpha_3) \times tan(\alpha_2) + tan(\alpha_2) \times tan(\alpha_1))] \quad \text{(C-7)}$$

$$Volume(Fully\ Obscured) = Volume(Cuboid) + Volume(Half\ Cuboids) + Volume(Pyramids) = abt - \frac{t^2}{2}[a(tan(\alpha_1) + tan(\alpha_3)) + b(tan(\alpha_2) + tan(\alpha_4))] + \frac{t^3}{3}(tan(\alpha_1) + tan(\alpha_3))(tan(\alpha_2) + tan(\alpha_4)) \quad \text{(C-8)}$$

The partially obscured region is given by:

$$Volume(Partially\ Obscured) = abt - Volume(Fully\ Obscured)$$

$$=$$

$$t^2\left[\frac{a}{2}(tan(\alpha_1)+tan(\alpha_3))+\frac{b}{2}\big(tan(\alpha_2)+tan(\alpha_4)\big)-\right.$$

$$\left.\frac{t}{3}(tan(\alpha_1)+tan(\alpha_3))(tan(\alpha_2)+tan(\alpha_4))\right] \qquad \text{(C-9)}$$

To simplify eqns (C-8) and (C-9) further, we consider a symmetric camera arrangement (i.e. $\alpha_1 = \alpha_2 = \alpha_3 = \alpha_4 = \alpha$) and a cubic object (i.e. $a = b = c$).

$$Volume(Fully\ Obscured) = a^2t - 2at^2tan(\alpha) + \frac{4t^3}{3}tan^2(\alpha) \qquad \text{(C-10)}$$

$$Volume(Partially\ Obscured) = 2at^2tan(\alpha) - \frac{4t^3}{3}tan^2(\alpha) \qquad \text{(C-11)}$$

where the assumptions for trapezoidal-shape (see eqns C-1 and C-2) both reduce to

$$tan(\alpha) < \frac{a}{2t} \qquad \text{(C-12)}$$

Pyramidal Fully Obscured Region (simplified with $\alpha_1 = \alpha_2 = \alpha_3 = \alpha_4 = \alpha$ and $a = b = c$)

If $tan(\alpha) \geq \frac{a}{2t}$, the fully obscured volume will converge to a pyramidal shape (see green in figure 20)

The volume of the green pyramid (fully obscured region) is given by:

$$Volume(Fully\ Obscured) = \frac{1}{3} \times a \times a \times h = \frac{a^3}{6tan(\alpha)} \quad , \qquad \text{(C-13)}$$

where the height h is found easily by trigonometry.

The partially obscured region is now given by:

$$Volume(Partially\ Obscured)$$
$$= abt - Volume(Fully\ Obscured) - Volume(Fully\ Obscured)$$
$$\times \left(\frac{t-h}{t}\right)^3$$

where the last term is the white optically accessible region in figure C-4. Note, however, that this equation, when simplified, reduces to the same form as equation (C-11).

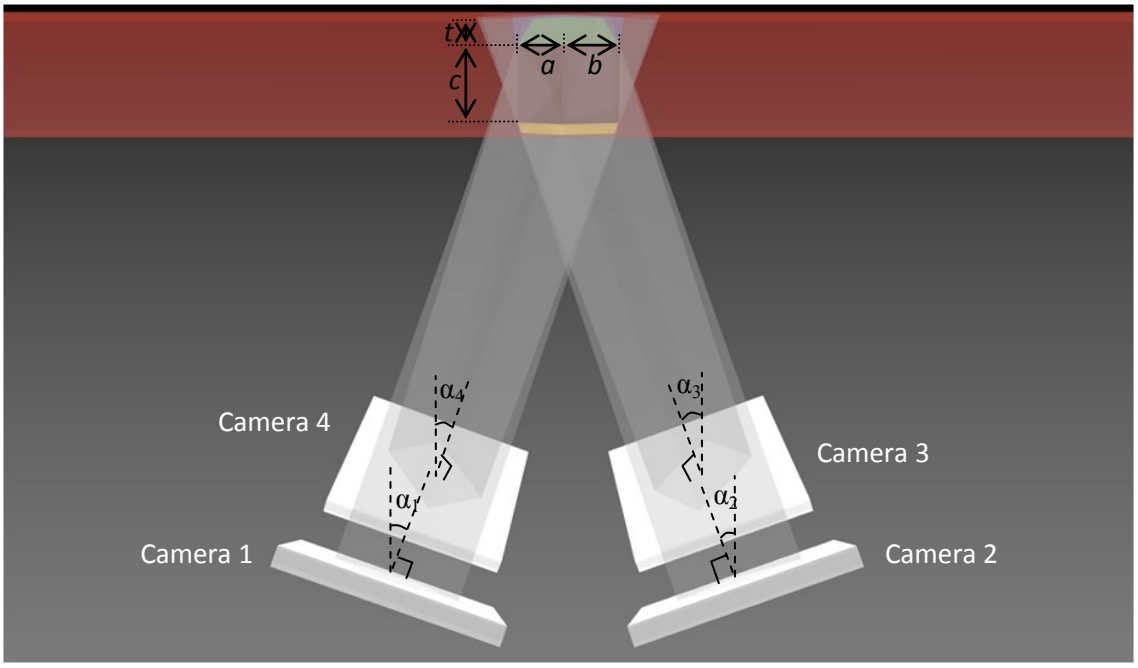

Figure C-1: Schematic diagram of a specific "4-corners" camera arrangement. The inclination angles of cameras 1-4, with respect to the vertical direction, are α_1, α_2, α_3, and α_4 respectively. The dimensions of the cuboid are *a* (length) x *b* (width) x *c* (depth), where *a* and *b* are parallel to the laser sheet, and the side faces of the object are aligned with the camera viewing angles. The distance from the rear of the object (relative to the cameras) to the rear edge of the laser sheet is given by *t*.

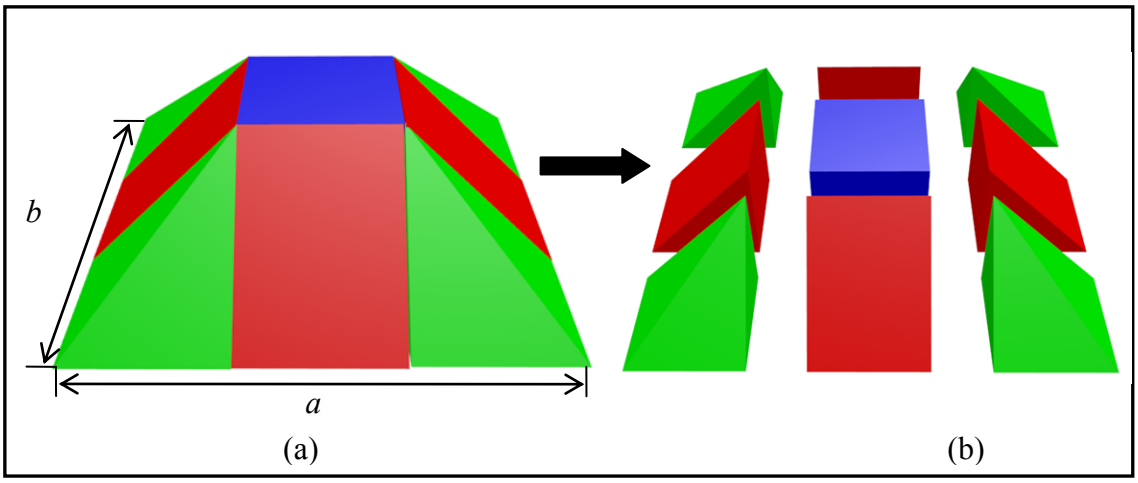

Figure C-2: Schematic representation of the (a) trapezoidal fully obscured region, and (b) an exploded view of the various subvolumes.

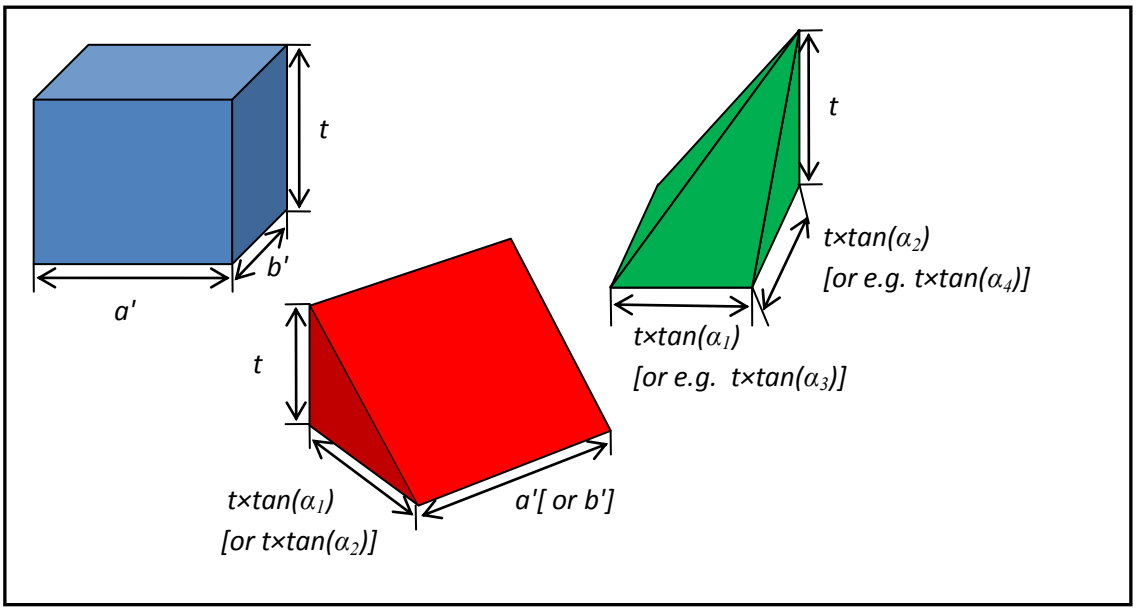

Figure C-3: Schematic drawing and dimensions of a cuboid (blue), half cuboid (red) and pyramid (green) that make up the trapezoid.

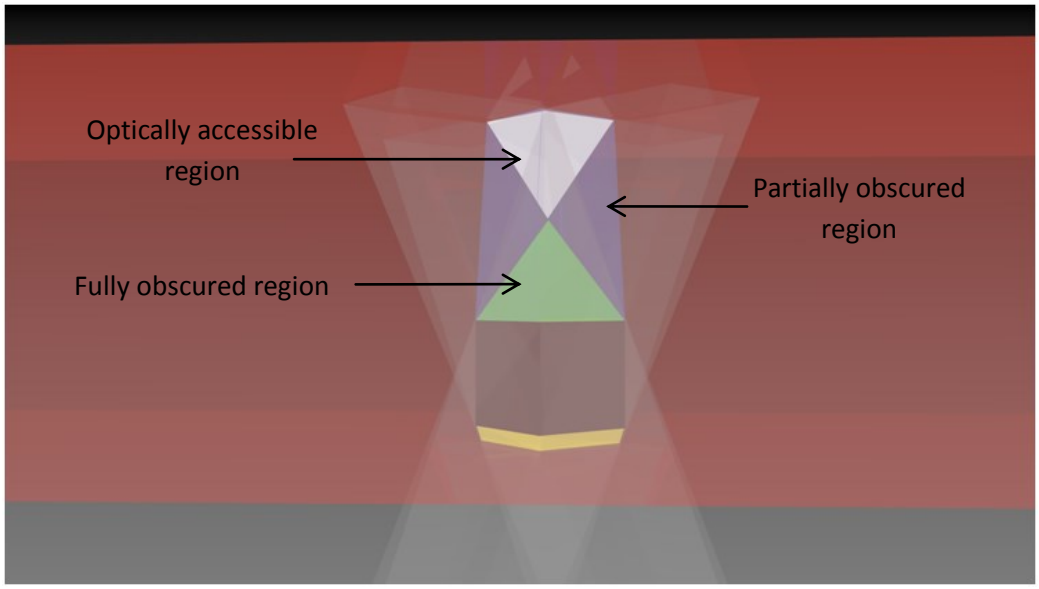

Figure C-4: Schematic diagram of a specific "4-corner" camera arrangement where *t* is large such that *tan (α) > a/2t*. The white region is optically accessible by all cameras.

Appendix D: Proof of {$||\underline{d\boldsymbol{u}/dt}|| \leq ||\underline{\boldsymbol{u}}|| \times MPSR$} for steady state, irrotational flow

Consider a flow field vector, **u,** the acceleration, $d\boldsymbol{u}/dt$**,** of the flow at the location at location $\boldsymbol{x}$ *is:*

$$\frac{d\boldsymbol{u}}{dt} = \frac{\partial \boldsymbol{u}}{\partial t} + \boldsymbol{u} \cdot \nabla \boldsymbol{u} \tag{D-1}$$

For steady state,

$$\partial u/\partial t = 0 \tag{D-2}$$

For irrotational flow,

$$\nabla u = \boldsymbol{D}, \tag{D-3}$$

where $\boldsymbol{D}$ is a symmetric deformation tensor.

Proof:

$$LHS = \left\|\frac{d\boldsymbol{u}}{dt}\right\| = \left\|\frac{\partial \boldsymbol{u}}{\partial t} + \boldsymbol{u} \cdot \nabla \boldsymbol{u}\right\|$$

$$= \|\boldsymbol{u} \cdot \nabla \boldsymbol{u}\| \quad \text{(after substituting equation D-2)}$$

$$= \|\boldsymbol{u} \cdot \boldsymbol{D}\| = \|\boldsymbol{D}\boldsymbol{u}\| \quad \text{(after substituting equation D-3)}$$

$$\leq \|\boldsymbol{D}\|\|\boldsymbol{u}\| \quad \text{(property of matrix norm)}$$

$$= \left(max_{x \neq 0} \frac{\|\boldsymbol{D}\boldsymbol{x}\|}{\|\boldsymbol{x}\|}\right)\|\boldsymbol{u}\|$$

$$= \left(max_{x \neq 0} \frac{\|\lambda \boldsymbol{x}\|}{\|\boldsymbol{x}\|}\right)\|\boldsymbol{u}\| \quad (\lambda \text{ is an eigenvalue})$$

$$= \left(max_{x \neq 0} \frac{\|\lambda\|\|\boldsymbol{x}\|}{\|\boldsymbol{x}\|}\right)\|\boldsymbol{u}\|$$

$$= \|\lambda\|_{\boldsymbol{max}}\|\boldsymbol{u}\|$$

$$= \underline{\|\boldsymbol{u}\| \times MPSR} = RHS\ (Q.E.D.)$$